SQT

ORI TR 1679

(NASA-CR-163207) A PROPAGATION EFFECTS HANDBOOK FOR SATELLITE SYSTEMS DESIGN. A SUMMARY OF PROPAGATION IMPAIRMENTS ON 10-100 GHz SATELLITE LINKS, WITH TECHNIQUES FOR SYSTEM DESIGN Final (Operations Research, HC A17/MF A01 G3/32

N80-25520

Unclas 22953

A PROPAGATION EFFECTS HANDBOOK FOR SATELLITE SYSTEMS DESIGN

A Summary of Propagation Impairments on 10-100 GHz Satellite Links, with Techniques for System Design

March 1980

NASA

Communications Division
NASA Headquarters
Washington, DC 20456

ORI TR 1679

A
PROPAGATION EFFECTS HANDBOOK
FOR
SATELLITE SYSTEMS DESIGN

A Summary of Propagation
Impairments on 10-100 GHz
Satellite Links, with Techniques
for System Design

March 1980

NASA
Communications Division
NASA Headquarters
Washington, DC 20456

ABSTRACT

This Propagation Handbook provides satellite system engineers with a concise summary of the major propagation effects experienced on earth-space paths in the 10 to 100 GHz frequency range. The dominant effect - attenuation due to rain - is dealt with in some detail, in terms of both experimental data from measurements made in the U.S. and Canada, and the mathematical and conceptual models devised to explain the data.

In order to make the Handbook readily usable to many engineers, it has been arranged in two parts. Chapters II-V comprise the descriptive part. They deal in some detail with rain systems, rain and attenuation models, depolarization and experimental data. Chapters VI and VII make up the design part of the Handbook and may be used almost independently of the earlier chapters. In Chapter VI, the design techniques recommended for predicting propagation effects in earth-space communications systems are presented. Chapter VII addresses the questions of where in the system design process the effects of propagation should be considered, and what precautions should be taken when applying the propagation results. This chapter bridges the gap between the propagation research data and the classical link budget analysis of earth-space communications system.

PREFACE

This Handbook could never have been prepared without the twenty years of NASA and private industry supported research that precedes its publication. The authors at ORI have, in large measure, rearranged and organized work of other researchers to put their contributions into perspective with the overall development of the body of knowledge of tropospheric effects on earth-space microwave paths. The authors' main contributions have come in bridging between the results of others.

Therefore, the credit for this Handbook must go to those cited so liberally as references and to the NASA personnel of the Communications Division of the Office of Space and Terrestrial Applications who have sponsored and guided the development of this Handbook. The authors herein acknowledge their support technically and financially.

Finally, the authors acknowledge the numerous technical discussions, comments, written material, and general guidance provided by Dr. Louis J. Ippolito. To whatever extent this Handbook meets its objectives, it is in large measure due to Dr. Ippolito's guidance.

TABLE OF CONTENTS

PRECEDING PAGE BLANK NOT FILMED

CHAPTER IV. DEPOLARIZATION ON EARTH-SPACE PATHS 4-1

LIST OF FIGURES

LIST OF TABLES

LIST OF COMMON SYMBOLS

Note: Throughout the Handbook the following list of symbols have been employed wherever practicable.

<u>English</u>

a	coefficient in specific attenuation (aR^b - dB/km) relation
a'	multiplicative coefficient in diversity gain relation (dB)
$\tilde{a}$	coefficient in XPD relation
$a_{1t}, a_{2t}, a_{3t}, a_{4t}$	coefficients in DD equations
A	total attenuation (dB)
A_{div}	total attenuation with diversity (dB)
b	coefficient in specific attenuation (aR^b - dB/km) relation
b'	coefficient in diversity gain relation
$\tilde{b}$	coefficient in XPD relation
$b_{1t}, b_{2t}, b_{3t}, b_{4t}, b_{5t}, b_{6t}$	coefficients in DD equations
B	beamwidth (degrees)
B_n	noise bandwidth (Hz)
c	speed of light in free space
C_n^2	Tatarski model coefficient
cm	centimeter

d	raindrop diameter (dm)
d'	separation between earth terminals
d_a	antenna diameter (m)
D	horizontal projection (basal) length of the path
D'	parameter in DD model
$D_\phi(\rho)$	mean square phase variation
DD	Dutton-Dougherty
e	partial pressure of water vapor
f	frequency (GHz)
f_f	fluctuation frequency (Hz)
g	gram
G_D	diversity gain (dB)
G_R	gain reduction (dB)
G/T	performance parameter of a ground station
h	hour
h_p	Planck's constant = 6.626×10^{-34} Watt sec^2
h_t	height of turbulence
H	height of 0^oC isotherm (km)
$I(A)$	diversity advantage
I_c	coherent field component in Ishimaru model
I_i	incoherent field component in Ishimaru model
J-D	Joss-drizzle
J-T	Joss-thunderstorm
k	Boltzmann's constant = 1.38×10^{-23} joule/degree
km	kilometer
K_c	specific attenutation per unit water vapor density

K_ϕ	constant in phase variation model
l	effective path length (km)
l_c	effective path length of clouds
l_n	scale length of turbulent eddy (m)
l_o	parameter in Guassian rain distribution scaling
ℓ	scale length of turbulent eddy (m)
L_o	parameter in turbulence model
L_t	path length through turbulence
LP	Laws and Parsons
m	meter
mm	millimeter
M	average annual rainfall (not including snow)
M'	link margin (dB)
M_d	mass of dry air (kg)
M'_o	no rain link margin (dB)
M_w	mass of water vapor (kg)
MP	Marshall-Palmer
N	refractivity
$\overline{\Delta N^2}$	mean square fluctuations in the refractivity N
N_d	raindrop size distribution function ($m^{-3}mm^{-1}$) or (cm^{-4})
N_o	constant in raindrop size distribution function ($m^{-3}mm^{-1}$) or (cm^{-4})
N_R	number of raindrops at rainrate R
	pressure (N/m^2)
$P(\vert)$	conditional probability
P_{NOISE}	noise power (watts)

$P_t(R)$ =	percentage of year that t-minute rainfall rates R occur
r	path averaged rainrate (mm/h)
r_e	mean earth radius = 6377 km
R	instantaneous rainrate in mm/h at one location
$\overline{R_{1t}}$	parameter in Dutton-Doughterty Model
R_{ave}	path averaged rainrate (mm/h)
R_c	amount of water in a column (kg/m^2)
R_d	dry gas constant (joule/kg^{o}K)
R_w	wet gas constant (joules/kg ^{o}K)
R_{st}	parameter in DD Model
R'_t	parameter in DD Model
RH	relative humidity
R-H	Rice-Holmberg
s	path length along the path
S^2	signal variance
t	time
T	temperature (^{o}K or ^{o}C)
$\tilde{T}$	time period
$\tilde{T}_1$,etc.	instant in time period T
T_{2t}	parameter in DD Model
T_m	mean absorption temperature (^{o}K)
T_s	apparent sky temperature (^{o}K)
T_{st}	parameter in Dutton-Dougherty Model
$T_t(R)$	number of minutes the rainrate exceeds for t-minute intervals
v	specific volume (m^3/kg)
v_d	detector voltage

V_c	visibility in fog (km)
XPD	crosspolarization discrimination
XPI	crosspolarization isolation
XPR	crosspolarization ratio

Greek

α	specific attenuation (dB/km)
α_c	specific attenuation for clouds (dB/km)
β	ratio of rainfall during thunderstorms to total rainfall
β'	orientation of earth-terminal baseline
γ	multiplier in path averaged rain rate
δ	exponent in path averaged rain rate
θ	elevation angle (degrees)
λ	wavelength (m)
Λ	constant in raindrop size distribution function (cm^{-1})
ρ	distance along path
ρ_ϕ	distance between phase variation pints (m)
ρ_w	water vapor density
σ_1^2	amplitude variance
σ_2^2	angle-of-arrival variance (deg^2)
σ_x^2	log-amplitude variance of signal amplitude
σ_ϕ	r.m.s. phase fluctuation
σ_e	r.m.s. phase scintillations
τ	polarization tilt angle
$\Delta\tau$	group delay (m)
ϕ	azimuthal angle
$\Delta\phi$	group delay in radians

CHAPTER I

INTRODUCTION

The satellite communications system designer, considering the use of allocations at Ku-band and above, may have to deal with some harsh realities bearing on circuit availability. These are realities of the weather, and they can have a great impact on the final configuration and cost of the system. The realities are that attenuation due to "mere" rainfall is the largest determinant of circuit reliability in satellite communications systems above 10 GHz, and that in many parts of the U.S. this attenuation is so frequent and severe that it is simply not practical to achieve a normally reasonable level of circuit reliability (say, 99%) with a single Earth station. The rain margin, which for C-band systems amounted to a few decibels in the link budget, can become a huge number for systems at the higher frequencies--so large a number that the designer may be forced to reconsider the circuit performance objectives, or to consider a diversity Earth station.

Besides rain attenuation, there are other mechanisms affecting propagation through the troposphere that impair system performance to some degree and should also be of concern to the designer. These are gaseous and cloud attenuation, rain and ice depolarization, amplitude, phase, and angle-of-arrival scintillation, and sky noise. It is interesting to note that all this takes place in a minute fraction of the Earth-satellite path: less than 20 km out of 40,000. This first, or last, 0.05% of the path has been the subject of intense study for the past ten years, and work on the measurement, understanding and prediction of its propagation effects is continuing today. The system designer, wanting to gain a familiary with the results of this work, and to keep abreast of new developments, soon encounters difficulty in finding the information needed. This is partly because of the number of different journals used to report on research in the propagation area. In the IEEE for example, four societies (AP, COM, MTT, and AES) claim a legitimate interest in some aspects of the subject. Another problem is the lack of a good tutorial or textbook covering the many diverse topics involved.

NASA, which has supported a large part of the experimental work in the propagation area, perceived the need for a handbook of some description that would bring together, under one cover, most of what the system designer needs to know about tropospheric propagation above 10 GHz. This volume is the outcome of a program, sponsored by NASA, to produce such a Handbook.

This Propagation Handbook for satellite system engineers provides a concise summary of the major propagation effects experienced on earth-space paths in the 10 to 100 GHz frequency range. The dominant effect--attenuation due to rain--is dealt with in some detail, in terms of both experimental data from measurements made in the U.S. and Canada, and the mathematical and conceptual models devised to explain the data.

Other effects such as clear air attentation and depolarization are also presented. In the case of clear air attenuation, adequate coverage has been given in other publications and so only a summary of the estimation techniques is presented. The estimation of depolarization due to rain and ice has not been developed to the degree required for preparing good design estimates for satellite systems. Therefore, a comprehensive chapter on depolarization has been included that attempts to consolidate the work of several investigators in this area.

In order to make the Handbook readily usable to many engineers, it has been arranged in two parts. The next four chapters comprise the descriptive part. They deal in some detail with rain systems, rain and attenuation models, depolarization and experimental data. This descriptive part of the Handbook is intended to provide background for system engineers who want more detail than that presented in the later design chapters.

Chapters VI and VII make up the design part of the Handbook and may be used almost independently of the earlier chapters. In Chapter VI, the design techniques recommended for predicting propagation effects in earth-space communications systems are presented. Some selection has been made from alternative models in order that only one design technique be utilized. This selection was made based on the ability of the technique to model the experimental results. The chapter includes step-by-step procedures for using the prediction models and numerous examples.

Chapter VII addresses the questions of where in the system design process the effects of propagation should be considered, and what precautions should be taken when applying the propagation results. The unadvised use of propagation results in the link margin can result in overdesign. This chapter bridges the gap between the propagation research data and the classical link budget analysis of earth-space communications system. This chapter presents a generalized design procedure, and illustrates its use through extensive examples.

CHAPTER II

CHARACTERISTICS OF RAIN AND RAIN SYSTEMS

2.1 INTRODUCTION

The attenuating and depolarizing effects of the troposphere, and the statistical nature of these effects, are chiefly determined by both the macroscopic and microscopic characteristics of rain systems. The macroscopic characteristics include items such as the size, distribution and movements of rain cells, the height of melting layers and the presence of ice crystals. The microscopic characteristics include the size distribution, density and oblateness of both rain drops and ice crystals. The combined effect of the characteristics on both scales leads to the cumulative distribution of attenuation and depolarization versus time, the duration of fades and depolarization periods, and the specific attenuation/depolarization versus frequency. In this chapter, we discuss how the characteristics are described and measured, and how the microscopic and macroscopic aspects are statistically related to each other. We also describe how one major propagation effect, specific attenuation, can be estimated. This information will serve as background for the rain and attenuation models of the next chapter.

2.2 TYPES AND SPATIAL DISTRIBUTIONS OF RAIN

2.2.1 Stratiform Rain

In the midlatitude regions, stratiform rainfall is the type of rain which typically shows stratified horizontal extents of hundreds of kilometers, durations exceeding one hour and rain rates less than about 25 mm/h (1 inch/h). This rain type usually occurs during the spring and fall months and results, because of the cooler temperatures, in vertical heights of 4 to 6 km. For communications applications, these stratiform rains represent a rain rate which occurs for a sufficiently long period that the link margin may be required to exceed the attenuation associated with a one-inch per hour rain rate. As shown below, this is much easier to do at frequencies below the 22 GHz water absorption line, than for frequencies above the H_2O line.

2.2.2 Convective Rain

Convective rains arise because of vertical atmospheric motions resulting in vertical transport and mixing. The convective flow occurs in a cell whose horizontal extent is usually several kilometers. The cell usually extends to heights greater than the average freezing layer at a given location because of the convective upwelling. The cell may be isolated or embedded in a thunderstorm region associated with a passing weather front. Because of the motion of the front and the sliding motion of the cell along the front, the high rain rate duration is usually only several minutes. These rains are the most common source of high rain rates in the U.S. and Canada.

2.2.3 Cyclonic Storm

Tropical cyclonic storms (hurricanes) sometime pass over the eastern seaboard during the August-October time period. These circular storms are typically 50 to 200 km in diameter, move at 10-20 kilometers per hour, extend to melting layer heights up to 8 km and have high (greater than 25 mm/h) rain rates.

2.2.4 Long-Term Distributions

The stratiform and cyclonic rain types cover large geographic locations and so the spatial distribution of total rainfall from one of these storms is expected to be uniform. Likewise the rain rate averaged over several hours is expected to be rather similar for ground sites located up to tens of kilometers apart.

Convective storms, however, are localized and tend to give rise to spatially nonuniform distributions of rainfall and rain rate for a given storm. S.C. Bloch, et al (1978) at EASCON 78, showed a movie of an image-enhanced weather radar display which clearly showed the decay and redevelopment of a convective cell while passing over Tampa Bay. Clearly the total rainfall and rain rate varies significantly over the scale of 10 km for this region. The effect is attributed to the presence of the large water mass and the heat-island associated with Tampa.

Over more uniform terrain, Huff and Shipp (1969) have observed precipitation correlation coefficients of 0.95 over 5 mile extents for thunderstorms and rainshowers in Illinois. The correlation was also higher along the path of storm motion compared to perpendicular to the path, as would be expected. Note that this correlation is computed for the period of the storm and is not the instantaneous spatial correlation coefficient required to estimate the effectiveness of ground station site diversity.

2.2.5 Short-Term Horizontal Distributions

Radars operating at nonattenuating frequencies have been utilized to study both the horizontal and vertical spatial components of convective rain systems. A typical horizontal distribution (actually observed at 1.4 degrees elevation angle) is shown in Figure 2.2-1 for a thunder shower in New England (Crane and Blood - 1979). Here rain rate variations of 100:1 are observed over ranges of 10 km for a shower containing four intense cells. Similar measurements have been made by Goldhirsh (1976), at Wallops Island, VA. Goldhirsh (1976) has also observed that the rain cells are elongated along the northeast-southwest direction (the direction of motion). This direction also correlated well with the average or median wind directions. The impact of this result is that the fading was maximum and the space diversity gain a minimum in the northeast-southwest direction. (Space diversity is described in detail in Chapter VI.)

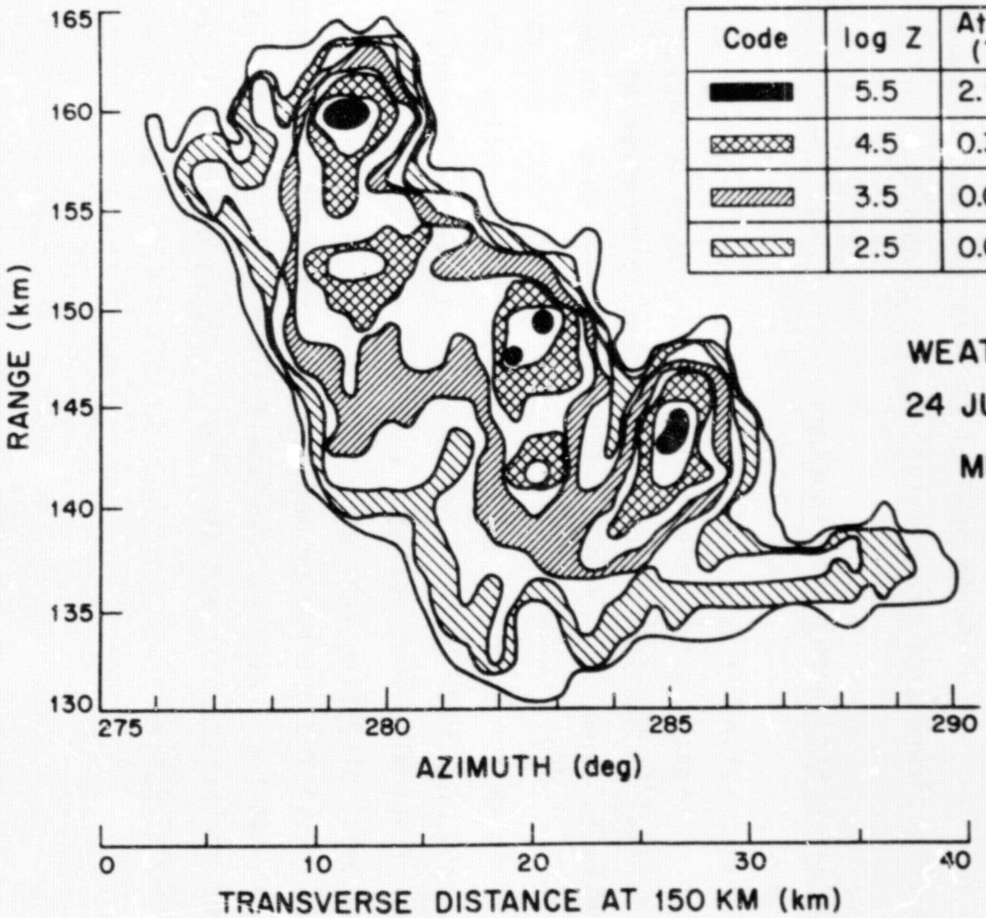

Contours 5 dB Apart

Code	log Z	Attenuation (7.78 GHz)	Rate ($Z = 200R^{1.6}$)
(solid)	5.5	2.1 dB/km	4 in./hr (100 mm/hr)
(cross-hatched)	4.5	0.3 dB/km	1 in./hr (24 mm/hr)
(dense hatching)	3.5	0.04 dB/km	0.2 in./hr (6 mm/hr)
(light hatching)	2.5	0.006 dB/km	0.05 in./hr (1 mm/hr)

WEATHER RADAR DATA

24 JUL 1967   2052 GMT

MILLSTONE HILL RADAR

1.4° EL, 275° - 290° AZ

Figure 2.2-1. Weather Radar Map for New England Showers

2.2.6 Short-Term Vertical Distributions

The calibrated radars are also ideal for measurement of the vertical profile of rain events. The median reflectivity profiles for a group of rain cells measured from the ground as a function of rain rate is presented in Figure 2.2-2 (Goldhirsh and Katz - 1979). The numbers in parentheses are the number of cells measured and the abscissa is the reflectivity factor based on the relation $Z = 200\ R^{1.6}\ mm^6/m^3$. These experimental results clearly demonstrate that the rain rate is uniform up to 4 km altitude and then decreases dramatically at altitudes in the 6 to 8 km range. This decrease is also associated with the 0^oC isotherm height. Note how the median isotherm height increases with the updraft, convective, high rain rate cells. This effect will be used later in a Global Rain Prediction Model along with the seasonal dependence of the median isotherm height.

Above this isotherm, the hydrometeors exist in the form of ice crystals and snow. These forms of hydrometeors do not contribute significantly to the attenuation, but they can give rise to depolarization effects.

2.3 SPECIFIC RAIN ATTENUATION

2.3.1 Scattering

Rain drops both attenuate and scatter microwave energy along an earth-space path. From the basic Rayleigh scattering criteria (the dimensions of the scatterer are much smaller than the wavelength) and the fact that the median rain drop diameter is approximately 1.5 mm, one would expect that Rayleigh scattering theory should be applied in the frequenc (wavelength) range from 10 GHz (3cm) to 100 GHz (3mm). However, Rayleigh scattering also requires that the imaginary component of the refractive index be small, which is not the case for water drops (Kerker - 1969). Because of this effect and the wide distribution of rain drop diameters, the Rayleigh scattering theory appears to apply only up to 3 GHz (Rogers - 1978). Above 3 GHz Mie scattering

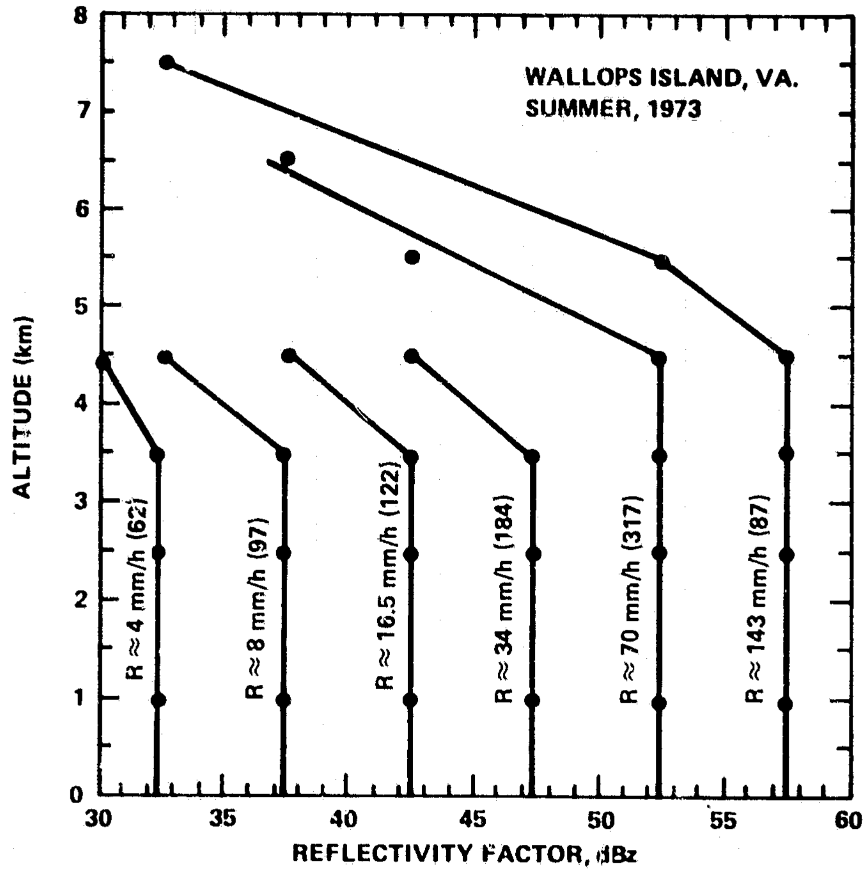

Figure 2.2-2. Median Reflectivity Factor Profiles for Given Ground Categories as Measured at Wallops Island, VA, During Summer of 1973.

applies and is the primary technique utilized for specific rain attenuation (attenuation per unit length, dB/km) calculations. Mie scattering accounts for the deficiencies of Rayleigh scattering and has proven to be the most accurate technique.

2.3.2 Drop Size Distributions

Several investigators have studied the distribution of rain drop sizes as a function of rain rate and type of storm activity. The three most commonly used distributions are

Laws and Parsons (LP)

Marshall-Palmer (MP)

Joss-thunderstorm (J-T) and drizzle (J-D)

In general the Laws and Parsons distribution (Laws and Parsons - 1943) is favored for design purposes because it has been widely tested by comparison to measurements for both widespread (lower rain rates) and convective rain (higher rain rates) at the present time. Also in the higher rain rate regime (≥ 25 mm/hr) and at frequencies above 10 Ghz, the LP values give higher specific rain attenuations (Olsen, et al - 1978) than the J-T values (Joss, et al - 1968). In addition, it has been observed that the raindrop temperature is most accurately modeled by the $0^{o}C$ data rather than $20^{o}C$, since for most high elevation angle earth-space links the raindrops are cooler at high altitudes and warm as they fall to earth.

An example of the measured number distribution of raindrops with drop diameter as a function of rain rate R (mm/h) is given in Figure 2.3-1. Here the measurements of Laws and Parsons (1943) and Marshall and Palmer (1948) are fitted by an exponential relation of the form

$$N_D = N_0 e^{-\Lambda D} \text{ cm}^{-4}$$

where

$$N_0 = 0.08 \text{ cm}^{-4}$$

and

$$\Lambda = 41 R^{-0.21} \text{ cm}^{-1}$$

Note that the units in the equations and Figure 2.3-1 are different. Multiply the N_D by 10^5 to convert to the units of Figure 2.3-1. The number of raindrops with diameters between D and D + δD in a volume V (cm^3) at rain rate R is

$$N_R = N_D(\delta D)V$$

As shown in Figure 2.3-1, the measured data deviates from the exponential relation for diameters below 1.5 mm. However, the larger drops tend to dominate the specific attenuation at the higher rain rates of most concern for the system engineer, and so this deviation tends not to be reflected in the integral over drop diameters utilized in specific attenuation calculations.

Joss, et al (1968) have found significant variations of N_D and Λ for different types of rainfall based on one year's measurements at Locarno, Switzerland. These results are presented in Table 2.3-1; however, the climatic regions where the Joss statistics apply have not been determined. Therefore, it appears best to utilize the Laws and Parsons results, realizing that in certain areas of the U.S. and Canada they have not been verified.

TABLE 2.3-1
Values of N_0, Λ Versus Rain Event as Determined by Joss, et al (1968)

Rainfall Type	N_0 (cm^{-4})	Λ (cm^{-1})
drizzle	0.3	$57R^{-0.21}$
widespread	0.07	$41R^{-0.21}$
thunderstorm	0.014	$30R^{-0.21}$

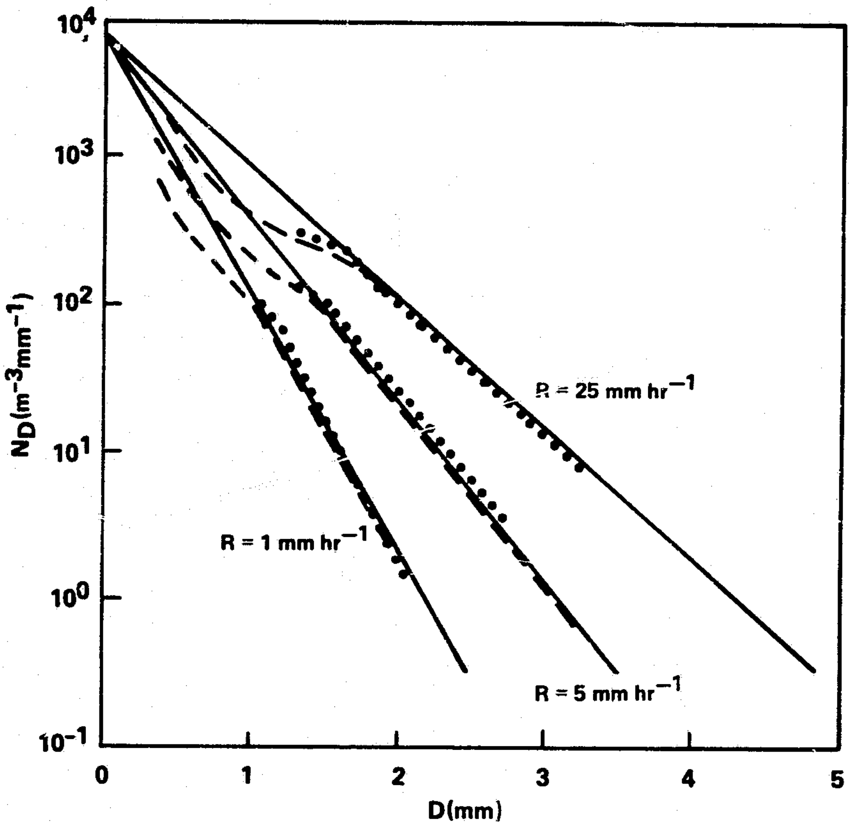

Figure 2.3-1. Rain Drop Size Distribution Function Compared With Experimental Results

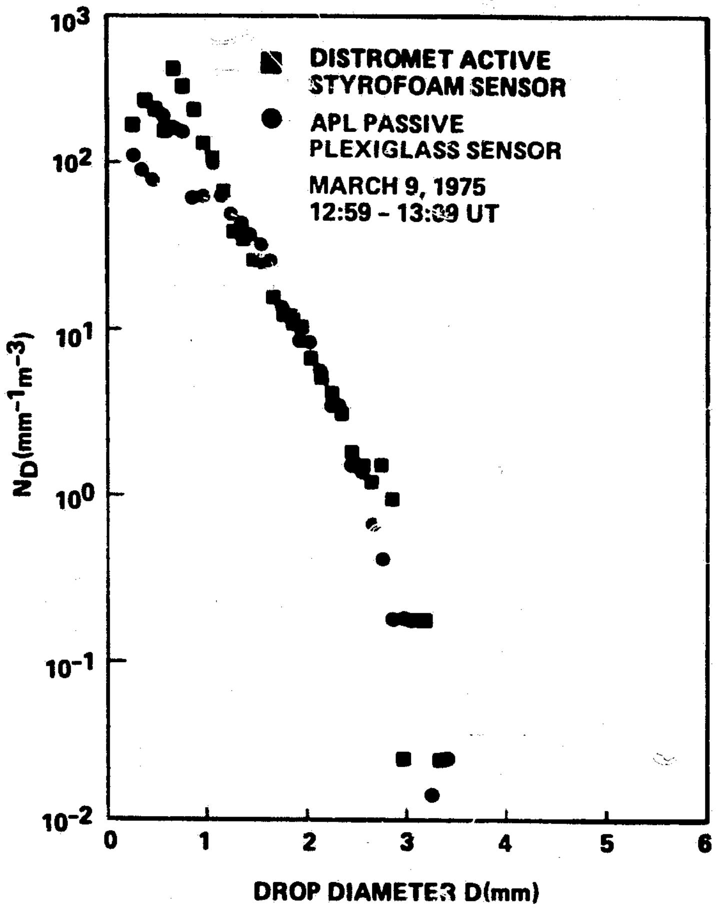

Figure 2.3-2. Raindrop Size Distribution Measured With Two Disdrometers

2.3.3 Measurement Techniques for Drop Size Distributions

Experimenters have employed a wide variety of techniques to measure raindrop size distributions in situ. These include: (1) optical systems requiring imaging or scattering light from raindrops, (2) replicating techniques where a permanent record of each drop size is made such as the flour method (Laws and Parsons - 1943), dyed filter paper (Marshall and Palmer - 1948), sugar coated nylon or foil impactors, (3) capacitive techniques due to changing dielectric constant, and (4) impact types of sensors (Rowland - 1976).

Today the impact-type of sensor (called a disdrometer after drop distribution meter), is the favored technique. The Applied Physics Laboratory has developed two styles of disdrometer with decided advantages over the commercially available Distromet Ltd unit. These three types have been described by Rowland (1976) and their calibration has been compared. A typical experimental result for two disdrometers measuring the same rain event on 9 March 1975, is shown in Figure 2.3-2. Note that the data for the APL passive plexiglas sensor which utilizes a piezoelectric crystal to "hear" the impact of raindrops may be invalid below a 1 mm/h rain rate because of noise in the preamplifier. Normally, this data would more clearly follow the Distromet active styrofoam sensor data.

2.3.4 Estimates of the Specific Attenuation

The scattering properties of raindrops and the dropsize distributions are inputs for the calculation of the attenuation per kilometer (specific attenuation) of a uniform rain at rain rate R.

It has been empirically observed (Ryde and Ryde - 1945) that the specific attenuation α (dB/km) is related to the rain rate R (mm/h) by a relation

$$\alpha = a(f)R^{b(f)}$$

where the coefficients a and b are functions of frequency. At this time the most thorough calculations of have been made by Olsen, et al (1978). These calculations extend from 1 to 1000 GHz and have been presented in both tabular and graphical format for several raindrop distributions and temperatures. For the U.S. and Canada the 0^oC numbers are most applicable (Rogers - 1978). Table 2.3-2 (Olsen, et al 1978) is given below for selected frequencies of interest. The LP_L and LP_H refer to Laws and Parsons drop size distributions associated with rain rates R from 1.27 to 50.8 mm/h and 25.4 to 152.4 mm/h, respectively. Olsen, et al (1978) have also provided analytic approximations for a(f) and b(f) which are quite adequate for use by system engineers. These are

$$a(f) = 4.21 \times 10^{-5}(f)^{2.42} \qquad 2.9 \le f \le 54 \text{ GHz}$$
$$= 4.09 \times 10^{-2}(f)^{0.699} \qquad 54 \le f \le 180 \text{ GHz}$$

and

$$b(f) = 1.41\ (f)^{-0.0779} \qquad 8.5 \le f \le 25 \text{ GHz}$$
$$= 2.63\ (f)^{-0.272} \qquad 25 \le f \le 164 \text{ GHz}$$

where f is in GHz. Thus for 20 GHz

$$\alpha = a(f)R^{b(f)} \text{ dB/km}$$

$$= 4.21 \times 10^{-5}(20)^{2.42}\ R^{1.41(20)^{-0.0779}} \text{ dB/km}$$

$$= 0.059\ R^{1.117} = 2.19 \text{ dB/km @ R= 25.4 mm/hr.}$$

The value in Table 2.3-2 for this frequency is $0.0626\ R^{1.119}$ = 2.34 dB/km @ R = 25.4 mm/hr, an error of 6%.

Based on the Olson, et al (1978) results, the specific attenuation relations given in Table 2.3-3 are recommended in the 10 to 100 GHz frequency range. Unless noted otherwise, these specific attenuations will be utilized throughout this handbook.

Table 2.3-2

Regression Calculations for a and b in $\alpha = aR^b$ (dB/km) as Functions of Frequency and Dropsize Distribution, Rain, Temperature = 0^oC

FREQ. (GHz)	a					b				
	LP_L	LP_H	MP	J-T	J-D	LP_L	LP_H	MP	J-T	J-D
10	1.17×10^{-2}	1.14×10^{-2}	1.36×10^{-2}	1.69×10^{-2}	1.14×10^{-2}	1.178	1.189	1.150	1.076	0.968
11	1.50×10^{-2}	1.52×10^{-2}	1.73×10^{-2}	2.12×10^{-2}	1.41×10^{-2}	1.171	1.167	1.143	1.065	0.977
12	1.86×10^{-2}	1.96×10^{-2}	2.15×10^{-2}	2.62×10^{-2}	1.72×10^{-2}	1.162	1.150	1.136	1.052	0.985
15	3.21×10^{-2}	3.47×10^{-2}	3.68×10^{-2}	4.66×10^{-2}	2.82×10^{-2}	1.142	1.119	1.118	1.010	1.003
19.04	5.59×10^{-2}	6.24×10^{-2}	6.42×10^{-2}	8.68×10^{-2}	4.76×10^{-2}	1.123	1.091	1.001	0.957	1.017
19.3	5.77×10^{-2}	6.46×10^{-2}	6.62×10^{-2}	8.99×10^{-2}	4.90×10^{-2}	1.122	1.089	1.100	0.954	1.018
20	6.26×10^{-2}	7.09×10^{-2}	7.19×10^{-2}	9.83×10^{-2}	5.30×10^{-2}	1.119	1.083	1.097	0.946	1.020
25	0.105	0.132	0.121	0.173	8.61×10^{-2}	1.094	1.029	1.074	0.884	1.033
28.56	0.144	0.196	0.166	0.243	0.115	1.071	0.983	1.052	0.839	1.041
30	0.162	0.226	0.186	0.274	0.128	1.061	0.964	1.043	0.823	1.044
34.8	0.229	0.340	0.264	0.368	0.177	1.023	0.909	1.008	0.784	1.053
35	0.232	0.345	0.268	0.372	0.180	1.022	0.907	1.007	0.783	1.053
40	0.313	0.467	0.362	0.451	0.241	0.981	0.864	0.972	0.760	1.058
50	0.489	0.669	0.579	0.629	0.387	0.907	0.815	0.905	0.709	1.053
60	0.658	0.796	0.801	0.804	0.558	0.850	0.794	0.851	0.682	1.035
70	0.801	0.869	1.00	0.833	0.740	0.809	0.784	0.812	0.661	1.009
80	0.924	0.913	1.19	0.809	0.922	0.778	0.780	0.781	0.674	0.980
90	1.02	0.945	1.35	0.857	1.10	0.756	0.776	0.753	0.663	0.953
100	1.08	0.966	1.48	0.961	1.26	0.742	0.774	0.730	0.637	0.928

Note: Values for 19.04, 19.3, 28.56 and 34.8 GHz obtained from D. V. Rogers, Comsat Lab., Clarksburg, MD

Table 2.3-3

Recommended Specific Attenuation Approximations

Frequency Range	Specific Attenuation, α (dB/km) (R in mm/h, f in GHz)
10 - 25 GHz	$\alpha = 4.21 \times 10^{-5}(f)^{2.42}\ R^{1.41(f)^{-0.0779}}$
25 - 54 GHz	$\alpha = 4.21 \times 10^{-5}(f)^{2.42}\ R^{2.63(f)^{-0.272}}$
54 - 100 GHz	$\alpha = 4.09 \times 10^{-5}(f)^{0.699}\ R^{2.62(f)^{-0.272}}$

The specific attenuations for several of the common earth-space bands are shown in Figure 2.3-3 for rain rates from 0.1 to 10 inches/h (2.54 to 254 mm/h) using the equations in Table 2.3-3. The 85 and 94 GHz curves overlap the 50 GHz data because of inaccuracies in the approximations in Table 2.3-3. More accurate results are obtained from interpolation of Table 2.3-2.

An earlier calculation of the specific attenuation coefficients by Crane (1966) may be compared to the results listed above. Crane employed the Laws and Parsons (1943) number density model to obtain the aR^b power law relation coefficients. The results of these earlier calculations are given in Table 2.3-4 and these same results are plotted in Chapter 3. In general, these older results are bracketed by the LP_L and LP_H values of Olsen, et al (1978) given in Table 2.3-2. However, this is not always the case and some discrepancies have been found. Ippolito (1979) has noted that generally the Olsen et al (1978) results compare more favorably with the experimental data than the Crane (1966) results when substituted in the same model.

2.4 RAINFALL DATA

The largest long-term sources of rainfall data in the U.S. and Canada are their respective weather services. The data collected by these agencies is an excellent starting data base for rain rate estimation. However, in situ measurements are still the most accurate, but quite expensive technique for acquiring rain rate statistics.

2.4.1 U.S. Sources

2.4.1.1 Published Data. In the U.S., the National Weather Service's National Climatological Center* prepares and maintains extensive precipitation records obtained from Weather Service Offices and over 12,000 observers and agencies. This rain data is available in several documents available from the National Climatological Center. Several of the key publications of interest to the earth-space path engineer are:

*National Climatic Center, Federal Building, Asheville, North Carolina 28801

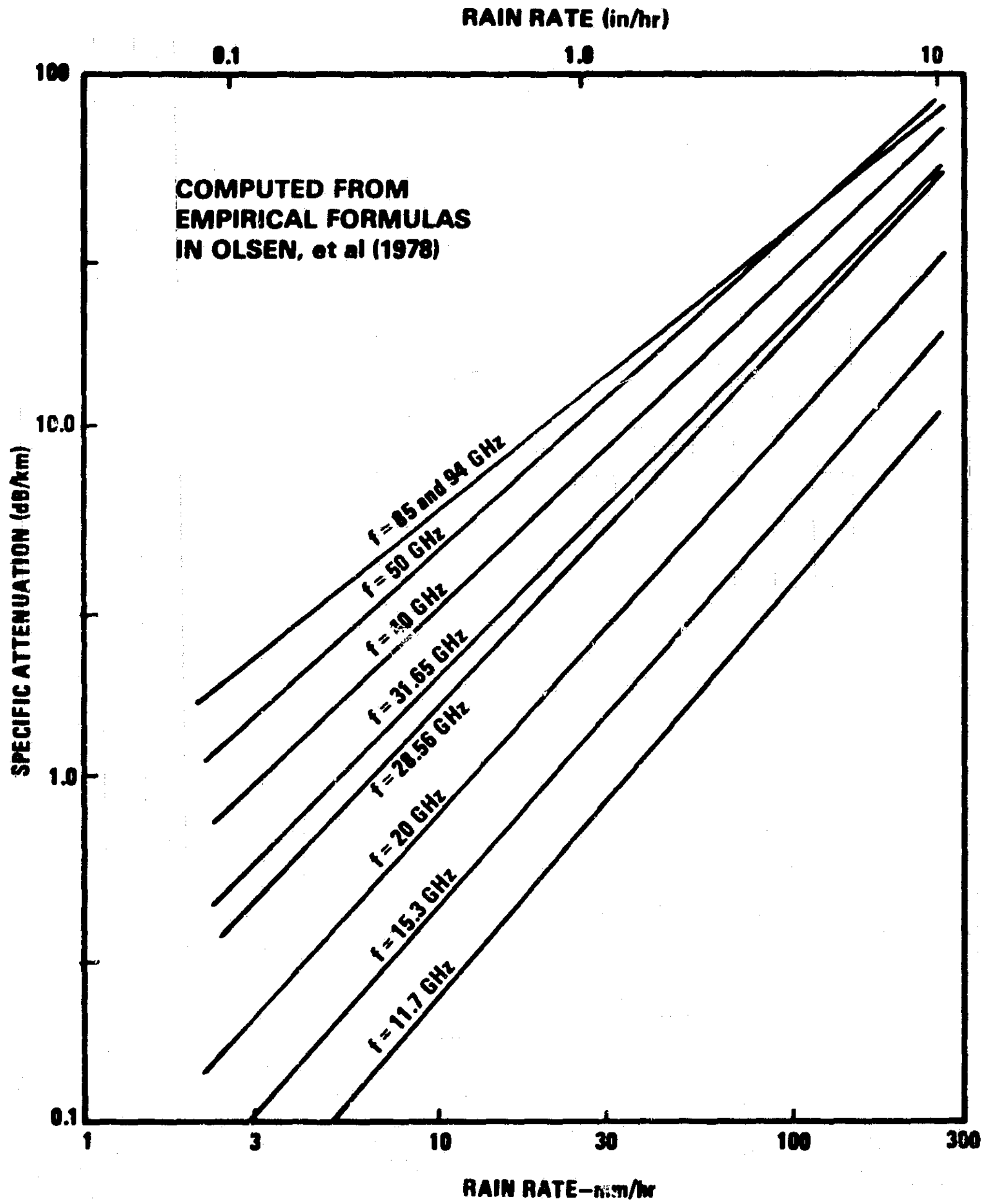

Figure 2.3-3. Specific Attenuation Versus Rain Rate for Common Earth-Space Frequencies

Table 2.3-4

Parameters for Computing Specific Attenuation:
$\alpha = aR^b$, 0^oC, Laws and Parson Distribution
(Crane-1966)

Frequency f - GHz	Multiplier a(f)	Exponent b(f)
1	0.00015	0.95
4	0.00080	1.17
5	0.00138	1.24
6	0.00250	1.28
7.5	0.00482	1.25
10	0.0125	1.18
12.5	0.0228	1.145
15	0.0357	1.12
17.5	0.0524	1.105
20	0.0699	1.10
25	0.113	1.09
30	0.170	1.075
35	0.242	1.04
40	0.325	0.99
50	0.485	0.90
60	0.650	0.84
70	0.780	0.79
80	0.875	0.753
90	0.935	0.730
100	0.965	0.715

- Hourly Precipitation Data (HPD)
    - 15 minute rain rate resolution
    - published monthly by state
    - District of Columbia included in the Virginia HPD
    - available about 6 months following data of recording
    - $0.65 per copy
    - $8.30 per year

- Climatological Data (CD)
    - 1 hour rain rate resolution
    - published monthly by state(s)
    - District of Columbia included in the Maryland and Delaware CD
    - Washington National Airport WSO included in the Virginia CD
    - available about 3 months following date of recording
    - $0.45 per copy
    - $5.85 per year

- Climatological Data - National Summary
    - greatest 24 hour rain rate data
    - published monthly
    - available about 4 months following date of recording
    - $0.60 per copy
    - $8.30 per year

- Climatological Data - National Summary, Annual Summary
    - one 5 minute rain rate resolution event per month
    - available about 18 months following last date of recording
    - $1.10 per copy

- o Local Climatological Data (LCD)
  - hourly rain rate resolution
  - published monthly by location
  - available about 4 months following date of recording
  - $0.25 per copy, $3.30 per year
  - annual issue also published for each location, $0.30
- o Storm Data
  - published monthly for the U.S.
  - describes type of storm and extent of damage.
  - $0.40 per copy, $4.80 per year

The local Climatological Data is available for the 291 stations shown in Table 2.4-1; however, the Hourly Precipitation Data is available for many more stations.

Examples of the precipitation-related data available in each of these publications are given in Figures 2.4-1 to 2.4-5. Comparing the results for either the Baltimore Weather Station Office (WSO) at the Airport (AP) or the Beltsville results, one observes that precipitation data up to 15-minute resolution is available in the HPD's, while the monthly CD lists only the total precipitation per day (see Figure 2.4-2). The monthly CD, National Summary, lists the total precipitation per month in liquid form and the total snow or ice pellet depth at most airports. Also included (see Figure 2.4-3) is the number of thunderstorms recorded during the month. In the Annual Summary of the National CD (see Figure 2.4-4) the total precipitation, snowfall (all frozen precipitation except hailstones) and the amount and date(s) of the highest precipitation accumulation during the year for periods of 5 to 180 minutes are given. Unfortunately it only includes one 5 minute event per month, only the highest will be indicated in the data. Additional techniques to retrieve more data will be described below.

The Local Climatological Data (LCD) provides the rainfall by hour at each of the 291 stations shown in Table 2.4-1. An example for Asheville, NC,

Table 2.4-1

Local Climatological Data Stations

U.S. DEPARTMENT OF COMMERCE
NATIONAL OCEANIC AND ATMOSPHERIC ADMINISTRATION
ENVIRONMENTAL DATA SERVICE

(Stations for which Local Climatological Data are issued, as of January 1, 1978)

ALABAMA

abc BIRMINGHAM
abc HUNTSVILLE
abc MOBILE
abc MONTGOMERY

ALASKA

abc ANCHORAGE
abc ANNETTE
abc BARROW
abc BARTER ISLAND
abc BETHEL
abc BETTLES
abc BIG DELTA
abc COLD BAY
abc FAIRBANKS
abc GULKANA
abc HOMER
abc JUNEAU
abc KING SALMON
abc KODIAK
abc KOTZEBUE
abc McGRATH
abc NOME
abc ST PAUL ISLAND
abc TALKEETNA
abc UNALAKLEET
abc VALDEZ
abc YAKUTAT

ARIZONA

abc FLAGSTAFF
abc PHOENIX
abc TUCSON
abc WINSLOW
abc YUMA

ARKANSAS

abc FORT SMITH
abc LITTLE ROCK

CALIFORNIA

abc BAKERSFIELD
abc BISHOP
abc BLUE CANYON
ac EUREKA
abc FRESNO
abc LONG BEACH
abc LOS ANGELES AIRPORT
ac LOS ANGELES CIVIC CENTER
abc MT SHASTA
abc OAKLAND
abc RED BLUFF
abc SACRAMENTO
abc SANDBERG
abc SAN DIEGO
SAN FRANCISCO
abc AIRPORT
ac CITY
abc SANTA MARIA
abc STOCKTON

COLORADO

abc ALAMOSA
abc COLORADO SPRINGS
abc DENVER
abc GRAND JUNCTION
abc PUEBLO

CONNECTICUT

abc BRIDGEPORT
abc HARTFORD

DELAWARE

abc WILMINGTON

DISTRICT OF COLUMBIA

abc WASHINGTON - NATIONAL AP
abc WASHINGTON - DULLES INT'L AP

FLORIDA

abc APALACHICOLA
abc DAYTONA BEACH
abc FORT MYERS
abc JACKSONVILLE
abc KEY WEST
ac LAKELAND
abc MIAMI
abc ORLANDO
abc PENSACOLA
abc TALLAHASSEE
abc TAMPA
abc WEST PALM BEACH

GEORGIA

abc ATHENS
abc ATLANTA
abc AUGUSTA
abc COLUMBUS
abc MACON
abc ROME
abc SAVANNAH

HAWAII

abc HILO
abc HONOLULU
abc KAHULUI
abc LIHUE

IDAHO

abc BOISE
abc LEWISTON
abc POCATELLO

ILLINOIS

ac CAIRO
CHICAGO
abc MIDWAY AIRPORT
abc O'HARE AIRPORT
abc MOLINE
abc PEORIA
abc ROCKFORD
abc SPRINGFIELD

INDIANA

abc EVANSVILLE
abc FORT WAYNE
abc INDIANAPOLIS
abc SOUTH BEND

IOWA

abc BURLINGTON
abc DES MOINES
abc DUBUQUE
abc SIOUX CITY
abc WATERLOO

KANSAS

abc CONCORDIA
abc DODGE CITY
abc GOODLAND
abc TOPEKA
abc WICHITA

KENTUCKY

abc LEXINGTON
abc LOUISVILLE

LOUISIANA

abc ALEXANDRIA (1)
abc BATON ROUGE
abc LAKE CHARLES
abc NEW ORLEANS
abc SHREVEPORT

MAINE

abc CARIBOU
abc PORTLAND

MARYLAND

abc BALTIMORE

MASSACHUSETTS

abc BOSTON
ac BLUE HILL OBS
abc WORCESTER

MICHIGAN

abc ALPENA
DETROIT
abc CITY AIRPORT
abc DETROIT METRO AP
abc FLINT
abc GRAND RAPIDS
abc HOUGHTON LAKE
abc LANSING
ac MARQUETTE
abc MUSKEGON
abc SAULT STE MARIE

MINNESOTA

abc DULUTH
abc INTERNATIONAL FALLS
abc MINNEAPOLIS - ST. PAUL
abc ROCHESTER
abc ST. CLOUD

MISSISSIPPI

abc JACKSON
abc MERIDIAN

MISSOURI

abc COLUMBIA
abc KANSAS CITY
abc ST. JOSEPH
abc ST. LOUIS
abc SPRINGFIELD

MONTANA

abc BILLINGS
abc GLASGOW
abc GREAT FALLS
abc HAVRE
abc HELENA
abc KALISPELL
abc MILES CITY
abc MISSOULA

NEBRASKA

abc GRAND ISLAND
abc LINCOLN
abc NORFOLK
abc NORTH PLATTE
abc OMAHA
ac OMAHA (NORTH) (2)
abc SCOTTSBLUFF
ac VALENTINE

NEVADA

abc ELKO
abc ELY
abc LAS VEGAS
abc RENO
abc WINNEMUCCA

NEW HAMPSHIRE

abc CONCORD
ac MT WASHINGTON

NEW JERSEY

ATLANTIC CITY
abc AIRPORT
a STATE MARINA
abc NEWARK
ac TRENTON

NEW MEXICO

abc ALBUQUERQUE
abc CLAYTON
abc ROSWELL

NEW YORK

abc ALBANY
abc BINGHAMTON
abc BUFFALO
NEW YORK
abc CENTRAL PARK
abc J.F. KENNEDY INT'L AP
abc LaGUARDIA FIELD
abc ROCHESTER
abc SYRACUSE

NORTH CAROLINA

abc ASHEVILLE
abc CAPE HATTERAS
abc CHARLOTTE
abc GREENSBORO
abc RALEIGH
abc WILMINGTON

NORTH DAKOTA

abc BISMARCK
abc FARGO
abc WILLISTON

OHIO

abc AKRON-CANTON
CINCINNATI
ac ABBE OBS.
abc AIRPORT
abc CLEVELAND
abc COLUMBUS
abc DAYTON
abc MANSFIELD
abc TOLEDO
abc YOUNGSTOWN

OKLAHOMA

abc OKLAHOMA CITY
abc TULSA

OREGON

abc ASTORIA
abc BURNS
abc EUGENE
abc MEDFORD
abc PENDLETON
abc PORTLAND
abc SALEM
abc SEXTON SUMMIT

PACIFIC ISLANDS

abc GUAM
abc JOHNSTON
abc KOROR
abc KWAJALEIN
abc MAJURO
abc PAGO PAGO
abc PONAPE
abc TRUK (MOEN)
abc WAKE
abc YAP

PENNSYLVANIA

abc ALLENTOWN
abc AVOCA, WILKES-BARRE-SCRANTON AP
abc ERIE
abc HARRISBURG
abc PHILADELPHIA
PITTSBURGH
abc AIRPORT
ac CITY
abc WILLIAMSPORT

RHODE ISLAND

ac BLOCK ISLAND
abc PROVIDENCE

SOUTH CAROLINA

CHARLESTON
abc AIRPORT
a CITY
abc COLUMBIA
abc GREENVILLE SPARTANBURG

SOUTH DAKOTA

abc ABERDEEN
abc HURON
abc RAPID CITY
abc SIOUX FALLS

TENNESSEE

abc BRISTOL
abc CHATTANOOGA
abc KNOXVILLE
abc MEMPHIS
abc NASHVILLE
ac OAK RIDGE

TEXAS

abc ABILENE
abc AMARILLO
abc AUSTIN
abc BROWNSVILLE
abc CORPUS CHRISTI
abc DALLAS-FORT WORTH
abc DEL RIO
abc EL PASO
ac GALVESTON
abc HOUSTON
abc LUBBOCK
abc MIDLAND
abc PORT ARTHUR
abc SAN ANGELO
abc SAN ANTONIO
abc VICTORIA
abc WACO
abc WICHITA FALLS

UTAH

abc MILFORD
abc SALT LAKE CITY

VERMONT

abc BURLINGTON

VIRGINIA

abc LYNCHBURG
abc NORFOLK
abc RICHMOND
abc ROANOKE
ab WALLOPS ISLAND

WASHINGTON

abc OLYMPIA
abc QUILLAYUTE AIRPORT
abc SEATTLE-TACOMA AP
ac SEATTLE URBAN SITE
abc SPOKANE
abc STAMPEDE PASS
ac WALLA WALLA
abc YAKIMA

WEST INDIES

abc SAN JUAN, P.R.

WEST VIRGINIA

abc BECKLEY
abc CHARLESTON
abc ELKINS
abc HUNTINGTON
ac PARKERSBURG

WISCONSIN

abc GREEN BAY
abc LA CROSSE
abc MADISON
abc MILWAUKEE

WYOMING

abc CASPER
abc CHEYENNE
abc LANDER
abc SHERIDAN

a. Monthly summary issued. b. Monthly summary includes available 3 hourly observations c. Annual Summary issued.

Subscription Price Local Climatological Data $2.55 per year including annual issue if published. $1.85 extra for foreign mailing. Single copy $.20 for monthly issue, $.20 for annual issue. These costs are per city (location) requested. A loose set of all of the above annual issues is on sale for $20.00, a soft-bound set for $25.00. Make checks payable to DOC, NOAA, NCC, send payments to National Climatic Center, Federal Building, Asheville, NC 28801.

(1) September 1977 was the last monthly issue; last published Annual Summary was 1976.

(2) June 1977 was the first monthly issue; available data published for entire year.

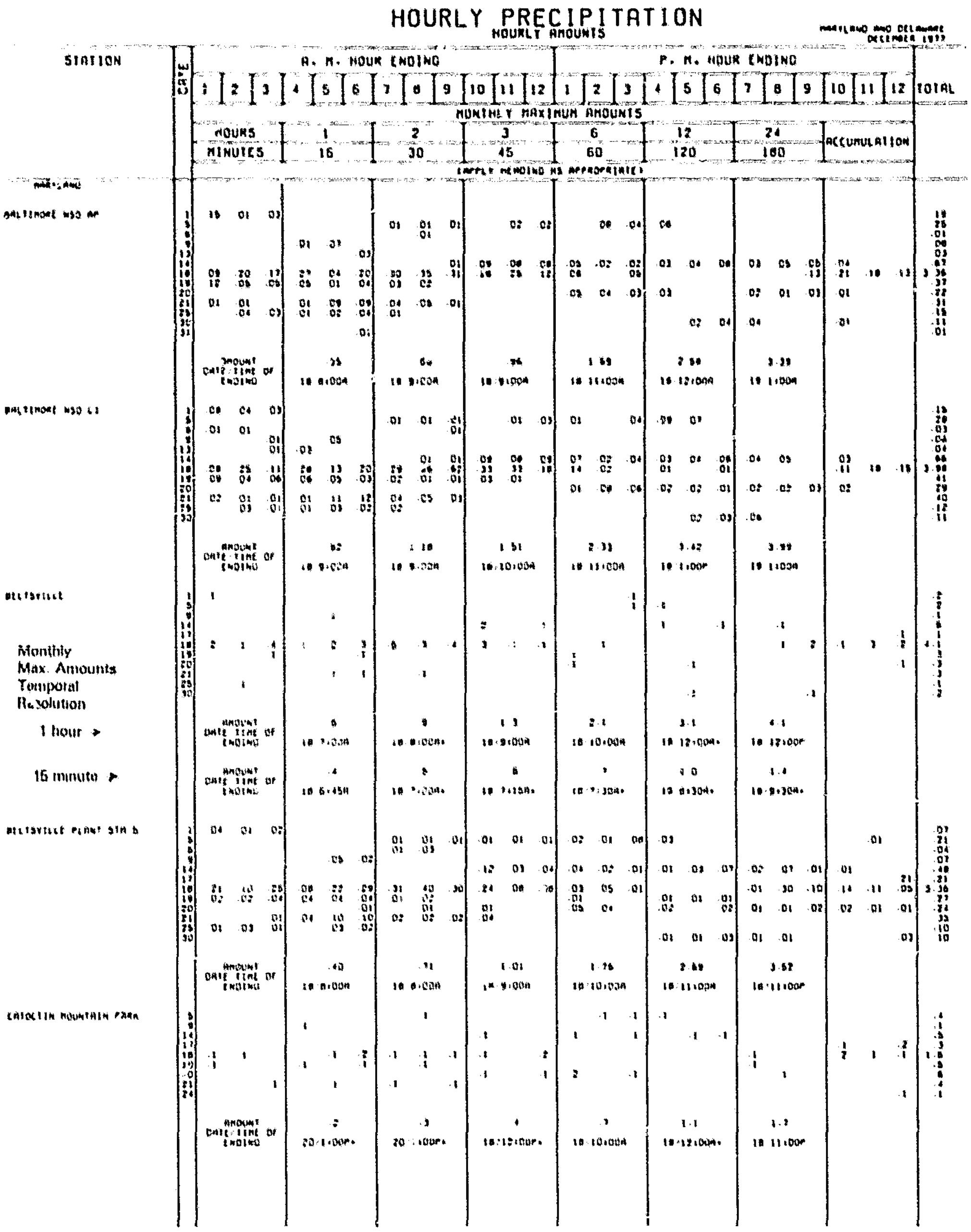

Figure 2.4-1. An Example of the Hourly Precipitation Data (HPD) Issued Monthly by State

MONTHLY SUMMARIZED STATION AND DIVISIONAL DATA

MARYLAND AND DELAWARE
APRIL 1978

STATION	TEMPERATURE													PRECIPITATION									
										NO. OF DAYS								SNOW, SLEET			NO. OF DAYS		
										MAX.		MIN.											
	AVERAGE MAXIMUM	AVERAGE MINIMUM	AVERAGE	DEPARTURE FROM NORMAL	HIGHEST	DATE	LOWEST	DATE	DEGREE DAYS	90° OR ABOVE	32° OR BELOW	32° OR BELOW	0° OR BELOW	TOTAL	DEPARTURE FROM NORMAL	GREATEST DAY	DATE	TOTAL	MAX. DEPTH ON GROUND	DATE	.10 OR MORE	.50 OR MORE	1.00 OR MORE
MARYLAND																							
* * *																							
LOWER SOUTHERN 03																							
LA PLATA 1 W	68.3	39.9M	54.1M	- 1.6	89	1	32	28+	323	0	0	2	0	2.78	- .32	.90	26	.0	0		4	3	0
MECHANICSVILLE 1 SE	68.5	42.7	55.6		85	1	33	16	285	0	0	0	0	3.44		.87	27	.0	0		7	4	0
OWINGS FERRY LANDING	64.7	39.7	52.2	- 3.7	86	1	31	9	376	0	0	2	0	2.08	- 1.10	.58	26	.0	0		5	2	0
PATUXENT RIVER	63.5M	44.8	54.2M		86	1	39	28+	317	0	0	0	U	2.99		1.44	26	.0	0		4	2	1
SOLOMONS	64.4M	45.4	54.9M	- 1.1	83	11+	40	28+	297	0	0	0	0	3.42	.29			.0	0				
DIVISION			54.2	- 1.5										2.94	- .20			.0					

DAILY PRECIPITATION

MARYLAND AND DELAWARE
APRIL 1978

STATION	TOTAL	DAY OF MONTH																													
		1	2	3	4	5	6	7	8	9	10	11	12	13	14	15	16	17	18	19	20	21	22	23	24	25	26	27	28	29	30	31
MARYLAND																																
* * *																																
UPPER SOUTHERN 04																																
ANNAPOLIS POLICE BRKS	1.97			.05	.06			.08					.05							.84	.40						.06	.05				
BALTIMORE WSO AP W	1.26		.04	.10	T		.01	.04				.05							.30	.69	.02	T		T				.01				
BELTSVILLE	1.15				.03			.08					.08							.56	.19						.23					
BELTSVILLE PLANT STA $	1.11				T			.10					.05							.54	.15						.27	T				
COLLEGE PARK	1.14			T	T	T		.07					.06							.59	.14	T	T		T		.31	.01	T			
DALECARLIA RESVR D C	1.47							.09					.03							.62	.27						.49		.01			
GLENN DALE BELL STA	1.77			.04				.10					.19							.60	.43						.36	.05				
LAUREL 3 W	1.07		T	.04	T		.05	T				.02							.32	.52							.12	T				
NATIONAL ARBORETUM D C	1.38				.01			.06					.11							.58	.19	.01					.27	.03	T			
UPPER MARLBORO 3 NNW	1.56				T			.10					.08							.50	.46						.35	.07				

Figure 2.4-2. An Example of the Climatological Data Issued Monthly by State

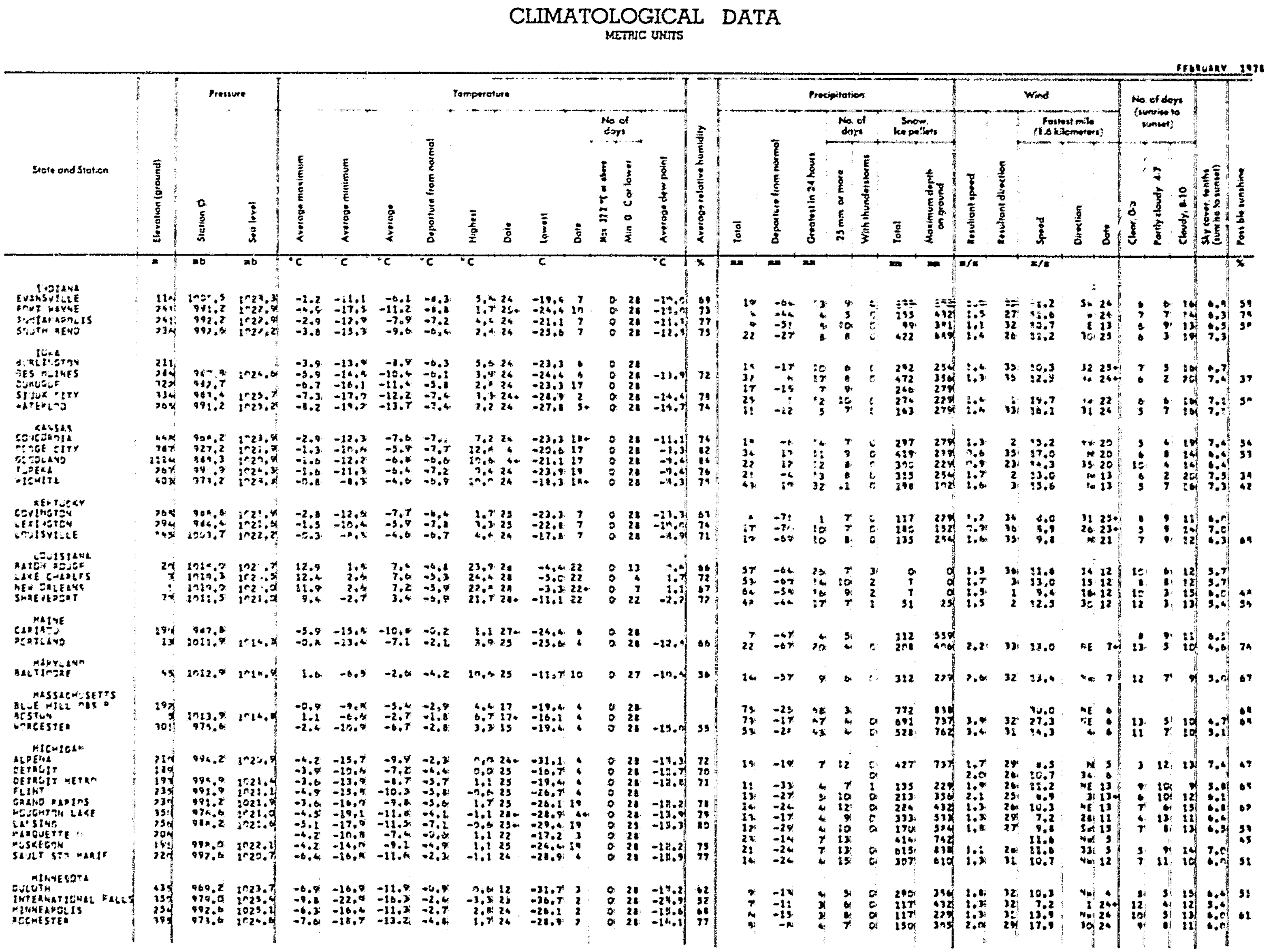

Figure 2.4-3. An Example of National Summary of Climatological Data Issued Monthly

ANNUAL CLIMATOLOGICAL DATA
METRIC UNITS

YEAR 1976

State and Station	Temperature – Averages – Daily maximum	Temperature – Averages – Daily minimum	Temperature – Averages – Annual	Temperature – Extremes – Highest	Date	Temperature – Extremes – Lowest	Date	Heating degree days	Cooling degree days	Precipitation – Total	Precipitation – Greatest in 24 hours	Date (s)	Snow – Total	Snow – Greatest in 24 hours	Date (s)	Relative humidity – 1:00am EST	7:00am EST	1:00pm EST	7:00pm EST	Wind – Average speed	Resultant speed	Resultant direction	Fastest mile (1.6 kilometers) – Speed	Direction	Date	Average sky cover sunrise to sunset	Number of days – Sunrise to sunset – Clear, 0-0.3	Partly cloudy, 0.4-0.7	Cloudy, 0.8-1.0	Precipitation .25mm or more	Snow 25.4mm or more	Thunderstorms	Heavy fog	Max. temp. 32.2°C and above	Max. temp. 0°C and below	Min. temp. 0°C and below	Min. temp. -17.8°C and below
	°C	C	C	C		C		Base 18.3°C	Base 18.3°C	mm	mm		mm	mm		%	%	%	%	m.s	m.s		m.s			Tenths											
MARYLAND [illegible]	[illegible]	7.1	12.8	34.4	2?	-15.?	JAN 1?	263?	638	11?3	125	SEP 15-16	34?	198	MAR 9	74	77	53	59	3.9	?.4	28	22.4	14	MAR 18	5.6	128	87	131	102	2	35	19	27	17	108	0

NORMALS, MEANS AND EXTREMES

YEAR 1976

State and Station	Elevation Ground (Meters)	Temperature (°C) – Normal (1941-1970) – January – Daily Maximum	January – Daily Minimum	July – Daily Maximum	July – Daily Minimum	Annual	Extremes – Length (Yrs)	Record Highest	Record Lowest	Normal Heating Degree Days (1941-1970) – January	Seasonal	Precipitation (Millimeters) – Normal (1941-1970) – Wettest Month	Driest Month	Annual	Extremes – Wettest Month	Driest Month	Maximum In 24 Hours	Snow – Mean Total – January	Seasonal	Snow – Extreme – Maximum In 24 Hours	Relative Humidity (Percent) – January – 7:00 a.m. EST	1:00 p.m. EST	7:00 p.m. EST	July – 7:00 a.m. EST	1:00 p.m. EST	7:00 p.m. EST	Wind Speed (m.p.s.) – Mean Speed – January	July	Fastest Mile (1.6 Kilometers)	Sunshine (% of Possible) – January	July	Annual Mean Number of Days – Sunrise to Sunset – Clear	Partly Cloudy	Cloudy	Precipitation .25mm or More	Snow, Sleet, Hail 25.4mm or More	Thunderstorms	Heavy Fog	Temperature – Max ≥ 32.2°C	Min ≤ 0°C	Min ≤ -17.8°C
MARYLAND BALTIMORE INTL AP	4?	5.5	-?.9	30.4	19.2	12.8	81 / 28	42.8 / 38.9	-40.0 / -21.7	544	2627	157	71	1028	466	0 / T	375 / 197	124	546	394	[illegible]	[illegible]	[illegible]	[illegible]	[illegible]	[illegible]	4.4	3.0	35.8	51	65	106	109	150	112	7	29	29	31	100	*

MAXIMUM SHORT DURATION PRECIPITATION

YEAR 1976

[illegible]

Figure 2.4-4

An Example of the Annual Summary of Climatological Data

LOCAL CLIMATOLOGICAL DATA

U.S. DEPARTMENT OF COMMERCE
NATIONAL OCEANIC AND ATMOSPHERIC ADMINISTRATION
ENVIRONMENTAL DATA SERVICE

ASHEVILLE, NORTH CAROLINA
NATIONAL WEATHER SERVICE OFC
ASHEVILLE AIRPORT
AUGUST 1975

LATITUDE 35° 26' N   LONGITUDE 82° 33' W   ELEVATION (GROUND) 2140 FT.   STANDARD TIME USED: EASTERN   WBAN #03812

Date	Temperature °F: Maximum	Minimum	Average	Departure from normal	Average dew point	Degree days base 65°: Heating	Cooling	Weather types on dates of occurrence (1 Fog, 2 Heavy fog X, 3 Thunderstorm, 4 Ice pellets, 5 Hail, 6 Glaze, 7 Duststorm, 8 Smoke, haze, 9 Blowing snow)	Snow, ice pellets or ice on ground at 07AM in.	Precipitation: Water equivalent in.	Snow, ice pellets in.	Avg. station pressure in. Elev. 2170 feet m.s.l.	Wind: Resultant direction	Resultant speed m.p.h.	Average speed m.p.h.	Fastest mile: Speed m.p.h.	Direction	Sunshine: Minutes	Percent of possible	Sky cover tenths: Sunrise to sunset	Midnight to midnight	Date
1	2	3	4	5	6	7A	7B	8	9	10	11	12	13	14	15	16	17	18	19	20	21	22
1	83	63	73	-1	66	0	8	2 8	0	0	0	27.89	17	4.6	5.3	10	20	483	58	6	6	1
2	85	61	73	-1	65	0	8	23	0	T	0	27.87	10	2.7	5.6	10	13	612	73	4	3	2
3	88	62	75	1	66	0	10	2	0	0	0	27.81	16	4.0	6.2	13	19	634	76	5	5	3
4	86	63	75	1	68	0	10	2	0	0	0	27.80	17	6.2	7.3	16	23	508	61	6	6	4
5	84	65	75	1	68	0	10	23	0	.25	0	27.76	24	.5	5.8	16	31	319	38	7	7	5
6	75	64	70	-4	67	0	5	1 8	0	.55	0	27.71	32	2.8	5.2	13	35	0	0	10	10	6
7	75	63	69	-5	65	0	4	1 8	0	T	0	27.84	07	1.8	5.8	12	36	59	7	9	9	7
8	75	59	67	-7	62	0	2	2 8	0	0	0	28.01	16	3.9	4.3	9	15	109	13	9	8	8
9	81	57	69	-5	62	0	4	2 8	0	0	0	28.02	12	1.6	4.2	10	17	341	41	9	8	9
10	71	63	67*	-7	66	0	2	2	0	.04	0	27.95	01	4.2	4.8	12	01	0	0	10	10	10
11	83	62	73	0	64	0	8	1	0	0	0	27.88	35	6.7	7.6	15	36	717	88	4	4	11
12	88	59	73	0	64	0	8	1 8	0	T	0	27.92	36	4.2	5.0	12	36	547	67	3	2	12
13	85	60	73	0	64	0	8	2 8	0	0	0	27.94	03	1.5	4.3	10	20	650	80	2	2	13
14	84	59	72	-1	66	0	7	23 8	0	.01	0	27.92	31	2.5	3.2	18	04	394	48	6	5	14
15	87	64	76	3	68	0	11	23 8	0	.10	0	27.88	22	.3	4.5	9	05	456	56	5	5	15
16	87	65	76	3	67	0	11	23 8	0	.31	0	27.87	04	1.8	5.3	16	31	488	60	5	6	16
17	86	63	75	2	68	0	10	23 8	0	.91	0	27.89	35	4.7	5.0	23	35	318	40	6	7	17
18	86	65	76	3	66	0	11	1 8	0	T	0	27.84	30	6.9	7.1	13	34	497	62	6	7	18
19	82	64	73	0	66	0	8	1 3 8	0	.05	0	27.88	32	1.4	5.6	12	24	318	40	7	7	19
20	83	64	74	1	67	0	9	2 8	0	.05	0	27.97	12	.5	4.9	8	13	406	51	4	5	20
21	84	64	74	2	67	0	9	2 8	0	0	0	28.04	18	3.7	5.2	12	19	475	59	3	3	21
22	87	63	75	3	67	0	10	2 8	0	0	0	28.02	22	2.3	5.9	14	34	502	63	5	5	22
23	89	63	76	4	68	0	11	2 8	0	T	0	28.00	31	4.6	5.6	10	34	593	75	3	5	23
24	88	65	77*	5	68	0	12	23 8	0	.73	0	27.94	05	1.3	3.5	16	34	493	62	4	4	24
25	89*	63	76	4	67	0	11	2	0	0	0	27.90	34	4.0	5.0	9	35	714	90	3	3	25
26	88	62	75	3	66	0	10	2 8	0	0	0	27.98	34	5.1	5.5	12	33	546	69	4	4	26
27	87	65	76	5	66	0	11	1 3	0	.50	0	28.05	01	2.5	5.9	17	10	205	26	9	9	27
28	80	63	72	1	66	0	7	2	0	.13	0	28.06	13	2.1	6.2	12	18	284	36	9	8	28
29	80	61	71	0	63	0	6	2 8	0	0	0	27.97	16	4.4	4.9	10	13	393	50	6	6	29
30	83	57*	70	-1	63	0	5	2	0	0	0	27.84	16	2.2	3.9	9	21	460	59	4	3	30
31	82	60	71	0	65	0	6	23	0	T	0	27.79	24	1.2	4.8	12	20	491	63	8	6	31
	SUM	SUM				TOTAL	TOTAL			TOTAL	TOTAL	FOR THE MONTH:						TOTAL	%	SUM	SUM	
	2589	1931				0	252	NUMBER OF DAYS		3.63	0	27.91	02	.7	5.3	23	35	13015	FOR MONTH	183	179	
	AVG.	AVG.	AVG.	DEP.	AVG.	DEP.	DEP.	PRECIPITATION		DEP.						DATE: 17		POSSIBLE		AVG.	AVG.	
	83.5	62.3	72.9	0.1	66	0	8	≥.01 INCH	12	-0.87								25081	52	5.9	5.9	
						SEASON TO DATE		SNOW, ICE PELLETS		GREATEST IN 24 HOURS AND DATES								GREATEST DEPTH ON GROUND OF SNOW, ICE PELLETS OR ICE AND DATE				
	NUMBER OF DAYS					TOTAL	TOTAL	≥1.0 INCH	0	PRECIPITATION		SNOW, ICE PELLETS						0				
	MAXIMUM TEMP.		MINIMUM TEMP.			0	706	THUNDERSTORMS	10	1.22	16-17	0										
	≥90°*	≤32°	≤32°	≤0°		DEP.	DEP.	HEAVY FOG X	24													
	0	0	0	0		0	-50	CLEAR 5	PARTLY CLOUDY 17	CLOUDY 9												

HOURLY PRECIPITATION (WATER EQUIVALENT IN INCHES)

Date	A.M. hour ending at: 1	2	3	4	5	6	7	8	9	10	11	12	P.M. hour ending at: 1	2	3	4	5	6	7	8	9	10	11	12	Date
1																									1
2															T										2
3																									3
4																									4
5													T		.02	.02	T	T		T	.10	.11			5
6					.01	.11	.08	T	T			T	T	.23	.04	.08	T		T	T					6
7												T	T												7
8																									8
9																									9
10								T	T	.01	.01	.01	T	T	.01	T	T								10
11																									11
12																T									12
13																									13
14														T						T	.01				14
15																	.01	.06	.03	T					15
16																		.31							16
17															.15	.75	.01			T	T				17
18																				T					18
19									T	T				T	T	.05									19
20															.05										20
21																									21
22																									22
23																T									23
24																.43	.30								24
25																									25
26																									26
27														T	.02	.03	T	.02	T			.14	.29	T	27
28	.02	T														.04	.06	.01							28
29																									29
30																									30
31																T									31

ASHEVILLE, NORTH CAROLINA

* EXTREME TEMPERATURES FOR THE MONTH: MAY BE THE LAST OF MORE THAN ONE OCCURRENCE.
\- BELOW ZERO TEMPERATURE OR NEGATIVE DEPARTURE FROM NORMAL.
* ≥ 70° AT ALASKAN STATIONS.
* ALSO ON AN EARLIER DATE, OR DATES.
X HEAVY FOG RESTRICTS VISIBILITY TO 1/4 MILE OR LESS.
T IN THE HOURLY PRECIPITATION TABLE AND IN COLUMNS 9, 10, AND 11 INDICATES AN AMOUNT TOO SMALL TO MEASURE.
THE SEASON FOR DEGREE DAYS BEGINS WITH JULY FOR HEATING AND JANUARY FOR COOLING.
DATA IN COLUMNS 6, 12, 13, 14, AND 15 ARE BASED ON 8 OBSERVATIONS PER DAY AT 3 HOUR INTERVALS.
WIND DIRECTIONS ARE THOSE FROM WHICH THE WIND BLOWS. RESULTANT WIND IS THE VECTOR SUM OF WIND DIRECTIONS AND SPEEDS DIVIDED BY THE NUMBER OF OBSERVATIONS. FIGURES FOR DIRECTIONS ARE TENS OF DEGREES FROM TRUE NORTH; I.E., 09=EAST, 18=SOUTH, 27=WEST, 36=NORTH, AND 00=CALM. WHEN DIRECTIONS ARE IN TENS OF DEGREES IN COL. 17, ENTRIES IN COL. 16 ARE FASTEST OBSERVED 1-MINUTE SPEEDS. IF THE * APPEARS IN COL. 17, SPEEDS ARE GUSTS.
ANY ERRORS DETECTED WILL BE CORRECTED AND CHANGES IN SUMMARY DATA WILL BE ANNOTATED IN THE ANNUAL SUMMARY.

SUBSCRIPTION PRICE: LOCAL CLIMATOLOGICAL DATA $2.55 PER YEAR INCLUDING ANNUAL ISSUE IF PUBLISHED. FOREIGN MAILING $2.10 EXTRA. SINGLE COPY: 20¢ FOR MONTHLY ISSUE; 15¢ FOR ANNUAL SUMMARY. MAKE CHECKS PAYABLE TO DEPARTMENT OF COMMERCE, NOAA. SEND PAYMENTS AND ORDERS TO NATIONAL CLIMATIC CENTER, FEDERAL BUILDING, ASHEVILLE, NORTH CAROLINA 28801.

I CERTIFY THAT THIS IS AN OFFICIAL PUBLICATION OF THE NATIONAL OCEANIC AND ATMOSPHERIC ADMINISTRATION, AND IS COMPILED FROM RECORDS ON FILE AT THE NATIONAL CLIMATIC CENTER, ASHEVILLE, NORTH CAROLINA, 28801

William H. Haggard

DIRECTOR, NATIONAL CLIMATIC CENTER

SUMMARY BY HOURS

Hour (local time)	Averages: Sky cover (tenths)	Station pressure in.	Temperature: Air °F	Wet bulb °F	Dew pt. °F	Relative humidity %	Wind speed m.p.h.	Resultant wind: Direction	Speed m.p.h.
01	5	27.92	65	65	65	99	3.0	06	.6
04	7	27.90	64	64	64	100	3.4	35	1.9
07	8	27.93	64	64	64	100	4.1	34	2.5
10	4	27.94	75	70	68	79	6.4	36	3.3
13	5	27.92	81	71	67	63	7.8	05	1.4
16	7	27.88	79	70	67	69	7.8	17	2.4
19	6	27.88	73	69	67	82	5.8	13	.8
22	4	27.92	68	67	66	94	3.7	13	.5

USCOMM - NOAA - ASHEVILLE   425
09/18/75

Figure 2.4-5. An Example of the Local Climatological Data for Asheville, NC is shown in Figure 2.4-5. In this publication the type of weather is provided so that one can ascertain if the rainfall is from a thunderstorm or a general wide-coverage weather system. The water equivalent of the snow is shown in the hourly precipitation data. Note that the same information is available on the Hourly Precipitation Data records but that the type of rainfall event is not noted in the latter.

Finally the National Climatic Center prepares a Storm Summary on a monthly basis. This information is of little value to system engineers since it emphasizes the damage done by the storm rather than the physics of the storm. For example, the most severe rain event in Asheville, NC, in 1975 occurred on August 24; however, this event is not indicated in the Storm Summary because it apparently caused no significant damage.

2.4.1.2 Rain Gauges. If more information is desired regarding higher rain rates associated with thunderstorms it can be obtained for most first-order Weather Service Office (defined as those offices manned by Weather Service personnel) sites. These sites generally have both tipping bucket and universal weighing gauge precipitation monitors. The tipping bucket gauges generally accumulate the number of 0.01 inch precipitation events in a day which is utilized to collaborate with the accumulation in the other gauges. However, some tipping bucket gauges employ a readout strip chart (triple register chart of operations recorder register) similar to that shown in Figure 2.4-6. By estimating the time between tips the rain rate may be estimated. The location of those stations having triple register charts was not available from the National Climatic Center.

The universal weighing gauge is also capable of providing rain rate information and is the main instrument utilized to provide the 5-minute to 1 hour precipitation data. This measurement is accomplished by reading directly from the 24-hour strip chart on the gauge. An example of one of these strip charts is shown in Figure 2.4-7. These charts are available dating back about 10 years from the National Climatic Center for 25 cents per chart. By measuring the slope of the line, the rain rate to at least 5 minute resolution may be obtained and even 1-minute rain rates may be inferred from some charts. It appears that these charts are the best source of information for short duration rate data.

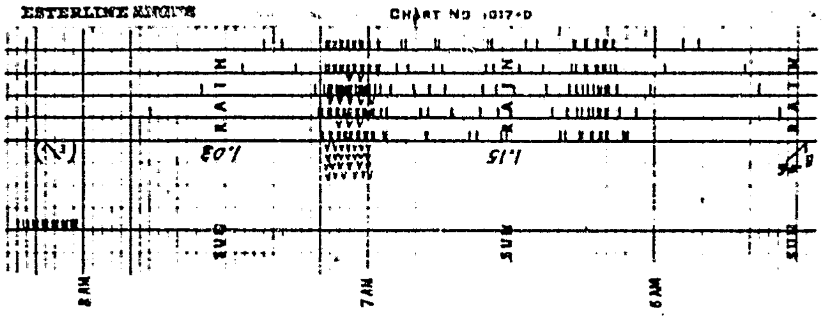

Figure 2.4-6. Example of Operations Recorder Record (de N.W.S. Field Measurements Handbook, No. 1, PG B7-9)

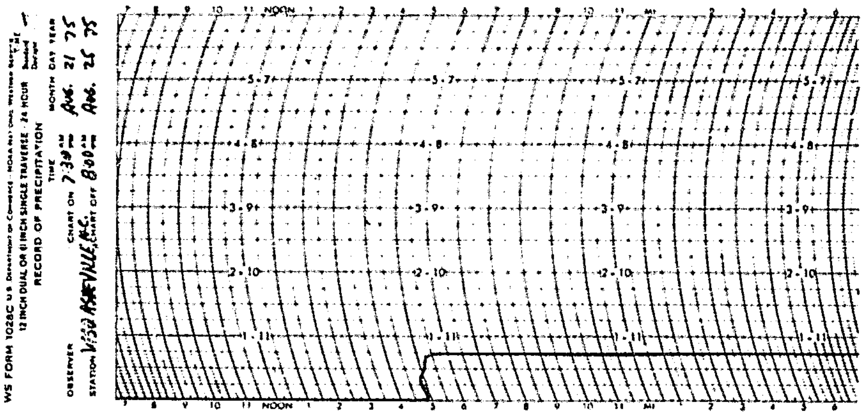

Figure 2.4-7. An Example of a Universal Weighing Gauge Strip Chart

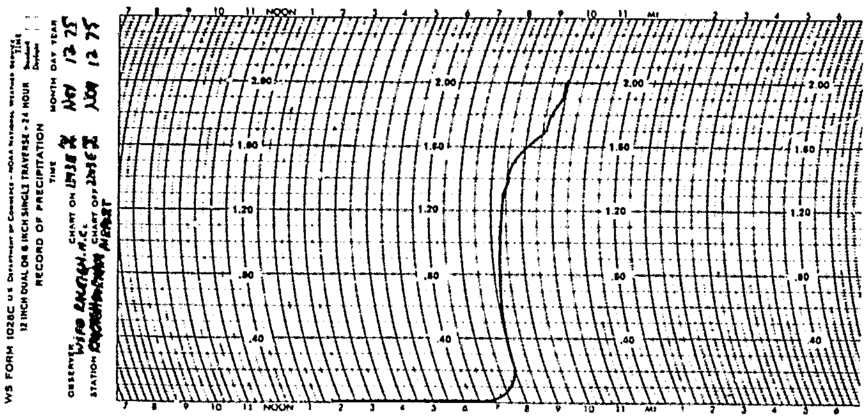

Figure 2.4-8. An Example of an Intense Rain Event

The last automated rain gauge utilized by the U.S. Weather Service is the Fischer-Porter gauge. This unit is a weighing gauge which punches a paper strip chart in a binary coded decimal (BCD) format every 15 minutes. The gauge may be set to record every 5 minutes, but that resolution is generally not utilized by the Weather Service. The gauge records to only the nearest 0.1 inch.

2.4.1.3 Estimating Rain Rate From Gauge Records. An example of how intense rain rates may be estimated is now given. The dates of the highest rain rate events are found in the CD, Annual Summary. Note that from Figure 2.4-4 the most intense rain rates (0.38 inches in 5 minutes) at the Asheville, NC, WSO occurred on August 24, ending at 1658 Eastern Standard Time. This occurred during a thunderstorm (see Figure 2.4-5) but it was not the most rain in a 24-hour period, which occurred on August 17. The amount of precipitation between 1500 and 1700 EST on August 17 is noted in the LCD in Figure 2.4-5. This process is utilized to determine the list of dates for the high rain rate events. Copies of the rain gauge charts for these dates are then obtained from National Climatological Center. For the August 24 event, the most accurate data appears directly on the gauge readout shown in Figure 2.4-7. By estimating the slope of the cumulative data, the rain rate just before 4 PM was more than 4.56 inch/hr (116 mm/hr) for the first several minutes. Interpolation yields a rate approaching 150 mm/hr for 2 minutes. Another example of a cloud burst is shown in Figure 2.4-8. Herein rain rates approaching 300 mm/hr (12 inches/hr) occurred at 8 PM and contributed to the airline crash at this airport at that time. Clearly the attenuation at a ground station would be significant for this severe 2 minute event (0.00038% of a year).

Bodtmann and Ruthroff (1974) have demonstrated a technique of estimating rain rate distributions directly from these rain gauge charts with 1-minute resolution. Since computing derivatives from these charts is notoriously inaccurate, considerable processing is necessary to get accurate results, especially at high rain rates. Figure 2.4-9 is an example of a Dallas, TX rain event cumulative and rain rate (1-minute integration) distribution. Clearly the method is powerful and readily adaptable to field measurements made using a commercial weighing gauge.

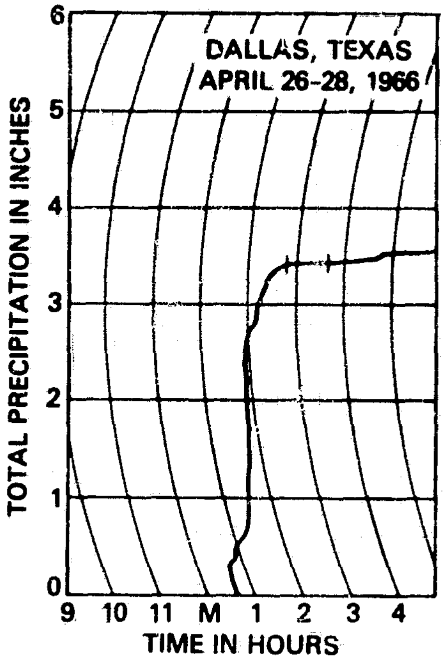

a) National Weather Service Weighing Gauge Chart

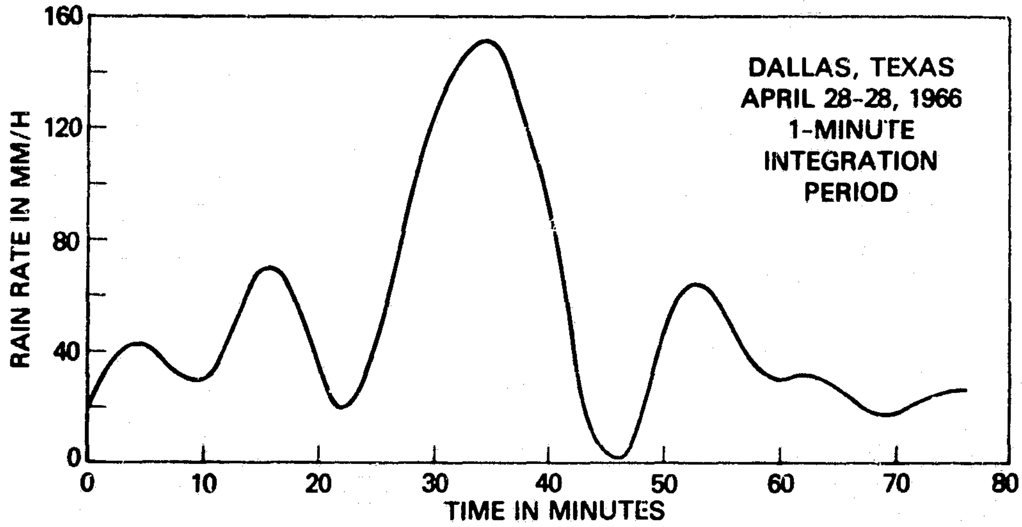

b) Rain Rates vs. Time Computed From Weighing Gauge Data

Figure 2.4-9. An Example of Generation of Rain Rate Data From a Weighing Gauge Chart

2.4.2 Canadian Sources

The Atmospheric Environment Office* prepares several documents containing rain and snow precipitation data. These documents† are:

- Monthly Record - Western Canada - Part 1
  - Provinces of British Columbia, Alberta, Saskatchewan and Manitoba
  - $21.60 foreign per year
  - $ 2.00 foreign per issue
- Monthly Record - Northern Canada - Part 2
  - Territories of Yukon and Northwest
  - $12.00 foreign per year
  - $ 1.00 foreign per issue
- Monthly Record - Eastern Canada - Part 3
  - Provinces of Ontario, Quebec, Nova Scotia and New Brunswick
  - $21.60 foreign per year
  - $ 2.00 foreign per issue
- Canadian Weather Review
  - published monthly
  - covers about 250 surface stations throughout Canada
  - $5.40 foreign per year

---

* Head Office, 4905 Dufferin Street, Downsview, Ontario M3H 5T4, Canada

† Available from: Supply and Services Canada, Publishing Centre, Hull, Quebec, KOA OS9, Canada. Make checks payable to Receiver General for Canada. Canadians should request domestic price schedule.

- $0.50 foreign per issue
- available about one month following the date of recording

- Snow Cover Data for Canada

  - published once per winter
  - covers all provinces/territories
  - $1.00 foreign per issue
  - available June/July of each year

The data in the Monthly Records (available about four months following recording) is of most importance to the earth space path engineer. As shown in Figure 2.4-10, the rainfall, snowfall and total precipitation are given for each day of the month. The Monthly Summary table indicates the number of thunderstorms, etc., and the recording rain gauge data for selected cities is given. These are the maximum amounts for the duration periods indicated on the date of occurrence. In addition, the number of hourly periods with rainfall accumulations between 0.01-0.09, 0.1-0.19, etc., inches is noted. These data are obtained from tipping bucket rain gauges measuring in increments of 0.01 inches.

The tipping bucket rain gauge data is available for many more Canadian locations. The charts from these gauges are available upon request from the Climatological Recording Services Branch of the Head Office in Downsview, Ontario, at a nominal charge.

2.4.3 Worldwide Sources

Many countries prepare meteorological data similar to the U.S. and Canada. Many of these are on file at the National Weather Service Library, Room 816, Gramax Bldg., 13th Street, Silver Spring, MD. One document, the Monthly Climatic Data for the World does list the number of days per month a station receives more than 1 mm of rain and the total rainfall per month. The data is coarse and can only provide a general indication of the precipitation

TABLE/TABLEAU 2 — **PRECIPITATION** — MARCH 1977 MARS

STATION		TOTAL	% OF NORMAL / % DE LA NORMALE	1	2	3	4	5	6	7	8	9	10	11	12	13	14	15	16	17	18	19	20	21	22	23	24	25	26	27	28	29	30	31	[illegible]
ONTARIO ONTARIO																																			
OTTAWA BRITANNIA	R/P	[illegible]					2.3	1.9							1.3	[illegible]	2.8	1.6													7.4	1.3	1.8		
	S/N	[illegible]			T																		0.5	0.3	[illegible]										
	P	[illegible]			T		2.3	1.9							1.9	[illegible]	2.0	1.6					0.5	0.3	[illegible]						7.4	1.3	1.8		
OTTAWA CDA	R/P	[illegible]	[illegible]				2.1	1.3							[illegible]	17.0	5.1	3.6						0.3							8.4	0.3	1.8		
	S/N	[illegible]	[illegible]	T	T		T	0.2	T	T										T			1.0	0.3	[illegible]	0.1									
N	P	[illegible]	[illegible]	T	T		2.1	1.5	T	T					[illegible]	17.0	5.1	3.6		T			1.0	0.6	[illegible]	0.1					8.4	0.3	1.8		[illegible]
OTTAWA INT'L A	R/P	74.1	[illegible]				0.4	0.4							T	36.1	12.5	T	1.3					0.3							8.8	1.4	1.4		
	S/N	37.2	77	T	T		0.5	1.2	T	T										T			1.1	T	21.8	2.9									
N	P	[illegible]	[illegible]	T	T		0.9	1.4	T	T					T	36.1	12.5	T	1.3	T			1.1	0.3	20.8	2.7					8.8	1.4	1.4		[illegible]
OTTAWA NRC	R/P	[illegible]	[illegible]				11.7									81.6	4.1	2.5	0.3												10.2		2.3		
	S/N	[illegible]	[illegible]					T		T													0.3		[illegible]										
	P	111.6	[illegible]				11.7	T		T						81.6	4.1	2.5	0.3				0.3		[illegible]						10.2		2.3		[illegible]

[illegible]

MARCH 1977 MARS — **RECORDING RAIN GAUGE DATA/ DONNEES DES PLUVIOGRAPHES** — TABLE/TABLEAU 7

STATION		MAXIMUM AMOUNTS (.01 inch) HAUTEUR MAXIMUM (en .01 de pouce) FOR DURATION INDICATED WITH DATES OF OCCURENCE POUR LES DUREES MENTIONEES ET DATES																HOURLY RAINFALL CHUTE DE PLUIE HORAIRE No. of occurrences in classes shown Fréquences par classe					
		5 min.		10 min.		15 min.		30 min.		60 min.		120 min.		6 hr.		12 hr.							
		AMOUNT VALEUR	DATE	AMOUNT VALEUR	DATE	AMOUNT VALEUR	DATE	AMOUNT VALEUR	DATE	AMOUNT VALEUR	DATE	AMOUNT VALEUR	DATE	AMOUNT VALEUR	DATE	AMOUNT VALEUR	DATE	.01–.09	.10–.19	.20–.49	.50–.99	1.00–1.99	2.00 or more ou plus
ONTARIO ONTARIO																							
OTTAWA INT'L A		04	30	05	04	08	13	13	13	19	04	32	13	78	13	111	13	46	11				
SAULT STE MARIE A		04	12	05	12	08	12	15	12	27	12	35	12	71	12	77	12	43	6	3			
SIMCOE		06	04	11	12	15	12	25	12	32	12	49	12	103	12	129	12	40	6	2			
SIOUX LOOKOUT A	*	02	27	03	27	04	27	08	27	13	27	13	27	14	27	14	27	3					
SUDBURY A	*	M		M		M		M		M		M		M		M		M	M				

MARCH 1977 MARS — **MONTHLY SUMMARY**

STATION	NUMBER OF DAYS WITH / NOMBRE DE JOURS AVEC										
	TEMPERATURES ≤ 0.0°C	THUNDERSTORMS ORAGES	RAIN OR DRIZZLE PLUIE OU BRUINE	FREEZING PRECIPITATION PRECIPITATIONS SE CONGELANT	HAIL GRELE	SNOW NEIGE	MEASURABLE PRECIPITATION PRECIPITATION MESURABLE	FOG BROUILLARD	SMOKE OR HAZE FUMEE OU BRUME SECHE	DUST OR BLOWING SAND POUSSIERE OU CHASSE - SABLE ELEVEE	BLOWING SNOW CHASSE - NEIGE ELEVEE
ONTARIO											
NORTH BAY A	24	1	6	1		7	12	5	1		
OTTAWA INT'L A	22	1	9	1		5	12	11	8		1
PETAWAWA A	27	1	8	[illegible]		4	10	5	4		
PETERBOROUGH A	26	2	9	1		[illegible]	12	2	6		1
PICKLE LAKE	31		3	3		10	12	3			1

Figure 2.4-10. Examples of the Canadian Monthly Record Precipitation Data

climate. An example is shown in Figure 2.4-11. This document is available for $0.70 per monthly copy about 9 months following the recording date from the National Climatic Center.

2.5 ESTIMATION OF RAIN RATE

The rain rate measurement is an inexact process because of the discrete nature of rainfall. Obviously, because rain falls as raindrops, the rain rate is computed by measuring the rain accumulation per given area for a known period of time at a point. The shortest period of time reported by the U.S. and Canadian Weather Services is five minutes. Assuming the rain rate is uniform for that period of time, the computed point rain rate and the "instantaneous" point rain rate are equal. However, the question arises as to how the apparent rain rate varies as the integration (computing) time is varied. This effect has been addressed experimentally by experimenters at the Bell Telephone Laboratories.

At Holmdel, NJ, measurements (Bodtmann and Ruthroff-1974) of the apparent rain rate versus the gauge integration period over a 2-year period have yielded the results in Figure 2.5-1. These results extend from 1.5 seconds to 2 minutes and are normalized to a one-minute integration time. Unfortunately, the measurement do not extend to a 5-minute integration time which would be very convenient for comparison of the Lin model with other rain models which employ a one-minute integration period (see Chapter 3). The variation between a 2-minute and a 5-minute integration time is expected to be significant for high rain rates. However, Figure 2.5-1 clearly shows that for rain rates below 50 mm/h the error due to the integration time is small. This effect arises because the low rain rate events tend to be spatially and temporally uniform, while the rain rates between 50 and 120 mm/h are dominated by spatially and temporally nonuniform convective rains.

Only the most severe cells create rain rates above 120 mm/h and these are highly variable. Therefore, a significant peak rain rate two or three times as high as the one-minute average can occur for one second during the

SURFACE DATA

OCTOBER 1977

STATION	LATITUDE (° ′)	LONGITUDE (° ′)	ELEVATION (METERS)	NUMBER OF DAYS OF OBSNS.	PRESSURE: MEAN STATION (MB)	PRESSURE: MEAN SEA LEVEL (MB)	TEMPERATURE: MEAN (°C)	TEMPERATURE: DEPARTURE (°C)	VAPOR PRESSURE: MEAN (MB)	VAPOR PRESSURE: DEPARTURE (MB)	PRECIPITATION: NO. OF DAYS ≥ 1 MM.	PRECIPITATION: TOTAL (MM)	PRECIPITATION: DEPARTURE (MM)	PRECIPITATION: QUINTILE	SUNSHINE: PERCENTAGE OF LONG-TERM AVERAGE (%)
CANADA-EASTERN															
ALERT	82 30 N	62 20 W	63	31	1003.7	1012.2	-18.9	+ 0.9	1.1	-0.1	4	9	- 7		
EUREKA	80 00 N	85 56 W	10	31	1008.5	1009.9	-21.0	+ 0.5	1.2	+0.1	1	4	- 3		
RESOLUTE	74 43 N	94 59 W	67	31	998.0	1006.9	-14.3	+ 0.3	2.1	+0.2	6	22	+ 6		106
CLYDE	70 27 N	68 33 W	6	31	1002.1	1005.4	- 7.6	- 1.2	3.2	-0.3	11	55	+ 21		
HALL BEACH	68 47 N	81 15 W	8	31	1004.9	1005.8	- 9.4	+ 1.6	3.0	+0.2	9	27	+ 4		
BAKER LAKE	64 18 N	96 00 W	13	31	1007.0	1008.6	- 5.1	+ 2.4	4.0	+0.5	10	57	+ 37		
CORAL HARBOUR	64 12 N	83 22 W	64	31	999.0	1007.3	- 5.8	+ 2.2	3.9	+0.4	16	46	+ 17		
FROBISHER BAY	63 45 N	68 33 W	34	31	1002.3	1006.7	- 3.8	+ 0.9	4.0	+0.2	13	52	+ 18		97
CHURCHILL	58 45 N	94 04 W	29	31	1005.5	1009.1	2.5	+ 3.6	5.7	+0.6	6	23	- 15		142
INOUCDJOUAC	58 27 N	78 07 W	5	31	1008.1	1008.7	1.7	+ 2.1	6.3	+0.7	14	71	+ 22	5	131
FORT CHIMO	58 06 N	68 25 W	37	31	1004.4	1009.1	0.1	+ 0.4	5.4	+0.2	12	48	+ 9		
TROUT LAKE	53 50 N	89 52 W	220	31	987.0	1014.2	4.9	+ 3.1	6.2	-0.1	[illegible]	47	- 6		
NITCHEQUON	53 12 N	70 54 W	536	31	948.7	1014.0	0.9	+ 0.3	5.7	0.0	13	64	- 16		
MOOSONEE	51 16 N	80 39 W	10	31	1013.4	1014.7	5.3	+ 1.4	6.8	-0.4	6	58	- 15		173
ARMSTRONG	50 17 N	80 54 W	323	31			4.1	+ 1.0			5	34	- 25		147
KAPUSKASING	49 25 N	82 28 W	227	31	998.4	1016.5	4.3	- 0.3	6.5	-0.8	9	69	- 3		
GERALDTON	49 42 N	86 57 W	331			U									
SEPT-ILES	50 13 N	66 16 W	55	31	1006.6	1013.4	4.8	+ 0.9	6.5	-0.2	14	157	+ 74		107
GOOSE	53 19 N	60 25 W	49	31	1005.2	1011.3	3.2	0.0	5.9	-0.1	10	78	+ 15		102
NORTH BAY	46 22 N	79 25 W	371	31	972.4	1017.4	5.4	- 1.2	7.2	-1.0	9	62	- 22		128
MANIWAKI	46 23 N	75 58 W	170	31	995.8	1016.7	5.8	- 1.1	7.2	-0.9	9	63	- 5		106
TORONTO/MALTON INT AP	43 41 N	79 38 W	173	31	996.2	1017.3	8.0	- 1.5	8.5	-1.1	6	69	+ 10		
MONTREAL/DORVAL INT AP	45 28 N	73 45 W	36	31	1011.6	1016.0	7.6	- 1.4	8.5	-0.4	11	113	+ 35		
BAGOTVILLE	48 [illegible] N	71 00 W	159	31	995.6	1015.2	5.6	- 0.1	6.7	-0.6	10	61	- 2		
CHATHAM	47 [illegible] N	65 27 W	34	31	1009.6	1013.7	7.2	- 0.2	8.1	-0.2	16	257	+174	5	87
STEPHENVILLE	48 32 N	58 33 W	26	31	1009.6	1012.8	7.8	+ 0.6	8.4	0.0	17	183	+ 84		
GANDER INT AP	48 57 N	54 34 W	151	31	993.8	1012.4	6.3	0.0	8.1	+0.1	14	127	+ 26		90
SHEARWATER	44 38 N	63 30 W	51	31	1008.7	1015.0	9.8	+ 0.2	10.2	0.0	13	142	+ 33		108
SYDNEY	46 10 N	60 03 W	62	31	1006.8	1014.4	8.7	- 0.4	8.7	-1.1	13	130	+ 15	4	70
SHELBURNE	43 43 N	65 15 W	30			U									
SABLE ISLAND	43 56 N	60 01 W	4	31	1015.4	1015.9	11.7	+ 0.1	11.7	0.0	14	122	+ 12	4	70
ST. JOHN'S (TORBAY)	47 37 N	52 45 W	141			U									
ST PIERRE AND MIQUELON															
ST PIERRE	46 46 N	56 10 W	5	31	1013.9	1014.5	9.1	+ 0.2	9.8	+0.4	13	87	- 50	1	112
UNITED STATES-NORTHEAST															
INTERNATIONAL FALLS	48 34 N	93 23 W	361	31	975.0	1016.7	6.3	- 0.1				20	- 23		
DULUTH	46 50 N	92 11 W	432	31	975.4	1017.3	6.8	- 0.6				81	+ 23		104
ST. CLOUD	45 35 N	94 11 W	318	31	979.0	1017.6	7.8	- 0.9							
SAULT STE. MARIE	46 28 N	84 22 W	221	31	993.8	1016.0	7.1	- 0.8	8.1	0.0	8	47	- 25	2	81
BURLINGTON	44 28 N	73 09 W	104	31	1001.8	1016.6	8.1	- 1.2	8.2		10	128	+ 58	5	88
CARIBOU	46 52 N	68 01 W	146	31	991.5		5.4	- 0.2				135	+ 51		
DES MOINES	41 32 N	93 39 W	294	31	986.8	1018.0	11.3	- 1.1	9.4	-0.2	10	130	+ 75	5	82
COLUMBIA	38 49 N	92 13 W	274	31	990.1	1018.5	13.1	- 1.3				112	+ 25		85
CHICAGO	41 47 N	87 45 W	190	31	995.6	1018.3	11.0	- 2.0	8.9	-0.8	9	42	- 24	2	76
ST. LOUIS	38 45 N	90 23 W	172	31	998.3	1018.9	13.1	- 2.0	11.5	+0.7	7	96	+ 25	4	94
DAYTON	39 54 N	84 13 W	306	31	985.8	1018.6	11.0	- 2.1	8.6		9	98	+ 49	5	76
COLUMBUS	40 00 N	82 53 W	254	31	986.5	1018.5	13.1	- 1.3	8.3	-1.9	9	65	+ 17	4	85
BUFFALO	42 56 N	78 44 W	215	31	989.3	1017.5	9.8	- 1.1	9.1	0.0	9	66	- 10	3	91
NEW YORK LA GUARDIA	40 46 N	73 54 W	9	31	1005.4	1016.9	12.7	- 1.8	11.1	-0.3	2	148	+ 73	5	
BOSTON	42 22 N	71 02 W	9	31	1011.4	1016.0	12.9	- 0.1	11.2	+0.6	2	118	+ 41	5	85
BLUE HILL OBS	42 13 N	71 07 W	195	31	992.1	1015.2	10.7	- 1.1	10.6	+0.5	12	153	+ 71	5	89
CHATHAM	41 40 N	69 58 W	16			U									
WASHINGTON DULLES	38 57 N	77 27 W	98			U									
WASHINGTON NATIONAL	38 51 N	77 02 W	20	31	1013.5	1017.8	15.0	- 0.4	11.0	-0.7	7	136	+ 68	5	84

Figure 2.4-11. An Example of the Monthly Climatic Data for the World

ORIGINAL PAGE IS OF POOR QUALITY

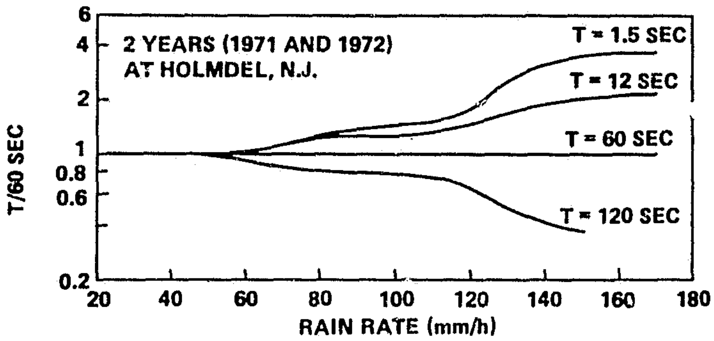

Figure 2.5-1. Rain Rate Distribution Versus Gauge Integration Time

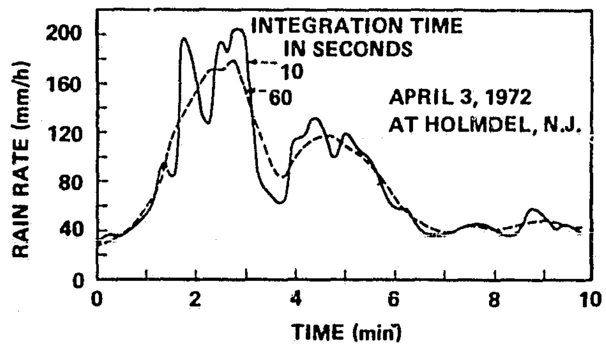

Figure 2.5-2. Integrating Rain Gauge Results for Two Integration Times

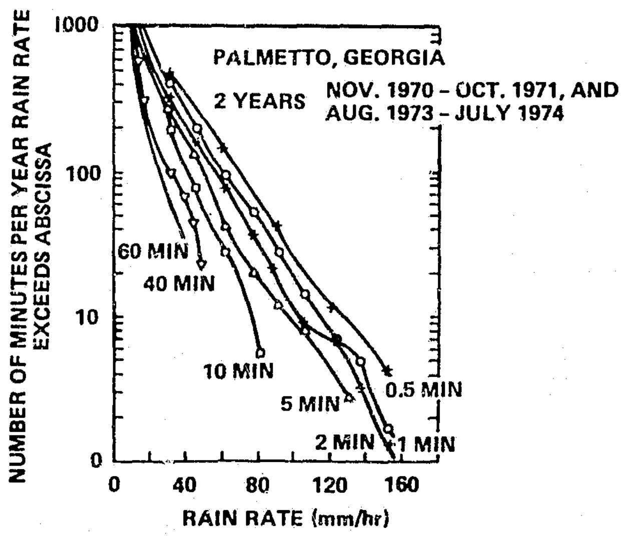

Figure 2.5-3. Cumulative Rain Rate Statistics Versus Integration Period

one-minute period. As an example, a typical rain rate versus time profile comparing the one-minute and ten-second integration times is shown in Figure 2.5-2 (Bodtmann and Ruthroff-1974).

The impact of varying integration times can be significant for both the measurement of cumulative rain rate statistics (related to cumulative attenuation statistics) and rain rate duration measurements (related to attenuation fade duration. Lin (1978) has experimentally determined the effect of the integration time on cumulative statistics. The results for Palmetto, GA are shown in Figure 2.5-3. Clearly the difference between a 1-minute and 30-second integration time is significant. Similar results for rain rate duration statistics are not available.

2.6 REFERENCES

Block, S.C., D. Davidson and D.D. Tang (1978), "Rain-Attenuation Experience With the Tampa Triad Using 19-GHz Comstar Satellite Beacon Signals," Record, EASCON '78, September 25-27, Arlington, Va., pp. 379-384.

Bodtmann, W.F. and C.L. Ruthroff (1974), "Rain Attenuation on Short Radio Paths: Theory, Experiment and Design," Bell Syst. Tech. Jrnl., Vol. 53, pp. 1329-1349.

Crane, R.K. (1966), "Microwave Scattering Parameters for New England Rain," MIT Lincoln Lab. Tech. Rpt. 426, ASTIA Doc. AD647798

Crane, R.K. and D.W. Blood (1979), "Handbook for the Estimation of Microwave Propagation Effects - Link Calculations for Earth-Space Paths," ERT Doc. No. P-7376-TR1, prepared under NASA Contract NAS5-25341.

Goldhirsh, J. (1976), "Path Attenuation Statistics Influenced by Orientation of Rain Cells," IEEE Trans. Ant. Prop., Vol. AP-24, No. 6, pp. 792-799.

Goldhirsh, J. and I. Katz (1979), "Useful Experimental Results for Earth-Satellite Rain Attenuation Modeling," IEEE Trans. Ant. Prop., Vol. AP-27, No. 3, pp. 413-415.

Huff, F.A. and W.L. Shipp (1969), "Spatial Correlations of Storm, Monthly and Seasonal Precipitation," Jrnl. Appl. Meteorology, Vol. 8, August, pp. 542-550.

Ippolito, L.J. (1979), private communication.

Joss, J., J.C. Thams and A. Waldvogel (1968), "The Variation of Raindrop Size Distributions at Locarno," Proc. Int. Conf. Cloud Phys., Toronto, Canada, pp. 369-373.

Kerker, M. (1969), The Scattering of Light and Other Electromagnetic Radiation, Academic Press, New York.

Laws, J.O. and D.A. Parsons (1943), "The Relation of Raindrop Size to Intensity," Trans. Am. Geophys. Union, Vol. 24, pp. 452-460.

Lin, S.H. (1978), "Empirical Calculation of Microwave Path Attenuation Distributions on Earth-Satellite Paths," Record, EASCON '78, Arlington, Va., pp. 372-378.

Marshall, J.S. and W.M. Palmer (1948), "The Distribution of Raindrops With Size," Jrnl. Meteorology, Vol. 5, pp. 165-166.

Olsen, R.L., D.V. Rogers and D.B. Hodge (1978), "The aR^b Relation in the Calculation of Rain Attenuation," IEEE Trans. Ant. Prop., Vol. AP-26, pp. 318-329.

Rogers, D.V. (1978), private communications.

Rowland, J.R. (1976), "Comparison of Two Different Raindrop Disdrometers," 17th Conf. Radar Meteorology, Seattle, Wa., pp. 398-405.

Ryde, J.W. and D. Ryde (1945), "Attention of Centimetre and Milimetre Waves by Rain, Hail, Fogs, and Clouds," Rpt. No. 8670, Research Laboratory of the General Electric Company, Wembley, England.

CHAPTER III

AN OVERVIEW OF SEVERAL RAIN AND ATTENUATION MODELS

3.1 INTRODUCTION

3.1.1 Summary of Models

During the 1970s several models for estimation of the cumulative attenuation statistics on earth-space millimeter paths have been developed. Each of these models appears to have advantages and disadvantages depending on the specific application. In this chapter an attempt is made to briefly summarize the key features of five commonly used models without reiterating all of the details. One of these models, The Global Model, is recommended for use as the design tool in Chapter VI because it is both accurate and easy to apply without the need for a specialized computer program.

Table 3.1-1 summarizes the key inputs, outputs and other important features of the five models in their current format. These models are:

- Rice-Holmberg
- Dutton-Dougherty
- Global
- Lin
- Piecewise Uniform Rain Rate

Nearly all of these models are being updated and modified based on recent experimental results and analyses. In addition, other models prepared by

Table 3.1-1. Summary of Model Parameters

MODEL	INPUTS	OUTPUTS	COMMENTS
Rice-Holmberg	Total annual rainfall ratio of thunderstorm rain to total rain	Prob. of exceedance of rain rate	
Dutton-Dougherty	Same as Rice-Holmberg plus link parameters*, ground station weather parameters, and rainfall rate	Prob. of exceedance of attenuation including clear air and rain contributions	Requires use of computer program
Global	Geographic region, link parameters*, and rain rate	Prob. of exceedance for rain rate and corresponding attenuation	Relatively easy to apply with nomographs provided
Lin	Five-minute rain rate statistics and link parameters*	Attenuation for a given rain rate	Assumes prob. of exceedance of five-minute rain rate is known for given location. Only tested in eastern US.
Piecewise Uniform	Rain rate statistics and link parameters*	Attenuation for a given rain rate	Assumes prob. of exceedance of rain rate is known for given location.

* Link parameters include quanities such as: frequency, elevation angle, ground station location and elevation, etc.

major communications companies, such as Comsat, are utilized (Gray and Brown-1979), but these are generally not published in the open literature and so are not considered here.

The models provide either rain rate statistics or attenuation statistics. Generally, these statistics can be related by use of the specific attenuation and effective path length relations. Specific attenuation has been described in Chapter II, while the effective path length will be summarized at the end of this chapter. For example, the Rice-Holmberg model only computes the exceedance probability statistics for rain rate, but this is relatable to attenuation by use of the specific attenuation and the effective path length.

The Dutton-Dougherty and Global models provide the attenuation statistics given the geographic and link parameters. That is, they give the rain rate statistics within the model.

The Lin and Piecewise Uniform Rain Rate models require a known set of rain rate statistics to generate the attenuation statistics. These models relate a specific ground point rain rate to the simultaneous attenuation along the path.

3.1.2 Concepts of Rainfall Statistics

3.1.2.1 Cumulative Statistics. The cumulative statistics for either rain rate or attenuation are usually presented as the probability of exceedance (abscissa) versus the rain rate or attenuation (ordinate). They represent stable statistics averaged over a period sufficiently long that variations in the lowest frequency component of the time distribution are averaged. For rain rate and rain attenuation the period corresponding to the lowest frequency is generally considered to be one year. Higher frequency components are the seasonal and daily variation of the rain rate. For example, in the eastern US, the higher frequency components arise because more rain falls in the summer than in the winter, and more rain falls between noon and 6 PM than between 6 AM and noon local time. Some people have suggested that the 11-year solar cycle is the lowest frequency component, but this has not been observed by the Weather Service.

Based on the above considerations the cumulative statistics for several years are required before "stable" annual statistics are obtained. For this reason, experimentally generated data bases for both rain and attenuation are not generally good until 5 or 10 years of data are included. However, because of the limited lifetime of the beacon satellites, attenuation data at a known frequency and elevation angle is generally not available for this length of period (Kaul et al-1977). Therefore data from several satellites launched over a long period are required. Since they are not at the same frequency and elevation angle, these results must be scaled in order to be combined. Frequently this process has not been done accurately, resulting in small segments of attenuation data which are not representative of the long term statistics.

Based on the above discussions it appears that the only present recourse is to utilize rain rate data as derivable from Weather Bureau or other long-term measurements. This leads to the exceedance curves for rain rate. The attenuation is then derived from the relations between rain rate and attenuation.

3.1.2.2 Outage Period Statistics. System designers are also interested in the average length of time a given threshold of rain rate or attenuation is achieved (also termed the outage time). In addition, the distribution of the outage time about the average is desired. Theoretical work of Lin (1973) has shown that the distribution is approximately lognormal.

Besides the outage time, Hyde (1979) has identified the desire to know the average time between outage periods within a given rain event, and the average time between outages between two rain events. The first case recognizes that outages above a given threshold of attenuation may occur several times during the same general rain event because the rain rate is highly time dependent during an event. For example, the passage of several rain cells associated with a given rain front will cause outages as each cell dominates the path attenuation. It is desirable to know the approximate period between these outages and the distribution of these outage periods as a function of threshold value and type of rain event. This type of data is expected to be dependent on the georgraphic region because the weather fronts are distorted by the presence of mountain ranges, lakes, cities, etc. Therefore, extrapolation to other regions is difficult unless their weather systems are similar.

The second case (average time between outages in two rain events) correlates the period between severe storms in a given region. This period is expected to be seasonally dependent because in most regions the high rain rate storms usually occur during a short period of the year. Again, some statistical estimate of the average period and the distribution of the periods would be desirable.

Generally, outage period data is not as readily available as the cumulative attenuation statistics data. Therefore, the designer must rely on the limited data bases available from CCIR (1978, Rpt 564-1), Comsat (Rogers and Hyde-1979) or Lin (1973). An estimate of the upper limit of the outage time is presented in Chapter VI.

3.2 RICE-HOLMBERG MODEL

3.2.1 Types of Storms

The Rice-Holmberg (RH) Model (Rice and Holmberg-1973) is based upon two rainfall types: convective ("Mode 1", Thunderstorm) rains and stratiform ("Mode 2", uniform) rains. The statistical model is based upon the sums of individual exponential modes of rainfall rates, each with a characteristic average rate R. According to this descriptive analysis

$$\text{rainfall} = \text{Mode 1 rain} + \text{Mode 2 rain}$$

The exponential distribution chosen to describe "Mode 1 rain" corresponds to a physical analysis of thunderstorms, while "Mode 2 rain," represented by the sum of two exponential distributions, is all other rain. In temperate climates only convective storms associated with strong updrafts, high radar tops, hail aloft and usually with thunder can produce the high rainfall rates identified by Mode 1. Only the highest rates from excessive precipitation data are used to determine parameters for Mode 1, which is intended to represent a physical mechanism as well as a particular mathematical form.

3.2.2 Sources of Data

The rainfall statistics in the RH model are based upon the following:

1) Average year cumulative distributions of hourly rates for the 10 years 1951 to 1960 and for a total of 63 stations, with 49 in the continental U.S. as summarized in the Weather Service Climatological Data for this period;
2) Distributions for 15-year averages with recording intervals of 6, 12, and 24 h for 22 of these stations (Jorgenson, et al-1969);
3) Accumulations of short-duration excessive precipitation for 1951 to 1960 for recording intervals of 5, 10, 15, 20, 30, 45, 60, 80, 100, 120, and 180 min for 48 U.S. stations;
4) A U.S. map of the highest 5-min rates expected in a two-year period (Skerganec and Samson-1970);
5) Maximum monthly rainfall accumulations and the average annual number of thunderstorm days for the period 1931 to 1960 for 17 U.S. stations and 135 additional stations reported by the World Meteorological Organization.

3.2.3 RH Model Parameters

The average annual total rainfall depth M is the sum of contributions M_1 and M_2 from the two modes:

$$M = M_1 + M_2 \text{ mm}$$

and the ratio of "thunderstorm rain" M_1 to total rain M is defined as

$$\beta = M_1/M$$

The number of hours of rainy t-min periods for which a surface point rainfall rate R is exceeded is the sum of contributions from the two modes:

$$T_t\ (R) = T_{1t}q_{1t}(R) + T_{2t}q_{2t}(R) \text{ hours}$$

There are 8766 hours per year, so $T_t(R)/87.66$ is the percentage of an average year during which t-min average rainfall rates exceed R mm/h. The data show that the average annual clock t-min rainfall rate for each of the modes is fairly constant. On the other hand, the total number of rainy t-min periods for each mode is relatively much more variable from year-to-year and between stations or climate regions. Rainfall climates defined by Barry and Chorley (1970) for the United States were found to correspond very well with observed regional variations of the parameter β.

The average annual total of t-min periods of Mode 1 and Mode 2 rainfall are T_{1t} and T_{2t}, respectively. The average annual Mode 1 and Mode 2 rainfall rates are therefore

$$\overline{R}_{1t} = M_1/T_{1t} \text{ mm/h}$$

$$\overline{R}_{2t} = M_2/T_{2t} \text{ mm/h}$$

Note that M_1 and M_2 are not functions of t, since the amount of rainfall collected over a long period of time does not depend on the short-term recording interval t. But the total number of hours T_{1t} or T_{2t} of rainy t-min intervals (collecting at least 0.01 in or 0.254 mm of rain per interval) will depend on t.

The factors $q_{1t}(R)$ and $q_{2t}(R)$ are the complements of cumulative time probabilities. That is, each factor is the time that a rate R is exceeded by Mode 1 or Mode 2 rain, divided by the total number of hours T_{1t} or T_{2t} that there is more than 0.254 mm of rain in a t-min period.

3.2.4 Time Intervals

The formulas to be presented are for t=1 clock-minute rates. Here clock-minutes are defined as beginning "on the minute" for a continuous t-minute period.

For the more general case where t>1 min, one more prediction parameter is required in addition to the two that have been defined as M and β. This additional parameter is the number of hours of rain per year, D. The formulas proposed here for $q_{1t}(R)$ and $q_{2t}(R)$ assume that the number of rainy days in an average year is

$$D/24 = 1 + M/8 \text{ rainy days}$$

where D is in hours and M is in millimeters. This relation has been found good, on the average, for continental U.S. stations. A comparison of the cumulative distributions versus the surface rainfall rate R for various values of t from 1 minute to 1 day is shown in Figure 3.2-1. Clearly, for β=0.125 and M=1000mm, the values for t=1 and 5 minutes are nearly equal, but longer periods give a significantly different value for $T_t(R)$.

3.2.5 Model Results for One-Minute Intervals

For t=1, the more general formulas are almost independent of D, so that

$$q_{1t}(R) = \exp(-R/\overline{R}_{1t})$$

$$q_{2t}(R) = 0.35 \exp(-0.453074\ R/\overline{R}_{2t})$$

$$+0.65 \exp(-2.857143\ R/\overline{R}_{2t})$$

and the annual average Mode 1 and Mode 2 rates $\overline{R}_{1t}$ and $\overline{R}_{2t}$ are very nearly equal to 33.333 and 1.755505 mm/h, respectively. Then $T_1(R)$ may be written as

$$T_1(R) = M \left\{ 0.03 \exp(-0.030R) + 0.21(1-\beta) \left[\exp(0.258R) + 1.86 \exp(-1.63R) \right] \right\} \text{ h.}$$

Use of this relation allows normalized cumulative time distributions to be calculated. Figure 3.2-2 is an example of this result for t=1 minute and β values from 0 to 0.75. Typical values for β and M throughout the US and Canada are given in Figures 3.2-3 and 3.2-4, respectively. Note that the values quoted in Figure 3.2-4 are in inches rather than millimeters required for M. Rice and Holmberg (1973) have also presented values throughout the world in their original article.

3.3 DUTTON-DOUGHERTY MODEL

The Dutton-Dougherty (DD) Model (Dutton and Dougherty-1973, Dutton-1977) includes attenuation due to both rain and gases. The rainfall rate distributions it uses are based on a series of modifications to the Rice-Holmberg Model (Dutton, et al-1974). The DD Model has been incorporated into a computer program which is available to users from the National Telecommunications and Information Administration.

3.3.1 Model Modifications

The Rice-Holmberg (RH) Model determines the number of hours of rainy t-minute periods, $T_t(R)$, for which a surface rain rate, R, is expected to be exceeded. The value $T_t(R)$ is given in the RH model (continuing their notation) as

$$T_t(R) = T_{1t}q_{1t}(R) + T_{2t}q_{2t}(R) \text{ hours} \tag{3.3-1}$$

where

$$q_{1t}(R) = \exp(-\overline{R}/R_{1t}) \tag{3.3-2}$$

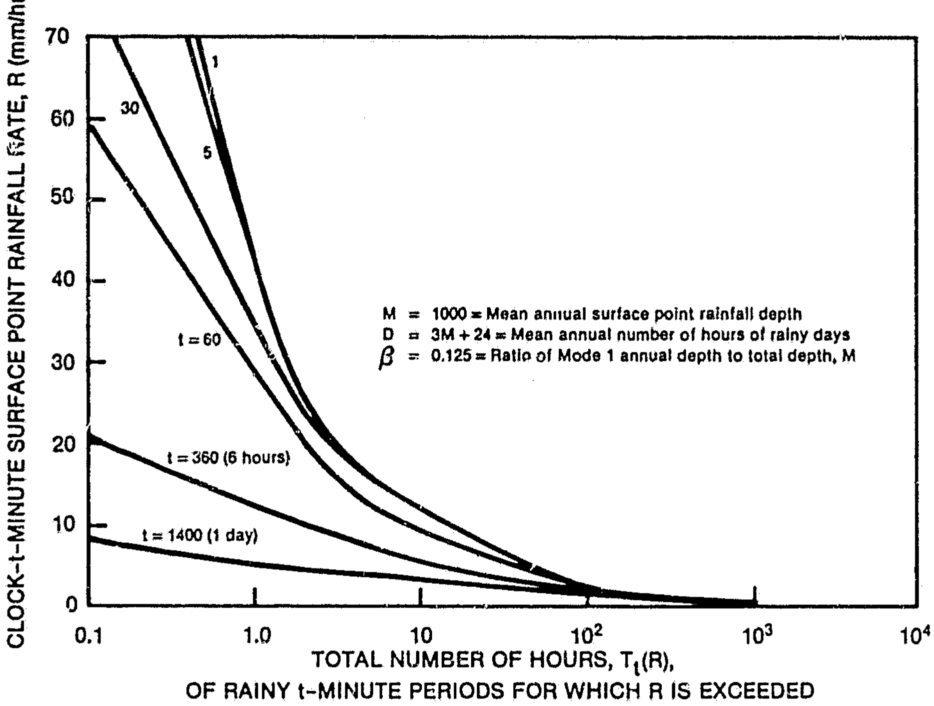

Figure 3.2-1. Average Year Cumulative Time Distributions

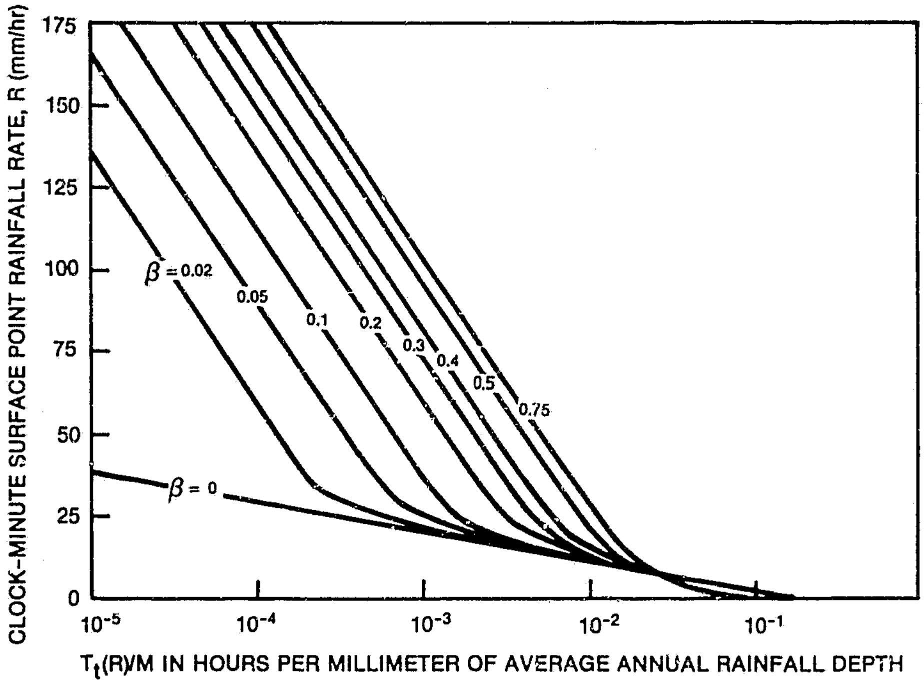

Figure 3.2-2. Normalized Cumulative Time Distributions

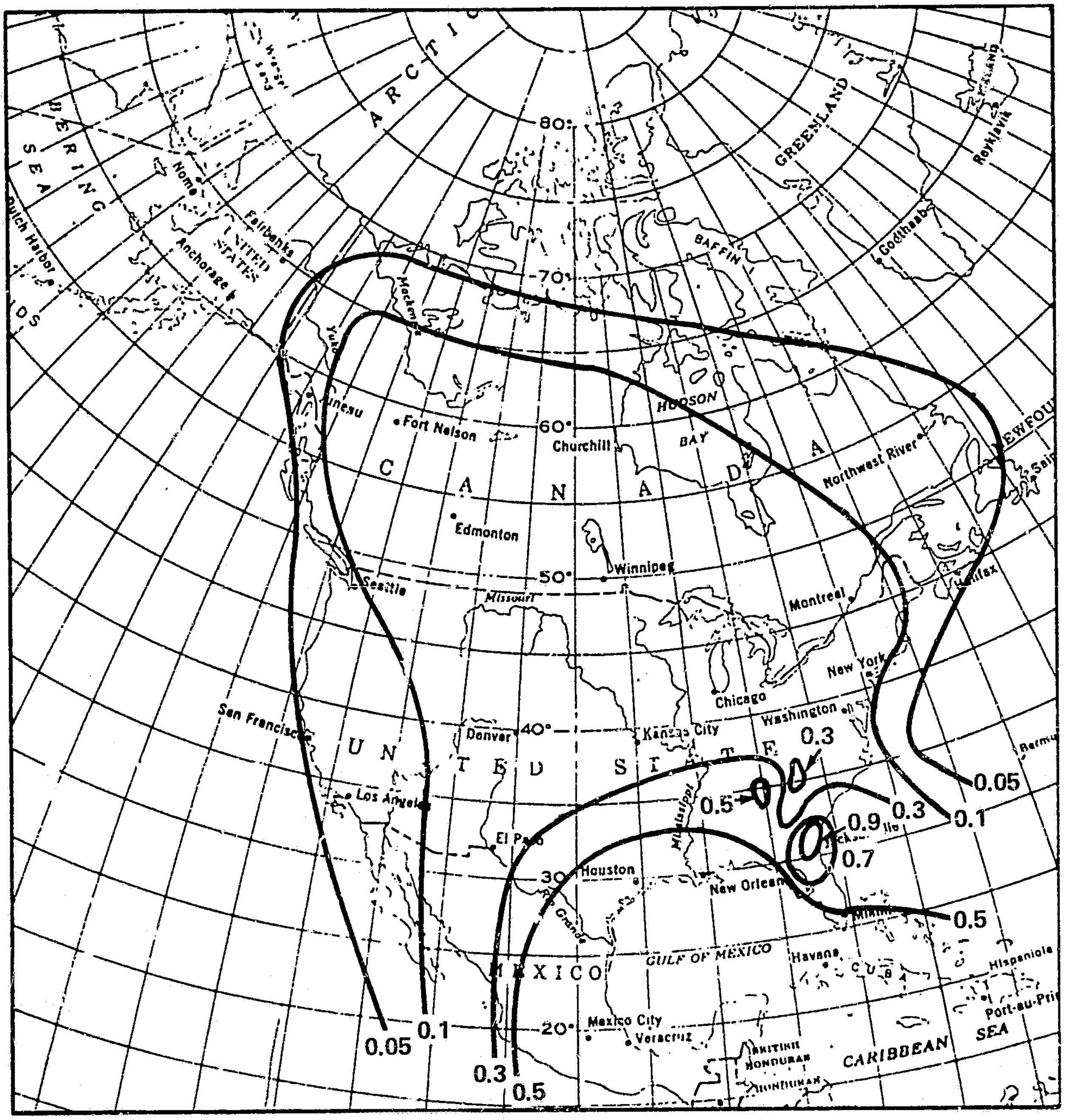

Figure 3.2-3. The Parameter β in the Rice-Holmberg Model Over the U.S. and Canada

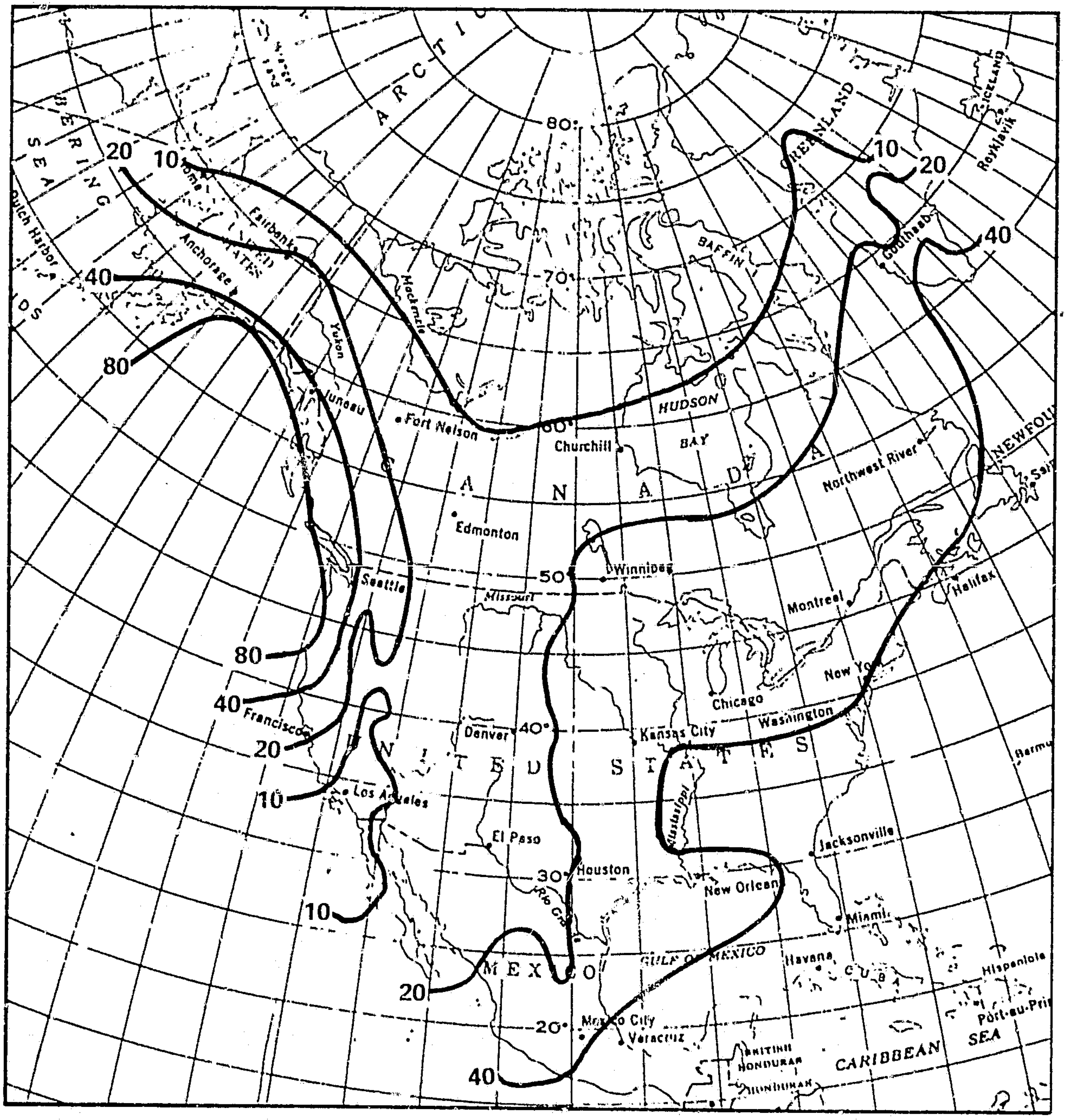

Figure 3.2-4. Mean Annual Precipitation in Inches in U.S. and Canada (1 inch = 25.4 mm)

$$q_{2t}(R) = 0.35 \exp(-0.453074\, R/\overline{R}_{2t})$$

$$+0.65 \exp(-2.857143\, R/\overline{R}_{2t}) \qquad (3.3\text{-}3)$$

$$T_{1t} = \beta M/\overline{R}_{1t} \text{ hours} \qquad (3.3\text{-}4)$$

$$T_{2t} = (1-\beta)M/\overline{R}_{2t} \text{ hours} \qquad (3.3\text{-}5)$$

The first modification of the RH model was the replacement of (3.3-1) through (3.3-3) with

$$T_t(R) = \begin{cases} T_{1t} \exp(-R/\overline{R}_{1t}) & R \geqslant R_c \\ (T_{1t} + T_{2t}) \exp(-R/R_t') & R < R_c \end{cases} \qquad (3.3\text{-}6)$$

Where R_c is a "crossover" rain rate between a convective mode of rainfall ($R \geq R_c$) and stratiform mode of rainfall ($R < R_c$). This biexponential representation of $T_t(R)$ is strictly analogous to the rainfall conceptions of Rice and Holmberg (1973), except that their "mode 2" rainfall is given by the second term of (3.3-1). From (3.3-6) is clear that R_c can be evaluated by setting

$$T_{1t} \exp(-R_c/\overline{R}_{1t}) = (T_{1t} + T_{2t}) \exp(-R_c/R_t') \qquad (3.3\text{-}7)$$

because it represents the intersection of the two curves in (3.3-6). Thus, we obtain

$$R_c = \overline{R}_{1t}R_t'/(\overline{R}_{1t}-R_t') \ln[(T_{1t}+T_{2t})/T_{1t}] \qquad (3.3\text{-}8)$$

The second modification of the R-H model was the direct estimation of T_{1t}, T_{2t}, $\overline{R}_{1t}$, and R_t' from M, β, and D. This was achieved by using a multiple linear regression to obtain a best fit of T_{2t}, $\overline{R}_{1t}$, and R_t' in terms of all, some or none (a constant) of the parameters M, β, and D. It was not necessary to fit T_{1t}, since it is given very simply in terms of M, β, and $\overline{R}_{1t}$ by (3.3-4). The resulting best fits were of the form

$$\overline{R}_{1t} = a_{1t}M + a_{2t}\beta + a_{3t}D + a_{4t} \pm S_1 \qquad (3.3\text{-}9)$$

$$T_{2t} = b_{1t}M + b_{2t} \pm S_2 \qquad (3.3\text{-}10)$$

$$R_t = b_{3t}M + b_{4t}\beta + b_{5t}D + b_{6t} \pm S_3 \qquad (3.3\text{-}11)$$

where the coefficients are $a_{1t}...a_{4t}$ and $b_{1t}...b_{6t}$, and the sample standard errors of estimate are $S_1...S_3$.

The third modification is the portion of the distribution that lies between the rainfall rates of 5 and 30 mm/hour, since two difficulties arise if the equation (3.3-6) is used exclusively for the entire distribution:

1) the transition between curves at R_c is decidedly not smooth, and
2) predictions via (3.3-6) can be noted to be as much as 50 percent below the RH model in the same vicinity.

In order to partially alleviate these difficulties, it was arbitrarily determined that

$$T_1(R) = T_{st}\exp(-\sqrt[4]{R}/R_{st}) \qquad (3.3\text{-}12)$$

could be reasonably fit to the data, with proper curvature and simplicity, for $1 \le t \le 60$ min and $5 \le R \le 30$ mm/hour. Since the 5 to 30 mm/hour range can be expected to straddle R_c for most climatological circumstances, T_{st} and R_{st} can be found via the boundary conditions

$$T_{st}\exp(-\sqrt[4]{30}/R_{st}) = T_{1t}\exp(-30/\overline{R}_{1t}) \qquad (3.3\text{-}13)$$

and

$$T_{st}\exp(-\sqrt[4]{5}/R_{st}) = (T_{1t} + T_{2t})\exp(-5/R_t') \qquad (3.3\text{-}14)$$

For $t > 60$ min (i.e., t=360, 1440 min), the formulation (3.3-6) fits the R-H model sufficiently well over the entire rain rate distribution for operational purposes, so that no additional modification of (3.3-6) is necessary. In summary, then, the resultant modification of the R-H model is:

$$T_t(R) = \begin{cases} T_{1t} \exp(-R/\bar{R}_{1t}) & R > 30 \text{ mm/h} \\ T_{st} \exp(-\sqrt[4]{R}/R_{st}) & 5 \text{ mm/h} \leq R \leq 30 \text{ mm/h} \\ (T_{1t} + T_{2t}) \exp(-R/R_t') & R < 5 \text{ mm/h} \end{cases} \quad (3.3\text{-}15)$$

for 1 min $\leq t \leq$ 60 min. and

$$T_t(R) = \begin{cases} T_{1t} \exp(-R/\bar{R}_{1t}) & R \geq R_c \\ (T_{1t} + T_{2t}) \exp(-R/R_t') & R < R_c \end{cases} \quad (3.3\text{-}16)$$

for $t > 60$ min.

3.3.2 Additions to the Rain Model

Dutton (1977) has estimated the variance and confidence levels of the rain rate prediction, and Dougherty and Dutton (1978) have estimated the year-to-year variability of rainfall within a given rain zone.

Extending the rain model to include attenuation on earth-space paths, Dutton (1977) has assumed the Marshall and Palmer (1948) raindrop distribution. Also they have included some degree of modeling of rainfall in the horizontal direction. This is achieved by means of what is termed the "probability modification factor" on earth-space links.

The probability modification factor, F, is given by

$$F \cong \frac{(f/15)^2}{A(f,\theta)} (0.274 + 0.987) \quad (3.3\text{-}17)$$

the factor cannot exceed unity, however. In (3.3-17), f is the frequency in GHz, θ is the elevation angle to the satellite in degrees, and $A(f,\theta)$ is the path attenuation in dB. The form was derived from rain storm cell size data given in a particularly useful form by Rogers (1972). The Rogers' data, however, were all taken in the vicinity of Montreal, Canada. It would be desirable to have more globally diverse data in order to derive a more general probability modification factor.

The probability modification factor, applied strictly to attenuation, multiplies the percent of time, P_0, during an average year that a point rainfall rate is expected at a given location. The multiplied value represents the percent of time, P, $(P \leq P_0)$, that attenuation corresponding to R_0 is expected along the path to a satellite. Thus, in effect, a point-to-path rain rate conversion, accounting for horizontal inhomogeneity is developed.

In the DD model the surface rainfall rate is translated into liquid water content per unit volume, L_0, accumulating at the ground. The liquid water content at some height, h, above the ground, L(h), can be modeled as a function of L_0 (Dutton - 1971). The modeling of L(h) is different for the stratiform and convective rain systems. In the stratiform modeling L(h) is assumed constant to the rain-cloud base, then decreases to zero at the storm top height H. In the convective modeling L(h) increases slightly to the rain-cloud base and then decreases to zero at H.

Attenuation per unit length, $\alpha(f,h)$, due to rain can be calculated from L(h) via expressions of the form

$$\alpha(f,h) = a(f)[L(h)]^{b(f)} \qquad (3.3\text{-}18)$$

using the data of Crane (1966). Hence, the distinction between the Rayleigh region (f < 10 GHz, approximately) and the Mie region (f > 10 GHz) is implicit in (3.3-18), because the coefficients a(f) and b(f) are frequency dependent. In the Rayleigh region, it can be shown that b(f)=1. An interpolation scheme on Crane's data obtains a(f) and b(f) for any frequency in the 10 to 95 GHz region.

Variance of attenuation of earth-space links is, as yet, not directly assessable by theoretical formulation. Thus, it is necessary to input, say, two additional rain rate distributions corresponding to the lower and upper confidence limits of R_0 in order to evaluate corresponding confidence limits on an attenuation distribution. This, of course, assumes no variance in the many parameters surrounding the attenuation formulation. This is clearly not so, and indicates that the procedure for evaluating attenuation confidence limits is still in need of refinement.

3.3.3 Dutton-Dougherty Computer Model

Dutton has developed an updated computer program (Steele-1979 and Janes, et al - 1978) to predict the distribution of mean annual attenuation. Entitled DEGP77, the program also computes the phase delay and reflectively due to rain, clouds and atmospheric gases. The required inputs to the program are:

- Frequency
- Earth station antenna elevation angle
- Indentification of data stations
- Height above surface
- Cloud attenuation distribution
- Ratio of thunderstorm to non-thunderstorm rain
- Time available
- Rainfall rate
- Values for average annual atmospheric pressure, humidity, and temperature

The program is valid for frequencies from 1 to 30 GHz and for satellite elevation angles greater than 5 degrees. The program is available on cards or as a listing from the Institute for Telecommunication Sciences, NTIA, Boulder, CO 80303, attn: Dr. E. J. Dutton, (303) 499-1000 x 3646 or FTS 323-3646.

3.4 THE GLOBAL MODEL

The Global Model has been developed in two forms. Both of these forms utilize cumulative rain rate data to develop cumulative attenuation statistics. The first form, called the Global Prediction Model (CCIR-1978a, Doc. P/105-E, 6 June), employs a path averaging parameter "r" to relate the point rain rate to the average rain rate along the path from the ground station to the point where the hydrometeors exist in the form of ice crystals. The later form of the model (Crane and Blood - 1979) includes path averaging implicitly, and adjusts the isotherm heights for various percentages of time to account for the types of rain structures which dominate the cumulative statistics for the respective percentages of time. Both forms will be described here because the latter is the recommended form for use by system designers, but the earlier form is computationally easy to implement and allows rapid computation with a hand-held calculator.

3.4.1 Rain Model

The rain model employed in both forms of the attenuation model is used for the estimation of the annual attenuation distribution to be expected on a specific propagation link. It differs from most other rain models in that it is based entirely on meterological observations, not attenuation measurements. The rain model, combined with the attenuation estimation, was tested by comparison with attenuation measurements. This procedure was used to circumvent the requirement for attenuation observations over a span of many years. The total attenuation model is based upon the use of independent, meteorologically derived estimates for the cumulative distributions of point rainfall rate, horizontal path averaged rainfall rate, the vertical distribution of rain intensity, and a theoretically derived relationship between specific attenuation and rain rate obtained using median observed drop size distributions at a number of rain rates.

The first step in application of the model is the estimation of the instantaneous point rain rate (R_p) distribution. The Global Prediction Model provides median distribution estimates for broad geographical regions; eight climate regions A through H are designated to classify regions covering the entire globe. Figures 3.4-1 and 3.4-2 show the geographic rain climate regions for the continental and ocean areas of the earth. The United States and European portions are further expanded in Figures 3.4-3 and 3.4-4 respectively.

The climate regions depicted by the Global Model are very broad. The upper and lower rain rate bounds provided by the nearest adjacent region have a ratio of 3.5 at 0.01 percent of the year for the proposed CCIR climate region D, for example, producing an attendant ratio of upper-to-lower bound attenuation values of 4.3 dB at 12 GHz. This uncertainty in the estimated attenuation value can be reduced by using rain rate distributions tailored to a particular area if long term statistics are available. For convenience, region D has further been subdivided into regions D_1, D_2 and D_3 for the United States area only (Figure 3.4-3).

The values of R_p may be obtained from the rain rate distribution curves of Figure 3.4-5. Figure 3.4-5a shows the curves for the eight global climate regions designated A through H for one minute averaged surface rain rate as a function the percent of year that rain rate is exceeded. The distributions for the Region D subdivisions are shown in Figure 3.4-5b. Numerical values for R_p are provided in Table 3.4-1.

3.4.2 Description of the Rain Attenuation Region

A path averaged rainfall rate $R = rR_p$, where r is defined as the effective path average factor, is useful for the estimation of attenuation for a line-of-sight radio relay system but, for the estimation of attenuation on a slant path to a satellite, account must be taken of the variation of specific

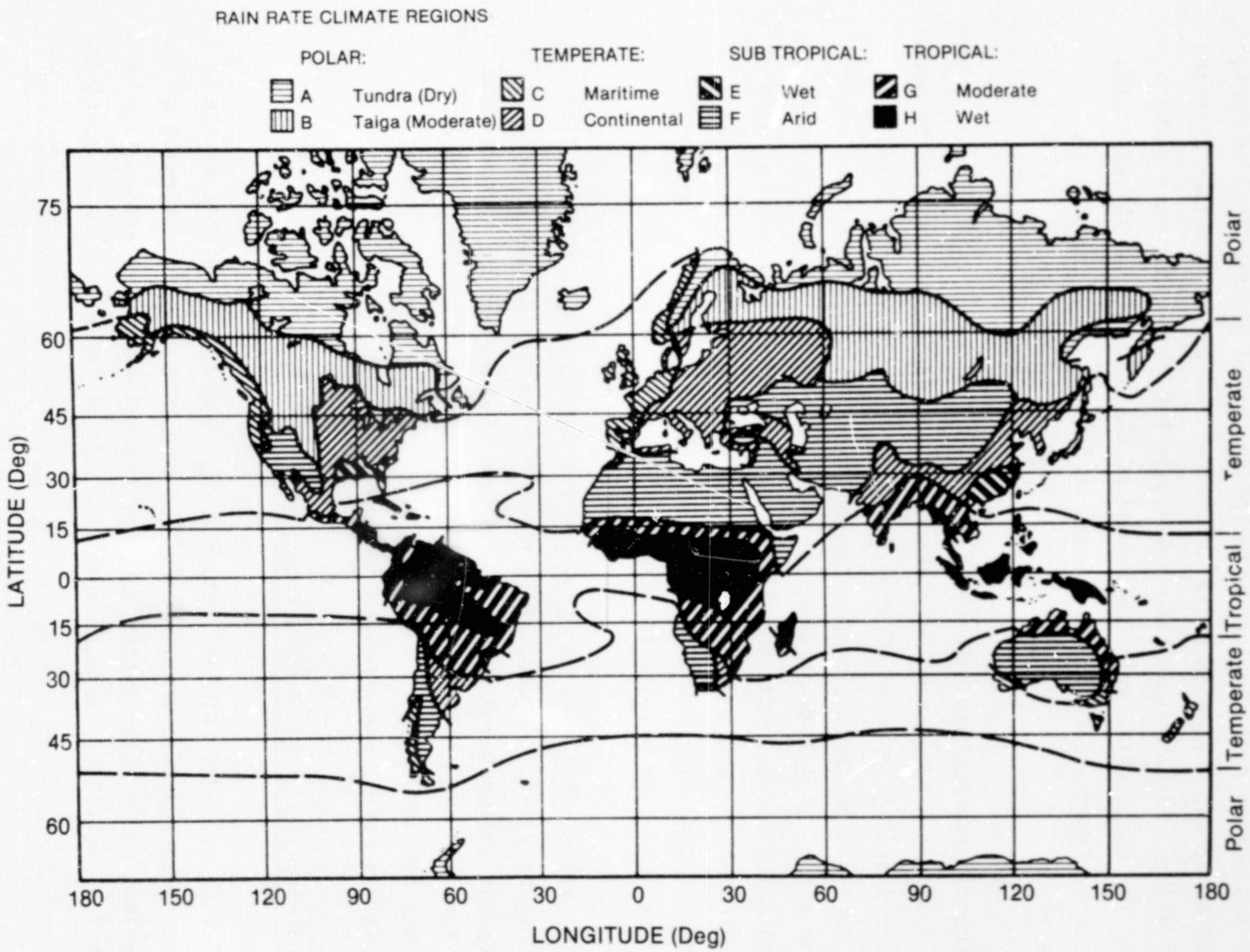

Figure 3.4-1. Global Rain Rate Climate Regions for the Continental Areas

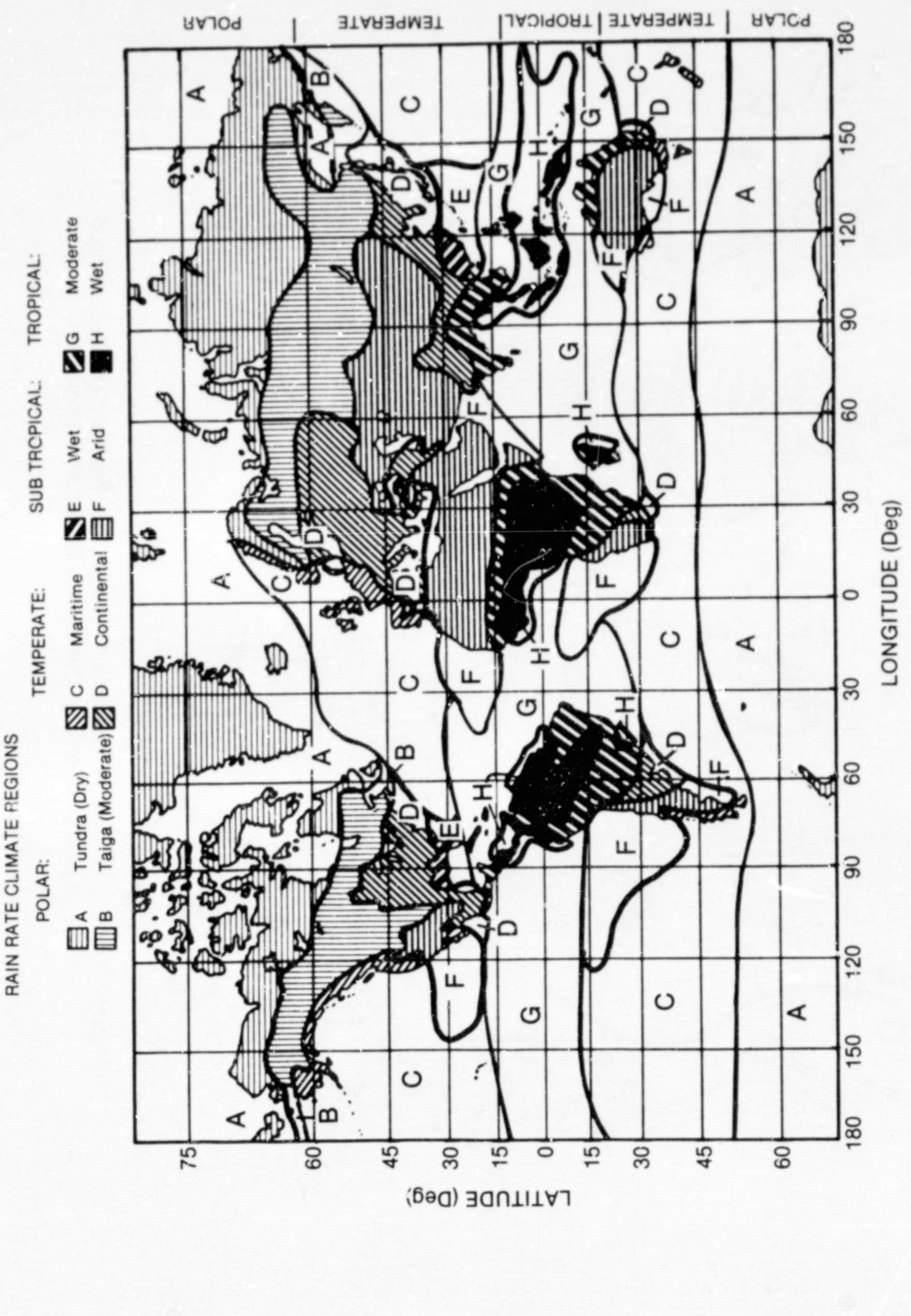

Figure 3.4-2. Global Rain Rate Climate Regions Including the Ocean Areas

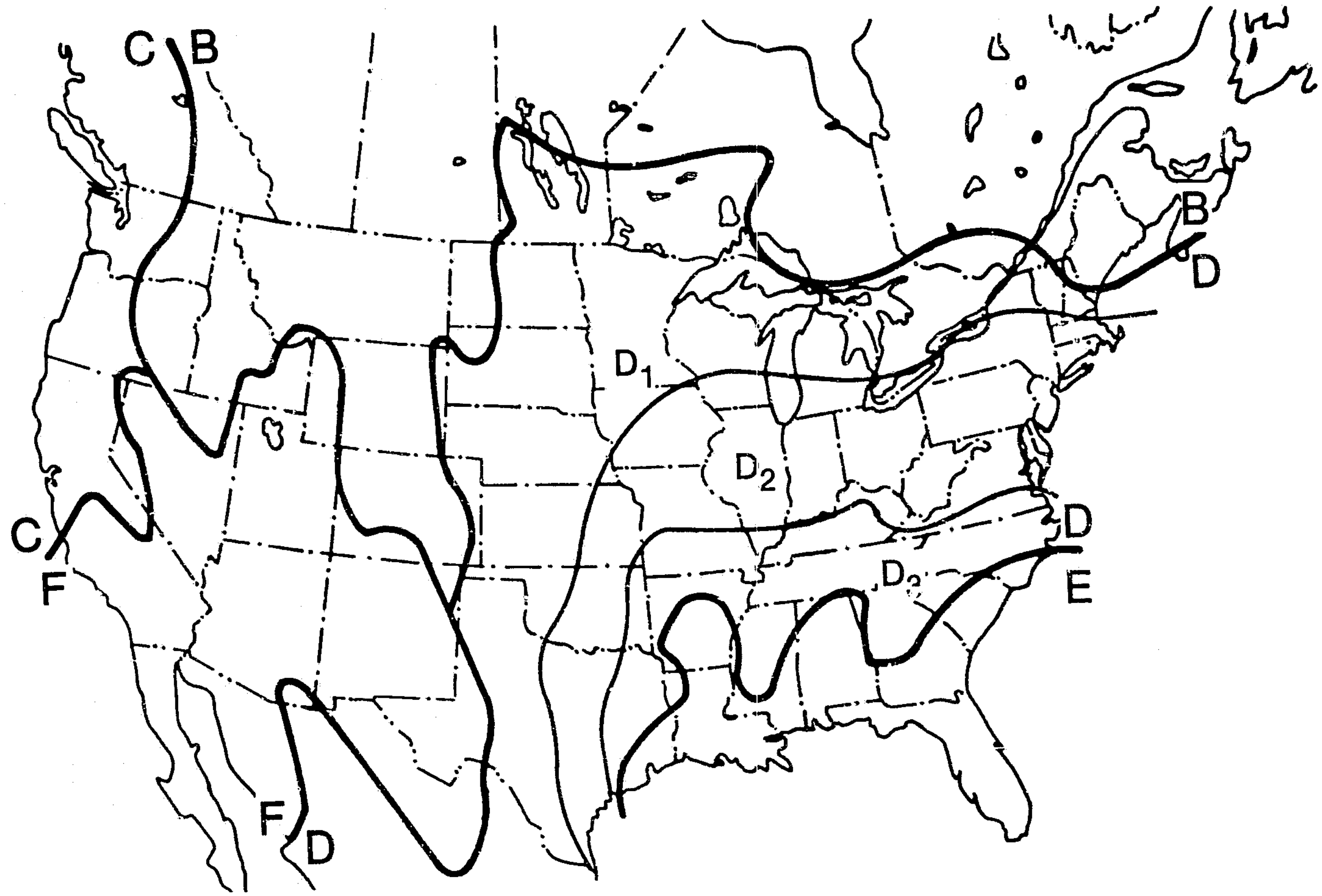

Figure 3.4-3. Rain Rate Climate Regions for the Continental United States Showing the Subdivision of Region D

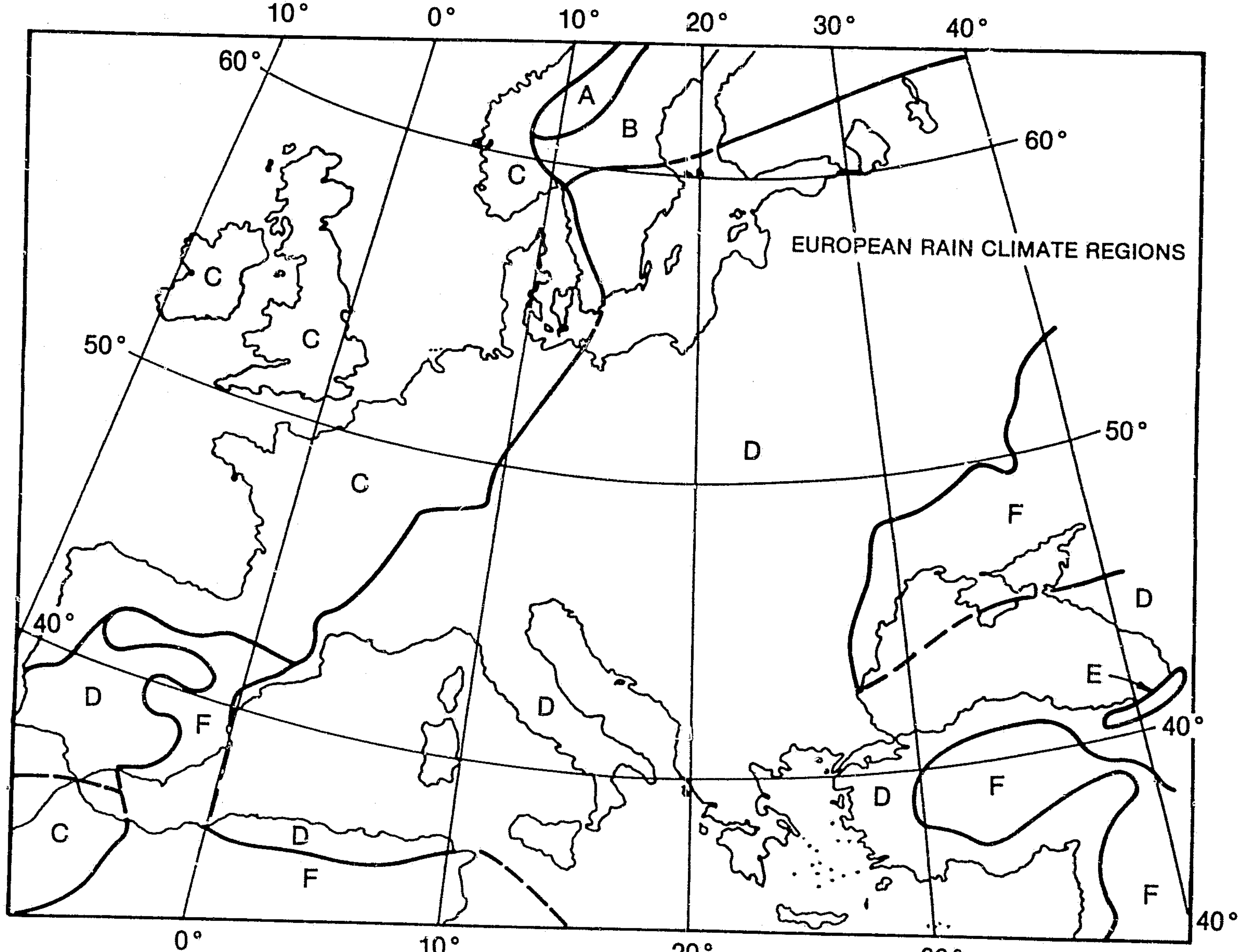

Figure 3.4-4. Rain Rate Climate Regions for Europe

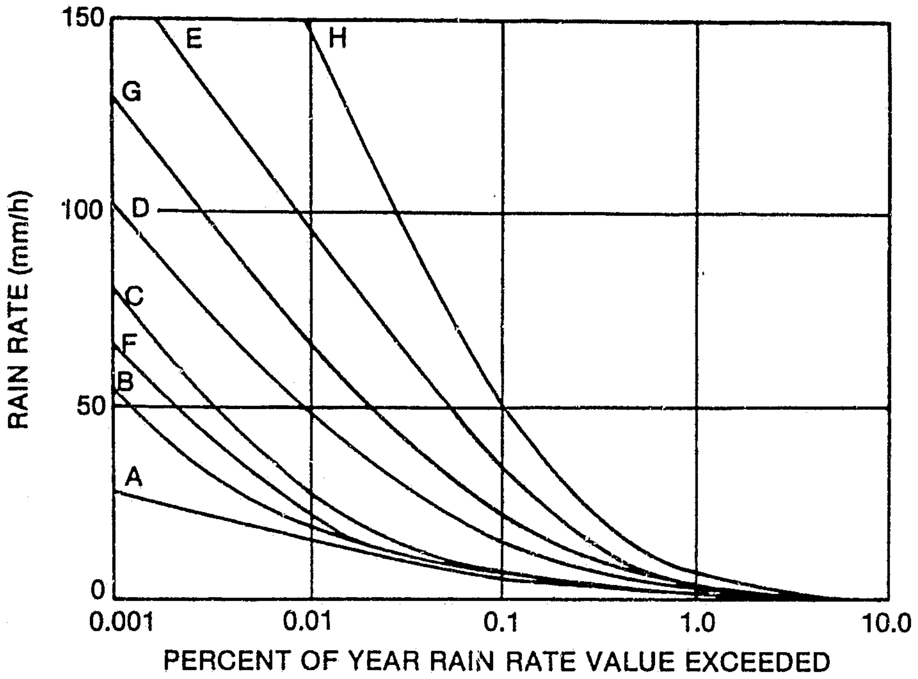

(a) Climate Regions A to H

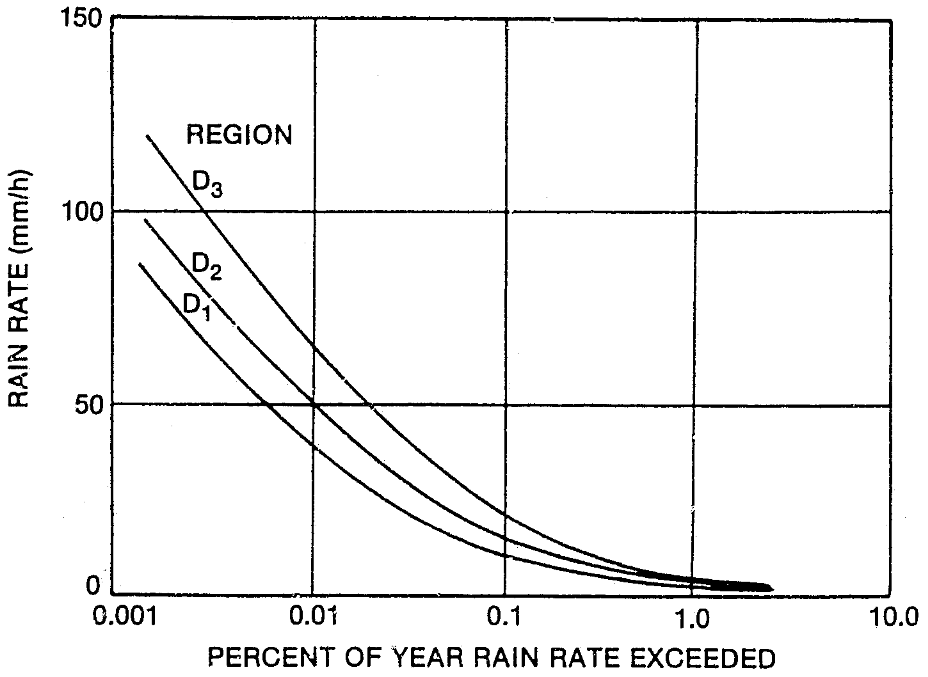

(b) Climate Regions D divided into three subregions (D_2 = D above)

Figure 3.4-5. Point Rain Rate Distributions as a Function of Percent of Year Exceeded

Table 3.4-1

Point Rain Rate Distribution Values (mm/hr)

Versus Percent of Year Rain Rate is Exceeded

Percent of Year	Rain Climate Region:										Minutes Per Year	Hours Per Year
	A	B	C	D_1	D_2	D_3	E	F	G	H		
0.001	28	54	80	90	102	127	164	66	129	251	5.3	0.09
0.002	24	40	62	72	86	107	144	51	109	220	10.5	0.18
0.005	19	26	41	50	64	81	117	34	85	178	26	0.44
0.01	15	19	28	37	49	63	98	23	67	147	53	0.88
0.02	12	14	18	27	35	48	77	14	51	115	105	1.75
0.05	8	9.5	11	16	22	31	52	8.0	33	77	263	4.38
0.1	6.5	6.8	72	11	15	22	35	5.5	22	51	526	8.77
0.2	4.0	4.8	4.8	7.5	9.5	14	21	3.8	14	31	1052	17.5
0.5	2.5	2.7	2.8	4.0	5.2	7.0	8.5	2.4	7.0	13	2630	43.8
1.0	1.7	1.8	1.9	2.2	3.0	4.0	4.0	1.7	3.7	6.4	5260	87.66
2.0	1.1	1.2	1.2	1.3	1.8	2.5	2.0	1.1	1.6	2.8	10520	175.3

attenuation with height. The atmospheric temperature decreases with height and, above some height, the precipitation particles must all be ice particles. Ice or snow do not produce significant attenuation; only regions with liquid water precipitation particles are of interest in the estimation of attenuation. The size and number of rain drops per unit volume may vary with height. Measurements made using weather radars show that the reflectivity of a rain volume may vary with height but, on average, the reflectivity is roughly constant with height to the height of the 0^oC isotherm and decreases above that height. The rain rate may be assumed to be constant to the height of the 0^oC isotherm at low rates and this height may be used to define the upper boundary of the attenuating region. A high correlation between the 0^oC height and the height to which liquid rain drops exist in the atmosphere should not be expected for the higher rain rates because large liquid water droplets are carried aloft above the 0^o height in the strong updraft cores of intense rain cells. It is necessary to estimate the rain layer height appropriate to the path in question before proceeding to the total attenuation computation since even the 0^oC isotherm height depends on latitude and general rain conditions.

As a model for the prediction of attenuation, the average height of the 0^o isotherm for days with rain was taken to correspond to the height to be expected one percent of the year. The highest height observed with rain was taken to correspond to the value to be expected 0.001 percent of the year, the average summer height of the -5^oC isotherm. The latitude dependences of the heights to be expected for surface point rain rates exceeded one percent of the year and 0.001 percent of the year were obtained from the latitude dependences provided by Oort and Rasmussen (1971). The resultant curves are presented in Figure 3.4-6. For the estimation of model uncertainty, the seasonal rms uncertainty in the 0^oC isotherm height was 500 m or roughly 13 percent of the average estimated height. The value of 13 percent is used to estimate the expected uncertainties to be associated with Figure 3.4-6.

The correspondence between the $0^{o}C$ isotherm height values and the excessive precipitation events showed a tendency toward a linear relationship between R_p and the $0^{o}C$ isotherm height H_0 for high values of R_p. Since, at high rain rates, the rain rate distribution function displays a nearly linear relationship between R_p and log P (P is probability of occurrence), the interpolation model used for the estimation of H_0 for P between 0.001 and one percent is assumed to have the form, $H_0 = \underline{a} + \underline{b} \log P$. The relationship was used to provide the intermediate values displayed in Figure 3.4-6a. In Figure 3.4-6b are shown the $0^{o}C$ isotherms for various latitudes and seasons.

3.4.3 Attenuation Model

The complete model for the estimation of attenuation on an earth-space path starts with the determination of the vertical distance between the height of the earth station and the $0^{o}C$ isotherm height ($H_0 - H_g$ where H_g is the ground station height) for the percentage of the year (or R_p) of interest. The path horizontal projection distance (D) can then be obtained by:

$$D = \begin{cases} (H_o - H_g)/\tan\theta & \theta \geqslant 10^\circ \\ E\psi \ (\psi \text{ in radians}) & \theta < 10^\circ \end{cases} \qquad (3.4\text{-}1)$$

where

H_0 = height of $0^{o}C$ isotherm

H_g = height of ground terminal

θ = path elevation angle

and

$$\psi = \sin^{-1}\left\{\frac{\cos\theta}{H_o + E}\left[(H_g + E)^2 \sin^2\theta + 2E(H_o - H_g) + H_o^2 - H_g^2 - (H_g + E)\sin\theta\right]^{1/2}\right\} \qquad (3.4\text{-}2)$$

where

E = effective earth's radius (8500 km).

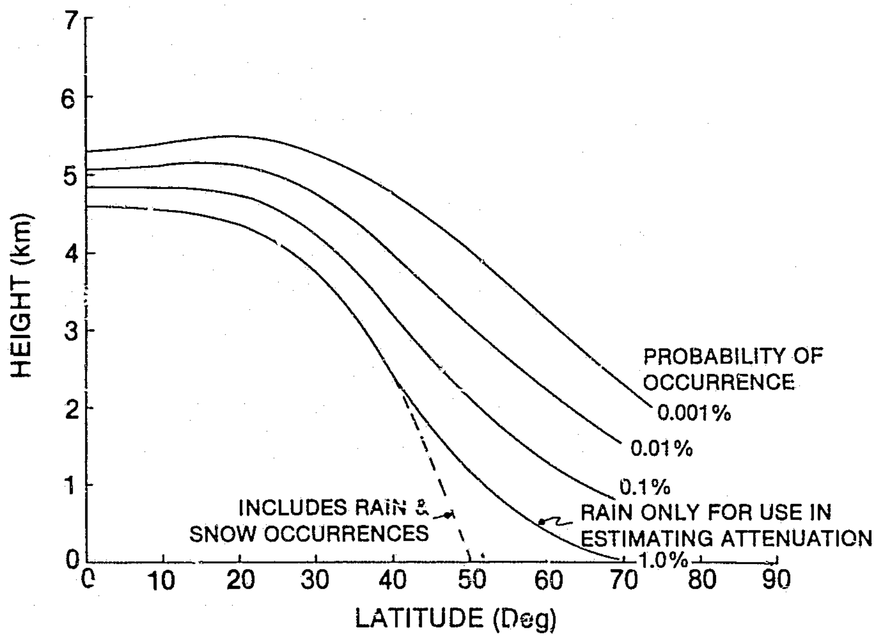

a) Variable Isotherm

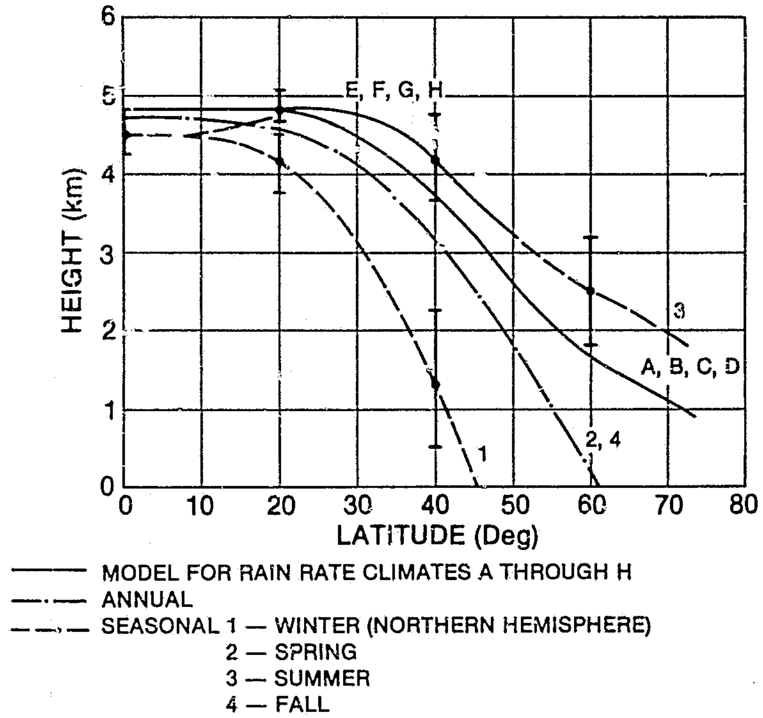

b) 0°C Isotherm Height

Figure 3.4-6. Effective Heights for Computing Path Lengths Through Rain Events

The specific attenuation may be calculated for an ensemble of rain drops if their size and shape number densities are known. Experience has shown that adequate results may be obtained if the Laws and Parsons (1943) number density model is used for the attenuation calculations (Crane-1966) and a power law relationship is fit to calculated values to express the dependence of specific attenuation on rain rate (Olsen et al-1978). The parameters a and b of the power law relationship:

$$\alpha = a R_p^{\,b}$$

where α = specific attenuation (dB/km) (3.4-3)

R_p = point rain rate (mm/hour)

are both a function of operating frequency. Figures 3.4-7 and 3.4-8 give the multiplier, a(f) and exponent b(f), respectively, at frequencies from 1 to 100 GHz. The appropriate a and b parameters may also be obtained from Table 3.4-2 and used in computing the total attenuation from the model.

3.4.3.1 Path Averaged Rain Rate Technique. The path averaged rain rate exceeded for a specified percentage of the time may differ significantly from the surface point rain rate exceeded for the same percentage of the time. The estimation of the path averaged values from the surface point values requires detailed information about the spatial correlation function for rain rate. Adequate spatial data are not currently available. A sufficient number of observations using rain guage networks are available to provide a basis for a point to path average model. Observations for 5 and 10 km paths are presented in Figures 3.4-9 and 3.4-10, respectively. The effective path average factor, r, represents the relationship between point and path averaged rain rate as

$$R_{path} = r \cdot R_p \qquad (3.4\text{-}4)$$

where R_{path} and R_p are the path and point rainfall rates at the same probability of occurrence.

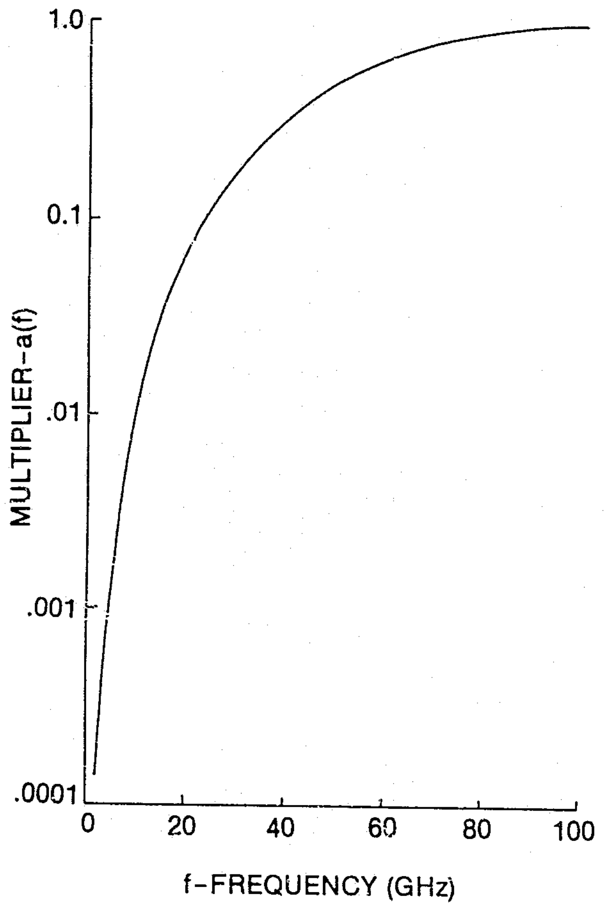

Figure 3.4-7. Multiplier Coefficient in the Specific Attenuation Relation

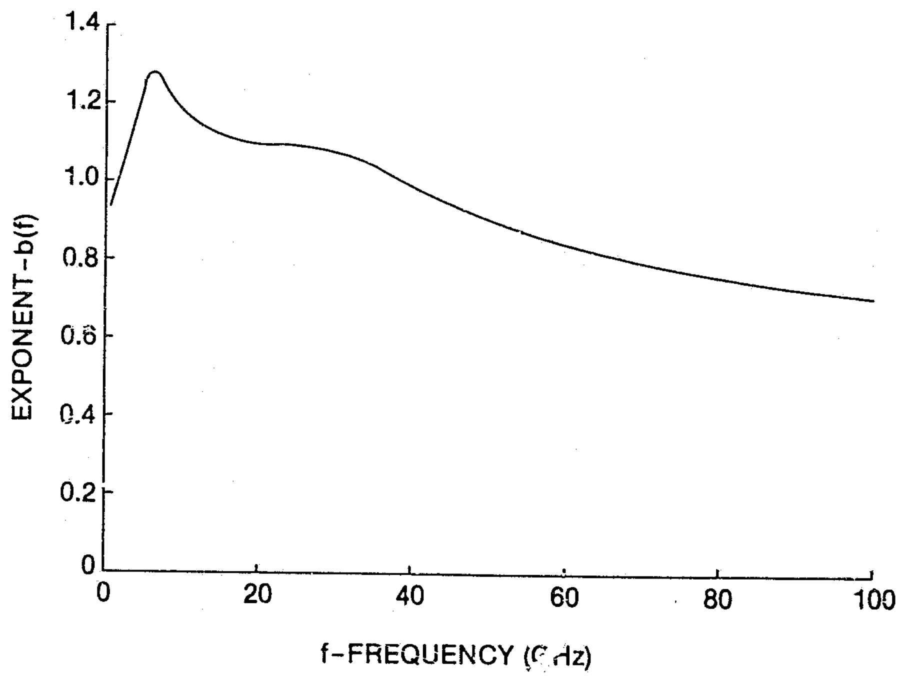

Figure 3.4-8. Exponent Coefficient in the Specific Attenuation Relation

Table 3.4-2

Parameters for Computing Specific Attenuation:
$= aR^b$, 0^oC, Laws and Parson Distribution
(Crane-1966)

Frequency f - GHz	Multiplier a(f)	Exponent b(f)
1	0.00015	0.95
4	0.00080	1.17
5	0.00138	1.24
6	0.00250	1.28
7.5	0.00482	1.25
10	0.0125	1.18
12.5	0.0228	1.145
15	0.0357	1.12
17.5	0.0524	1.105
20	0.0699	1.10
25	0.113	1.09
30	0.170	1.075
35	0.242	1.04
40	0.325	0.99
50	0.485	0.90
60	0.650	0.84
70	0.780	0.79
80	0.875	0.753
90	0.935	0.730
100	0.965	0.715

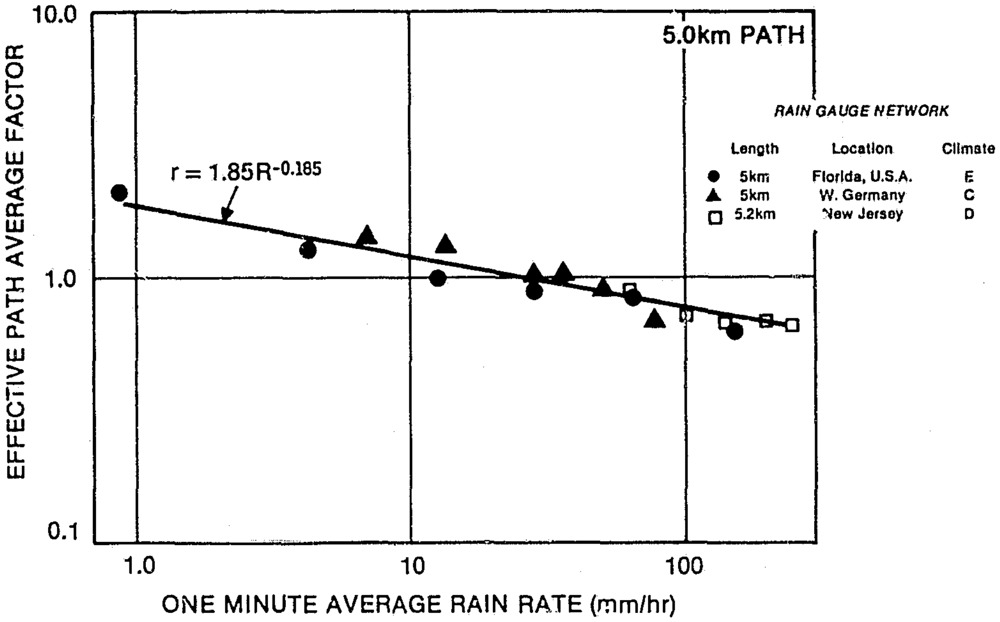

Figure 3.4-9. Effective Path Average Factor Versus Rain Rate, 5 km Path

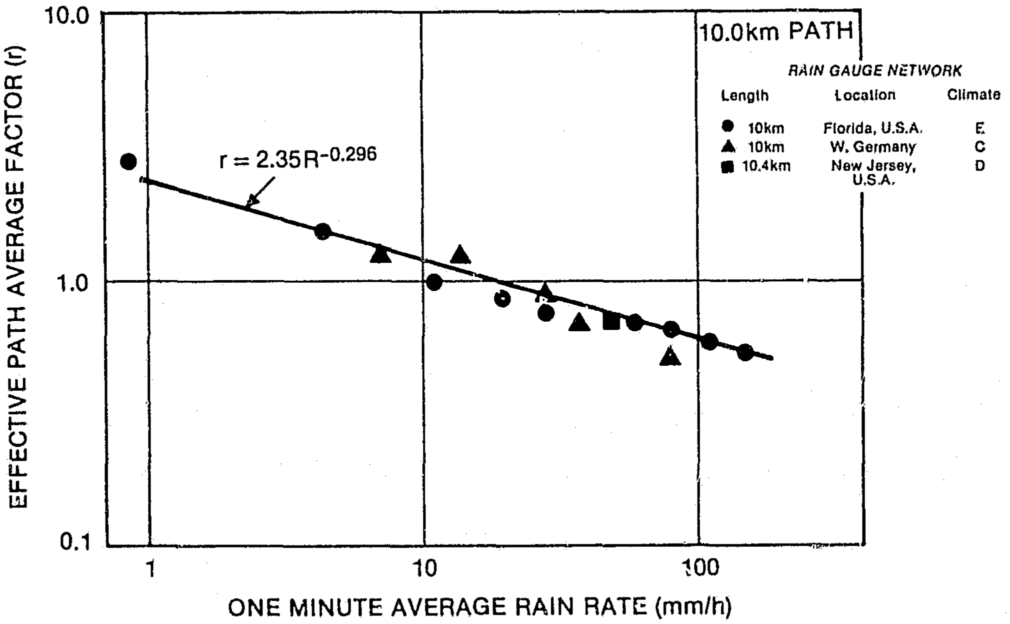

Figure 3.4-10. Effective Path Average Factor Versus Rain Rate, 10 km Path

Figure 3.4-11 represents the construction of an effective path average factor using data from paths between 10 and 22.5 km in length. The values of r were obtained by assuming that the occurrence of rain with rates in excess of 25 mm/hour were independent over distances larger than 10 km. The estimation of path averaged rain rate then depends upon modeling the change in occurrence probability for a fixed path average value, not the change in path average value for a fixed probability. Using D_0 as the reference path length (D_0 = 22.5 km for Figure 3.4-11), the exceedance probabilities for the path averaged values were multiplied by D_0/D where D was the observation path length to estimate the path average factor for a path of length D_0.

The path attenuation caused by rain is approximately determined from the path averaged rain rate by

$$A \approx L\, r\, a\, R_p^{\,b} \qquad (3.4\text{-}5)$$

where A is path attenuation, L is the length of the propagation path or D_0, whichever is shorter, r is the effective path average factor, R_p is the point rainfall rate exceeded P percent of the time, and a and b are coefficients used to estimate specific attenuation for a given rain rate. Using this model and propagation paths longer than 22.5 km, the effective path average factor for 22.5 km path may be calculated from simultaneous point rain rate distribution and attenuation distribution data. Results for a number of paths in rain rate climates C and D are presented in Figure 3.4-12. The line plotted on this figure is the power law relationship fit to all the data displayed in Figure 3.4-11. The observations at 13 and 15 GHz are in excellent agreement with the model based solely on rain gauge network data. At lower frequencies, the discrepancy is larger, being as much as a factor of 2. At 11 GHz, the model appears to underestimate the observed attenuation by a factor of 2. It is noted that simultaneous point rain rate observations were used in the construction of Figure 3.4-12, not the rain rate distributions for each climate region. Since fades due to multipath must be

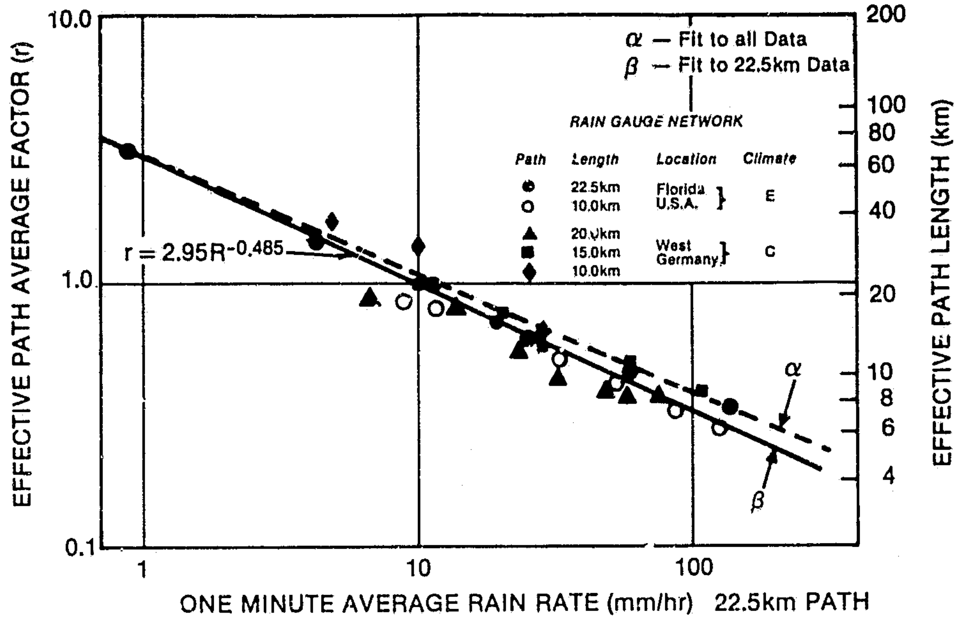

Figure 3.4-11. Effective Path Average Factor Versus Rain Rate

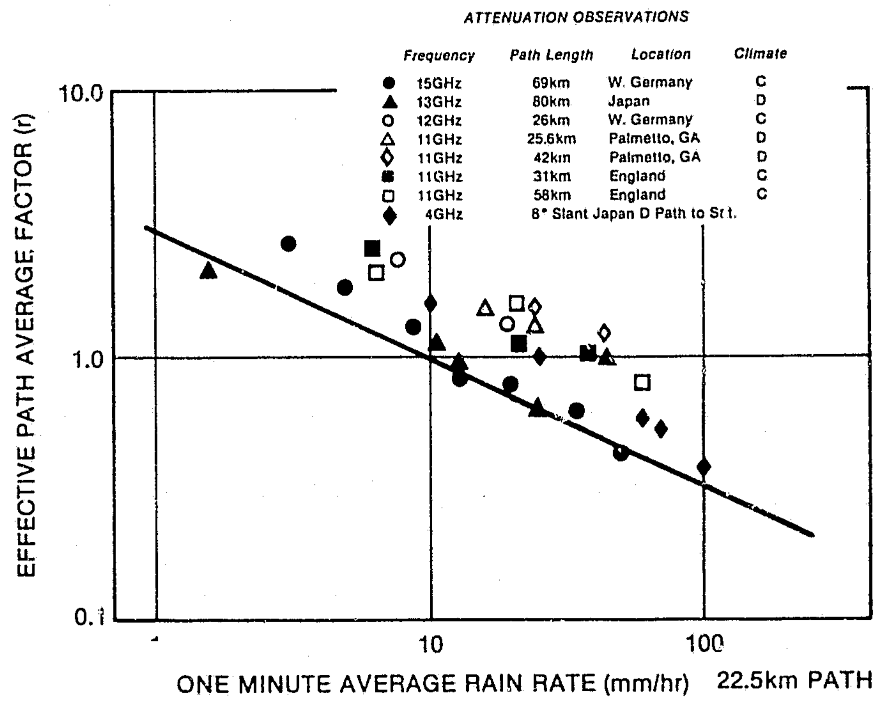

Figure 3.4-12. Effective Path Average Factor Versus Rain Rate Derived from Attenuation Measurements

removed from the analysis prior to making the comparison in Figure 3.4-12 and multipath effects tend to be relatively more important at frequencies below 13 GHz, the lack of agreement displayed in Figure 3.4-12 may be due to effects other than rain.

A power law approximation to the effective path average factors depicted in Figures 3.4-9 through 3.4-11 may be used to model the behavior of the effective path average factor for paths shorter than 22.5 km. Letting the effective path average factors be expressed by

$$r \approx \gamma(D)\, R_p^{-\delta(D)} \tag{3.4-6}$$

where D is the surface projection of the propagation path and the model curves for $\gamma(D)$ and $\delta(D)$ are given in Figure 3.4-13 and 3.4-14. Figure 3.4-15 displays the dependence of the modeled effective path average factor on point rain rate.

Attenuation prediction for Earth-space paths requires the estimation of rain rate along a slant path. Statistical models for rain scatter indicate that the reflectivity, hence, specific attenuation or rain rate, is constant from the surface to the height of the 0^{o}C isotherm (Goldhirsh and Katz-1979). By assuming that the specific attenuation is statistically independent of height for altitudes below the 0^{o}C isotherm the path averaged rain rate (or specific attenuation) can be estimated using the model in Figures 3.4-13 and 3.4-14. For application, the surface projection of the slant path below the melting layer is used to define the surface path length, D. The attenuation on an Earth-space path for an elevation angle higher than 10^{o} is given by:

$$A = \frac{H}{\sin\theta}\; a(f)\, \gamma(D)\, R_p^{\,b(f)-\delta(D)} \tag{3.4-7}$$

where H is the height of the 0^{o}C isotherm (see Figure 3.4-6b), θ is the elevation angle ($\theta > 10^{o}$) and $D = H/\tan\theta$. For application at elevation

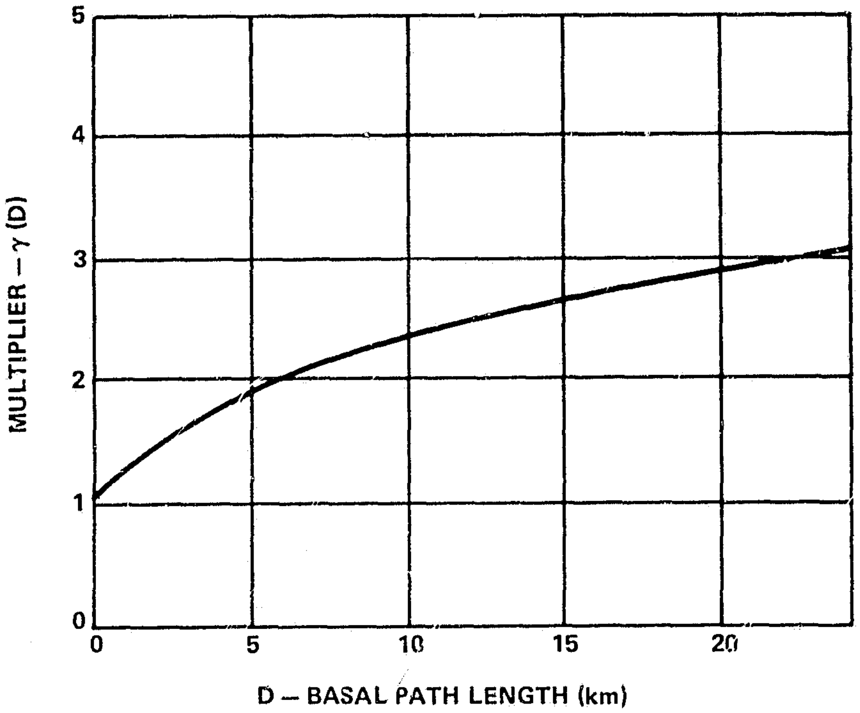

Figure 3.4-13. Multiplier in the Path Averaging Model

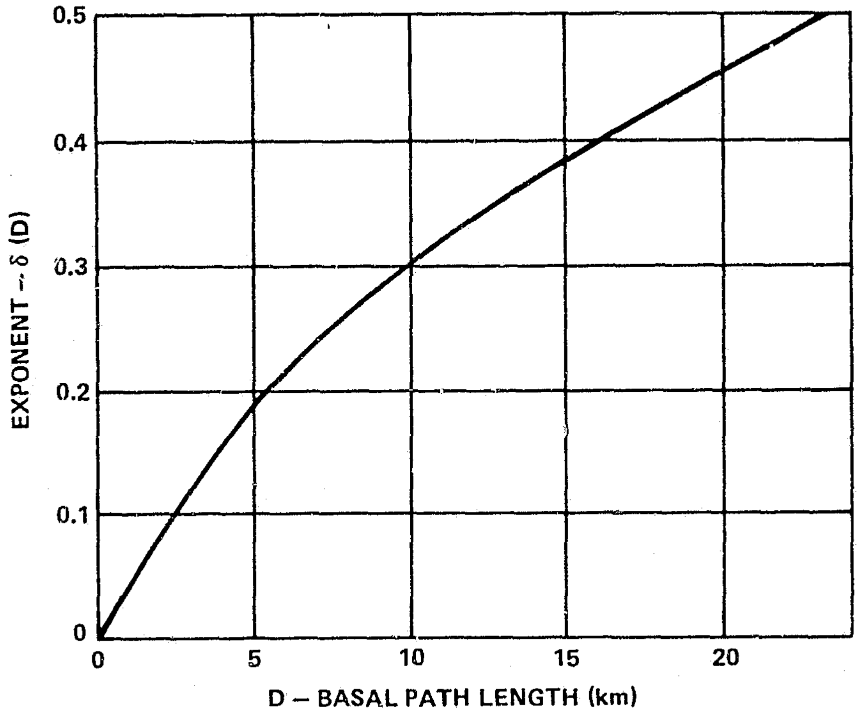

Figure 3.4-14. Exponent in the Path Averaging Model

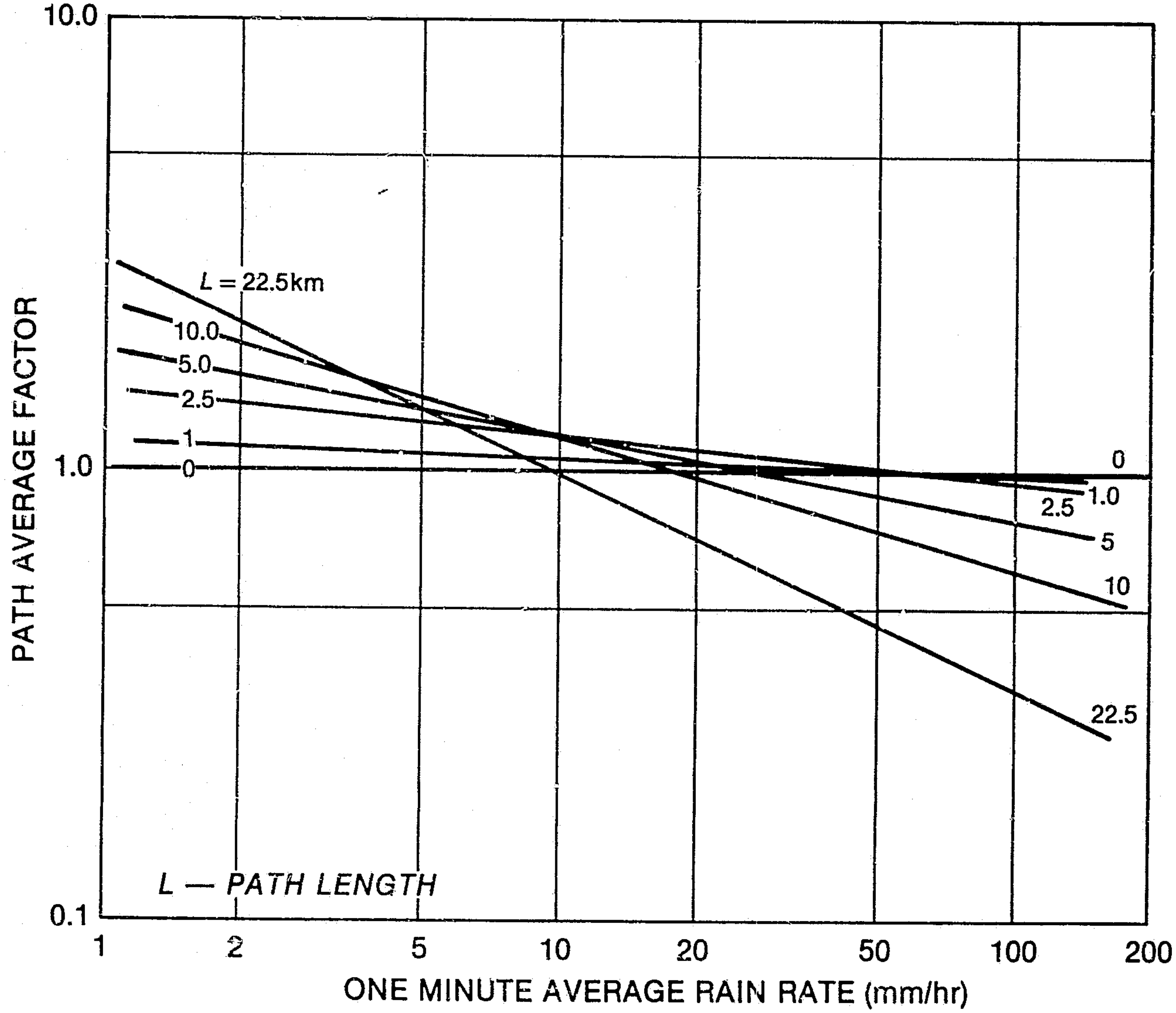

Figure 3.4-15. Effective Path Average Factor Model for Different Path Lengths

angles lower than 10^o, the effect of refraction by the troposphere and of the earth's curvature should be taken into account in the calculation of D. If D exceeds 22.5 km, a D_o of 22.5 km is used for the calculation of the effective path average factor and the occurrence probabilities are multiplied by D/D_o.

3.4.3.2 Variable Isotherm Height Technique. The variable isotherm height technique uses the fact that the effective height of the attenuating medium changes depending on the type of rainfall event. Also, various types of rainfall events selectively influence various percentages of time throughout the annual rainfall cycle. Therefore, a relation exists between the effective isotherm height and the percentage of time that the rain event occurs. This relation has been shown earlier in Figure 3.4-6a. Again the total attenuation is obtained by integrating the specific attenuation along the path. The resulting equation to be used for the estimation of slant path attenuation is:

$$A = \frac{a R_p^b}{\cos\theta}\left[\frac{e^{UZb}-1}{Ub} - \frac{X^b e^{YZb}}{Yb} + \frac{X^b e^{YDb}}{Yb}\right]; \theta \geqslant 10^\circ \tag{3.4-8}$$

where U, X, Y and Z are empirical constants that depend on the point rain rate. These constants are:

$$U = \frac{1}{Z}\left(e^{YZ} \ln X\right) \tag{3.4-9}$$

$$X = 2.3 R_p^{-0.17} \tag{3.4-10}$$

$$Y = 0.026 - 0.03 \ln R_p \tag{3.4-11}$$

$$Z = 3.8 - 0.6 \ln R_p \tag{3.4-12}$$

for lower elevation angles $\theta < 10^{o}$

$$A = \frac{L}{D} a R_p^b \left[\frac{e^{UZb}-1}{Ub} - \frac{X^b e^{YZb}}{Yb} + \frac{X^b e^{YDb}}{Yb} \right] \quad (3.4\text{-}13)$$

where

$$L = [(E + H_g)^2 + (E + H_o)^2 - (E + H_g)(E + H_o) \cos \psi]^{1/2} \quad (3.4\text{-}14)$$

ψ = path central angle defined above.

The following steps apply the variable isotherm height rain attenuation model to a general Earth-to-space path:

Step 1 - At the Earth terminal's geographic latitude and longitude, obtain the appropriate climate region: A to H (1 of 8 regions), using either Figure 3.4-1 (land areas), 3.4-2 (includes ocean areas), 3.4-3 (United States) or 3.4-4 (Europe). If long term rain rate statistics are available for the location of the ground terminal, they should be used instead of the model distribution functions.

Step 2 - Select probabilities of occurrence (P) covering the range of interest in terms of the percent of time rain rate is exceeded (e.g., .01, .1 or 1%).

Step 3 - Obtain the terminal point rain rate R_p (mm/hour) using Figures 3.4-5a or 3.4-5b curves, or Table 3.4-1 or long term measured values if available of rain rate versus the percent of year rain rate is exceeded at the climate region and probabilities of occurrence (Step 2).

Step 4 - For an Earth-to-space link through the entire atmosphere, obtain the rain layer height from the height of the 0^{o} isotherm (melting layer) H_o at the path latitude (Figure 3.4-6a). The heights will vary correspondingly with the probabilities of occurrence (Step 2). To interpolate, plot H_o (P) vs Log P and use a straight line to relate H_o to P.

C-2

Step 5 - Obtain the horizontal path projection D of the oblique path through the rain volume:

$$D = \frac{H_o - H_g}{\tan\theta}; \theta \geq 10^\circ \tag{3.4-15}$$

$H_o = H_o(P)$ = height (km) of isotherm for probability P

H_g = height of ground terminal (km)

θ = path elevation angle

Step 6 - Test D ≤ 22.5 km; if true, proceed to the next step. If D ≥ 22.5 km, the path is assumed to have the same attenuation value as for a 22.5 km path but the probability of occurrence is adjusted by the ratio of 22.5 km to the path length:

$$\text{new probability of occurrence, } P' = P\left(\frac{22.5\text{km}}{D}\right)$$

where D = path length projected on surface (>22.5 km).

Step 7 - Obtain the parameters a(f) and b(f), relating the specific attenuation to rain rate, from Table 3.4-2 or Figures 3.4-7 and 3.4-8, or equivalent observed data.

Step 8 - Compute the total attenuation due to rain using R_p, a, b, θ, D

$$A = \frac{a R_p^b}{\cos\theta}\left[\frac{e^{UZb}-1}{Ub} - \frac{X^b e^{YZb}}{Yb} + \frac{X^b e^{YDb}}{Yb}\right]; \theta \geq 10^\circ \tag{3.4-16}$$

where A = total path attenuation due to rain (db)

a,b = parameters relating the specific attenuation to rain rate (from Step 7), $\alpha = aR_p^b$ = specific attenuation

R_p = point rain rate (Step 3)

θ = elevation angle of path

D = horizontal path distance (from Step 5)
$Z \leq D \leq 22.5$ km

or alternatively, if $D < Z$,

$$A = \frac{a\, R_p^{\,b}}{\cos\theta}\left[\frac{e^{UbD}-1}{Ub}\right] \qquad (3.4\text{-}17)$$

or if $D = 0$, $\theta = 90^0$,

$$A = (H - H_g)(a\, R_p^{\,b}) \qquad (3.4\text{-}18)$$

3.5 THE LIN MODEL

3.5.1 Empirical Formulas

The set of empirical formulas presented here for earth-satellite path attenuation is an extension of those obtained previously for terrestrial microwave radio paths (Lin-1978). In the case of terrestrial paths, the calculation of the expected rain attenuation distribution from a long term (20 years) distribution of 5-minute point rain rates has been accomplished using empirical formulas deduced from available rain rate and rain attenuation data measured on nine 11 GHz radio paths (5-43 km) at five different U.S. locations (Lin-1977).

These empirical formulas for terrestrial paths, are (Lin's notation (1978) reverses the role of α and β)

$$\alpha(R) = a\, R^b \text{ dB/km} \qquad (3.5\text{-}1)$$

$$\beta(R,L) = \alpha(R)\, L \left[1 + \frac{1}{\bar{L}(R)}\right]^{-1} \text{dB} \qquad (3.5\text{-}2)$$

where

$$\overline{L}(R) \approx \frac{2636}{R - 6.2} \text{ km} \qquad (3.5\text{-}3)$$

R is the 5-minute point rain rate in mm/h, L is the radio path length in km, β(R,L) is the path rain attenuation in dB at the same probability level as that of R, and the parameters a and b are functions (Setzer-1970, Chu-1974, Saleh-1978) of the radio frequency, as shown in Figure 3.5-1. (Strictly speaking, the parameters a and b are also functions of wave polarization.)

3.5.2 Rain Path Averaging

If the rain rates were uniform over a radio path of length L, the path rain attenuation β(R,L) would be simply $\alpha(R) \cdot L$, representing a linear relationship between β and L. However, actual rainfalls are not uniform over the entire radio path, and therefore the increase of β(R,L) with L is nonlinear.

Two factors in the empirical method account for the radio path averaging effect. First, the method is based upon the long term distribution of 5-minute point rain rates in which the 5-minute time averaging partially accounts for the fact that the radio path performs a spatial averaging of non-uniform rain rates (Freeny and Gabbe-1969, Drufuca and Zawadzki-1973, Bussey-1950). A 5-minute average of the rain rate seen at a point corresponds to spatially averaging approximately 2.1 km of vertically variable rain rates, assuming 7 meters/second average descent velocity of rain drops.

Figure 3.5-2 shows how the point rain rate distribution, from two years of measurements at Palmetto, Georgia, depends on the average time intervals (range: 0.5-60 minutes). The probability of a 5-minute rain rate exceeding the 40 mm/h threshold is 1/2 that of a 0.5-minute rain rate exceeding the same threshold. From another viewpoint, increasing the averaging time interval from 0.5 to 5 minutes reduces the 0.01 percentile (i.e., 53 minutes/year) rain rate from 87 to 58 mm/h.

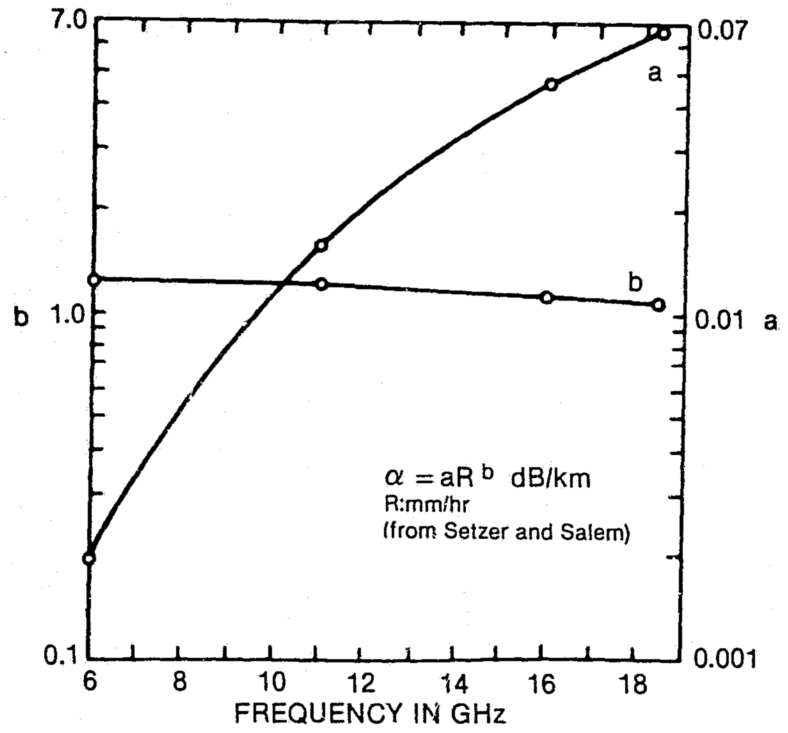

Figure 3.5-1. Dependence of Parameters a and b on the Radio Frequency

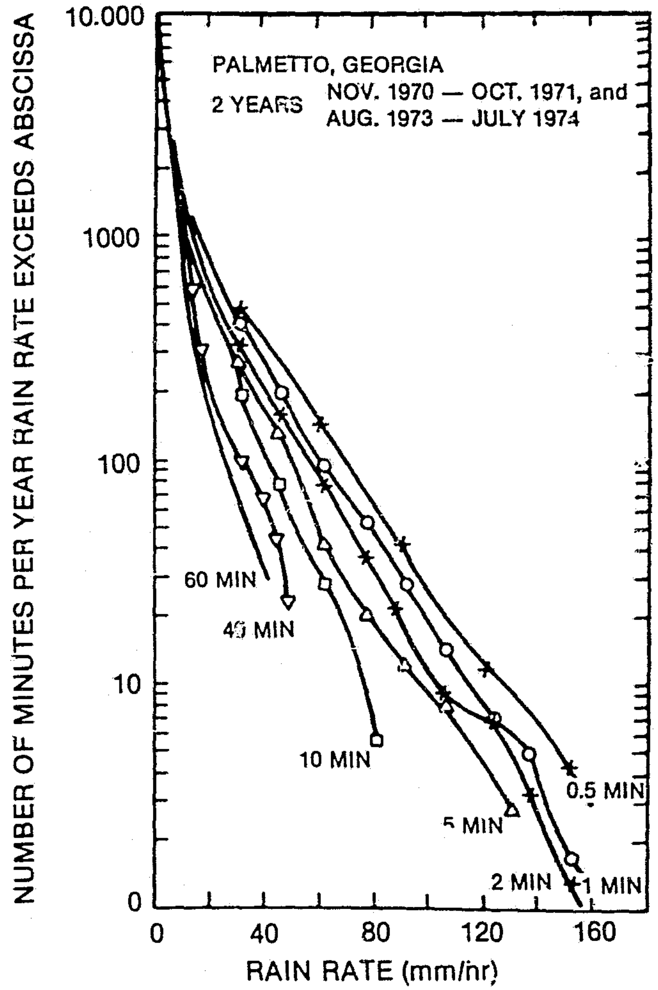

Figure 3.5-2. Dependence of Rain Rate Distribution on Tipping Bucket Rain Gauge Integration Time From Two Years of Measurement at Palmetto, Georgia

However, since most radio paths of interest are longer than 2.1 km, the fixed 5-minute average interval cannot adequately account for all the path length variations. This deficiency is compensated for by the factor

$$\left[1 + \frac{1}{L(R)}\right]^{-1} \tag{3.5-4}$$

In other words, the auxiliary nonlinear factor represents the empirical ratio between the 5-minute point rain rate R and the radio path average rain rate $R_{av}(L)$ at the same probability level. Since the significant difference between the 5-minute point rain rate and the 0.5-minute point rain rate in Figure 3.5-2 already accounts for the major portion of the difference between the radio path average rain rate $R_{av}(L)$ and the 0.5-minute point rain rate, the auxiliary factor is a weak nonlinear function of L. Obviously, many different analytic functions can be used to approximate this mildly nonlinear behavior. The single parameter function is selected for its simplicity. The adequacy of this simple approximation is supported by the rain rate and rain attenuation data measured on nine, 11-GHz, terrestrial radio paths at five U.S. locations (Lin-1977).

3.5.3 Earth-Satellite Path Length

To extend the method to earth-satellite paths, let H be the long-term average height of the freezing level in the atmosphere, measured relative to sea level. The effective average length of the earth-satellite path affected by rain is then

$$L = (H - H_g)/\sin\theta \tag{3.5-5}$$

where θ is the satellite elevation angle as viewed from the earth station, and H_g is the ground elevation measured from the sea level. The radar measurements of rainfall reflectivity at Wallops Island, Virginia indicate that on the average rainy day (CCIR-1977)

$$H \approx 4 \text{ km} \tag{3.5-6}$$

Thus, given the elevation angle θ, the ground elevation H_g and the distribution of 5-minute point rain rates, we can calculate the rain attenuation distribution on the earth-satellite path through the use of equations 3.5-1, 2 and 5.

Notice that equation 3.5-5 implies that the path rain attenuation β (R,L) varies exactly as the cosecant of the elevation angle θ with this simple extension of the terrestrial model. Also note that these simple formulas are valid only on the long term average. The short term relationships between the surface point rain rate and the earth-satellite path rain attenuation, on a storm-by-storm basis, have been observed to be erratic and difficult to predict.

3.6 PIECEWISE UNIFORM RAIN RATE MODEL

A quasi-physical model of real rains has been developed at the Virginia Polytechnic Institute and State University (Persinger, et al-1979) to eliminate the need for effective path lengths. The model accounts for the nonuniform spatial rain rate distribution and permits direct evaluation of the effective path length integral, $A=\int \alpha \, dl$, for an arbitrary propagation path. The piecewise uniform rain rate model is based on the following two simplifying assumptions: a) the spatial rain rate distribution is uniform for low rain rates, and b) as peak rain rate increases, the rain rate distribution R(l) becomes increasingly nonuniform.

The model utilizes an effective rain extent wherein the rain is of height H (above a flat earth) and of basal length B (in a plane containing the line-of-sight path and the local vertical at the earth terminal location). The rain height values follow from the 0^oC isotherm heights (CCIR-1978a, Doc. F5/003). For simplicity the U.S. will be divided into three latitude classes yielding

$$H = \begin{cases} 3.5 \text{ km} & \text{High-latitude (above } 40^\circ) \\ 4.0 \text{ km} & \text{Mid-latitude} \\ 4.5 \text{ km} & \text{Low-latitude (below } 33^\circ) \end{cases} \quad (3.6\text{-}1)$$

Confidence in these values can be gained by examining attenuation data from several experiments at different locations, elevation angles, and frequencies. Applying the first assumption, that R is constant for low rain rates (say 10 mm/h), reduces the effective path length integral to $A = L\alpha$, i.e. L equals L_e for low rain rates. Then $L = A/\alpha$ for R = 10 mm/h is used to calculate L from attenuation data. So for each experiment there is a value of L and θ leading to the points in Figure 3.6-1. The code numbers (such as B8, C3,...) denote the experiments listed in Persinger, et al (1978). The points on Figure 3.6-1 fall near the height H and also serve as a guide in the selection of the basal extent value of

$$B = 10.5 \text{ km} \quad (3.6\text{-}2)$$

The calculation of rain path length L is summarized as

$$L = \begin{cases} H \csc\theta \ ; \ \theta > \theta_0 \\ B \sec\theta \ ; \ \theta \leq \theta_0 \end{cases} \quad (3.6\text{-}3)$$

where H, B and $\theta_0 = \tan^{-1}(H/B)$ yield 23.2°, 20.9°, and 18.4° for low, mid, and high latitude classes, respectively.

The nonuniform rain rate distribution is modeled by dividing the rain path L into N equal intervals, each containing uniform rain. This piecewise uniform rain rate distribution reduces the effective path length integral to

$$A = \frac{L}{N} \sum_{i=1}^{N} \alpha(R_i) \text{ dB} \quad (3.6\text{-}4)$$

where R_i is the rain rate for the i^{th} rain cell. A ten-cell model would in general provide the fine detail of the rain distribution. Comparisons to

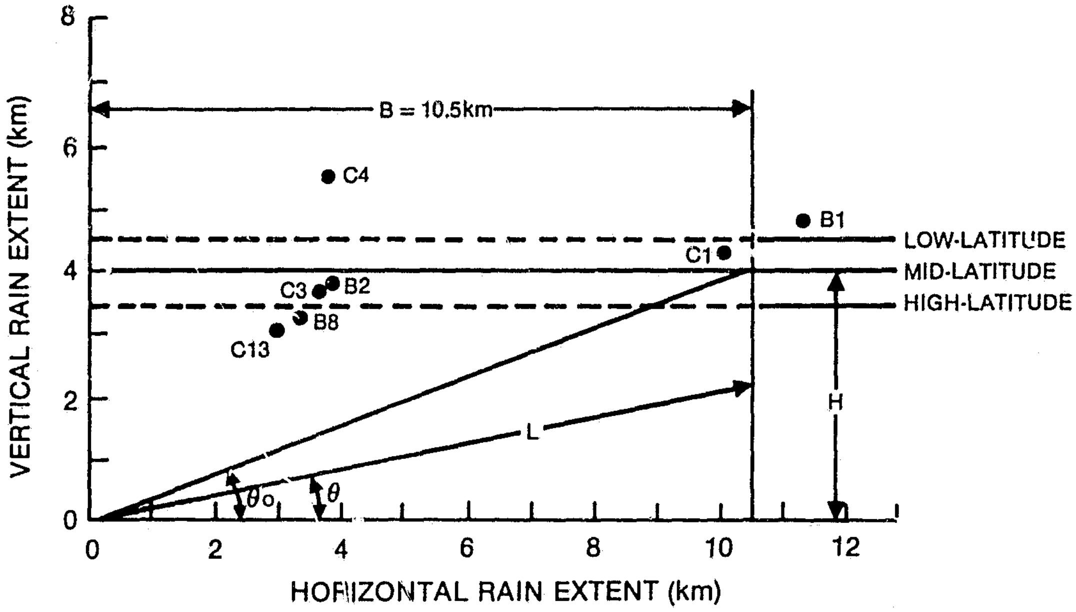

Figure 3.6-1. Rain Extent Model

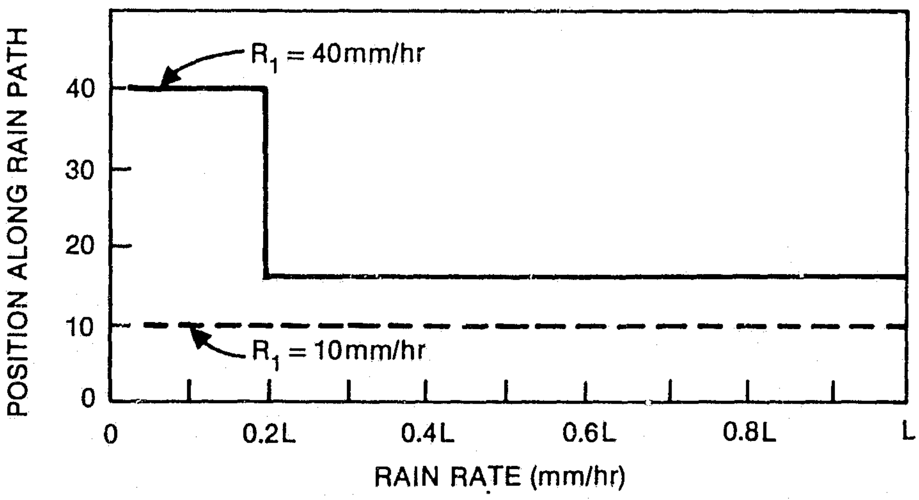

Figure 3.6-2. Rain Rate Distribution Model as Function of Position Along the Rain Path

measured attenuation data have indicated that a two-level model provides good results. The ten-cell, two-level model is

$$R(\ell) = \begin{cases} R_1 & ; \quad 0 \leqslant \ell \leqslant CL \\ R_x & ; \quad CL \leqslant \ell \leqslant L \end{cases} \qquad (3.6\text{-}5)$$

where R_1 is the rain rate at the earth terminal location. The unknowns are C, the fraction of the path over which rain rate R_1 extends (it is a multiple of 0.1), and x, the exponent which specifies the rain rate of the remaining cells through the following functional form

$$R_x = \begin{cases} R_1 & ; \; R_1 \leqslant 10 \text{ mm/h} \\ R_1(R_1/10)^x & ; \; R_1 > 10 \text{ mm/h} \end{cases} \qquad (3.6\text{-}6)$$

The attenuation expression then reduces to

$$A = \left[C\,\alpha(R_1) + (1-C)\alpha(R_x) \right] L \quad \text{dB} \qquad (3.6\text{-}7)$$

Attenuation and rain rate data pairs from experiments were used to determine x and C such that the predicted attenuation best fit the measured values over the range of rain rates for the experiments. Typical results were

$x = -0.66$ and $C = 0.2$

A plot of the rain rate distribution model using these values is shown in Figure 3.6-2.

The Piecewise Uniform Rain Rate Model has been combined with a scattering model to form a Rain Propagation Prediction Program. This program predicts the attenuation, cross-polarization isolation and the phase as a function of rain rate. The input format allows changes in system parameters so that the effects of rain on millimeter wave propagation as a function of frequency, location and elevation angle can be predicted. The program is written in FORTRAN and its operational format is outlined in Figure 3.6-3 and described in detail in Persinger and Stutzman (1978). The reader is referred to the above reference for a full description of the subroutines and a listing of the 1040 program cards. The program is operationally efficient and accurately predicts measured experimental data (Persinger, et al-1979).

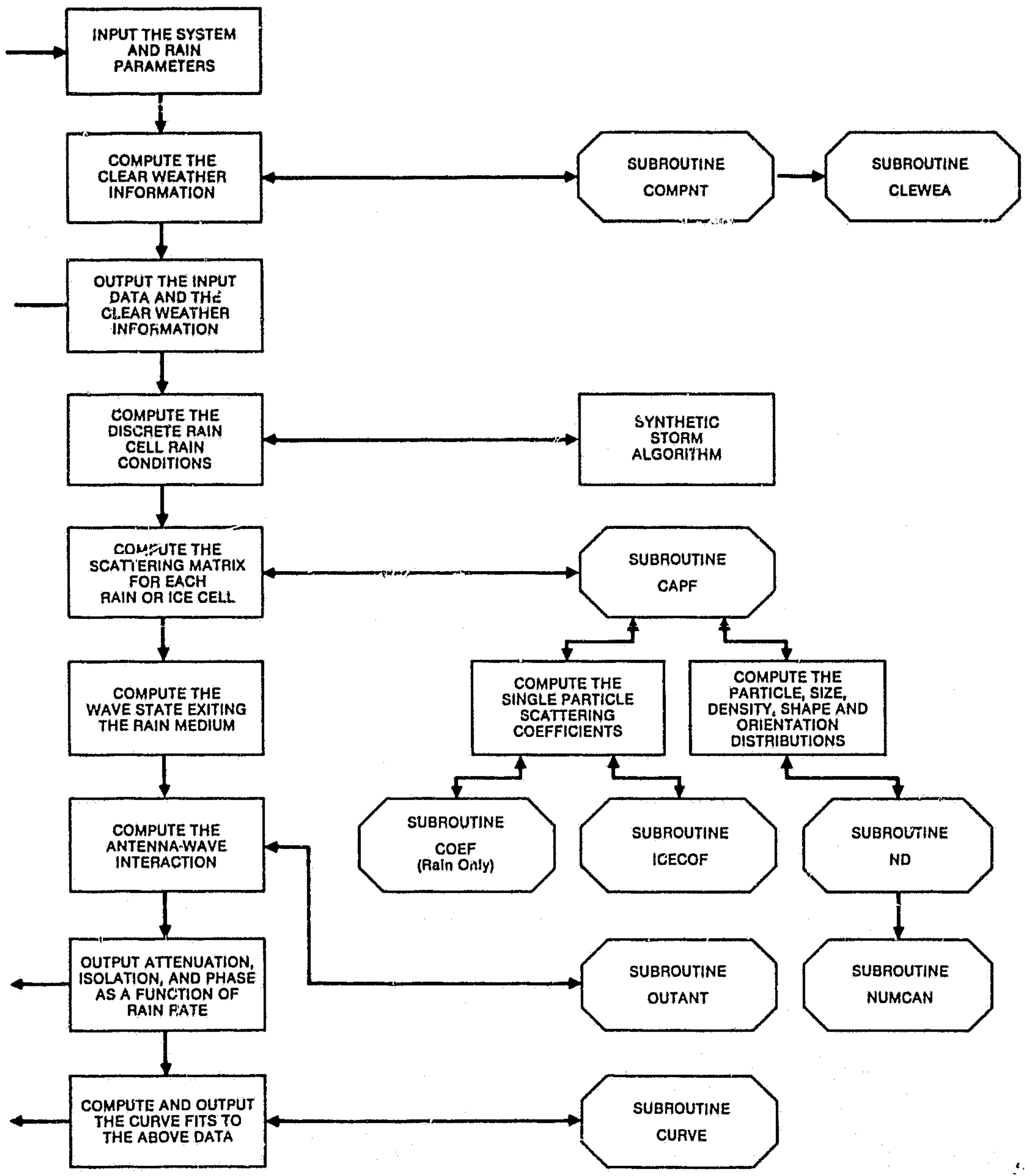

Figure 3.6-3. Block Diagram of the Rain Propagation Prediction Program

3.7 THE EFFECTIVE PATH LENGTH CONCEPT

3.7.1 Definition of Effective Path Length

The effective path length L_e is usually defined as that parameter which relates the specific attenuation to the total attenuation along the earth-space path. Mathematically it is written

$$A = aR^bL_e$$

Alternatively, L_e is the hypothetical path length of uniform rain rate R which will produce the same total path attenuation as the real varying rain rate does along the path. The form of L_e and the technique employed for its derivation has been quite variable. For example, in some cases it is termed effective path length and in others the path averaging factor.

Since rains are not usually uniform over the extent of the storm (rain cells of higher rain rates are small compared to the extent of the storm), the total attenuation is

$$A = \int_0^L \alpha_1 \, d\ell \qquad (3.7\text{-}1)$$

where A is the total attenuation at a given frequency and time through the storm of extent L along the path ℓ. α_1 is the high resolution specific attenuation (attenuation per meter) which assumes that α_1 is uniform over each meter. Of course the rain rate is also a function of ℓ. Now the effective path length in kilometers is

$$L_e = \frac{A}{\alpha_{avg}} \qquad (3.7\text{-}2)$$

where α_{avg} is an analytically determined attenuation per kilometer assuming a uniform average rain rate. The average rain rate is based on rain rate measurements taken over a long period of time. The measured attenuation is also indirectly a function of average rain rate. Measured attenuation and measured rain rate data are compared on an equal probability of occurrence basis over a long time base. This removes the instantaneous time dependence of the measurements. Note that if rain rate is not a function of length ℓ, $A = \alpha_{avg}L$, and the effective path length would equal the physical rain extent L. This is one limit which occurs for low rain rates. For example, for stratiform rains the rain rate is nearly spatially uniform.

3.7.2 Frequency Dependence of Effective Path Length

Some frequency dependence to the effective path length has been observed at higher rain rates. To investigate the frequency dependence of L_e consider the ratio of two L_e's for two frequencies f_1 and f_2. Namely,

$$\frac{L_e(f_1)}{L_e(f_2)} = \frac{\alpha_{avg}(f_1)}{\alpha_{avg}(f_2)} \frac{\int_0^L \alpha_1(f_1)\, d\ell}{\int_0^L \alpha_1(f_2)\, d\ell} = r_p r_m^{-1} \tag{3.7-3}$$

where r_m is the ratio of the measured attenuations, and r_p is the ratio of the predicted attenuations assuming uniform rain conditions, which is also the ratio of predicted specific attenuations. For the effective path length to be independent of frequency, r_m must equal r_p and the effective path length versus rain rate must be identical for the two frequencies. Experimental results shown in Figure 3.7-1 demonstrate that for two frequencies (19 and 28 GHz) and rain rates exceeding one inch per hour the effective path length of the higher frequency is as much as 20% longer than the lower frequency. This is an effect which must be considered when frequency scaling attenuation measurements over a wide frequency range (also see Chapter 2).

3.7.3 Effective Path Length Versus Measurement Period

Experimentally determined effective path lengths for varying measurement periods (such as annual and worst month) show a high variability. For example, in Figure 3.7-2 each curve was developed from equal probability attenuation - rain rate measurements for the period indicated. Two trends are apparent. First, the monthly curves show a decreasing path length with

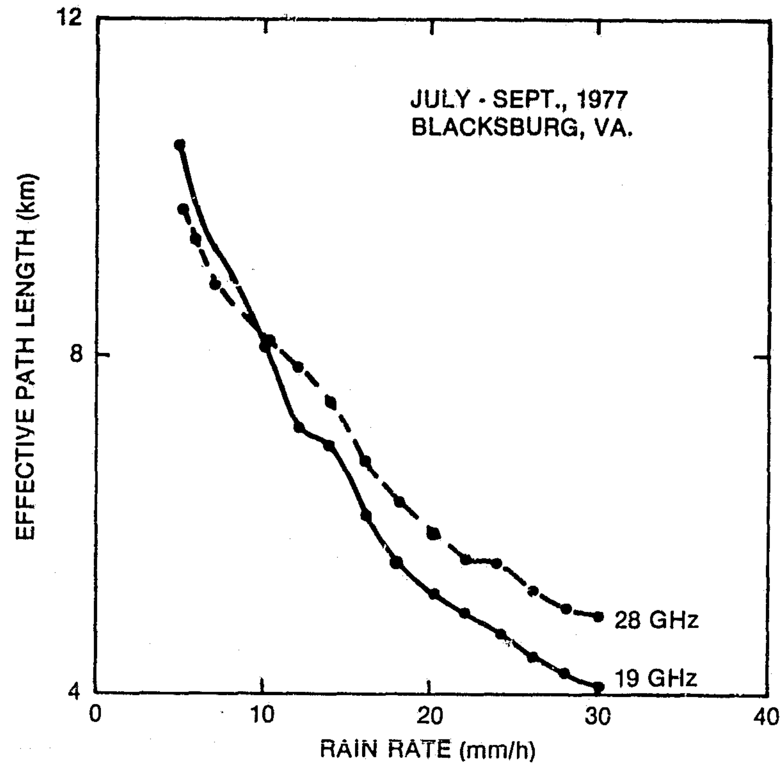

Figure 3.7-1. Effective Path Lengths for the VPI & SU COMSTAR 19 and 28 GHz Systems

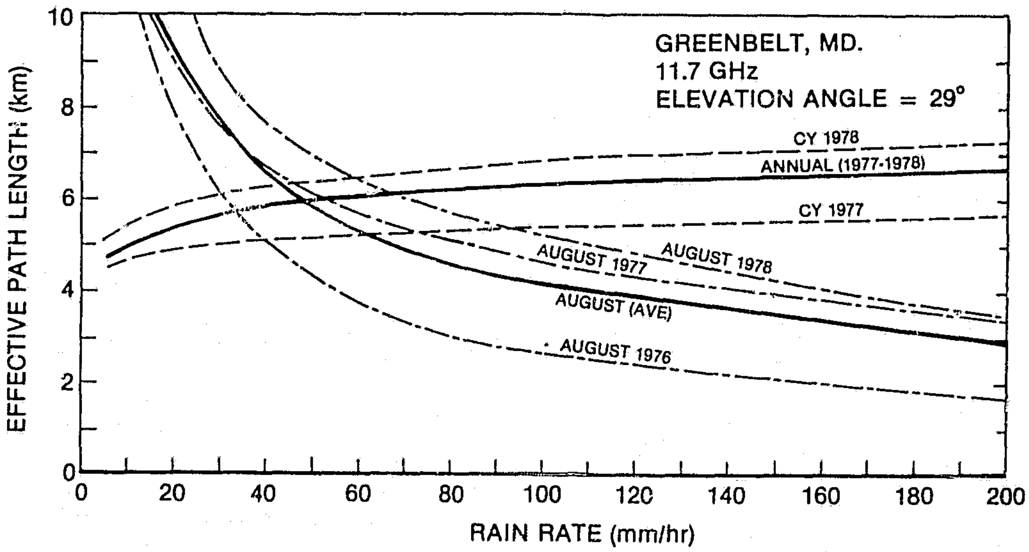

Figure 3.7-2. Effective Path Length for Annual & Worst Month Periods

increasing rain rate, and second, the annual curves show a path length which increases slightly with rain rate. The first effect arises because the high rain rate events in August are primarily convective storms with intense localized rain rates. The second effect is probably accounted for because the winter rains in Maryland are more uniform in nature and the zero degree isotherm is significantly lower in winter. For this case L_e approaches L for cold weather low rain rate events. However, this effect has not always been observed (see below) and probably indicates that regions with low rainfall during the cold weather months will show a rain rate dependence similar to that for the worst month.

3.7.4 Comparison of Effective Length Factors

Several of the attenuation models utilize a factor easily related to L_e. It is of interest to compare these factors and determine their relative differences based on a similar set of assumptions. First consider the L_e factor in each model separately.

3.7.4.1 Dutton-Dougherty Model. In this model the effective path length , incorporated in the liquid water content factor L(h). For stratiform modeling L(h) is assumed constant to the rain-cloud base, then decreases to zero at H, the storm top height. For convective modeling L(h) increases slightly to the rain-cloud base, then decreases to zero at H. This is a very complex relation between rain rate and effective path length. Therefore, no attempt is made to define a single parameter L_e from this model.

3.7.4.2 Global Model. Both forms of the Global model employ a term which can be related to the effective path length. For the path averaging technique (Global Prediction Model)

$$L_e = \frac{H}{\sin\theta}\,\gamma(D)R_p^{-\delta(D)} \qquad (3.7\text{-}4)$$

where R_p is the point rain rate, H is the height of the 0^oC isotherm, D is the basal distance and γ and δ are the path averaging factors defined in

Section 3.4. For a 45^0 elevation angle at a sea-level ground station near 40^0N latitude

$$L_e = 9.14\ R_p^{-0.14}\ \text{km} \tag{3.7-5}$$

For the variable isotherm height form of the Global model,

$$L_e = \frac{1}{\cos\theta}\left[\frac{e^{UZb}-1}{Ub} - \frac{X^b e^{YZb}}{Yb} + \frac{X^b e^{YDb}}{Yb}\right] \tag{3.7-6}$$

where the terms are defined in Section 3.4.3.2. The value of L_e is a complex function of R_p since U, X, Y and Z (implicitly) are functions of R_p.

3.7.4.3 Lin Model. The Lin model utilizes two techniques for obtaining the average path length. The first is to temporally average the instantaneous rain rate to five minute intervals. The effect of this average process in terms of the effective path length comparison is unclear. However, as will be shown, the other parameter agrees well with the results of other models. Specifically Lin (1978) finds that

$$\begin{aligned} L_e &= \frac{4}{\sin\theta}\left[1 + \frac{4(R_p-6.2)}{2636\sin\theta}\right]^{-1} \\ &= \frac{2636}{659\sin\theta + R_p - 6.2} \end{aligned} \tag{3.7-7}$$

At θ = 45 degrees the result is

$$L_e = 2636\,(460 + R_p)^{-1} \tag{3.7-8}$$

3.7.4.4 Piecewise Uniform Rain Rate Model. The piecewise uniform rain rate model does not readily allow definition of a single L_e parameter. Therefore this parameter is not derived from this model.

3.7.4.5 Experimental Measurements. Ippolito (1978) has employed over sixty months of long term attenuation and rain rate statistics at 11.7, 15, 20 and 30 GHz to derive an effective path length based on experimental measures. The result is

$$L_e = \frac{9.065}{\sin\theta} R_p^{-0.296} \text{ km} \quad (3.7\text{-}9)$$

for elevation angles from 20 to 90 degrees. At 45 degrees elevation angle

$$L_e = 12.82 R_p^{-0.296} \quad (3.7\text{-}10)$$

3.7.4.6 Comparison of Effective Path Lengths. Assuming a ground station at sea level, 40 degrees North latitude and observing at 45 degrees elevation angle, the L_e factors are plotted in Figure 3.7-3 for the two forms of the Global model, the Lin model and the experimental results of Ippolito (1978) and CTS results (Ippolito-1979). The latter experimental results (labeled $L_{e,\ exp(11.7GHz)}$ in Figure 3.7-3) were scaled from the 29 degree elevation angle measurements made at Greenbelt, MD to CTS, to 45 degrees using the ratio of the cosecants of the two angles. The original data is the annual curve for 1977 and 1978 shown in Figure 3.7-2. This data is the longest set of continuous, single-site effective path length data published to date for CTS and therefore more weight should be given this curve.

The most important result in Figure 3.7-3 is that the use of an effective path length between 4 and 5 kilometers is reasonable. A significant variation occurs below 30 mm/h which may arise due to the presence of winter rains, but this remains unproven. Fortunately for most design problems the most accurate estimates of effective path length are required for annual percentages in the range from 0.01 and 0.001 percent of a year, and in this range both the experimental and model-generated effective path lengths are approximately 4 to 5 km. However, assuming a $\pm$ 1 km error bound on L_e the

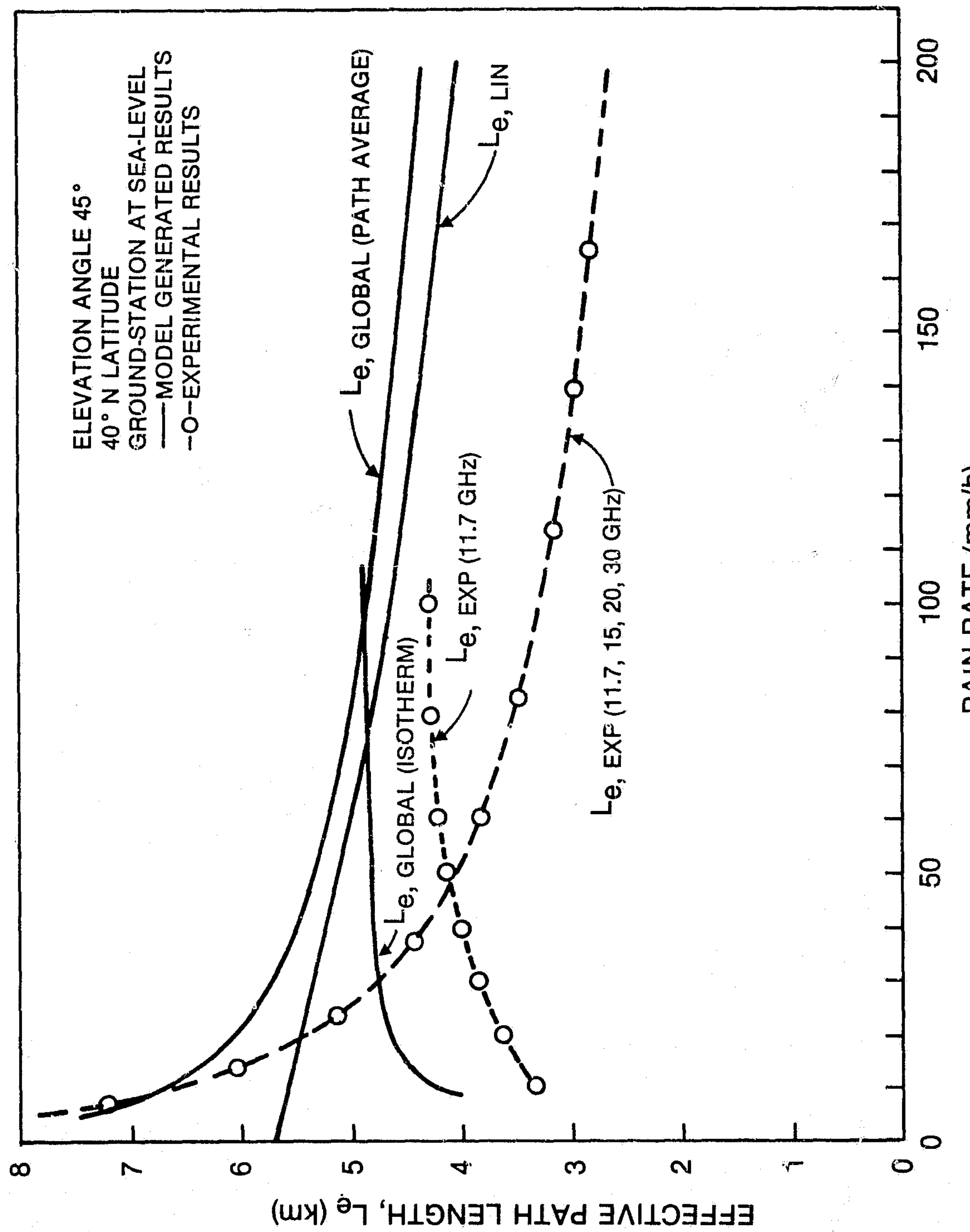

Figure 3.7-3. A Comparison of Effective Path Lengths

error in estimating L_e is about $\pm$ 1dB. If L_e is directly related to the total attenuation, at least a $\pm$ 1dB error bound must be placed on the estimate of the path attenuation. This error bound will increase as the elevation angle decreases.

3.8 REFERENCES

Barry, R.C. and R.J. Chorley (1970), Atmosphere, Weather and Climate, Holt, Reinhart and Winston, Inc., New York, p. 205.

Bussey, H.E. (1950), "Microwave Attenuation Statistics Estimated from Rainfall and Water Vapor Statistics," Proc. IRE, Vol. 38, pp. 781-785.

CCIR (1977), "Influence of the Non-Ionized Atmosphere on Wave Propagation," CCIR Study Groups Period 1974-1978, DOC. 5/169-E, May 10, United States of America, Modification to Report 233-3 (REV. 76).

CCIR (1978), "Propagation in Non-Ionized Media", Volume V, XIV Plenary Session, Kyoto, Japan.

CCIR (1978a), Special Preparatory Meeting (WARC-79) Documents.

Chu, T.S. (1974), "Rain Induced Cross-Polarization at Centimeter and Millimeter Wavelengths," B.S.T.J., Vol. 53, pp. 1559-1579.

Crane, R.K. (1966), "Microwave Scattering Parameters for New England Rain," MIT Lincoln Laboratory Report 426, ASTIA Doc. AD-647798.

Crane, R.K. and D.W. Blood (1979), "Handbook for the Estimation of Microwave Propagation Effects - Link Calculations for Earth-Space Paths," Environmental Research and Technology Rpt. No. 1, Doc. No. P-7376-TRL.

Dougherty, H.T. and E.J. Dutton (1978), "Estimating Year-to-Year Variability of Rainfall for Microwave Applications," IEEE Trans. Comm., Vol. COM-26, No. 8, pp. 1321-1324.

Drufuca, G. and I.I. Zawadzki (1973), "Statistics of Rain Gauge Records," Inter-Union Commission on Radio Meteorology (IUCRM) Colloquium on "The Fine Scale Structure of Precipitation and Electromagnetic Propagation," Nice, France, Conference Record, Vol. 2.

Dutton, E.J. (1971), "A Meteorological Model for Use in the Study of Rainfall Effects on Atmospheric Radio Telecommunications," Off. Telecomm. Rpt. OT/TRER-24, NTIS No. COM-75-10826/AS, Springfield, Va.

Dutton, E.J. (1977), "Earth-Space Attenuation Prediction Procedures at 4 to 16 GHz," Off. Telcom. Rpt. 77-123.

Dutton, E.J. and H.T. Dougherty (1973), "Modeling the Effects of Clouds and Rain Upon Satellite-to-Ground System Performance," Off. Telecom. Report 73-5, NTIS No. COM-75-10950, Springfield, Va.

Dutton, E.J., H.T. Dougherty and R.F. Martin, Jr. (1974), "Prediction of European Rainfall and Link Performance Coefficients at 8 to 30 GHz," Off. Telecom., Dept. of Commerce, NTIS No. AD/A-000804, Springfield, Va.

Freeny, A.E. and J.D. Gable (1969), "A Statistical Description of Intense Rainfall," B.S.T.J., Vol. 48, No. 6, pp. 1789-1851.

Goldhirsh, J. and I. Katz (1979), "Useful Experimental Results for Earth-Satellite Rain Attenuation Modeling," IEEE Trans. Ant. Prop., Vol. AP-27, No. 3, pp. 413-415.

Gray, L.F. and M.P. Brown, Jr. (1979), "Transmission Planning for the First U.S. Standard C (14/11-GHz) INTELSAT Earth Station," Comsat Tech. Rev., Vol. 9, No. 1, pp. 61-89.

Hyde, G. (1979), private communication.

Ippolito, L.J. (1978), "Rain Attenuation Prediction at 10 to 100 GHz from Satellite Beacon Measurements," Abstract, Record, EASCON '78, September 25-27, Arlington, Va.

Ippolito, L.J. (1979), "11.7 GHz Attenuation and Rain Rate Measurements with the Communications Technology Satellite (CTS)," NASA TM 80283.

Janes, H.B., J.T. Collins and F.K. Steele (1978), "A Preliminary Catalog of Programs and Data for 10-100 GHz Radio System Prediction," Off. Telecomm. Rpt. 78-141.

Jorgenson, D.L., W.H. Klein and C.F. Roberts (1969), "Conditional Probabilities of Precipitation Amounts in the Conterminous United States," U.S. Dept. Comm., Env. Sci. Serv. Ad., Weather Bur., Silver Spring, Md., ESSA Tech Memo WBTM-T DL-18.

Kaul, R., D.V. Rogers and J. Bremer (1977), "A Compendium of Millimeter Wave Propagation Studies Performed by NASA," ORI Final Report, prepared under NASA Contract NAS5-24252.

Laws, J.O. and D.A. Parsons (1943), "The Relation of Raindrop-Size to Intensity," Am. Geophys. Union Trans., Vol. 24, pp. 274-276.

Lin, S.H. (1973), "Statistical Behavior of Rain Attenuation," B.S.T.J., Vol. 52, No. 4, pp. 557-581.

Lin, S.H. (1977), "Nationwide Long Term Rain Rate Statistics and Empirical Calculations of 11 GHz Microwave Rain Attenuation," B.S.T.J., Vol. 56, No. 9, pp. 1581-1604.

Lin, S.H. (1978), "Empirical Calculation of Microwave Rain Attenuation Distributions on Earth-Satellite Paths," Record, EASCON '78, Arlington, Va., pp. 372-378.

Marshall, J.S. and W.M. Palmer (1948), "The Distribution of Raindrops With Size," Jrnl. Meteorology, Vol. 51, pp. 165-166.

Olsen, R.L., D.V. Rogers and D.B. Hodge (1978), "The aR^b Relation in the Calculation of Rain Attenuation," IEEE Trans. Ant. Prop., Vol. AP-26, pp. 318-329.

Oort, A.H. and E.M. Rasmusson (1971), "Atmospheric Circulation Statistics," NOAA Professional Paper No. 5, U.S. Dept. Commerce.

Persinger, R.R. and W.L. Stutzman (1978), "Millimeter Wave Propagation Modeling of Inhomogeneous Rain Media for Satellite Communication Systems," VPI & SU Interim Rpt. 1978-1.

Persinger, R.R., W.L. Stutzman, R.E. Castle and C.W. Bostian (1979), "Millimeter Wave Attenuation Prediction Using a Piecewise Uniform Rain Rate Model," preprint to be published in IEEE Trans. Ant. Prop.

Rice, P.L. and N.R. Holmberg (1973), "Cumulative Time Statistics of Surface-Point Rainfall Rates," IEEE Trans. Comm., Vol. COM-21, No. 10, pp. 1131-1136.

Rogers, D.V. and G. Hyde (1979), "Diversity Measurements of 11.6-GHz Rain Attenuation at Etam and Lenox, West Virginia," Comsat Tech. Rev., Vol. 9, No. 1, pp. 243-254.

Rogers, R.R. (1972), "Radar-Derived Statistics on Slant-Path Attenuation at 10 GHz," Radio Science, Vol. 7, No. 6, pp. 631-643.

Saleh, A.A.M. (1978), private communication.

Setzer, D.E. (1970), "Computed Transmission Through Rain at Microwave and Visible Frequencies," B.S.T.J, Vol. 49, No. 8, pp. 1873-1892.

Skerjanec, R.E. and C.A. Samson (1970), "Rain Attenuation Study for 15 GHz Relay Design," NTIS, AD-709-348, Springfield, Va.

Steele, F.K. (1979), private communication.

CHAPTER IV

DEPOLARIZATION ON EARTH-SPACE PATHS

4.1 INTRODUCTION

By using orthogonal polarizations, two independent information channels occupying the same RF frequency band can be transmitted over a single link. This technique is used in satellite communications systems to effectively increase the available spectrum. While the orthogonally-polarized channels are completely isolated in theory, some degree of interference between them is inevitable, owing to less-than-theoretical performance of spacecraft and Earth station antennas, and depolarizing effects on the propagation path. The main sources of this depolarization at millimeter wave frequencies are hydrometeor absorption and scattering in the troposphere.

4.1.1 Definition of Terms

Frequency reuse satellite communications systems utilize either orthogonal linear or circular polarization states. The orthogonal linear polarization (LP) states are normally referred to as vertical and horizontal, but except for Earth stations at the satellite's longitude, the polarization directions are rotated somewhat from the local vertical and horizontal references. The orthogonal circular states are left-hand and right-hand circular polarization (LHCP, RHCP), differing in the sense of rotation of the electric field vector. The "handedness" is defined as follows: a wave is RHCP if the sense of rotation of the field corresponds to the natural curl of the fingers of the right hand when the right thumb is pointed along the propagation direction. Likewise for LHCP. Thus a RHCP wave coming out of the paper would have an electric field rotating counterclockwise.

A measure of the degree of interference between the two orthogonally-polarized channels is the crosspolarization discrimination (denoted XPD), defined as follows: Let E_{ij} be the magnitude of the electric field at the receiver that is transmitted in polarization state i and received in the orthogonal polarization state j (i,j=1,2). E_{11} and E_{22} denote the copolarized waves E_{12} and E_{21} refer to the crosspolarized waves. This is illustrated in Figure 4.1-1. XPD is the ratio (in dB) of the power in the copolarized wave to the power in the crosspolarized wave that was transmitted in the same polarization state.

$$XPD = 20 \log \frac{E_{11}}{E_{12}} \tag{4.1-1}$$

If state "1" is RHCP and "2" is LHCP, for example, then the XPD is the ratio of the RHCP power to the LHCP power, given that only a RHCP wave was transmitted.

A closely related measure is the crosspolarization isolation (XPI), which compares the copolarized received power with the crosspolarized power that is received in the same polarization state:

$$XPI = 20 \log \frac{E_{11}}{E_{21}} \tag{4.1-2}$$

Again letting the states "1" and "2" refer to RHCP and LHCP, the XPI compares the power in the RHCP received wave that was transmitted as RHCP to the power that was transmitted as LHCP. XPI is the parameter that is most meaningful to system engineers, since it directly gives the carrier-to-interference ratio in

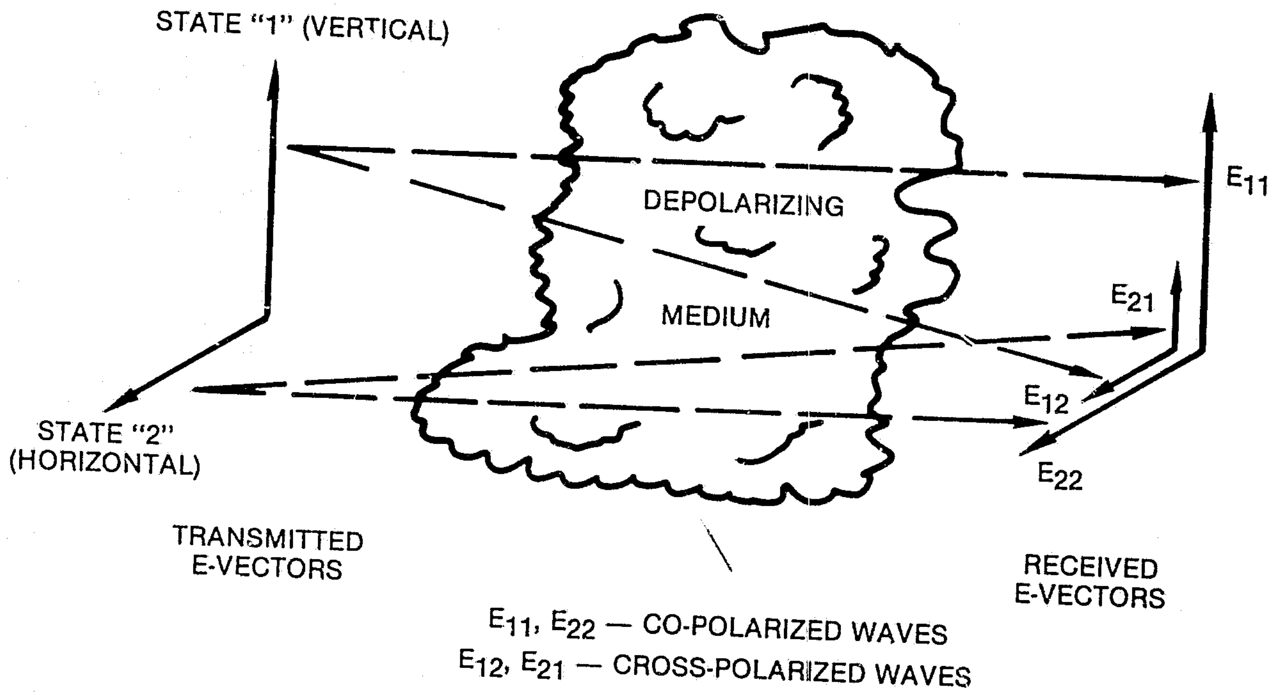

Figure 4.1-1. Definition of Co- and Crosspolarization

a received channel. However, XPD is the parameter that is most easily measured. It has been shown (Watson and Arbabi-1973) that XPI and XPD are the same if the hydrometeors responsible for the depolarization have certain symmetry properties. The geometric models that have been used for raindrops and ice crystals have the necessary symmetry, so XPI = XPD in theory. In practice, it has been found that there is not a significant difference between XPI and XPD.

Another term used to describe depolarization, cross polarization ratio (CPR), is the reciprocal of XPD. Other parameters in use, e.g., crosstalk discrimination, crosspolarization distortion, depolarization ratio, crosspolarization level, usually reduce to XPD or XPI.

In the discussion that follows, it is often important to distinguish between polarization properties of a wave in space, and the parameters that we actually measure at the output of the receiver. We shall use XPD to describe the wave properties and a different term, Isolation (I) (after Stutzman-1977) to describe the receiver output. In general,

$$I = \frac{\text{copolarized channel output power}}{\text{crosspolarized channel output power}}$$

Isolation takes into account the performance of the receiver antenna, feed, and other components as well as the propagating medium. When this performance is close to ideal, and/or the XPD of the wave is low (i.e. severe depolarization), then I=XPD. This will be discussed in more detail later.

4.1.2 Hydrometeor Sources of Depolarization

The major sources of depolarization on Earth-space paths are hydrometeors, ionospheric Faraday rotation, and multipath. The predominant source at millimeter wave frequencies is hydrometeors, and rain is the hydrometeor species that has the greatest effect.

4.1.2.1 Rain. To determine the attenuation due to rain, the raindrops are modelled as spheres of water suspended in space. Real raindrops are falling at their terminal velocity and, due to the complex aerodynamic and hydrostatic forces acting on them, they are in general not spherical. The very small drops (≤ 0.03 cm in diameter) are very nearly spherical, drops in the range of about 0.03 to 0.10 cm in diameter can be considered oblate spheroids, and drops with diameters larger than about 0.10 cm are asymmetric blobs with flat or concave bottoms (Pruppacher and Pitter-1971). Depolarization occurs because of this lack of spherical symmetry, along with the tendency for the drops to have a preferred orientation (i.e., top and bottom flattened). The effects of the rain-filled medium on a wave propagating through it are dependent on the orientation of the electric field vector with respect to the preferred drop orientation.

It is easy to picture the effect of the "flattened" raindrops on linearly polarized (LP) waves propagating horizontally: The fields of horizontal LP waves encounter more water, on the average, than do vertical LP wave fields, and so are subjected to more attenuation and phase shift. An LP wave at some arbitrary orientation, say 45° from the vertical, can be resolved into an equivalent set of component waves having horizontal and vertical polarization. After passing through the rain, the horizontal component has suffered a greater decreased in amplitude, so the polarization direction has been shifted toward the vertical. In addition, the differential phase shift between the components has caused the wave to become slightly elliptically polarized. These depolarizing effects of rain are described more rigorously later.

4.1.2.2 Ice Crystals. Most of the depolarizing effect of rain is produced by differential attenuation. Therefore rain depolarization and attenuation are fairly well correlated. Starting in 1975, when ATS-6 propagation experiments were well underway in Europe, researchers were surprised to see occasions of severe depolarization that were completely uncorrelated with rain attenuation. The cause of this "anomalous" depolarization has since been identified as oriented ice crystals. Ice can occur at altitudes above the freezing level in cirrus clouds and at the tops of cumulonimbus clouds. When something causes the ice crystal symmetry axes to align themselves, it brings on a polarization-selective phase effect. We are now fairly certain that the electrostatic fields associated with electrically-active storms are at least one aligning force. This is consistent with the observed abrupt changes in XPD coincident with lightning flashes.

Ice depolarization has been theoretically modelled in a manner analogous to rain depolarization. For that purpose, the ice crystals are assumed to be either oblate or prolate ellipsoids, corresponding respectively to "plates" and "needles," which are two distinct types of crystals that are known to exist in clouds. The model is in good agreement with observations and explains the rapid changes in the phase of the crosspolarized waves that accompany lightning flashes.

4.1.2.3 <u>Snow, Graupel and Hail.</u> The anisotropy that is responsible for depolarization by rain and high-altitude ice crystals apparently also exists in snow. From S-band and Ku-band radar measurements, Hendry, et. al. (1976) have observed significant differential phase shifts between the right-and left-hand CP radar returns in moderate to heavy snowi The differential phase shift along the propagation path was found to vary between 0.16° and 1.17° per km at 16.5 GHz, values comparable to that of moderate rainfall. Unlike rain, however, snow produces very little differential attenuation. The differential phase shift in snow should produce measureable depolarization on Earth-space paths, but little or no direct experimental evidence of this has been reported.

Graupel, or snow pellets, may also exhibit some anisotropy, and resulting depolarization. Hail particles, which have a rough spherical symmetry, probably would not cause depolarization. (McCormick and Hendry-1977).

4.2 MATHEMATICAL FORMULATIONS FOR DEPOLARIZATION

This section presents the mathematical background required to discuss the effects of the propagation medium characteristics and antenna performance on signals in dual polarization Earth-space links. It should enable the system designer to properly interpret experimental data and assess system performance, considering both the medium's depolarizing effects on the wave and the wave's interaction with the antenna system. Most of this development is from Stutzman (1977).

4.2.1 Specifying the Polarization State of a Wave

In the most general case, the tip of the electric field vector of a plane electromagnetic wave traces out an ellipse in the plane perpendicular to the direction of propagation. The polarization state of the wave is given by specifying the shape and orientation of the ellipse, along with the sense of rotation of the field vector. Figure 4.2-1 shows the general polarization ellipse and defines the notation. The electric field vector $\vec{\mathcal{E}}(t)$ is the resultant of sinusoidal components $\mathcal{E}_x(t)$ and $\mathcal{E}_y(t)$ which have different amplitudes E_1 and E_2 and a phase difference δ:

$$\begin{aligned}\vec{\mathcal{E}}(t) &= \hat{x}\,\mathcal{E}_x(t) + \hat{y}\,\mathcal{E}_y(t) \\ &= \hat{x}\,E_1 \cos\omega t + \hat{y}\,E_2 \cos(\omega t + \delta)\end{aligned} \qquad (4.2\text{-}1)$$

where $\hat{x}$ and $\hat{y}$ are unit vectors in the x and y directions, respectively, ω is the radian frequency, and t is time. The polarization ellipse is fully described by the angle, τ, between the ellipse major axis and the x-axis, and the ratio of the major and minor axes of the ellipse. This ratio is the magnitude of an important parameter known as the axial ratio, and is the ratio of the maximum to the minimum magnitude of the electric field vector. The axial ratio's sign is assigned to be positive if the vector rotation has a

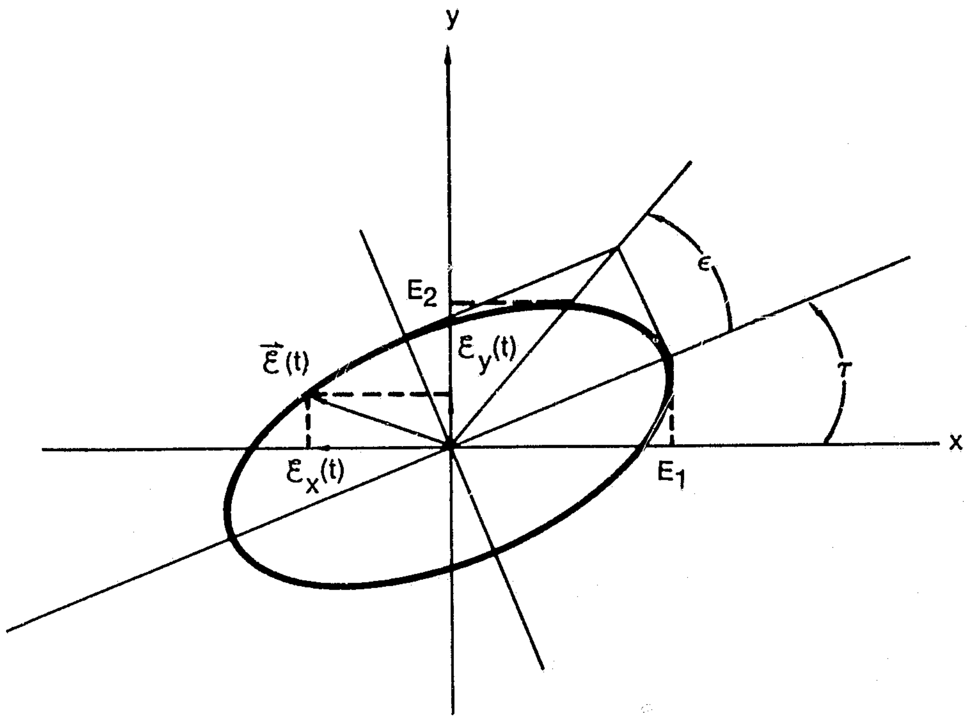

Figure 4.2-1. Polarization Ellipse

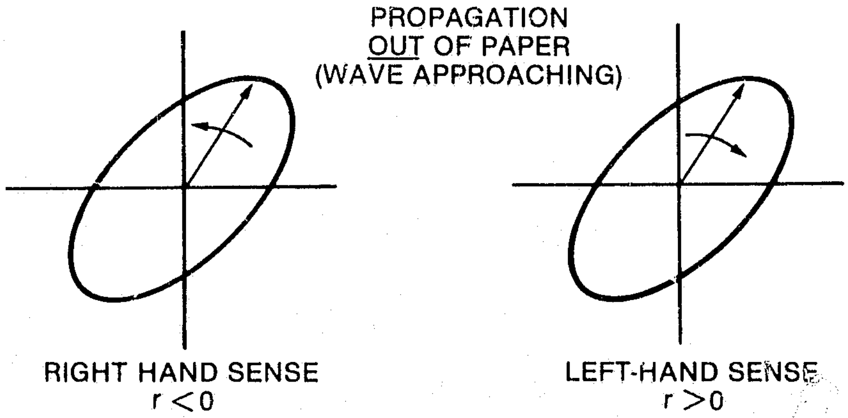

Figure 4.2-2. Definition of Sign of Axial Ratio, r

left-hand sense and negative for rotation with a right-hand sense. (See Figure 4.2-2.) Linearly polarized waves have an infinite axial ratio; circularly polarized waves have an axial ratio $r = \pm 1$, corresponding to LHCP and RHCP respectively.

It is convenient to define another parameter

$$\varepsilon = \cot^{-1} r \; ; -45° \leqslant \varepsilon \leqslant 45° \qquad (4.2\text{-}2)$$

The specifying parameters ε and τ are related to the quantities used to describe the fields earlier by

$$\varepsilon = \frac{1}{2} \sin^{-1}(\sin 2\gamma \sin\delta) \qquad (4.2\text{-}3)$$

$$\tau = \frac{1}{2} \tan^{-1} (\tan 2\gamma \cos\delta) \qquad (4.2\text{-}4)$$

$$\gamma = \tan^{-1} \frac{\text{max y-component of } \vec{\mathcal{E}}}{\text{max x-component of } \vec{\mathcal{E}}} = \tan^{-1} (E_2/E_1) \qquad (4.2\text{-}5)$$

There are other methods used to specify polarization state (Stutzman-1977). The Stokes parameter representation is a matrix formulation. The Poincare sphere is a mapping of polarization states into points on a unit sphere. The complex polarization factor is a single number specifying polarization state. All these various representations are directly relatable to the angles ε and τ, or δ and δ.

4.2.2 Wave-Antenna Interaction

The power available (P_R) at the output of an antenna illuminated by an incident plane wave of flux density S is

$$P_R = S\, A_e m_p \qquad (4.2\text{-}6)$$

where A_e is the effective aperture of the antenna in the direction of the incident wave, and m_p is the polarization mismatch factor. This factor is a real number between zero and one that depends on the degree of match of the polarization state of the wave and the antenna. The polarization state of a receiving antenna is defined as the state of the wave that the same antenna would transmit, but with time reversed. (A time-reversal changes the direction of propagation of a wave but retains the sense of rotation and axial ratio.) A RHCP incident wave, for example, is perfectly matched to a RHCP antenna. This means the antenna absorbs the maximum amount of power from the wave, and $m_p = 1$. A RHCP antenna absorbs no power from a LHCP wave, and $m_p = 0$. The general expression m_p, assuming arbitrary elliptical polarization states of both the antenna and the wave, is

$$m_p(w,a) = \frac{1}{2} + \frac{4r_w r_a + (r_w^2-1)(r_a^2-1)\cos 2(\tau_a-\tau_w)}{2(r_w^2+1)(r_a^2+1)} \qquad (4.2\text{-}7)$$

where r_a = axial ratio of antenna

r_w = axial ratio of wave

τ_a = major axis angle of antenna

τ_w = major axis angle of wave

We consider some examples to confirm that (4.2-7) is plausible:

Antenna RHCP, Wave LHCP

$r_a = -1,\ r_w = +1$

$$m_p = 1/2 + \frac{4(1)(-1) = (1-1)(1-1)}{2(1=1)(1-1)} = 1/2 - 1/2 = 0$$

Antenna LP, Wave CP

$$r_a = \infty , r_W = 1$$

By dividing the numerator anJ denominator of the second term of (4.2-7) by r_a^2, then taking the limit as $r \to \infty$, we find that $m_p = 1/2$, which is intuitively agreeable.

Antenna LP, Wave LP

$$r_a = r_W = \infty$$

Here we divide the numerator and denominator by $r_a^2 r_W^2$ and pass to the limit, giving

$$m_p = 1/2 + 1/2 \cos 2(\tau_a - \tau_w) = \cos^2(\tau_a - \tau_w) \qquad (4.2\text{-}8)$$

This equals one when the orientation of the linear polarization axes of the antenna and wave are aligned ($\tau_a = \tau_W$), and equals zero when the axes are orthogonal ($\tau_a - \tau_W = \pm 90^0$)

Antenna LP, Wave Elliptically Polarized

$$r_a = \infty \qquad r_W = r$$

Dividing through by r_a and taking the limit as before, we obtain

$$m_p = 1/2 + \frac{1/2\,(r^2-1)\cos 2(\tau_a - \tau_w)}{2(r^2+1)} \qquad (4\text{-}2.9)$$

Figure 4.2-3 is a polar plot of m_p versus the angle difference $\tau_a - \tau_W$, for r=1.5 and 2.

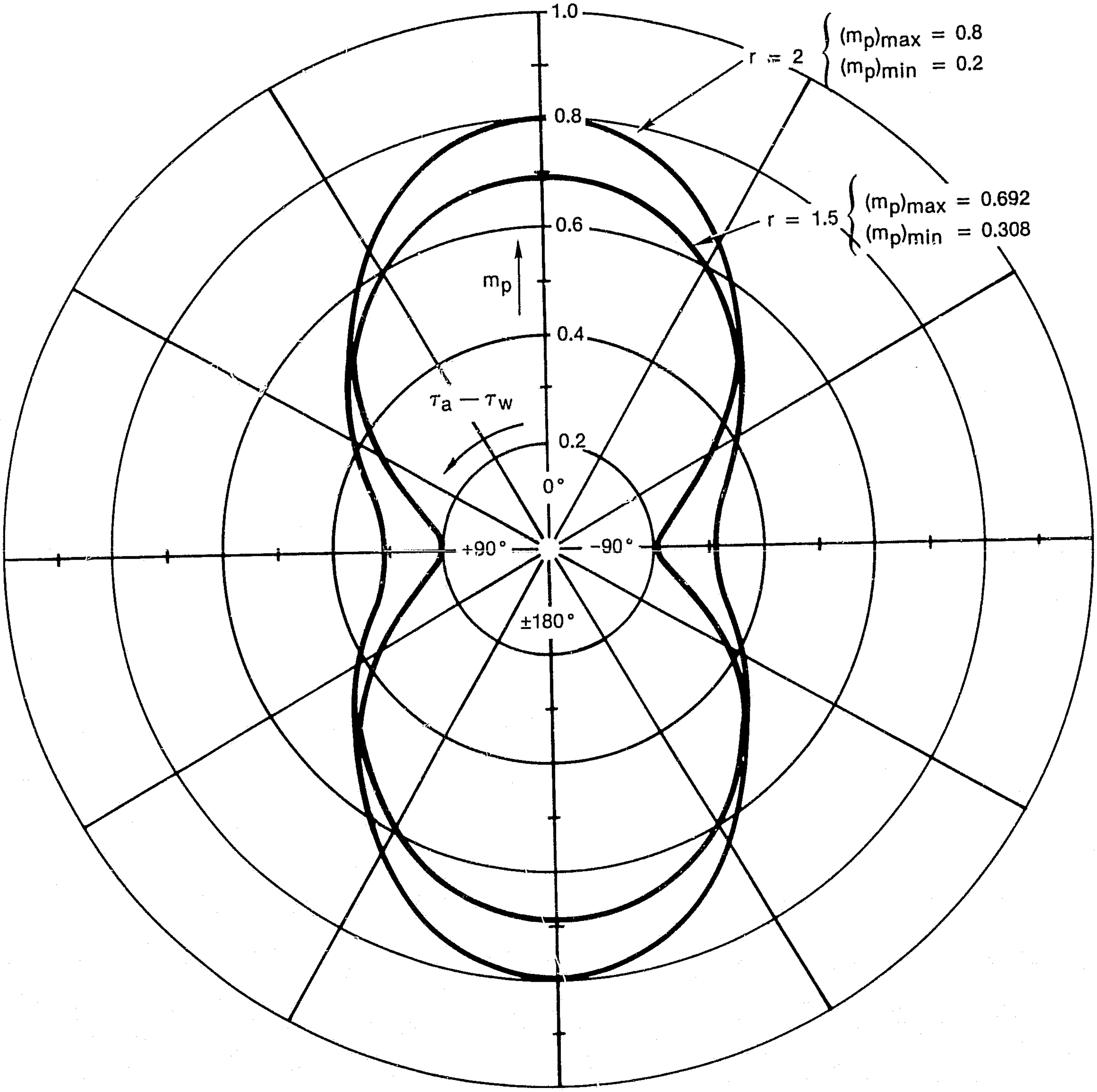

Figure 4.2-3. Polarization Mismatch Factor m_p for LP Antenna and Elliptically Polarized Waves

Letting

$$(m_p)_{max} = m_p \text{ for } \tau_a = \tau_w \text{ (aligned)}$$

$$(m_p)_{min} = m_p \text{ for } \tau_a = \tau_w + 90^0 \text{ (orthogonal)}$$

Some algebra yields

$$r = \left[\frac{(m_p)_{max}}{(m_p)_{min}}\right]^{1/2} \qquad (4.2\text{-}10)$$

This is confirmed in Figure 4.2-3.

This formula suggests a technique for measuring the axial ratio and principal axis orientation of a received wave: The power received by a linearly polarized antenna (e.g., a dipole) is measured as the antenna axis is rotated through 180^0 The ratio of the maximum to the minimum received power is then the square of the axial ratio of the wave, and the orientation of the wave's principal axis is just the antenna's orientation when maximum power is measured.

4.2.3 Cross Polarization Discrimination (XPD)

Having defined the polarization mismatch factor, we now present a more useful definition of XPD than that given earlier. Orthogonal polarization states are defined, in general, to have axial ratios that are equal in magnitude and opposite in sign (i.e., opposite in rotation sense), and have polarization ellipses with spatially orthogonal axes. Vertical/horizontal LP, and RHCP/LHCP are common examples of orthogonal states. The polarization mismatch factor for a wave with a given polarization state incident on an antenna that is matched to the orthogonal state is zero.

It is always possible to decompose a wave into two components with orthogonal polarization states. An arbitrary wave can be considered as being composed of a component with a polarization state matching the antenna, and a second component with the orthogonal state. The antenna extracts maximum power from the matched component, but completely rejects the orthogonal component. The polarization mismatch factor is then seen to be the proportion of the total flux density impinging on the antenna that is being carried by the polarization-matched wave component. Denoting the received wave's polarization state by the index w', and the antenna's polarization state by w, the antenna output power is

$$P = SA_e m_p(w',w) \qquad (4.2\text{-}11)$$

A second antenna with equal effective aperture A_e but with a polarization state w_o, that is exactly orthogonal to w, gives an output power

$$P_o = SA_e m_p(w',w_o) \qquad (4.2\text{-}12)$$

The XPD is the ratio of the orthogonal components of the wave,

$$XPD = 10 \log [m_p(w',w)/m_p(w',w_o)] \qquad (4.2\text{-}13)$$

assuming that the "w" polarization state is the one the system is designed to maximize, or the copolarized state. The "w_o" state is designated as crosspolarized.

Suppose a LP wave is received, and the copolarized state (w) is designated as horizonally polarized. Let $\tau = \tau_{w'}$ = the angle of the received wave with respect to horizonal. For this case,

$$m_p(w',w) = \cos^2\tau \qquad (4.2\text{-}14)$$

$$m_p(w',w_p) = \sin \tau \quad (4.2\text{-}15)$$

$$XPD = 10 \log (\cot^2 \tau) \quad (4.2\text{-}16)$$

Assume an elliptically polarized wave is received with axial ratio $r_{w'} = r$, and copolar is designated as LHCP. For this case,

$$r_w = +1, \; r_{w_0} = -1 \quad (4.2\text{-}17)$$

$$m_p(w',w) = (1/2) \frac{(r+1)^2}{r^2+1} \quad (4.2\text{-}18)$$

$$m_p (w',w_o) = (1/2) \frac{(r-1)^2}{r^2+1} \quad (4.2\text{-}19)$$

$$XPD = 20 \log [(r+1)/(r-1)] \quad (4.2\text{-}20)$$

XPD is plotted versus r for the elliptically polarized case in Figure 4.2-4. An alternate "axial ratio," AR_{dB}, is shown in the figure. This is commonly used and is related to r by

$$AR_{dB} = 20 \log |r| \quad (4.2\text{-}21)$$

In terms of this parameter, XPD is closely approximated by

$$XPD \approx 24.8 - 20 \log (AR_{dB}) \;, \text{ for } AR_{dB} < 10 \text{ dB} \quad (4.2\text{-}22)$$

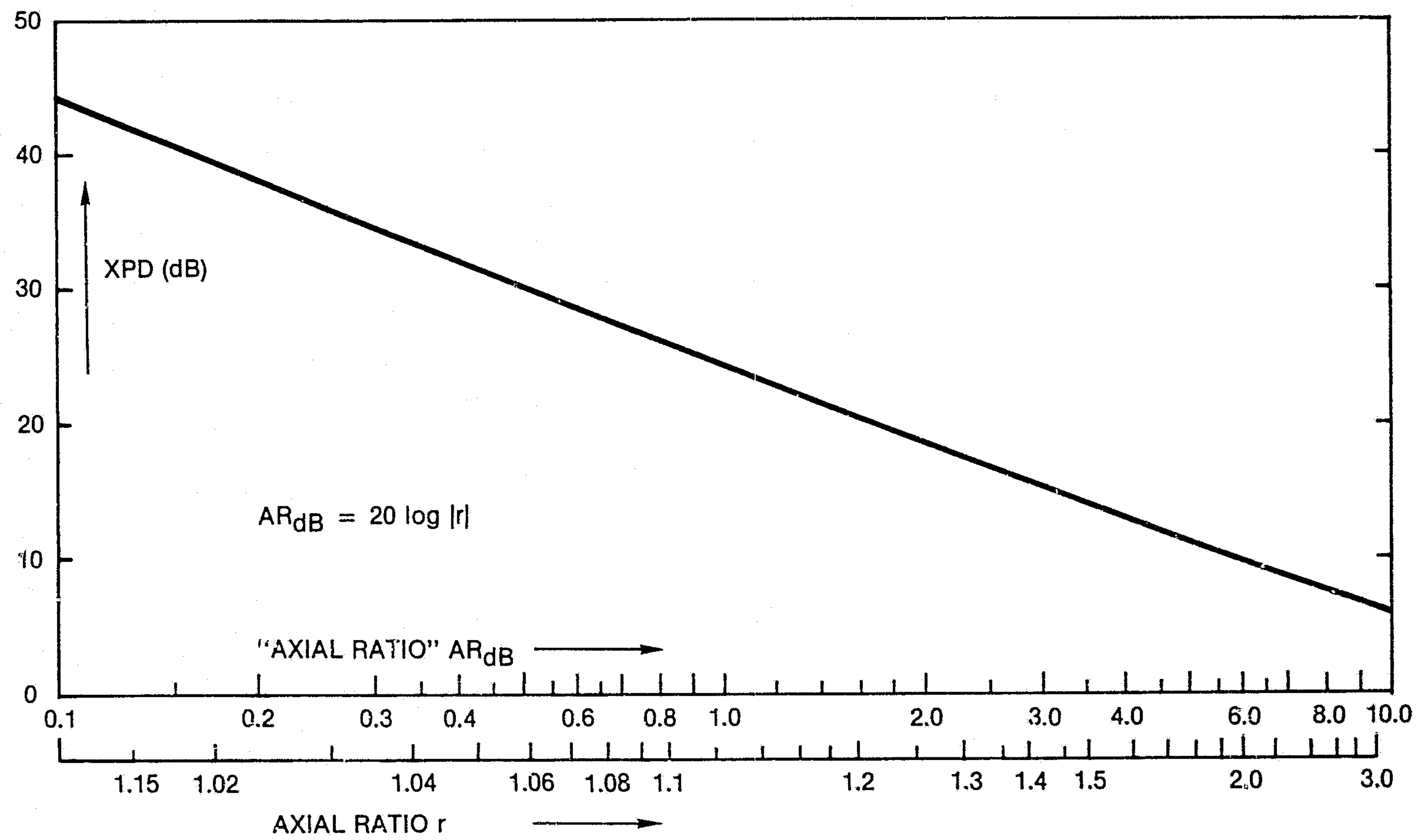

Figure 4.2-4. XPD vs. Axial Ratio of Elliptically Polarized Wave (LHCP is Copolarized.)

4.2.4 Effect of Non-Ideal Antenna Performance

The XPD describes the polarization characteristics of a received wave with respect to some "copolarized" reference. The true XPD could be measured with an ideal antenna, capable of being matched exactly to the co- and cross polarized state. Actual antennas are not ideal. They can be built with outputs that closely approximate the copolarized and crosspolarized components of the wave, but some degree of degradation is always present in their performance. Here we present a method of quantifying the polarization performance of the antenna and taking this performance into account in interpreting polarization measurements.

From this point on, the receive antenna polarization states that are close to the true co- and crosspolarized wave states will be distinguished from the true states by putting their names within quotation marks.

Isolation, I, is defined as the ratio of the output power available at the antenna's "copolarized" port (P_c) to the output power at the "crosspolarized" port (P_x). The polarization states coupled to the "copolarized" and "crosspolarized" ports are a_c and a_x, respectively. Since the antenna is non-ideal, a_c and a_x are not necessarily orthogonal, and a_c does not necessarily correspond to the pure copolarized state. Denoting the state of the received wave as w' and the wave's power flux density as $S_{w'}$, we have from (4.2-11):

$$I = 10 \log \frac{P_c}{P_x} = 10 \log \frac{S_{w'} A_e m_p(w', a_c)}{S_{w'} A_e m_p(w', a_x)} \quad (4.2\text{-}23)$$

$$= 10 \log \frac{m_p(w', a_c)}{m_p(w', a_x)}$$

It is useful to be capable of finding XPD in terms of I, which is measurable. The power available at the "copolarized" antenna port can be written in terms of the true copolarized and crosspolarized wave components, w and w_o:

$$P_c = A_e \left[S_w m_p(w,a_c) + S_{w_o} m_p(w_o,a_c)\right] \qquad (4.2\text{-}24)$$

Likewise for the "crosspolarized" power

$$P_x = A_e \left[S_w m_p(w,a_x) + S_{w_o} m_p(w_o,a_x)\right] \qquad (4.2\text{-}25)$$

S_w and S_{w_o} are the power flux density in the true copolarized and crosspolarized states, respectively. Now we have

$$I = 10 \log \frac{S_w m_p(w,a_c) + S_{w_o} m_p(w_o,a_c)}{S_w m_p(w,a_x) + S_{w_o} m_p(w_o,a_x)}$$

$$= 10 \log \frac{(xpd) m_p(w,a_c) + m_p(w_o,a_c)}{(xpd) m_p(w,a_x) + m_p(w_o,a_x)} \qquad (4.2\text{-}26)$$

where $\qquad xpd = S_w/S_{w_o} = \log^{-1} (XPD/10)$

Since the "copolarized" state of the antenna is assumed to be well-matched to the true copolarized wave component,

$$m_p(w_o,a_c) \ll m_p(w,a_c)$$

So this term is negligible and

$$I = 10 \log \frac{m_p(w,a_c)}{m_p(w,a_x) + m_p(w_o,a_x)/(xpd)} \qquad (4.2\text{-}27)$$

Note that when the antenna is nearly ideal,

$$m_p(w,a_c) \approx 1, \; m_p(w_o,a_x) \approx 1, \; m_p(w,a_x) \approx 0$$

and so $I \approx$ XPD. On the other hand, when the XPD is very high,

$$I \approx 10 \log \left[m_p(w,a_c)/m_p(w,a_x)\right] \qquad (4.2\text{-}28)$$

which is a function of the antenna only. This implies that a given antenna can be used to measure XPD to a given accuracy up to a certain maximum XPD value which is determined by the attenna performance parameters.

For the CP case, the equation for I becomes

$$I = 10 \log \frac{\frac{1}{2} + \frac{r_c}{r_c^2 + 1}}{\frac{1}{2}(xpd^{-1}+1) + \frac{r_x}{r_x^2 + 1}(xpd^{-1}-1)} \qquad (4.2\text{-}29)$$

where r_c and r_x are the axial ratios of the antenna's "copolarized" and "crosspolarized" states, respectively. Figure 4.2-5 shows I versus XPD for various values of axial ratio AR_{dB}. The "copolarized" and "crosspolarized" axial ratios are made equal in the figures, but I is actually nearly independent of r_x. The figure gives the amount of error to be expected when measuring XPD.

For the LP case, we obtain

$$I = 10 \log \frac{1 + Q_c \cos 2\tau_c}{(1+xpd^{-1}) - (1-xpd^{-1})\, Q_x \cos 2(\tau_x - 90°)} \qquad (4.2\text{-}30)$$

where $\quad Q_{c,x} = (r_{c,x}^2 - 1)/(r_{c,x}^2 + 1)$

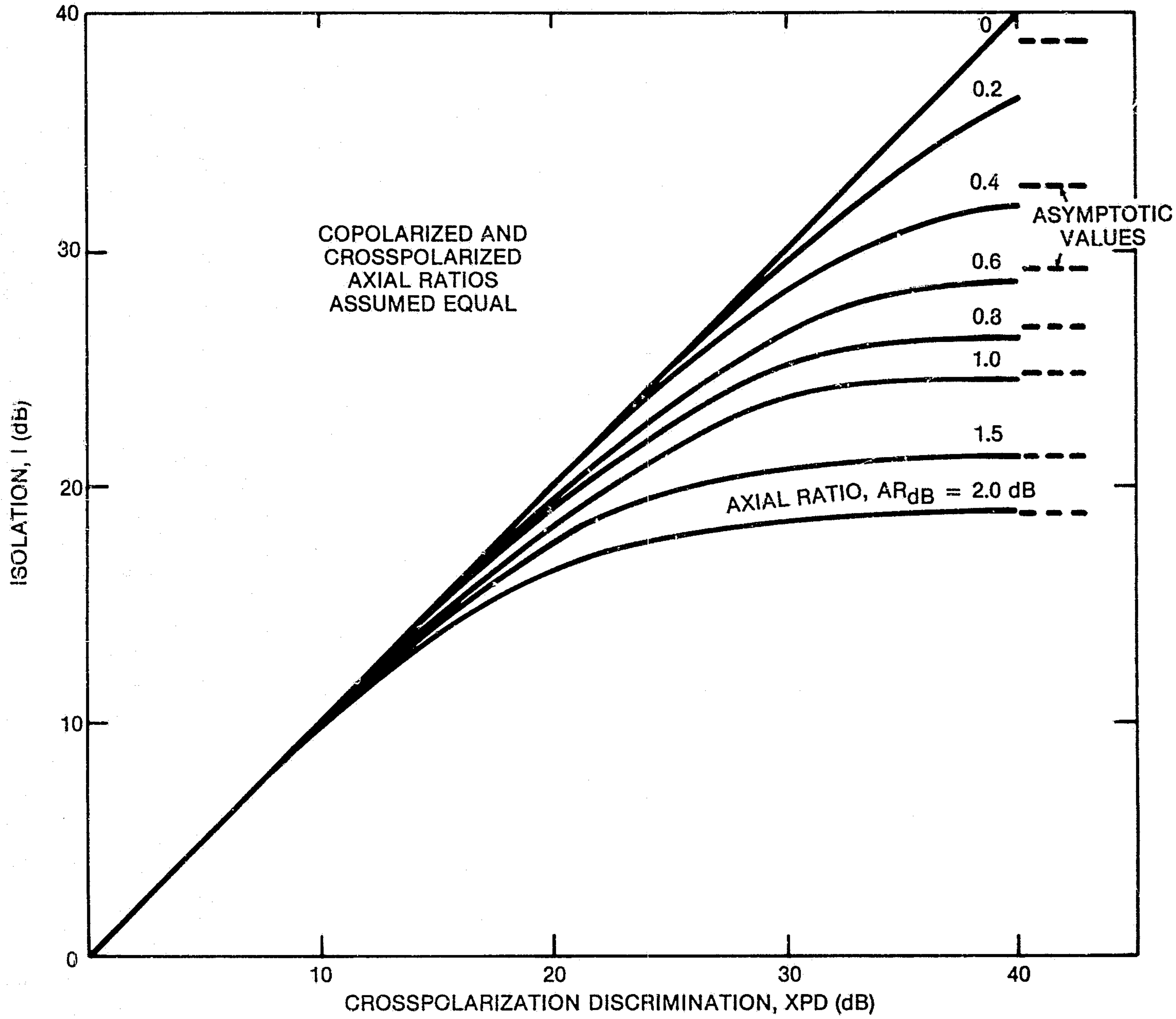

Figure 4.2-5. Isolation vs. XPD and Antenna Axial Ratio - <u>Circular</u> Polarized Case

where $$Q_{c,x} = \frac{r_{c,x}^2 - 1}{r_{c,x}^2 + 1}$$

$\tau_{c,x}$ = antenna "copolarized", "cross polarized" axis orientation angle

$r_{c,x}$ = antenna "copolarized", "crosspolarized" axial ratio

The copolarized wave axis is taken as the reference for the antenna axis orientation angles. Figures 4.2-6 and 4.2-7 show I versus XPD for various antenna axial ratios and axis misalignment angles. The first figure is for perfect axis alignment and varying axial ratio. As with the CP case, equal axial ratios for the "copolarized" and "crosspolarized" states were assumed, but isolation is practically independent of the "copolarized" axial ratio, r_c, when it is large (>20dB). Figure 4.2-7 shows the effect of axis misalignment for the AR_{dB}=30dB case. The antenna axes are assumed orthogonal, with $\tau_x = \tau_c - 90^o$, but the isolation is not strongly dependent on τ_c for $\tau_c < 10^o$.

4.3 RAIN DEPOLARIZATION

4.3.1 Theory of Rain Depolarization

Rain depolarization can be modelled using the same techniques applied to rain attenuation. The essential difference is that in examining depolarization, the raindrops are assumed to be oblate spheroids. The attenuation analysis assumed that the raindrops were spherical. Figure 4.3-1 shows the geometry for a dual LP wave incident on an oblate spheroidal raindrop. The raindrop is at an arbitrary orientation with respect to the direction of propagation of the wave. The orientation is specified by the angle α, between the propagation vector and the raindrops symmetry axis. The plane containing α will be referred to as the plane of incidence.

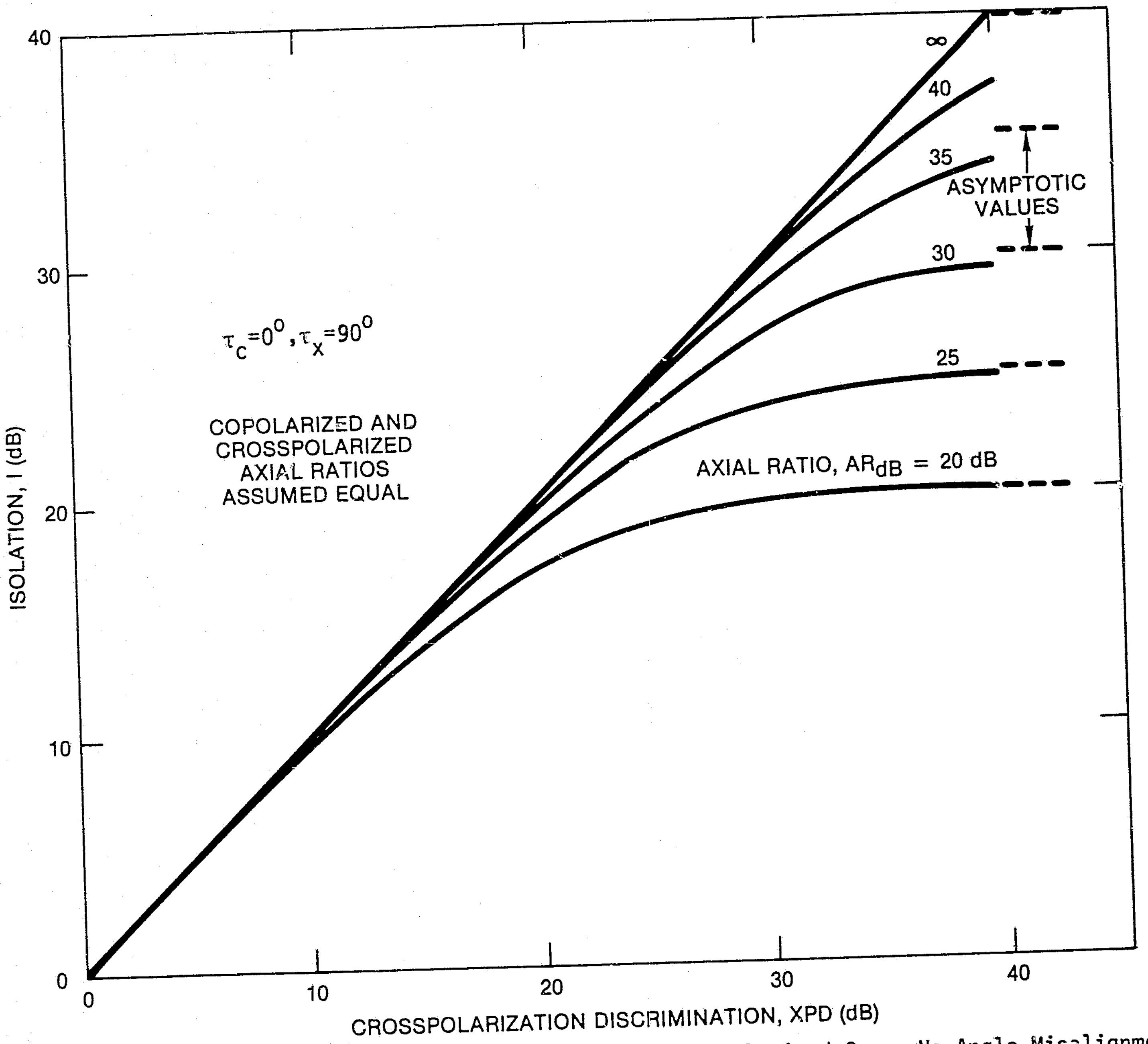

Figure 4.2-6. Isolation vs. XPD and Antenna Axial Ratio - Linear Polarized Case, No Angle Misalignment

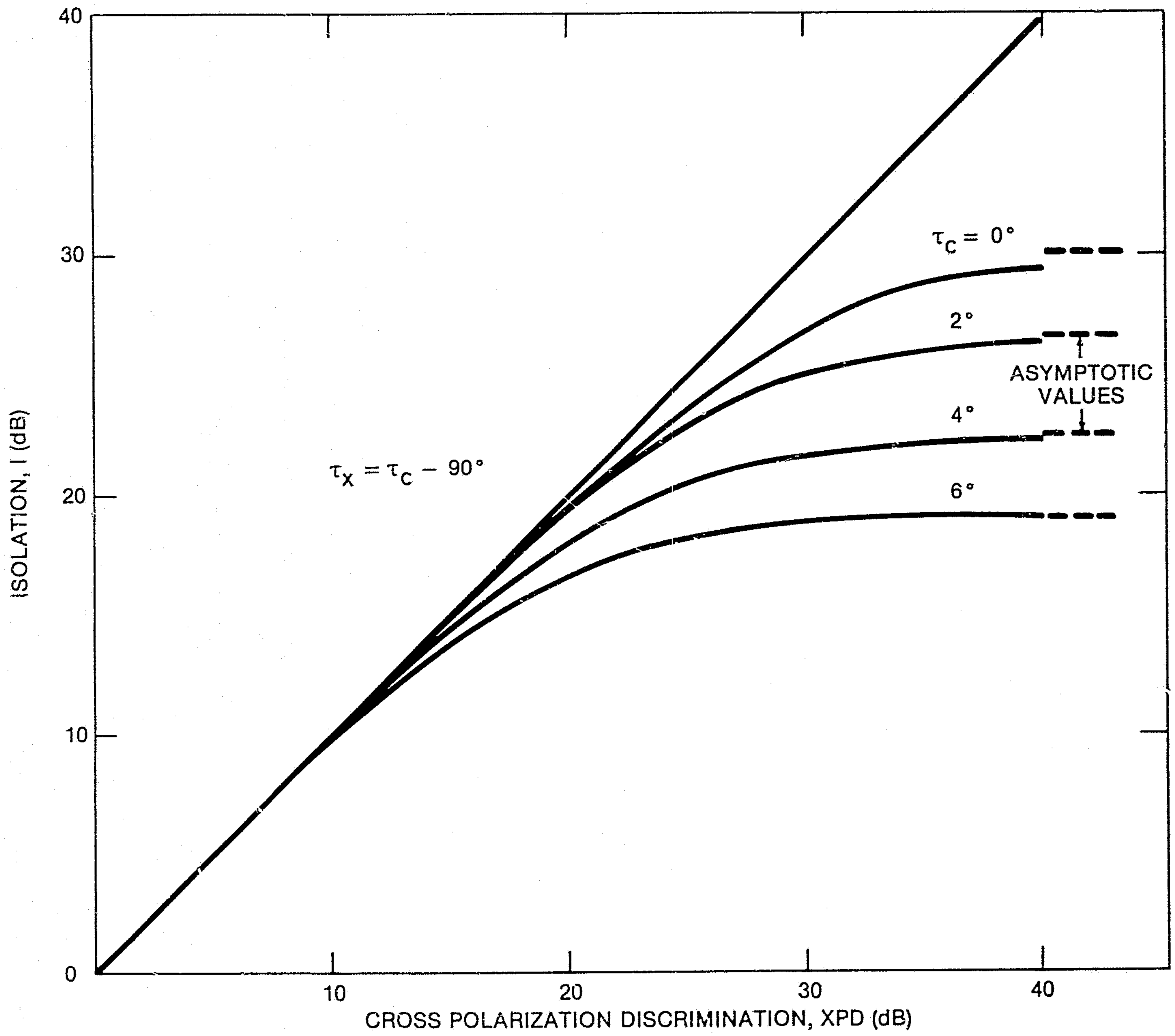

Figure 4.2-7. Isolation vs. XPD and Major Axis Misalignment - Linear Polarized Case, Axial Ratio, AR_{dB}=30 dB

E_x and E_y are electric field vectors of two orthogonal LP waves. They are in a plane normal to the propagation vector, and each one can be resolved into two components: a component in the plane of incidence, and a component normal to it. Parallel to these components, we define two symmetry axes, labeled I and II in the figure. The projection of the raindrop into the plane containing the electric field vectors is an ellipse, and axes I and II are its minor and major axes, respectively. Figure 4.3-2 shows this ellipse and how the electric fields are resolved into their "I" and "II" components.

The total electric field magnitudes in the I and II directions (E_I and E_{II}) are given by

$$\begin{bmatrix} E_I \\ E_{II} \end{bmatrix} = \begin{bmatrix} \cos\theta & -\sin\theta \\ \sin\theta & \cos\theta \end{bmatrix} \begin{bmatrix} E_x \\ E_y \end{bmatrix} = R \begin{bmatrix} E_x \\ E_y \end{bmatrix} \qquad (4.3\text{-}1)$$

where Θ, the canting angle, is the angle between the x and I axes.

Now consider a region of space containing many identical raindrops with the same orientation distributed throughout it. According to scattering theory, the effect of many scatterers along the propagation path of a wave is to multiply the electric field vector by a transmission coefficient of the form

$$T = \exp\left[-(a-j\phi)L\right] \qquad (4.3\text{-}2)$$

where L is the path length through the scattering region. The a term of the exponent produces attenuation of the wave, and ϕ produces a phase lag. This phase lag is in addition to the normal free-space phase retardation of the fields. Instead of a and ϕ , which have units of nepers per unit length and radians per unit length, respectively, the more useful parameters, A and Φ, are normally used:

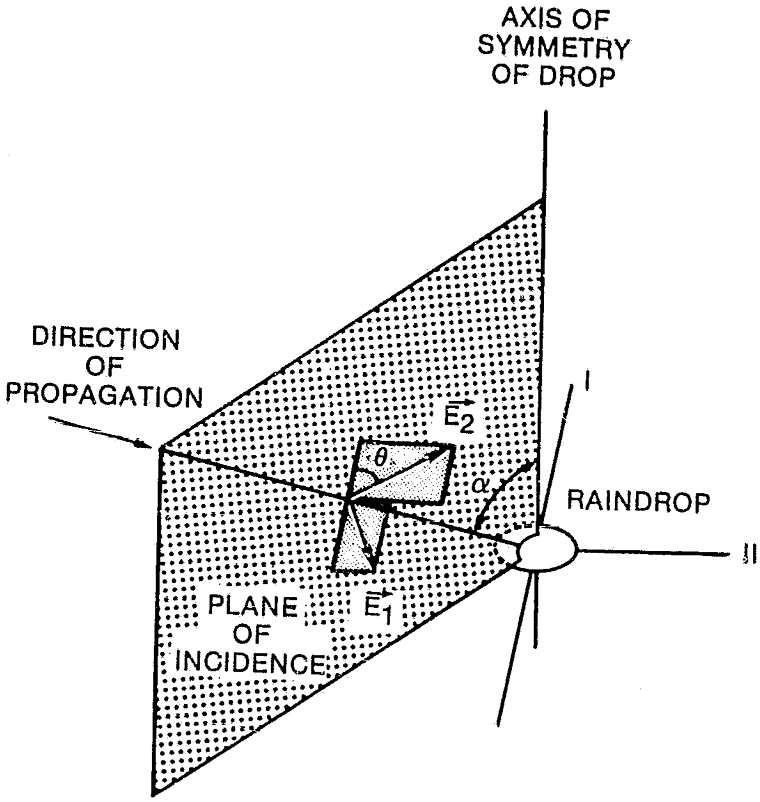

Figure 4.3-1. Geometry for Rain Depolarization Analysis

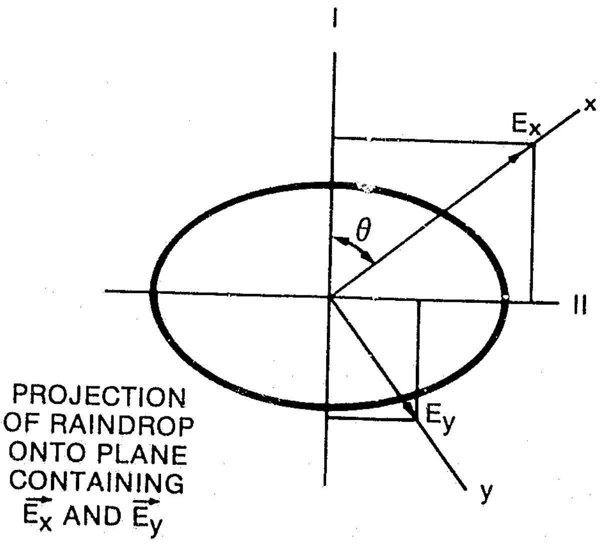

Figure 4.3-2. Resolution of Electric Fields into I and II Components

A = specific attenuation of power flux density of wave, in dB/km.

$= 20(\log_{10}e)a = 8.686\ a$

Φ = specific phase lag of wave, in degrees/km.

$= (180/\pi)\ \phi$

A region filled with oblate spheriodal raindrops must be characterized by two transmission coefficients: T_I, applied to the "I" component of the electric field, and T_{II}, applied to the "II" component. Denoting the fields of the wave incident on the scattering region by a subscript i, and the fields of the wave exiting the region by s (for scattered), we can write

$$\begin{bmatrix} E_{Is} \\ E_{IIs} \end{bmatrix} = \begin{bmatrix} T_I & O \\ O & T_{II} \end{bmatrix} \begin{bmatrix} E_{Ii} \\ E_{IIi} \end{bmatrix} = T \begin{bmatrix} E_{Ii} \\ E_{IIi} \end{bmatrix} \qquad (4.3\text{-}3)$$

Now the coordinate rotation R, defined above, can be applied to get an equation for the effect of the scattering region on the field vectors in the x and y directions.

$$\begin{bmatrix} E_{xs} \\ E_{ys} \end{bmatrix} = R^{-1}\, T\, R \begin{bmatrix} E_{xi} \\ E_{yi} \end{bmatrix} = T' \begin{bmatrix} E_{xi} \\ E_{yi} \end{bmatrix} \qquad (4.3\text{-}4)$$

Figure 4.3-3 shows how the three component transformations are successively applied to produce T'. The overall transformation matrix T' can be evaluated to yield

$$T' = \begin{bmatrix} t_{xx} & t_{xy} \\ t_{yx} & t_{yy} \end{bmatrix}$$

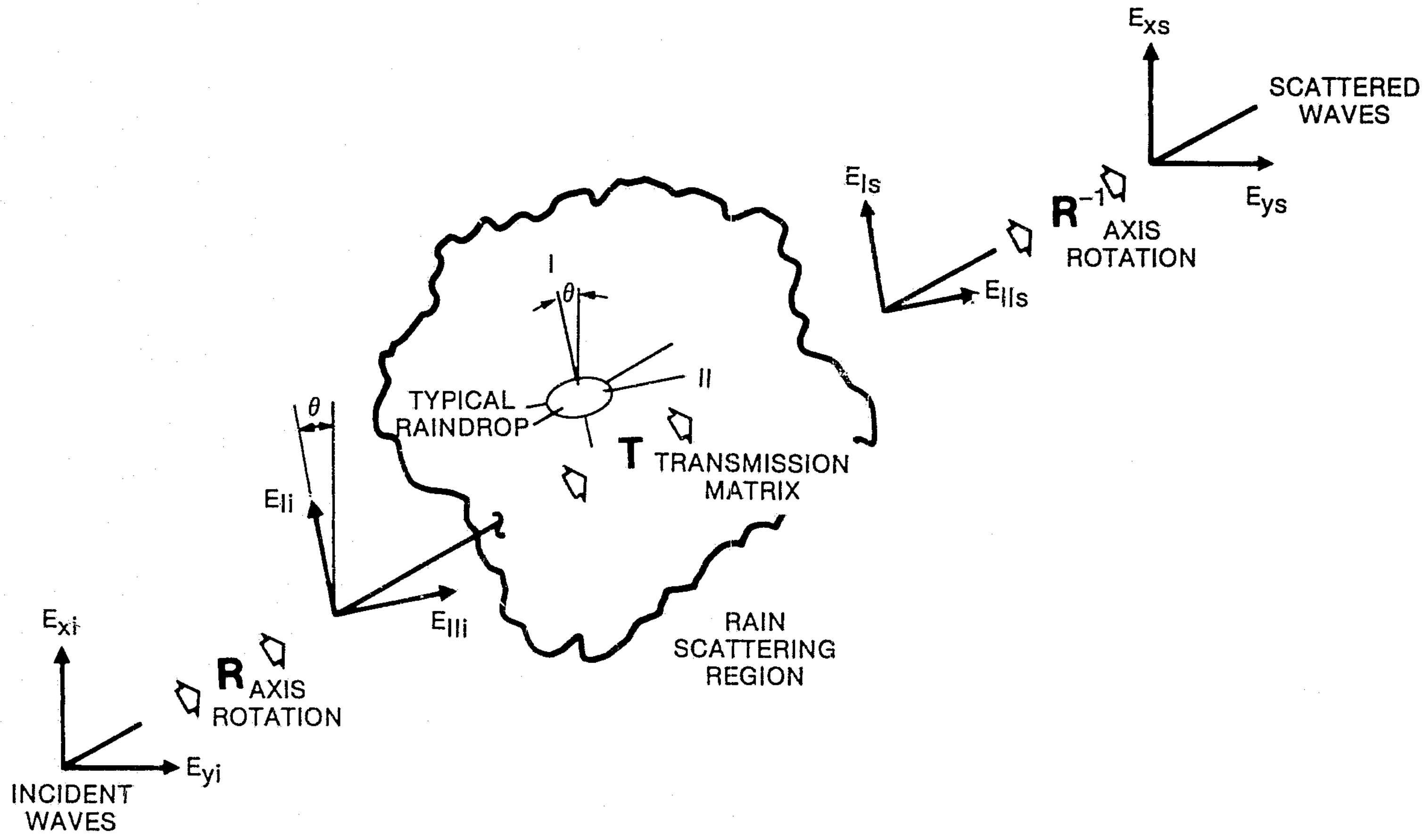

Figure 4.3-3. Components of Overall Transformation Matrix T Describing Rain Depolarization

$$t_{xx} = T_I \cos^2\theta + T_{II} \sin^2\theta \qquad (4.3\text{-}5)$$

$$t_{yy} = T_I \sin^2\theta + T_{II} \cos^2\theta$$

$$t_{xy} = t_{yx} = \frac{1}{2}(T_{II} - T_I) \sin^2\theta$$

Chu (1974) gives expressions for these paramters in terms of the As and Φs.

Calling the LP wave polarized in the x direction the copolarized wave, we can now obtain expressions for the XPD:

$$XPD_x = 10 \log \frac{|E_{xs}|^2}{|E_{ys}|^2} \quad \text{with } E_{yi} = 0$$

$$= 10 \log \frac{|t_{xx}|^2}{|t_{yx}|^2} \qquad (4.3\text{-}6)$$

$$= 20 \log \frac{1 + \gamma \tan^2\theta}{(\gamma - 1) \tan\theta}$$

where

$$\gamma = T_{II}/T_I = \exp\left[-(a_{II} - a_I)L + j(\phi_{II} - \phi_I)L\right]$$

Or, calling the *y*- direction the copolarized state,

$$XPD_y = 10 \log \frac{|E_{ys}|^2}{|E_{xs}|^2} \quad \text{with } E_{xi} = 0$$

$$= 10 \log \frac{|t_{yy}|^2}{|t_{xy}|^2} \qquad (4.3\text{-}7)$$

$$= 20 \log \frac{\gamma + \tan^2\theta}{(\gamma - 1) \tan\theta}$$

For the case of circular polarization' Chu (1974) shows

$$XPD_c = 10 \log (|t_{xx}/t_{yx}|^2)_{\theta=45^\circ} = 20 \log \frac{\gamma + 1}{\gamma - 1} \quad (4.3\text{-}8)$$

which is independent of the sense of rotation of the copolarized wave.

Thus far, we have assumed that all raindrops are of equal size and have the same orientation. The model must account for the distribution of sizes and shapes of raindrops and the distribution of angles θ and α that are present in the rain along the path. Scattering theory allows for this. The scattering effect of a single raindrop is determined as a function of some parameter (like size), then the distribution of that' parameter over the population of raindrops is used in calculating the transmission coefficients. The transmission coefficients (more exactly, the specific attenuations and phase lags, A and Φ) have been calculated in this manner as a function of rain rate by several authors . The first calculations (Oguchi and Hosoya-1974, Chu-1974, Watson and Arbabi-1974) used oblate spheroidal raindrops. The drops were assumed to be distributed according to the well-known Laws and Parsons distribution, and to have eccentricities that were directly related to their sizes, with the largest drops being the most deformed. Later work has considered the more realistic Pruppacher-Pitter (1971) drop shapes (Oguchi-1977). Figure 4.3-4 (from Morrison, et al -1973) is an example of the results of these calculations. These curves give the difference in the specific attenuation and ase between the I and II axes. The angle between the direction of propagation and the raindrop symmetry axis, α , is a parameter, and the canting angle, θ , is set to 25°. The differential attenuation and phase are of most interest because they actually determine XPD. As can be seen from the curves, the worst case for differential attenuation and phase corresponds to $\alpha = 90^\circ$. This agrees with intuition, since the projection ellipse of the drop onto the plane containing the field vectors has the greatest eccentricity for that case. For values of α different from 90^{0}, Chu (1974) shows that the following approximation is quite accurate:

$$A_{\parallel}-A_{\perp} = \sin^2\alpha\,(A_{\parallel}-A_{\perp})_{\alpha=90^\circ}$$

$$\Phi_{\parallel}-\Phi_{\perp} = \sin^2\alpha\,(\Phi_{\parallel}-\Phi_{\perp})_{\alpha=90^\circ} \qquad (4.3\text{-}9)$$

Accounting for the distribution of α and θ is more difficult than doing so for drop size and shape. We have little information about the distribution of the orientation of raindrops. It is expected that wind and wind gusts produce an appreciable spatial correlation in the orientation. In the absence of wind, a fairly symmetric distribution about the vertical would be expected.

The α component of drop orientation is usually considered to be equal to a constant 90^{0} for line-of-sight (horizontal) paths and the complement of the elevation angle for satellite (oblique) paths. The effect of α on XPD is apparently so small compared with the canting angle dependence that allowing for a distribution of α is not worthwhile.

The canting angle distribution, as it affects XPD, has been studied extensively. Thomas (1971) presents an experimentally determined canting angle distribution and derives an "average" angle of 15^{0}. He further notes that the crosspolarizing effects of canting angles of positive and negative sense tend to cancel, so the overall effect is proportional to the excess of one sense over the other. Based on some experimental evidence, he chooses 25% as the worst case imbalance of canting angle sense. The predicted worst case XPD, then, is roughly that produced by 25% of the raindrops at a 15^{0} canting

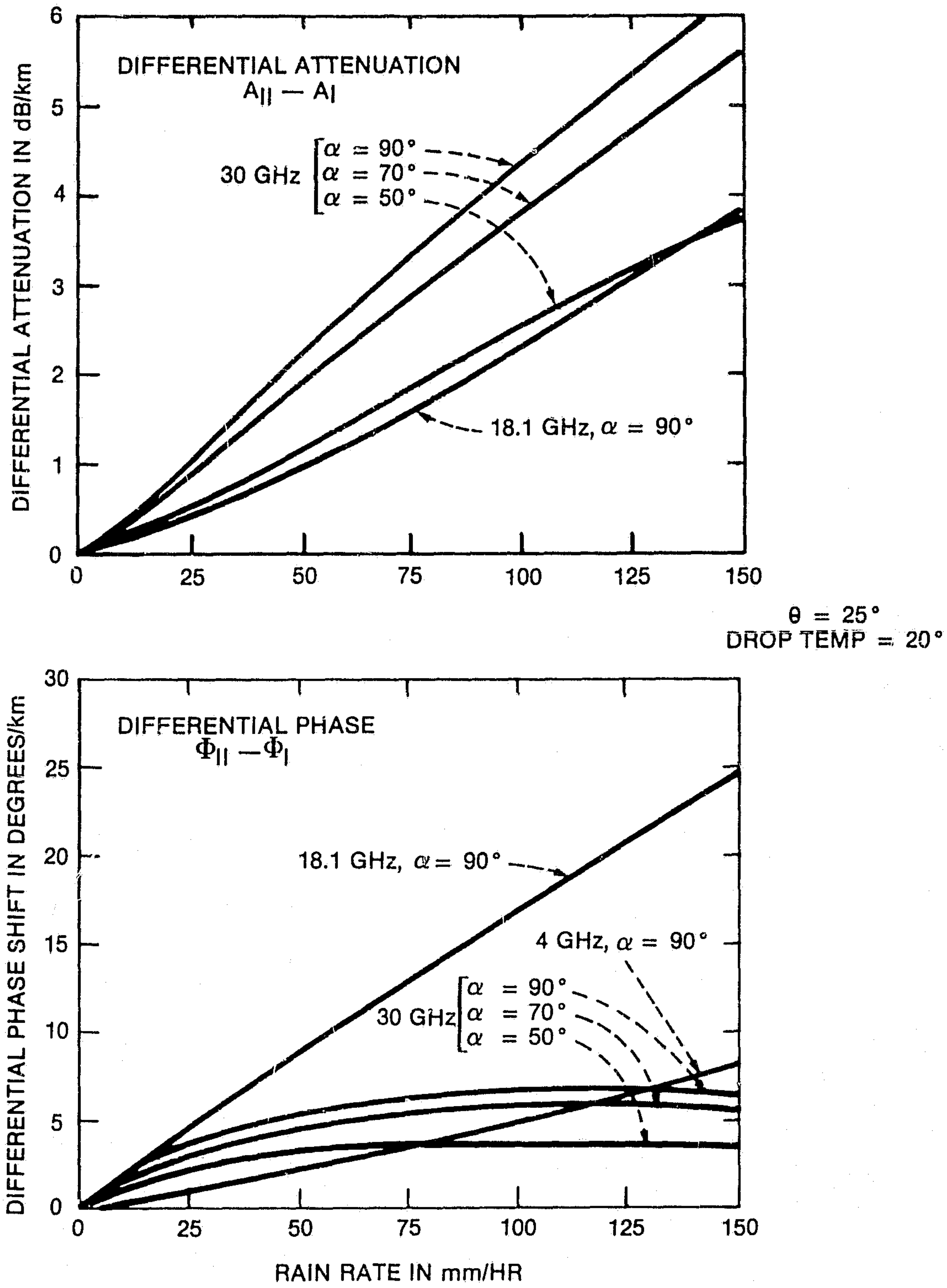

Figure 4.3-4. Differential Attenuation and Phase for Rain, From Morrison, et.al. (1973)

angle. Chu (1974) uses similar reasoning, but gives evidence that the mean canting angle is about 25^0, and that the effective angle sense imbalance is about 14%. Watson, et.al. (1973) calculate XPD versus rain rate at 11 GHz assuming a Gaussian canting angle distribution with a non-zero mean value, and uncorrelated drop orientations. The results were nearly the same as those assuming a fixed canting angle equal to the mean value.

Distributions of both α and θ can be accounted for by the following transformation (CCIR-1977):

$$\begin{bmatrix} a_I - j\phi_I \\ a_{II} - j\phi_{II} \end{bmatrix} = \begin{bmatrix} 1+m_\theta m_\alpha & 1-m_\theta m_\alpha \\ 1-m_\theta m_\alpha & 1+m_\theta m_\alpha \end{bmatrix} \begin{bmatrix} a_I' - j\phi_I' \\ a_{II}' - j\phi_{II}' \end{bmatrix} \qquad (4.3\text{-}10)$$

where the unprimed a's and ϕs are effective attenuation and phase constants and the primed ones correspond to $\alpha=90^0$. The canting angles and incidence angles are assumed to be randomly distributed with means $\bar{\theta}$ and $\bar{\alpha}$ variances σ_θ^2 and σ_α^2. The transformation parameters, assuming Gaussian distributions, are (Oguchi-1977)

$$m_\theta = \exp(-2\sigma_\theta^2)$$
$$m_\alpha = 1/2\,[1 + \exp(-2\sigma_\alpha^2)\sin 2\bar{\alpha}] \qquad (4.3\text{-}11)$$

where σ_θ and σ_α are in radians. The effective canting angle used in the formulas for XPD, etc. is $\bar{\theta}$. Substituting the effective attenuation and phase constants a, α into the formula for XPD ((4.3-6), making the small argument approximation

$$\gamma = \exp[-(a_{II}'-a_I')L + j(\phi_{II}'-\phi_I')L]$$
$$\approx 1 - (a_{II}'-a_I')L + j(\phi_{II}'-\phi_I')L \qquad (4.3\text{-}12)$$

and making further approximations based on the known values of the a's and ϕ's, we arrive at

$$\text{XPD} \approx -20 \log \left\{ \frac{1}{2} m_\theta m_\alpha L[(\Delta a')^2 + (\phi')^2]^{1/2} \sin 2\bar{\theta} \right\} \qquad (4.3\text{-}13)$$

where

$$\Delta a' = a_{||}' - a_{|}'$$

$$\Delta \phi' = \phi_{||}' - \phi_{|}'$$

This is good approximation for frequencies in the 4-50 GHz range and rain rates less then 150 mm/hr. If, in addition, we neglect the effect of the distribution of α and assume that the drops are oriented horizontally in the plane of incidence, as do Nowland, et.al. (1979), we can write

$$\sigma_\alpha^2 \ll 1$$

$$\bar{\alpha} = 90° - \varepsilon \qquad (4.3\text{-}14)$$

where ε is the antenna elevation angle. This implies

$$m_\alpha = \cos^2\varepsilon \qquad (4.3\text{-}15)$$

which further simplifies the approximation for XPD. The result is

$$\text{XPD} \approx -20 \log \left[\frac{1}{2} m_\theta L |\Delta k'| \cos^2\varepsilon \sin 2\bar{\theta} \right] \qquad (4.3\text{-}16)$$

with

$$|\Delta k'| = [(\Delta a')^2 + (\Delta \phi')^2]^{1/2}$$

4.3.2 Relationship between Depolarization and Attenuation due to Rain

An empirical relation has been observed between the exceedance statistics for attenuation and those for XPD on the same path. The relation is

$$XPD \approx \tilde{a} - \tilde{b} \log(CPA) \qquad (4.3\text{-}17)$$

where XPD is the value of cross-polarization discrimination not exceeded for a given percentage of the time, and CPA is the copolarized attenuation value in decibels, exceeded for the same percentage of the time. The empirical constant $\tilde{a}$ is typically found to be in the 30-50 dB range and $\tilde{b}$ is usually around 20. We present below the theoretical basis supporting this relation, and examine some of the experimental evidence for it.

Referring back to Section 4.3.1, we can obtain an expression for attenuation of the copolarized wave in a manner similar to finding the XPD. The copolarized attenuation, assuming a LP incident wave oriented in the x-direction, is given by

$$\begin{aligned} CPA &= -10 \log \frac{|E_{xs}|^2}{|E_{xi}|^2} \text{ with } E_{yi} = 0 \\ &= -10 \log |t_{xx}|^2 \\ &= -20 \log |T_{I} \cos^2\theta + T_{II} \sin^2\theta| \\ &= -20 \log |T_{I}[1 + (e^{-(\Delta a - j\Delta\phi)} - 1) \sin^2\theta]| \end{aligned} \qquad (4.3\text{-}18)$$

where Δa and $\Delta\phi$ are defined under equation (4.3-13). Using the small argument approximation (4.3-12) we can obtain

$$CPA_x \approx -20 \log [\exp(-a_I L \cos^2\theta - a_{II} L \sin^2\theta)]$$

$$= (A_I \cos^2\theta + A_{II} \sin^2\theta) L \qquad (4.3\text{-}19)$$

The same expression, with I and II subscripts interchanged, is found for CPA_y. Note that the above expression applies only when all the raindrops have the same orientation. Averaging over distributions of orientation angles α and θ, as was done earlier to find the XPD, we obtain

$$CPA_x = \frac{1}{2}[(A_I' + A_{II}') + m_\theta m_\alpha (A_I' - A_{II}') \cos 2\overline{\theta}\,]L \qquad (4.3\text{-}20)$$

where A_I' and A_{II}' are the attenuation coefficients, in dB/km, for $\alpha = 90^0$. Again assuming as before, that the raindrops are not distributed in α, and that $\alpha = 90^0 - \varepsilon$,

$$CPA_x = \frac{1}{2}[(A_I' + A_{II}') + m_\theta (A_I' - A_{II}') \cos^2\varepsilon \cos 2\overline{\theta}]L \qquad (4.3\text{-}21)$$

CPA_y is the same except that the sign of the second term is minus.

To relate XPD and CPA, we assume that the CPA, the attenuation coefficients A_I and A_{II}, the magnitude of the differential propagation constant, and the effective path length all bear a power law relation to the effective rain rate, R (Nowland, et al-1977):

$$CPA = a_o R^{b_o} L \qquad (4.3\text{-}22a)$$

$$A_I' = a_1 R^{b_1} \qquad (4.3\text{-}22b)$$

$$A_{||}' = a_2 R^{b_2} \tag{4.3-22c}$$

$$L = u R^{v} \tag{4.3-22d}$$

$$|\Delta k| = c R^{d} \tag{4.3-22e}$$

Substituting (4.3-22a-c) into (4.3-21) gives approximate expressions for a_o and b_o in terms of a_1, a_2, b_1 and b_2, which can be determined by regression fitting to the calculated propagation constants. The parameters u, v, c and d can also be determined by regression fitting to theoretical or empirical relations.

Substituting (4.3-22d) and (4.3-22e) into the formula for XPD, (4.3-16), gives XPD in terms of R and regression parameters. Likewise, using (4.3-22d) in (4.3-22a) gives CPA in terms of R and regression parameters. Elmininating R then relates XPD and CPA:

$$XPD \cong \tilde{a} - \tilde{b} \log CPA \tag{4.3-23}$$

with

$$\tilde{a} = 20\left(\frac{d+v}{b_o+v}\right) \log (a_o u) - 20 \log (\frac{1}{2} cu m_\theta \cos^2\varepsilon \sin 2\bar{\theta})$$

$$\tilde{b} = 20\left(\frac{d+v}{b_o+v}\right) \tag{4.3-24}$$

In the 11-14 GHz range, $b_o \simeq d$, which simplifies the formulas:

$$\tilde{a} \approx -20 \log \left(\frac{1}{2a_o} cm_\theta \cos^2\varepsilon \sin 2\bar{\theta}\right)$$

$$\tilde{b} \cong 20 \qquad (4.3\text{-}25)$$

Throughout the preceding development, linear polarization in the x direction was assumed. For LP waves in the y- direction, and 1 and 2 subscripts in the forulas for a_o and b_o are reversed. For CP waves, $\bar{\theta}$ is set to 45^o, which gives the lowest value of XPD.

A provisional formula based on the above is given in CCIR Report 564-1 (1978). The CCIR formula essentially sets

$$d \cong b_o$$

$$\frac{cm_\theta}{2a_o} \approx [f(GHz)]^{-3/2} \qquad (4.3\text{-}26)$$

$$\bar{\theta} \approx \tau = \text{polarization tilt angle with respect to horizontal}$$

to arrive at the "CCIR Approximation"

$$XPD = 30 \log |f(GHz)| - 40 \log (\cos \varepsilon)$$
$$-20 \log (\sin 2\tau) - 20 \log CPA \qquad (4.3\text{-}27)$$

The "exact" evaluation of the $\tilde{a}$ and $\tilde{b}$ coefficients requires first finding a_1, b_1, a_2, b_2, c and d by regression fitting to the parameters A_I, A_{II}, and $|\Delta k|$ versus rain rate and frequency. These parameters in turn are determined by the propagation constants (a_I, ϕ_I, etc.) corresponding to the raindrop symmetry axes. Nowland, et al (1977a) report the results of regression calculations performed in this manner for oblate spheroidal and Pruppacher-Pitter-form raindrops, for the Laws-and Parsons drop size distribution. More extensive results are included in CCIR Document 5/206 (1977). That report also contains the regression coefficients for path length, u and v. These are given as functions of elevation angle for three ranges of rain rate, and were computed based on an empirical formula for path length.

The orientation distribution of the raindrops is the rain characteristic about which we know the least. It enters into the computation in finding a_0 and b_0 from a_1, a_2, b_1 and b_2, and in finding $\tilde{a}$. As stated earlier, it is apparently quite safe to ignore the effect of the angular distribution in the plane of incidence (see Figure 4.3-1). This allows us to set $\alpha = 90^o - \varepsilon$, the complement of the elevation angle of the path. The drop orientation angle θ with respect to the polarization direction, measured in the plane normal to the path, can be expressed as the difference $\theta = \phi - \tau$ where ϕ is the drop canting angle and τ is the polarization direction, both measured with respect to the horizontal. Since τ is known, it is the statistics of ϕ that determines $\bar{\theta}$ and σ_θ (or m_θ), i.e.

$$\overline{\theta} = \overline{\phi} - \tau , \quad \sigma_\theta = \sigma_\phi \tag{4.3-28}$$

It is convenient to describe the distribution of ϕ by an equivalent canting angle ϕ_e, defined by

$$\sin 2|\phi_e - \tau| = m_\theta \sin 2|\phi - \tau| \tag{4.3-29}$$

The equivalent canting angle is the canting angle that identically oriented raindrops would need to have in order to produce the same XPD. Nowland, et al cite a measured value of 4^o for ϕ_e that is consistent with independently-determined values of $\bar{\phi}$ and σ_ϕ, but give other experimental results that show little consistency. More work is clearly needed in characterizing the canting angle.

4.3.3 Experimental Depolarization Data

The most extensive experimental investigations of depolarization above 10 GHz to date have been performed at Virginia Polytechnic Institute and State University (VPI & SU) at Blacksburg (Bostian and Dent - 1979), the University of Texas (UT) at Austin (Vogel - 1978), and the Bell Telephone Laboratories (BTL) in Holmdel, and Crawford Hill, N.J. (Arnold, et. al. - 1979). The signal sources for depolarization measurements conducted at these facilities have been beacons on the following spacecraft.

ATS-6	20 GHz, 30 GHz, LP
CTS	11.7 GHz, RHCP
COMSTAR	19.04 GHz, Vert. & Horiz. LP COMSTAR
	28.56 GHz, Vert. LP

Three COMSTAR spacecraft, D-1 through D-3, have been used.

In the experiments, the signal levels in the copolarized and cross polarized channels were measured, either continuously or during periods of rain. The measurement records were typically used to generate XPD and CPA statistics and plots of XPD versus CPA. Some results of these experiments are presented in section 6.7.2.

Both the VPI and SU and the UT data bases have been processed to give XPD vs CPA on an instantaneous basis, and on a statistical basis. In the former case, XPD values that were observed at the same time as the corresponding CPA value are plotted. In the latter case, the XPD value that was not exceeded for a particular percentage of time is plotted against the CPA value that was exceeded for the same time percentage. An instantaneous XPD vs CPA plot was prepared for each month, and a curve of the form $XPD = \tilde{a} - \tilde{b} \log CPA$ was fitted to it. Table 6.7-1 shows the $\tilde{a}$ and $\tilde{b}$ parameters giving the best fit for each monthly plot for the 1978 VPI and SU data. The parameter R^2, which indicates how well the data fits the analytical curve (R^2 = 1 for perfect fit), is given for each case. The best-fit $\tilde{a}$ and $\tilde{b}$ values are quite variable month-to-month, and some months have very low R^2 values. The UT data gave similar results. This indicates that the formula is probably not very reliable for predicting XPD versus CPA on an instananeous basis. Statistical plots, on the other hand, generally show very good fit to the formula. The VPI and SU CTS data (11.7 GHz) for the 1978 calendar year yielded $\tilde{a}$ = 41 dB and $\tilde{b}$ = 23.2 with R^2 = 0.95 when all data for CPA $<$ 5dB is ignored. The UT data, covering about 18 months, gave a = 41 dB, b = 20.6 with R^2 = 0.99.

Figure 6.7-3 shows how the experimentally determined values of $\tilde{a}$ and $\tilde{b}$ for various frequencies and polarizations compare with the theoretically determined values from the formulas given previously. The theoretical predictions in general overestimate the depolarizing effects of the rain.

In the BTL experiment, co- and crosspolarized signal phase as well as amplitude was measured. This allowed the investigators to calculate XPD for arbitrary polarization states by vector manipulations. The beacon signal used, from a COMSTAR satellite, was linear polarized and oriented at about 21° from the local horizontal. Through the data conversion process, XPD versus CPA was determined on a statistical basis for linear polarization oriented 0°, 45° and 90° from horizontal, and RHCP. Figure 4.3-5 shows the median 19 GHz curves for the true polarizations (21° from vertical and horizontal) and for vertical, horizontal and 45°. The experiment confirmed the theoretical result that maximum XPD occurs at 45°. Also, the XPD values calculated for RHCP were virtually identical to those at 45°, which curves fall between the 45° and the vertical/horizontal curves, and that XPD for horizontal polarization is greater than for vertical polarization. Both of these results agree with physical reasoning. A general agreement with the XPD = $\tilde{a}$ - $\tilde{b}$ log CPA relation is evident for the lower three curves, in that they tend to lie near a straight line on the semilogarithmic plot. The CCIR approximation (4.3-27) is shown on the plot for the tilt angles 21° and 45°. In this case, the CCIR approximation appears to underestimate the depolarization.

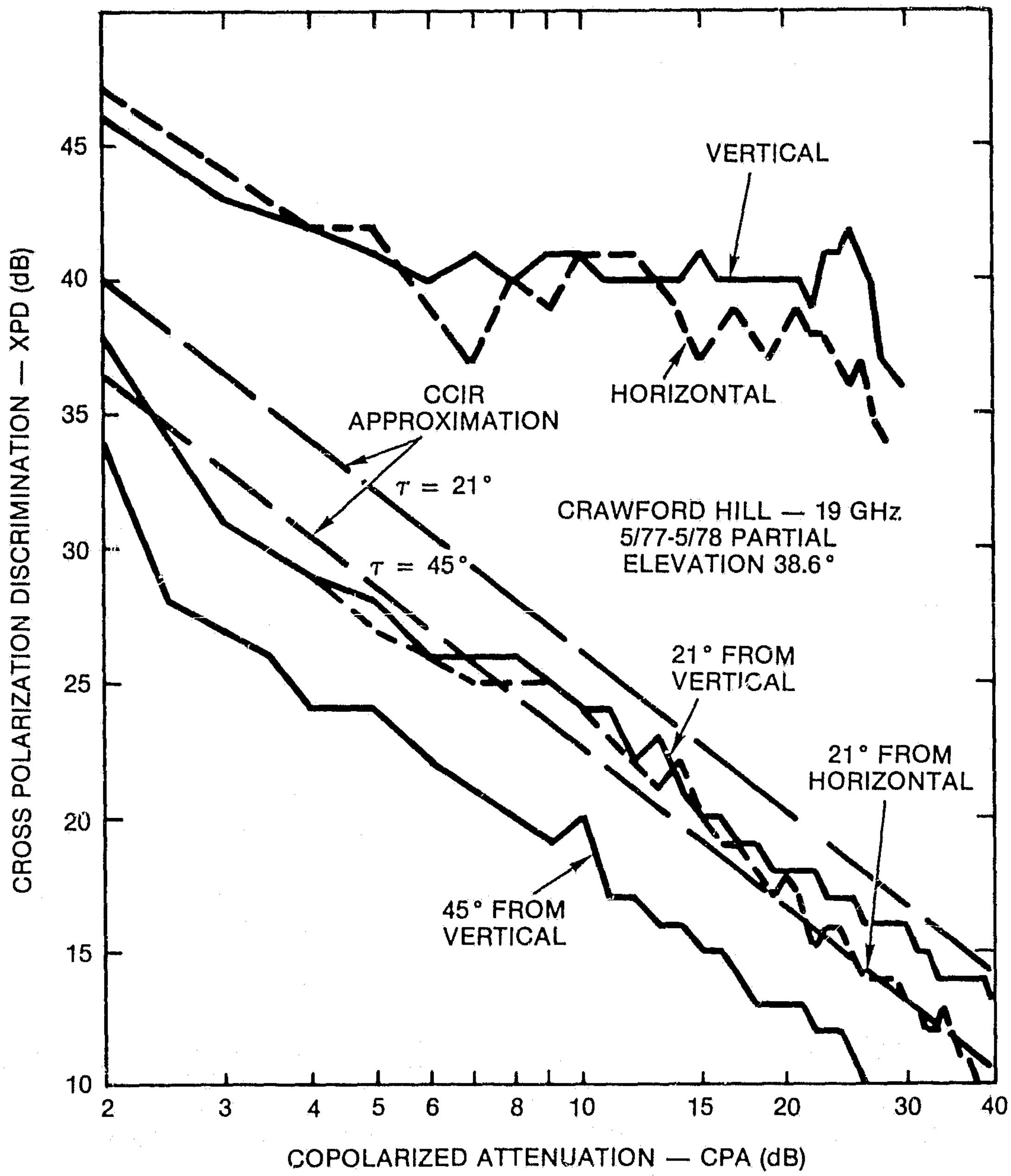

Figure 4.3-5. BTL COMSTAR Depolarization Experiment Results (Arnold, et.al. - 1979)

4.3.4 Phase of Crosspolarized Signal

Techniques have been developed for compensating for depolarization in dual-polarized satellite systems. They involve cancelling the crosstalk in one channel by inserting a properly levelled and phased sample of the opposite channel's signal. The signal sample used for cancelling must be exactly 180° out of phase from the crosspolarized signal for the technique to work. Its effectiveness depends, therefore, on how well the control system can determine and track the phase of the crosspolarized signal. This is a function of variability and rate of change of that phase.

Estimating the performance of crosstalk cancellation systems is one motivation for investigating crosspolarized signal phase. Another reason is that the signal phase is sensitive to certain properties of the rain medium (e.g. canting angle), and its measurement can aid in modelling the propagation properties of rain phenomena.

Overstreet and Bostian (1978) at VPI and SU derived a theoretical description of the phase between the copolarized and crosspolarized signals when rain depolarization is present. They assumed identically oriented raindrops, canted at an angle θ with respect to a copolarized reference direction, having known differential attenuation and phase and a known effective path length. Using Chu's differential attenuation and phase values for the frequencies and elevation angles of the CTS and COMSTAR D-2 beacons, they predicted the phase as a function of θ and rain rate, then found phase versus the XPD value for the same rain rate. The path lengths used were derived from attenuation statistics for those beacons at the VPI and SU station. For linearly polarized signals at 11 and 28 GHz, it was found that the phase was a fairly weak function of XPD and θ , typically remaining in a 45° sector for XPD values down to 15 dB over the expected range of θ . For circular polarization, it was found that the phase difference Δ_c is given by

$$\Delta_c = \pm 2\theta + \Delta_l(\theta = 45^{\circ}) \qquad (4.3\text{-}30)$$

where Δ_ℓ is the phase difference for LP waves, and the sign of the first term depends on wether RHCP or LHCP is copolarized. The LP phase difference at $\theta = 45^{o}$ is only weakly dependent on XPD, so the 2θ term predominates in Δ_c.

Experimental data from the CP CTS beacon at 11.7 GHz generally confirmed the theoretical expectations. The phase difference of the LP signal normally remained in a 20-30^{o} range during a rain depolarization event, whereas the CP signal phase difference varied widely during the course of a rain event. The phase versus XPD changes generally followed a characteristic sequence during convective storms. This indicated the changes in the nature of the depolarizing medium, primarily in predominant canting angle of the raindrops present, through the passage of the storm cell.

The experimental evidence suggests that crosstalk cancellation schemes would be more effective using LP than CP waves. The phase of the crosspolarized signal, which must be estimated by the cancellation system, is much less variable with linear polarization. In fact, setting the phase of the cancellation signal to a constant value would give a degree of effectiveness, while eliminating the need for a complex phase shifter control system.

4.3.5 Rate of Change of Depolarization

To more fully characterize depolarization, some quantitative description of the rate of change of the amplitude and phase of the crosspolarized signal would be desirable. This information would assist us in designing adaptive controls for crosstalk cancellation systems, and may also provide further insight into the nature of the meteorological process responsible for depolarization. However, there has apparently been little research effort expended to this end. Further experimental work, or further analysis of existing data bases, is needed in this area.

4.3.6 Rain Depolarization Dependence on Elevation Angle and Frequency

Knowledge of the dependence of crosspolarization discrimination on elevation angle and frequency is quite valuable because it allows us to extend the usefulness of time-consuming and costly measurements. Unfortunately, the present limited body of experimental evidence does not overwhelmingly support the theoretical scaling relations, so they must be used with caution.

The expression obtained earlier for XPD,

$$XPD = -20 \log [\frac{1}{2} m_\theta L |\Delta k'| \cos^2\varepsilon \sin 2\bar{\theta}] \quad (4.3\text{-}31)$$

can be rewritten to explicitly show the elevation angle and frequency dependencies. For the CP case, corresponding to the minimum XPD, we have $\bar{\theta}$ = 45^0, which gives

$$\begin{aligned} XPD = & -20 \log (L \cos^2\varepsilon) \\ & -20 \log |\Delta k'| \\ & -20 \log (m_\theta/2) \end{aligned} \quad (4.3\text{-}32)$$

Using the emprical relations (Nowland, et al-1977):

$$L = [7.41 \times 10^{-3} R^{0.766} + (0.232 - 1.8 \times 10^{-4} R) \sin \varepsilon]^{-1} \quad (4.3\text{-}33)$$

$$|\Delta k'| \cong c(f)\, R^{\,d(f)}$$

It is apparent that the first term in the XPD expression is a function of rain rate and elevation angle only, and the second term is a function of rain rate and frequency only. These terms are plotted in Figure 4.3-6. The last term can be considered constant, though it may also be a function of rain rate. For m_θ = 0.8, the last term is 8 dB.

Another depiction of the frequency dependence of XPD is shown in Figure 4.3-7. It shows the predicted XPD vs CPA relations for fixed frequencies and elevation angle. It is clear that, for any given rain rate, both CPA and XPD get worse as frequency increases. However, for a given value of CPA, XPD improves with frequency.

4.4 ICE DEPOLARIZATION

The second major casue of depolarization on Earth-space paths, besides rain, is the present of ice crystals in clouds at high altitudes. Ice crystal depolarization is different from rain depolarization in that it is not accompanied by appreciable copolarized attenuation. This is because the depolarization is caused primarily by differential phase shifts, rather than differential attenuation, which is responsible for rain depolarization. Another distinguishing characteristic is that the amplitude and phase of the crosspolarized signal often undergo abrupt, coincident changes with large excursions.

Much of what is known about ice crystal depolarization has been learned only very recently. Bostian and Allnut (1979) present a good summary of recent work in observing and explaining the phenomenon. Much of what follows is from that source.

4.4.1 Meteorological Presence of Ice

Clouds present above the freezing level consist, completely or in part, of ice crystals. Cirrus clouds, and the "anvil" that forms at the top of mature thunderstorms are all ice, and the upper parts of cumulonimbus clouds are predominately ice. The crystals that are present have one of two

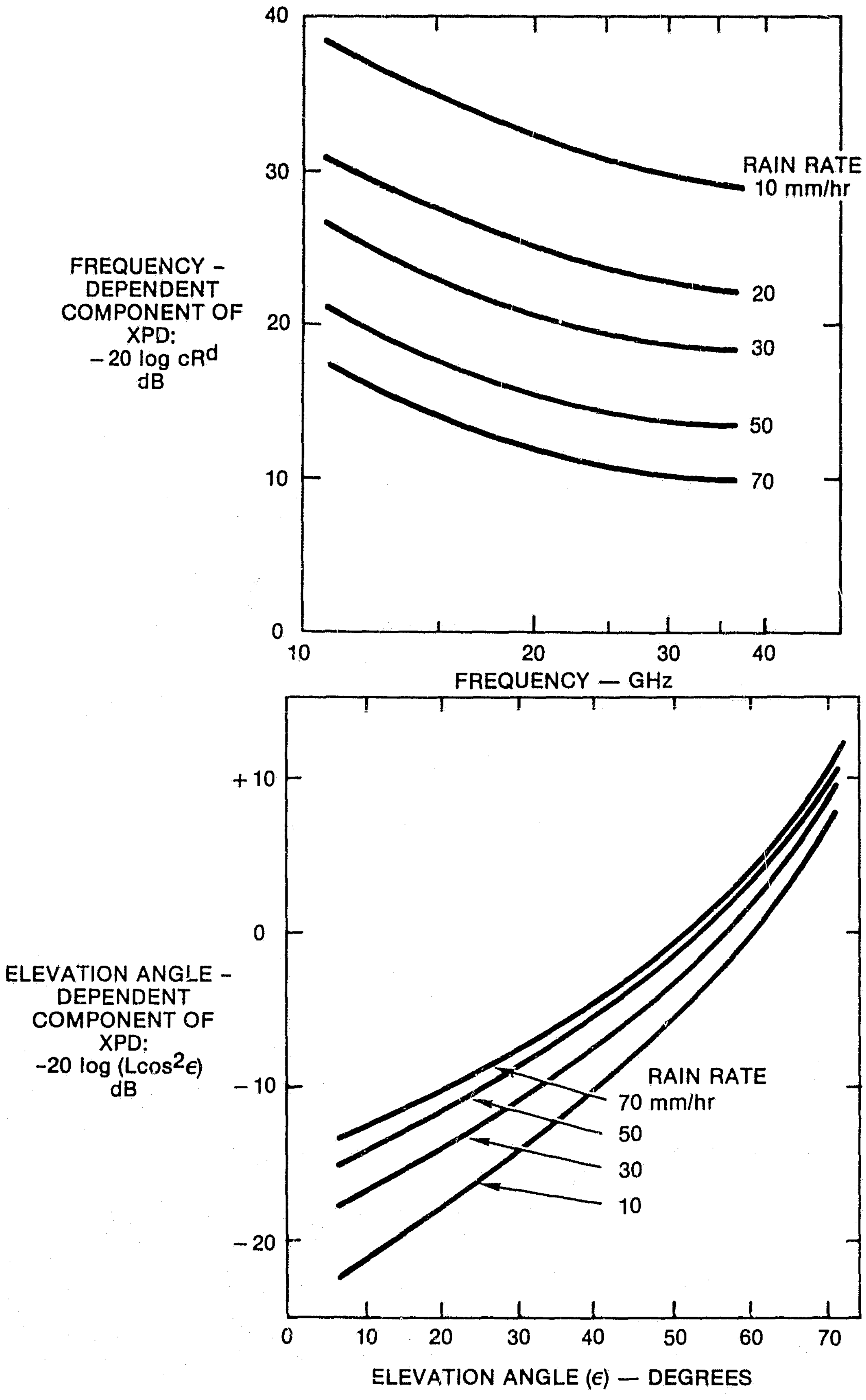

Figure 4.3-6. Frequency and Elevation Angle Dependence of XPD for CP

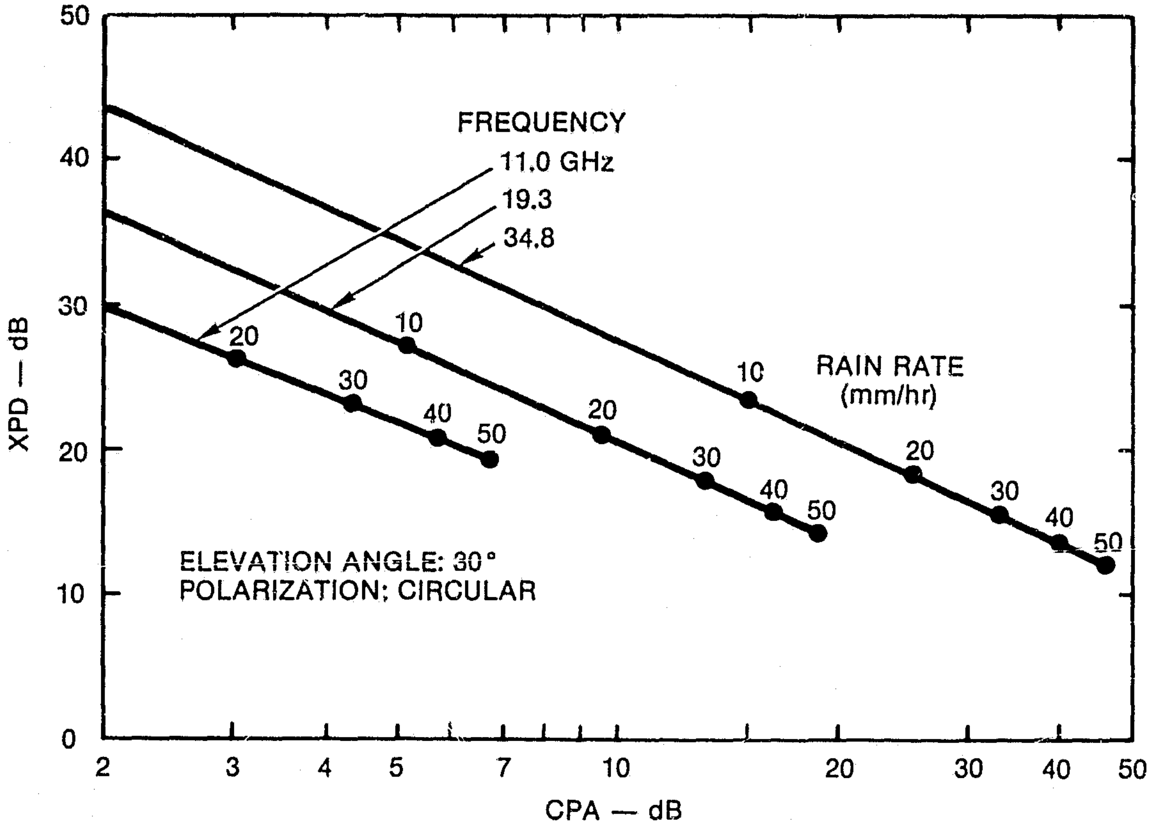

Figure 4.3-7. Frequency and Rain Rate Dependence of XPD and CPA

shapes determined by the temperature at the time of formation. Very cold temperatures, below about -25°C, favor the formation of needle-shaped crystals. Flat, plate-like crystals form in a moderately cold environment (-9° to -25°C). The dimensions of the crystals vary between about 0.1 and 1 mm.

Ice crystals form on dust particle nuclei in the atmosphere. The relative abundance of dust particles has been hypothesized as the reason for differences observed in ice depolarization at different locations. In maritime regions, the air contains relatively few dust particles compared with continental areas. As a result of this, maritime air tends to have fewer, but larger ice particles than continental air under similar conditions. It is believed that the presence of larger crystals accounts for the generally higher values of XPD observed in maritime versus inland locations (i.e., BTL versus VPI & SU).

Like raindrops, ice crystals are non-symmetrical and they have a dielectric constant much different from air. These are two of the necessary conditions for depolarization. A third condition, a preferred particle alignment, is also required. Oblate raindrops are aligned by aerodynamic forces, and their preferred alignment direction is affected by the prevailing winds. Aerodynamics also have a role in aligning ice particles, but it is believed electrostatic forces also play a large part. This belief is supported by many observations during thunderstorms of rapid XPD changes coinciding with lightning flashes. This coincidence may be explained by the following: Electric fields present in regions between oppositely-charged clouds exert torgues on the highly non-symmetrical ice crystals. When the field is sufficiently strong, these torgues become significant in comparison with the turbulent aerodynamic forces, resulting in an average alignment of the"needle" crystal axes and the "plate" crystal planes along the direction of the field lines. When a lightning discharge takes place between the clouds, charges are equalized and the electric field intensity drops. Aeroydnamic forces then predominate, and the crystals quickly lose their preference for a particular direction of orientation.

4.4.2 Model for Ice Depolarization

Propagation through a region containing ice crystals can be analyzed in a manner of analogus to that applied to rain. In the case of ice, the crystals are modelled as highly eccentric prolate spheroids ("needle" crystals) or oblate spheroids ("plate" crystals). Haworth, Watson and McEwan (1977) have performed this analysis. They assumed that due to aerodynamic forces, the "plate" crystals were oriented horizontally and the axes of the "needle" crystals stayed in the horizontal plane. Under this assumption, an electrostatic field has no effect on "plates", and aligns the "needles" along the horizontal component of the field. Figure 4.4-1 shows the magnitude of the predicted ice XPD. The "needle'-produced XPD varies with $\bar{\phi}$, the average orientation angle of the crystal axes measured in the horizontal plane. The parameter α is a measure of the degree of alignment of the crystal axes. When the axes are uniformly distributed in all directions, $\alpha = 0$, and when all crystals are oriented in the same direction, $\alpha = 1$.

The phase of the crosspolarized signal, as predicted by the model, undergoes an abrupt change of 180^0 as $\bar{\phi}$ pases through the values corresponding to the XPD peaks (crosspolarized signal nulls). These are at 80^0 and 130^0 in the figure. When α is below some critical value, however, (falling between 0.5 and 1.0 for the example shown) the double null and accompanying phase jump don't occur. This phase reversal phenomenon has been observed at the time of lightning flashes in thunderstorms (see Figure 9.7-8) and is accompanied by jump in XPD amplitude. Bearing the earlier discussion in mind, we would expect changes in α and $\bar{\phi}$ to accompany lightning discharges. The same behavior has also been detected during the passage of non-electrically-active clouds (Shutie, et. al.-1978). This means there must be some mechanism, probably wind shear, responsible for crystal alignment beside electrostatic fields.

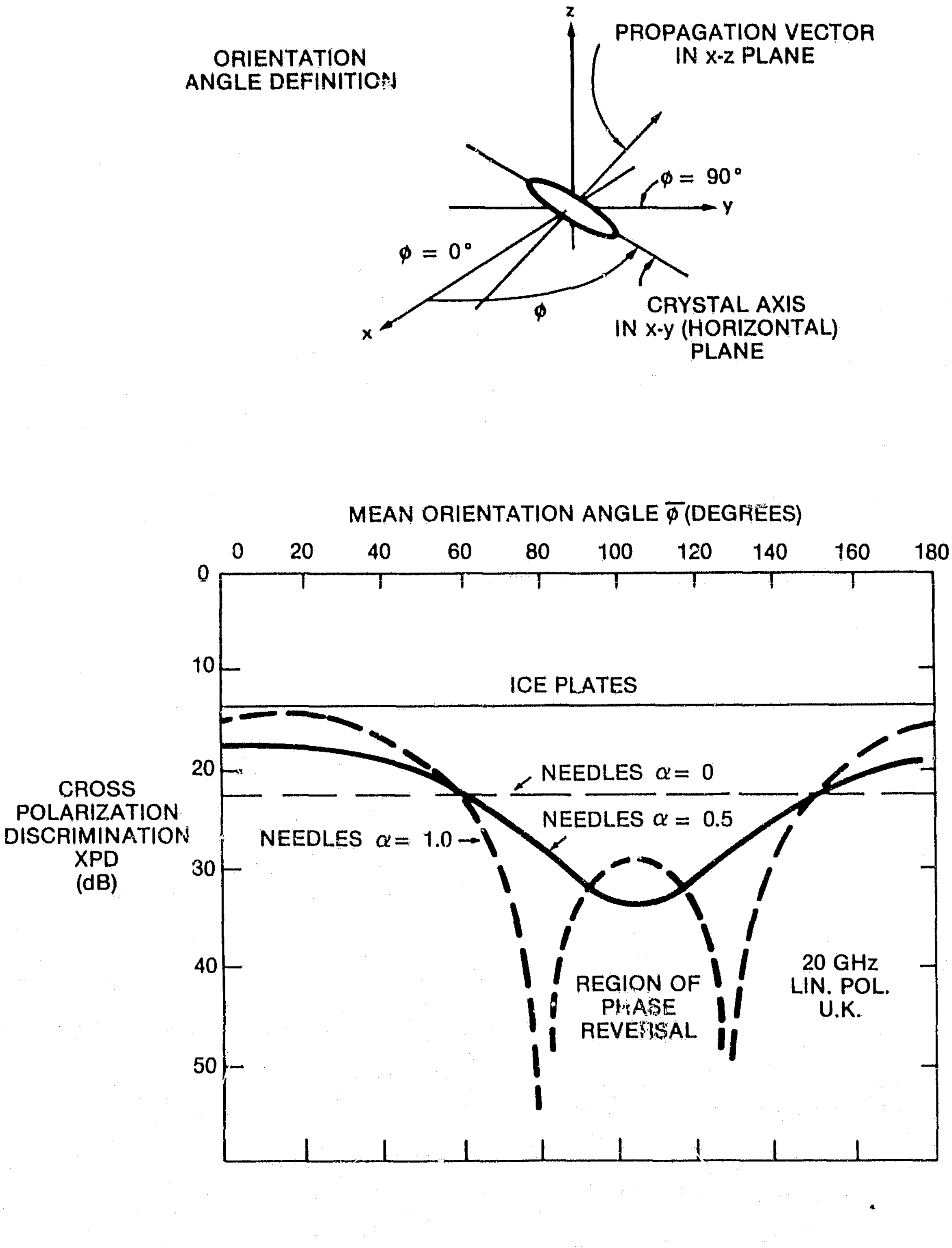

Figure 4.4-1. Definition of Orientation Angle ϕ and Predicted XPD

(From Bostian and Allnut, 1979)

4.5 REFERENCES

Arnold, H.W. et. al. (1979), "Characteristics of Rain and Ice Depolarization for a 19 and 28 GHz Propagation Path from a Comstar Statellite," Record, Int'l Conf. on Communications.

Bostian, C.W. and J.E. Allnut (1979), "Ice-Crystal Depolarization on Satellite-Earth Microwave Radio Paths," Proc. IEE, Vol. 126, p. 951.

Bostian, C.W. and J.R. Dent (1979), "CTS 11.7 GHz Isolation Data for the Calendar Year 1978," VPI & SU Report, prepared for NASA under Contract No. NAS5-22577.

CCIR (1977), Document 5/206 (Canada), "Techniques for the Prediction of Rain Depolarization Statistics at Microwave and Millimeter Wavelengths."

Chu, T.S. (1974), "Rain-Induced Cross-Polarization at Centimeter and Millimeter Wavelengths," Bell Syst. Tech. Jrnl, Vol. 58, No. 8, pp. 1557-1579.

Haworth, D.P., P.A. Watson, and N.J. McEwan (1977), "Model for the Effects of Electric Fields on Satellite-Earth Microwave Radio Propagation," Elect. Letters, Vol. 13, p. 562.

Hendry, A., G.C. McCormick and B.L. Barge (1976), "Ku-Band and S-Band Observations of the Differential Propagation Constant in Snow," IEEE Trans. Ant. Prop., Vol. AP-24, No. 4, pp. 521-525.

McCormick, G.C. and A. Hendry (1977), "Depolarization by Solid Hydrometeors," Electronics Letters, Vol. 13, No. 3.

Morrison, J.A., M.J. Cross, and T.S. Chu (1973), "Rain-Induced Differential Attenuation and Differential Phase Shift at Microwave Frequencies," B.S.T.J, Vol. 52, No. 4, pp. 599-604.

Nowland, W.L., R.L. Olsen, and I.P. Shkarofsky (1977a), "Theoretical Relationship Between Rain Depolarization and Attenuation," Electronics Letters, Vol. 13, No. 22, pp. 676-677.

Oguchi, T. (1977), "Scattering Properties of Pruppacher-and-Pitter Form Raindrops and Cross Polarization Due to Rain: Calculations at 11, 13, 19.3 and 34.8 GHz," Radio Science, Vol. 12, pp. 41-51.

Pruppacher, H.R. and R.L. Pitter (1971), "A Semi-empirical Determination of the Shape of Cloud and Rain Drops," J. Atmos. Science, Vol. 28, pp. 86-94.

Shutie, P.F., E.C. MacKenzie and J.E. Allnut (1978), "Relative Phase Measurements at 30 GHz Between Copolar and Induced Crosspolar Signals Produced by Ice Particles on a Satellite-to-Ground Link," Elect. Letters, Vol. 14, No. 4, p. 105.

Stutzman, W.L. (1977), "Mathematical Formulations and Definitions for Dual Polarized Reception of a Wave Passing Through a Depolarizing Medium (A Polarization Primer)," Virginia Polytechnic Institute & State Univ. Report, prepared under NASA Contract NAS5-22577.

Thomas, D.T. (1971), "Cross-Polarization Distortion in Microwave Radio Transmission Due to Rain," Radio Science, Vol. 6, No. 10, pp. 833-839.

Vogel, W.J. (1978), "CTS Attenuation and Cross-Polarization Measurements at 11.7 GHz," Final Report, Elect. Eng. Res. Lab., Univ. Texas at Austin, prepared under NASA Contract NAS5-22576.

Watson, P.A., and M. Arbabi (1973a), "Rainfall Crosspolarization at Microwave Frequencies," Proc. IEE, Vol. 120, No. 4, pp. 413-418.

Watson, P.A., and M. Arbabi (1973b), "Cross-Polarization Isolation and Discrimination," Electronics Letters, Vol. 9, N. 22, pp. 516-519.

CHAPTER V

PROPAGATION DATA BASES

Researchers have been performing experiments to gather propagation data on millimeter-wave Earth-space links for about a decade, and in the process, have accumulated sizable data bases. In this chapter, we describe the various satellites used in this work, and present summary results of the significant experiments conducted in the United States. The results presented are primarily cumulative attenuation statistics, though some depolarization measurements are included as well. This is, by necessity, a limited sampling of the existing data bases. We therefore preface the data by citing additional summaries of propagation data for the interested reader.

5.1 SUMMARIES OF EXPERIMENTAL DATA

The International Radio Consultative Committee (CCIR) publishes a summary of worldwide experimental data in the Recommendations and Reports issuing from its periodic plenary assemblies. Volume V of this publication, "Propagation in Non-Ionized Media," deals with all aspects of microwave propagation--both terrestrial and earth-to-space. Within Volume V, the data is presented as a series of reports and recommendations submitted to and adopted by the CCIR. Because of this presentation format, data of interest to designers may be found in several places. The most complete presentation of data is found in Report 564-1, "Propagation Data Required for Space Telecommunication Systems" (CCIR-1978a).

Another handbook being prepared under NASA contract, "Handbook for the Estimation of Microwave Propagation Effects," (Crane and Blood-1979), has additional experimental data and presents models of the propagation phenomena. The cumulative attenuation models presented by Crane and Blood are included in Chapters 3 and 6 of this Handbook.

Finally, an earlier document prepared for NASA in 1977 contains extensive experimental results obtained by NASA-sponsored experimenters. This document, entitled "A Compendium of Millimeter Wave Propagation Studies Performed by NASA" (Kaul, et al-1977), contains a reasonably complete summary and references to the 15.3 and 31.65 GHz (ATS-5) and the 13.2, 17.8, 20 and 30 GHz (ATS-6) data. Because of this document, only a summary of the ATS-5 and ATS-6 results is repeated herein. This summary should be used, along with the Compendium, for pre-1977 data. Emphasis will be placed on presenting data from the CTS and COMSTAR satellite systems.

5.2 SATELLITES USED FOR PROPAGATION RESEARCH

Within the United States and Canada, four satellite systems (seven satellites) have been utilized to obtain the bulk of the earth-space propagation data. A brief summary of the satellite characteristics that relate to propagation studies is given in Table 5.2-1. The COMSTAR system is comprised of three satellites. Only the D3 satellite is still operating at this writing in the beginning of 1980. The CTS satellite ceased operation for propagation researchers late in 1979.

Satellite propagation beacons are not the only means for collecting experimental data. Radars, radiometers (fixed and sun synchronous) and low-orbiting satellites can also provide valuable data, but usually with some deficiency. A general deficiency is the lack of polarization data available from these measurement techniques. Specifically, the expense of calibrating and operating radar systems and the attenuation saturation effect in radiometer systems limits their use.

Table 5.2-1

Satellite Parameters Related To Propagation Studies

Satellite	Launch Date	Satellite Position	Uplink Frequencies	Downlink Frequencies	Antenna
ATS-5	8/12/69	Initially over Indian Ocean, drifted to 108^{o} W. longitude; remained spinning at 76 rpm	31.65 GHz with sidebands at ±1, ±10, and ±50 MHz from carrier	15.3 GHz with sidebands at ±0.1, ±1, ±50 MHz from carrier	Linearly polarized conical horns with 20^{o} coverage and 19.1 dB boresight gain
ATS-6	5/30/74	94^{o} W. longitude for first year then move to 35^{o} E. long. and returned to 140^{o} W.	COMSAT Exp.: 13.19 - 13.2 GHz 17.74 - 17.8 GHz	COMSAT Exp.: 4.14 - 4.15 GHz 4.16 - 4.17 GHz NASA/GSFC Exp.: 20 and 30 GHz 8 sidetones Spaced ±180 MHz	COMSAT Exp.: Dual-frequency linearly polarized dish NASA/GSFC Exp.: 20 GHz: 6^{o} x 9^{o} horn 2^{o} dish 30 GHz: similar to above
CTS	1/17/76	116^{o} W.	14.0 - 14.5 GHz	11.7 GHz beacon 11.7 - 12.2 GHz	16^{o} horn, RHCP for beacon
COMSTAR (satellites D1, D2 and D3)	D1: 5/13/76 D2: 7/22/76 D3: 6/29/78	D1: 128^{o} W. long. D2: 95^{o} W. long. D3: 87^{o} W. long.		19.04 and 28.56 GHz	Linearly polarized offset parabolic dishes. 19.04 GHz switched between vertical and horizontal polarization. 28.56 GHz vertically polarized. Sidebands of 28.56 GHz ±528.9 MHz (D3) ±264.4 MHz (D1 and D2)

5.3 FORMAT OF DATA PRESENTED

Because of the volume and variety of data being presented by experimenters throughout the United States and Canada, it is impossible to claim that the following data is complete. However it is certainly representative of the tropospheric effects on earth-space paths for the location indicated.

To limit the volume of data presented, the cumulative attenuation statistics will be emphasized, since this is the most complete data base available and, from this, the rain rate and depolarization may be inferred (as described in Chapters 3 and 4). The results will be presented by frequency range or satellite beacon frequency, as appropriate.

To assist with the comparison of data from various experimenters, NASA has encouraged the use of a standardized cumulative statistics plot formats. The use of these formats, given in Figures 5.3-1 and 5.3-2, will permit experimental results from different sources to be overlaid for direct comparison. The forms cover from 0.0001 to 10 percent of the total period, which should be a sufficiently large range for most applications. The attenuation scales cover from 0-35 and 0-45 dB, which should be sufficient to cover the link margin range of most systems. The 45 dB graph is recommended for use above 15 GHz. These same forms may be utilized for depolarization statistics if the attenuation labels are changed to cross-polarization discrimination. Each chart should be labeled with the period of the measurement, frequency, location and elevation angle. This provides, on the figure, all the information needed for comparison of data.

5.4 EXPERIMENTAL CUMULATIVE ATTENUATION STATISTICS

5.4.1 11.7 GHz Data

The Communications Technology Satellite (CTS) has provided the opportunity for extensive long-term measurements of rainfall attenuation and

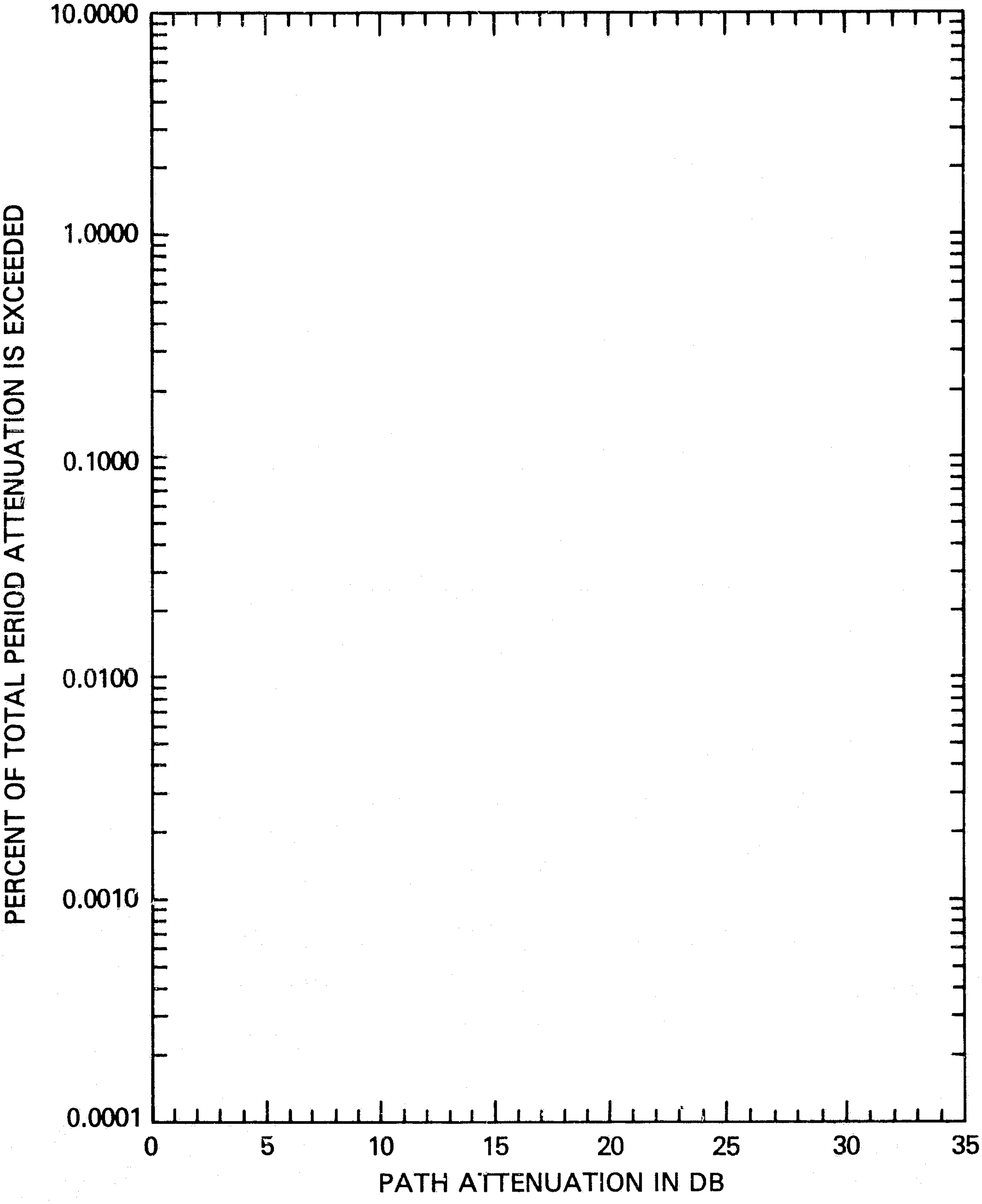

Figure 5.3-1 Cumulative Attenuation Graph for Use in the 11/14 GHz Bands

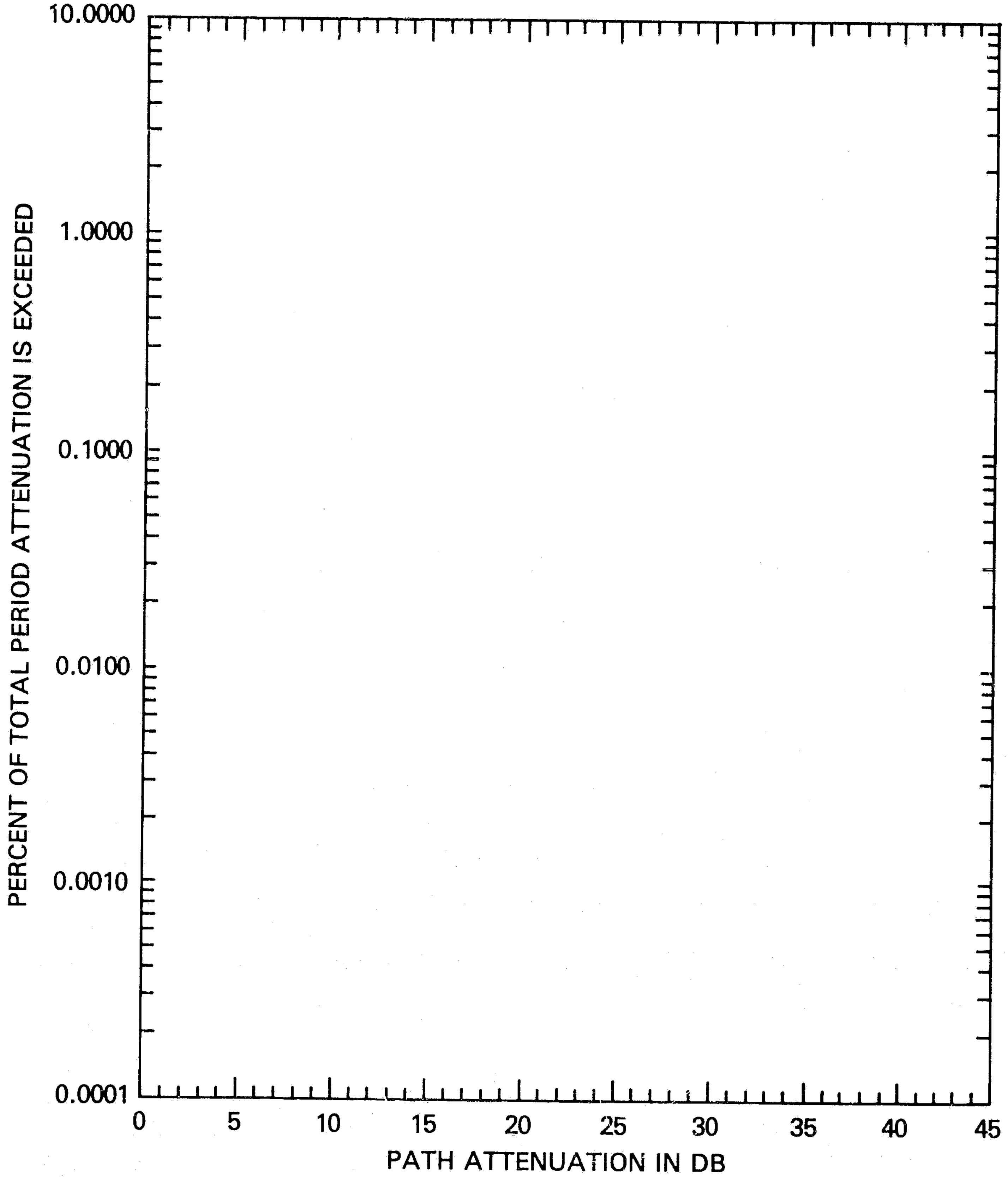

Figure 5.3-2. Cumulative Attenuation Graph for Use above 15 GHz

other propagation effects in the 11.7 to 12.2 GHz band. A continuous 11.7 GHz circularly polarized beacon has operated since launch except for two periods during solar eclipse (March 4 through April 16, 1976 and August 31 through October 17, 1976).

Figures 5.4-1 through 5.4-5 show the cumulative statistics for the five United States locations of (listing in order of ascending elevation angle):

Waltham, MA (GTE Laboratories, Inc.)
Holmdel, NJ (Bell Telephone Labs.)
Greenbelt, MD (NASA Goddard Space Flight Center)
Blacksburg, VA (Virginia Polytechnic Institute and State University)
Austin, TX (University of Texas at Austin)

All of the distributions are based on 12 calendar months of continuous data. Details of the recording methods and processing techniques are given in the references in each figure. Table 5.4-1 summarizes the attenuation statistics at each of the locations for 0.001, 0.005, 0.01, 0.05, 0.1, 0.5 and 1% of the observation period. Note that the data shows a wide range of variations, even for consecutive years at one location.

Elevation angle differences between the five locations prevents a direct comparison of the measured distributions. The distributions can be converted to a common elevation angle by assuming the precipitation to be horizontally stratified in the region of the elevation angle variations. Four of the sites have elevation angle differences of less than 9^o; and, except for the 49^o elevation angle at Austin, the sites differ by only a few degrees. Figure 5.4-6 presents annual 1978 distributions for each location converted to a 30 degree elevation angle. The distributions were converted to a 30^o elevation angle by the relation

$$A_{30} = (\sin\theta/\sin 30^o)\, A_\theta$$

where A_θ is the measured attenuation in dB at the elevation angle θ, and A_{30} is the attenuation at an elevation angle of 30^o. The distributions for the

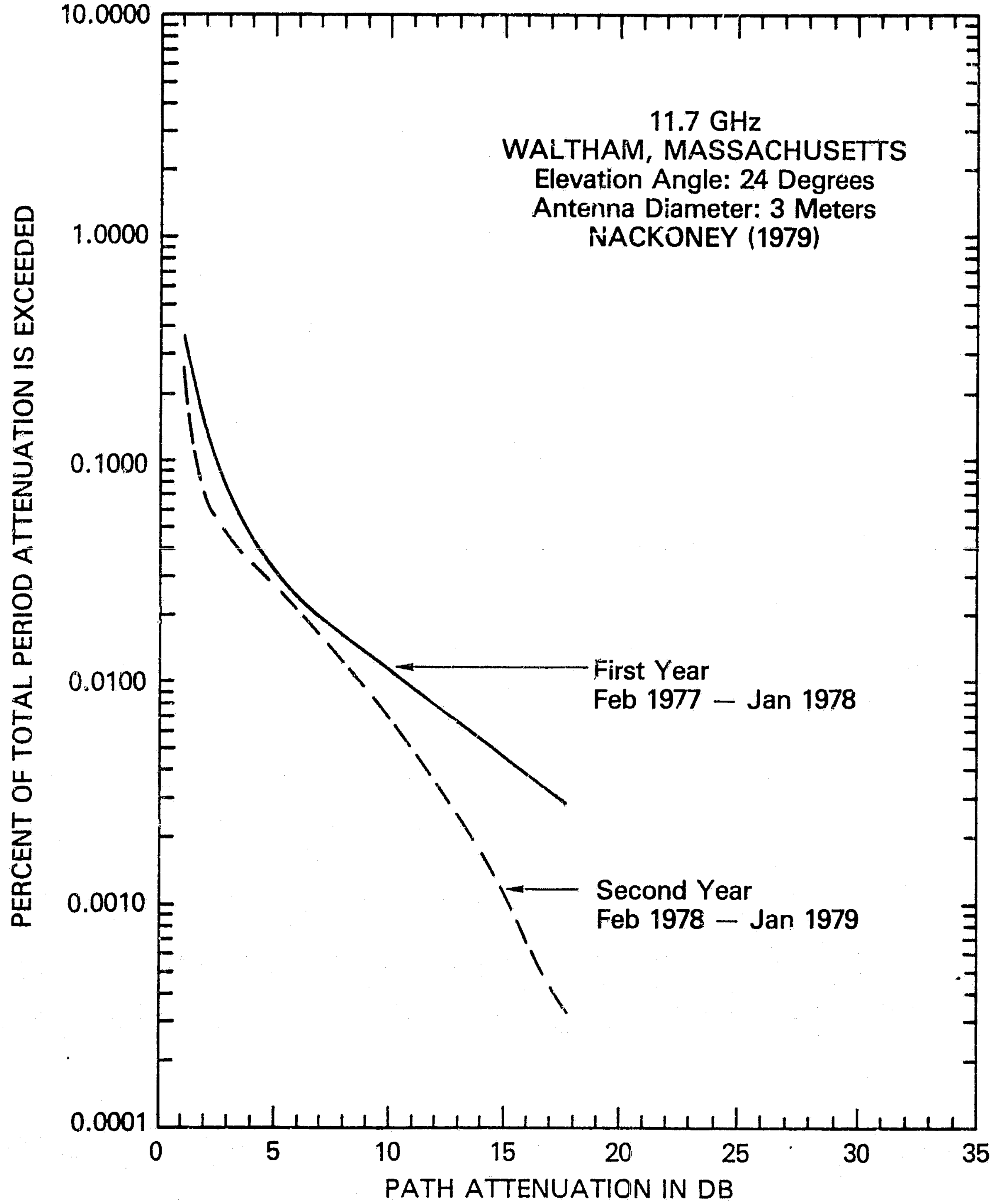

Figure 5.4-1 Annual 11.7 GHz Attenuation Distributions for Waltham, MA

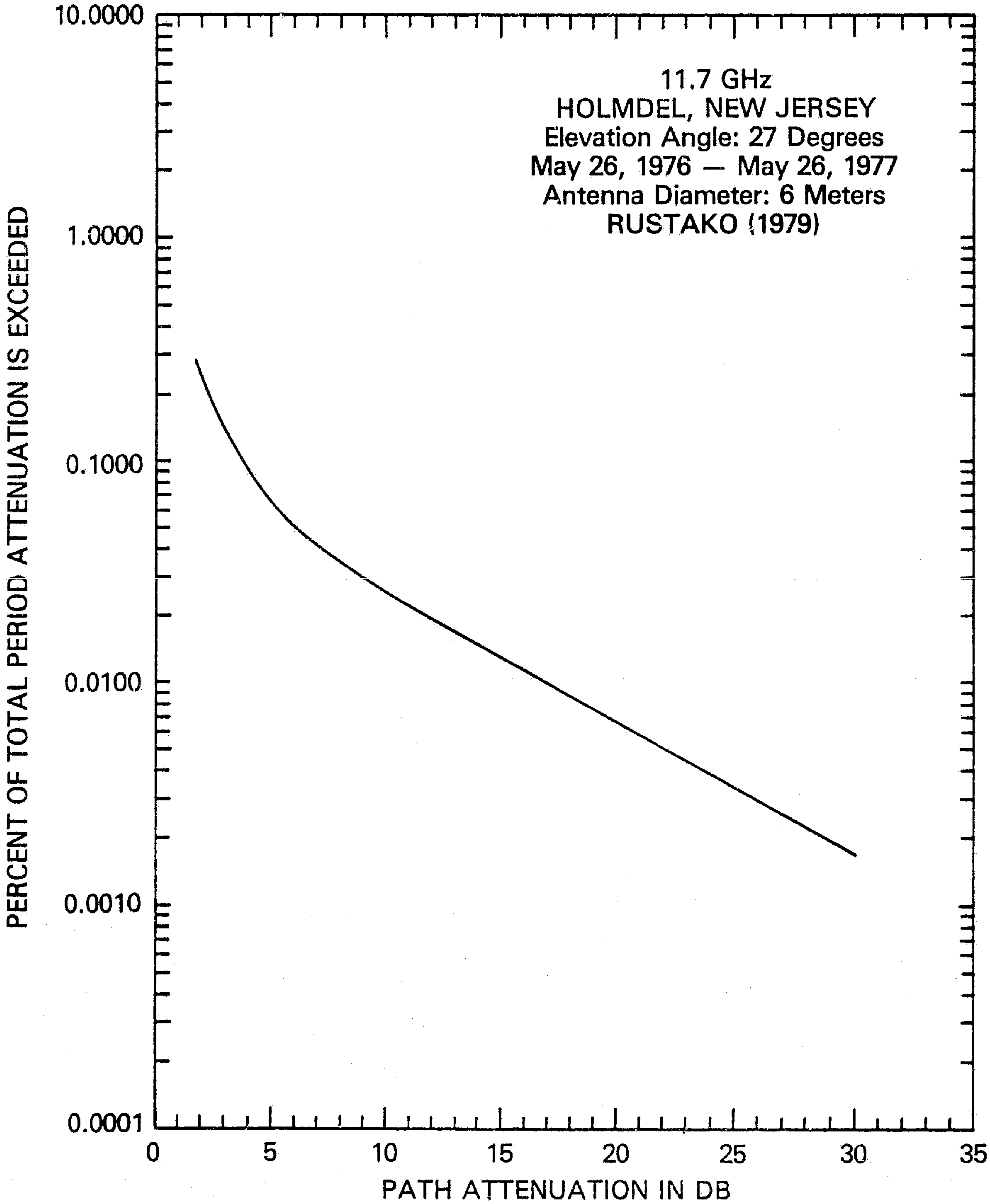

Figure 5.4-2 Annual 11.7 GHz Attenuation Distribution for Holmdel, NJ

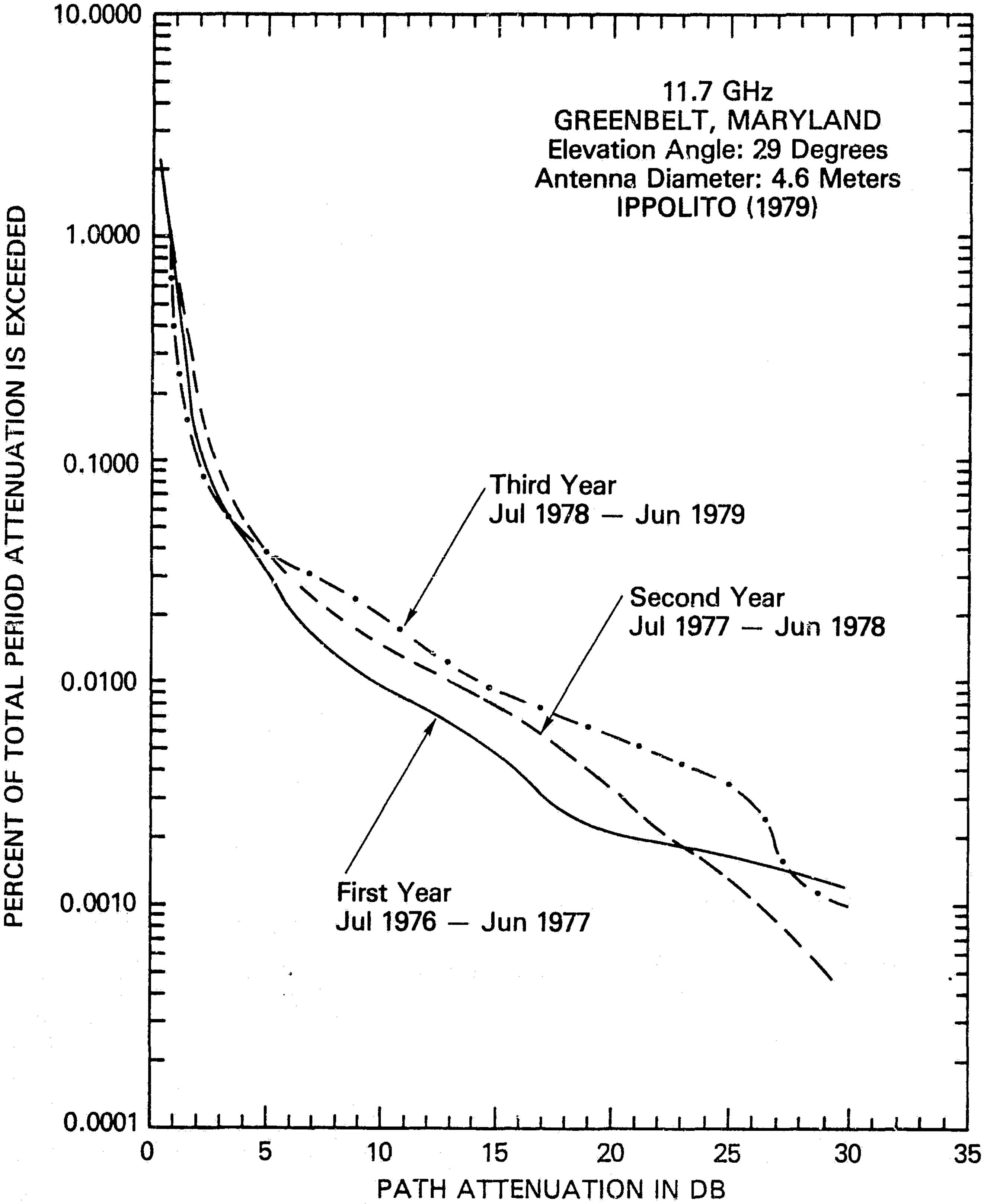

Figure 5.4-3 Annual 11.7 GHz Attenuation Distributions for Greenbelt, MD

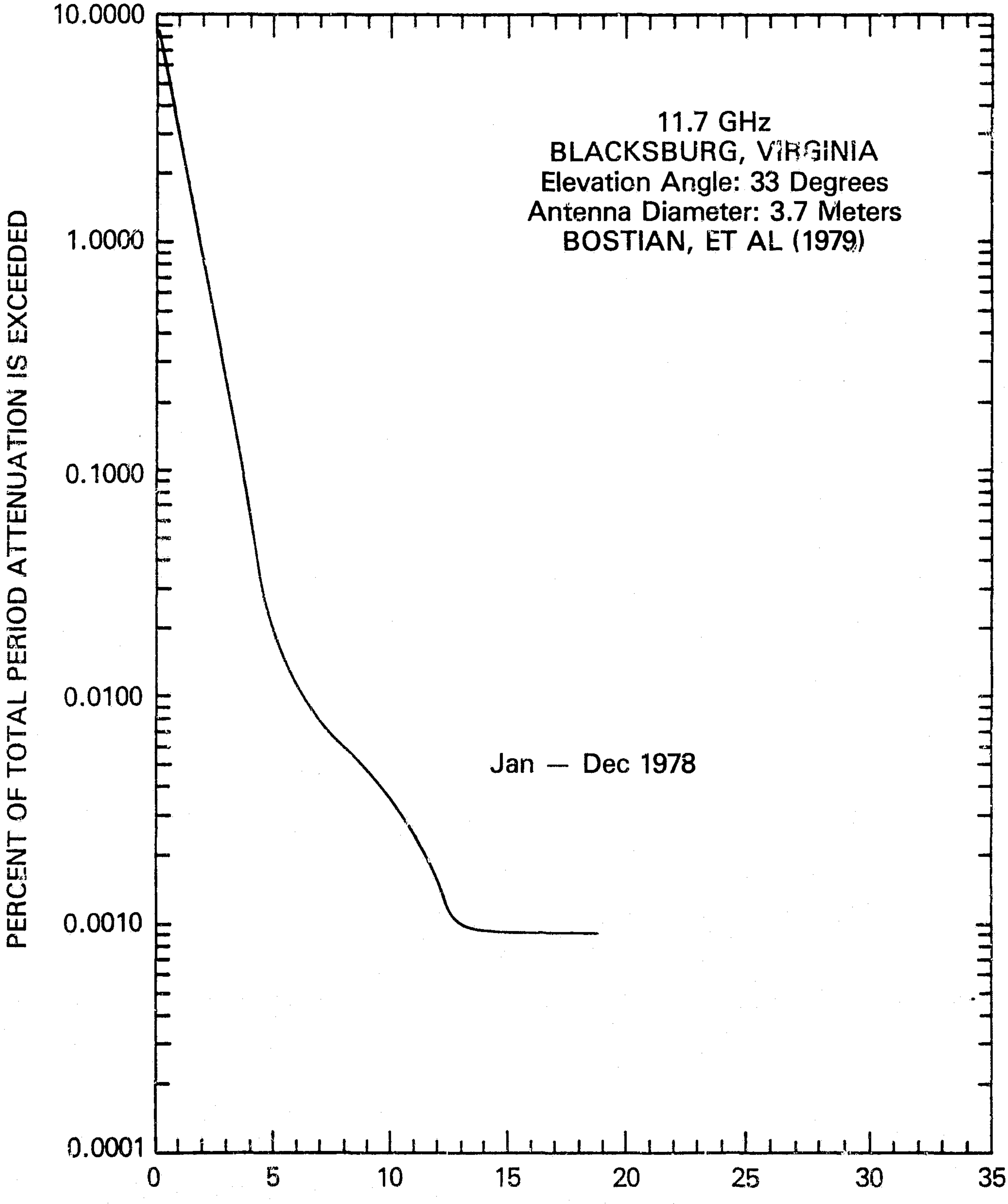

Figure 5.4-4 Annual 11.7 GHz Attenuation Distribution for Blacksburg, Va.

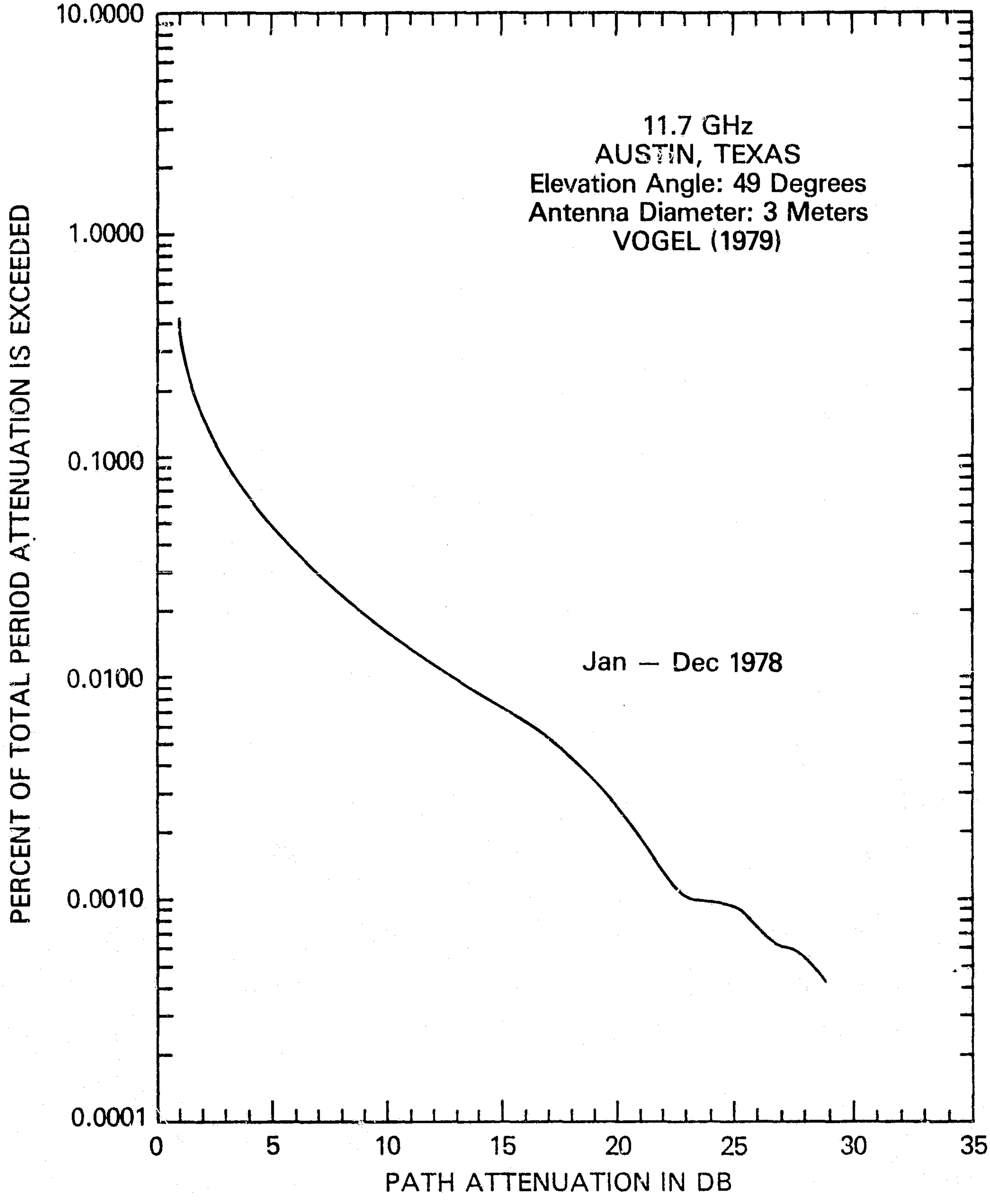

Figure 5.4-5 Annual 11.7 GHz Attenuation Distribution for Austin, TX

Table 5.4-1

Annual 11.7 GHz Attenuation Statistics Summary

LOCATION	ELEVATION ANGLE	TIME PERIOD	ATTENUATION (dB) FOR GIVEN PERCENT OUTAGE						
			1%	0.5%	0.1%	0.05%	0.01%	0.005%	0.001%
Waltham, MA	24^{0}	Feb '77 - Jan '78 Feb '78 - Jan '79	<1 <1	<1 <1	2.5 1.5	4 2.8	1[illegible].5 8.5	14.5 11	(23) 15.3
Holmdel, N.J.	27^{0}	May '76 - Apr '77 May '77 - Apr '78 May '78 - Apr '79	<1 <1 <1	1.5 1.2 1.2	4 3 2.8	6.5 4 3.5	17.5 10.5 8	22.5 13.5 11.8	>30 >30 >30
Greenbelt, MD	29^{0}	Jul '76 - Jun '77 Jul '77 - Jun '78 Jul '78 - Jun '79	<1 <1 <1	<1 1 <1	1.8 2.1 1.8	3.2 3.8 3.2	8.8 12 14	14.5 18 21	>30 26.4 29.2
Blacksburg, VA	33^{0}	Jan '78 - Dec '78	2	2.7	3.7	4.3	6.8	8.6	13
Austin, TX	49^{0}	Feb '78 - Jan '79	<1	1	3	5.5	13	18	23

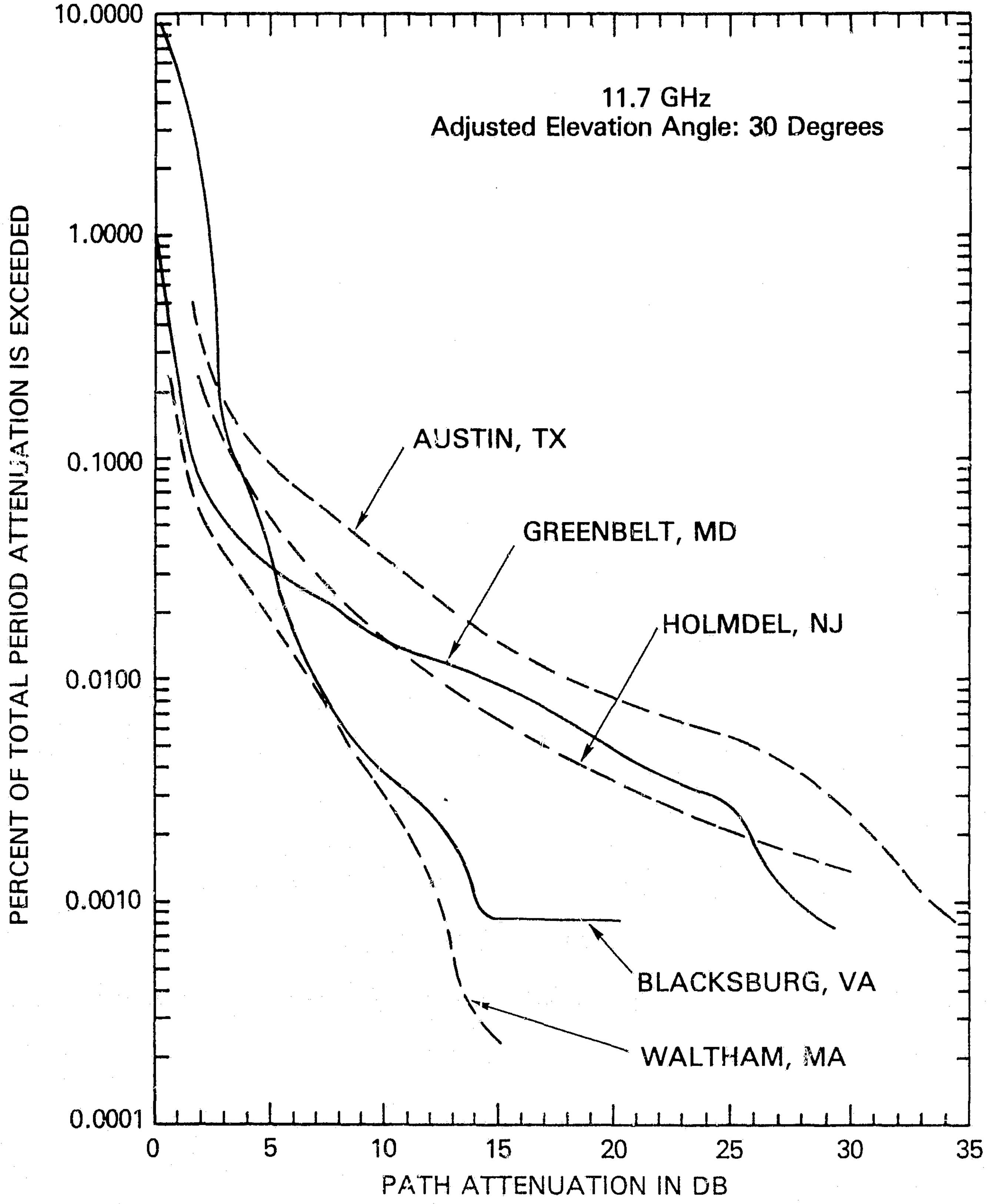

Figure 5.4-6 Comparison of Annual 11.7 GHz Attenuation Distribution of Measurements at Five Locations Adjusted to 30 Degrees Elevation Angle

two nearest locations, Greenbelt and Holmdel, show some similarity, while the distributions for Blacksburg and Waltham are significantly lower. Comparisons of this kind should be observed with some caution, however, since the distributions are based on only 12 months of continuous data, and local precipitation conditions will vary greatly from year to year (see above).

It is interesting to note, however, that all five locations are located in similar temperate continental rain climate regions. Two rainfall region models are available in CCIR publications, that of Rice and Holmberg (1973) described in CCIR Rep 563-1 (1978a), and the Global Precipitation Model of Crane (1980), presented in CCIR Document P/105-E (1978b). Both place the five locations discussed here in the same climate zones. Thus, attenuation prediction models based on the two above referenced procedures would yield similar attenuation distributions for all five locations. Such a similarity is not evident for the measured annual distributions presented here for those five locations.

Figure 5.4-7 presents distributions at three locations where long-term measurements, extending from 29 to 36 months duration, were available. The long-term distributions are much smoother than the individual 12 month distributions, and the curves for Holmdel and Greenbelt are very similar, particularly in the region from .01 to .0025%, which is the area of great interest for system design margin criteria. The results point out the desirability for multi-year continuous measurements in the evaluation of rain attenuation effects on communications system performance.

5.4.2 15-16 GHz Data

The 15 to 16 GHz experimental data base shown in Figure 5.4-8 is limited. The satellite beacon measurements were taken by NASA and COMSAT at North Carolina and Maryland. The earlier radiometer measurements by Bell Telephone Laboratories are included to supplement this satellite data. These radiometer measurements appear to agree with the satellite data up to 14 dB where the radiometer measurements stop because of sky temperature saturation. No other long-term 15 GHz data bases are known to exist in the US or Canada. However, the Tracking and Data Relay Satellite System will eventually provide extensive data for 7 to 22 degree elevation angles from White Sands, NM.

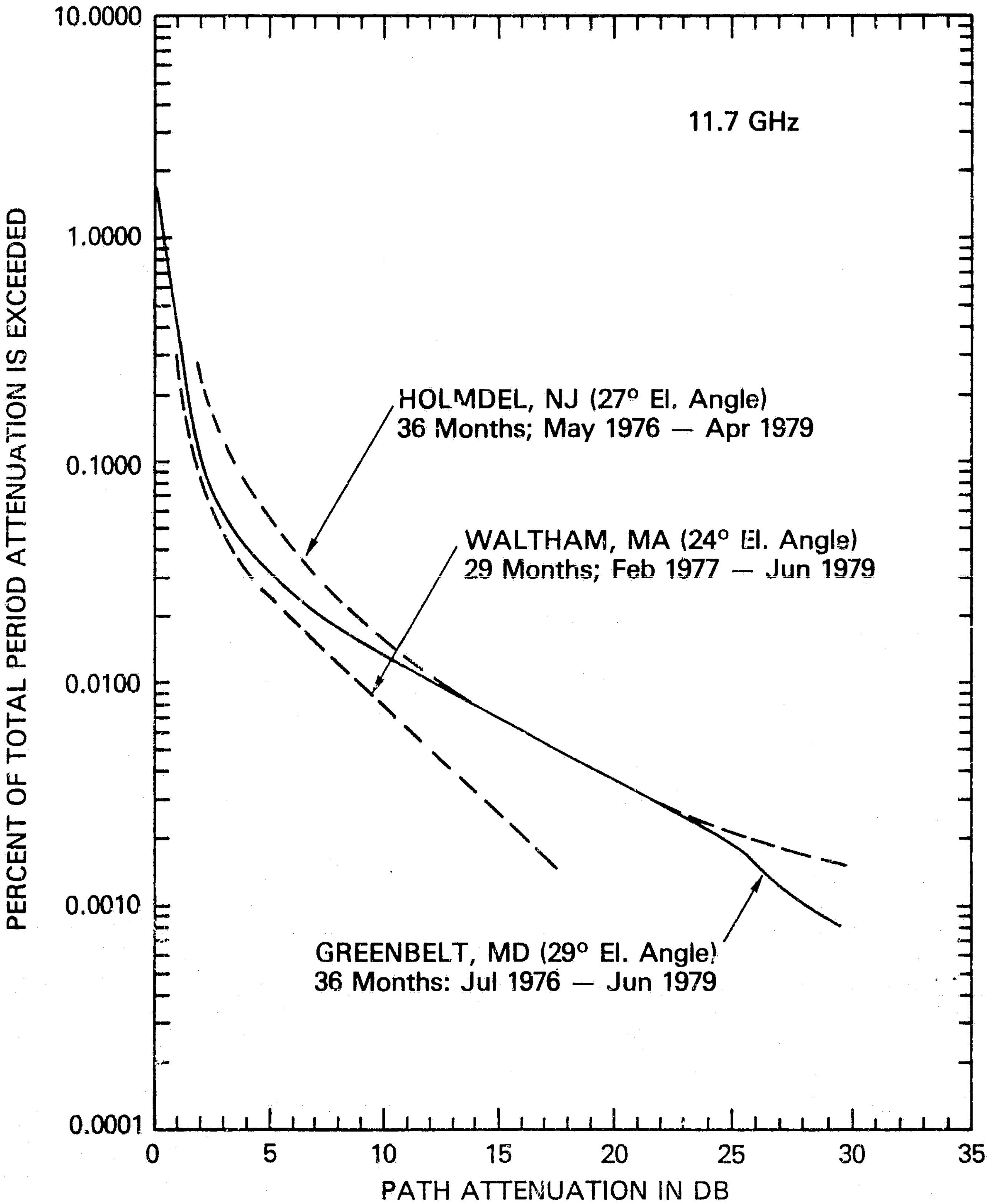

Figure 5.4-7 Long-Term 11.7 GHz Attenuation Distributions for Three Locations With Nearly Identical Elevation Angles

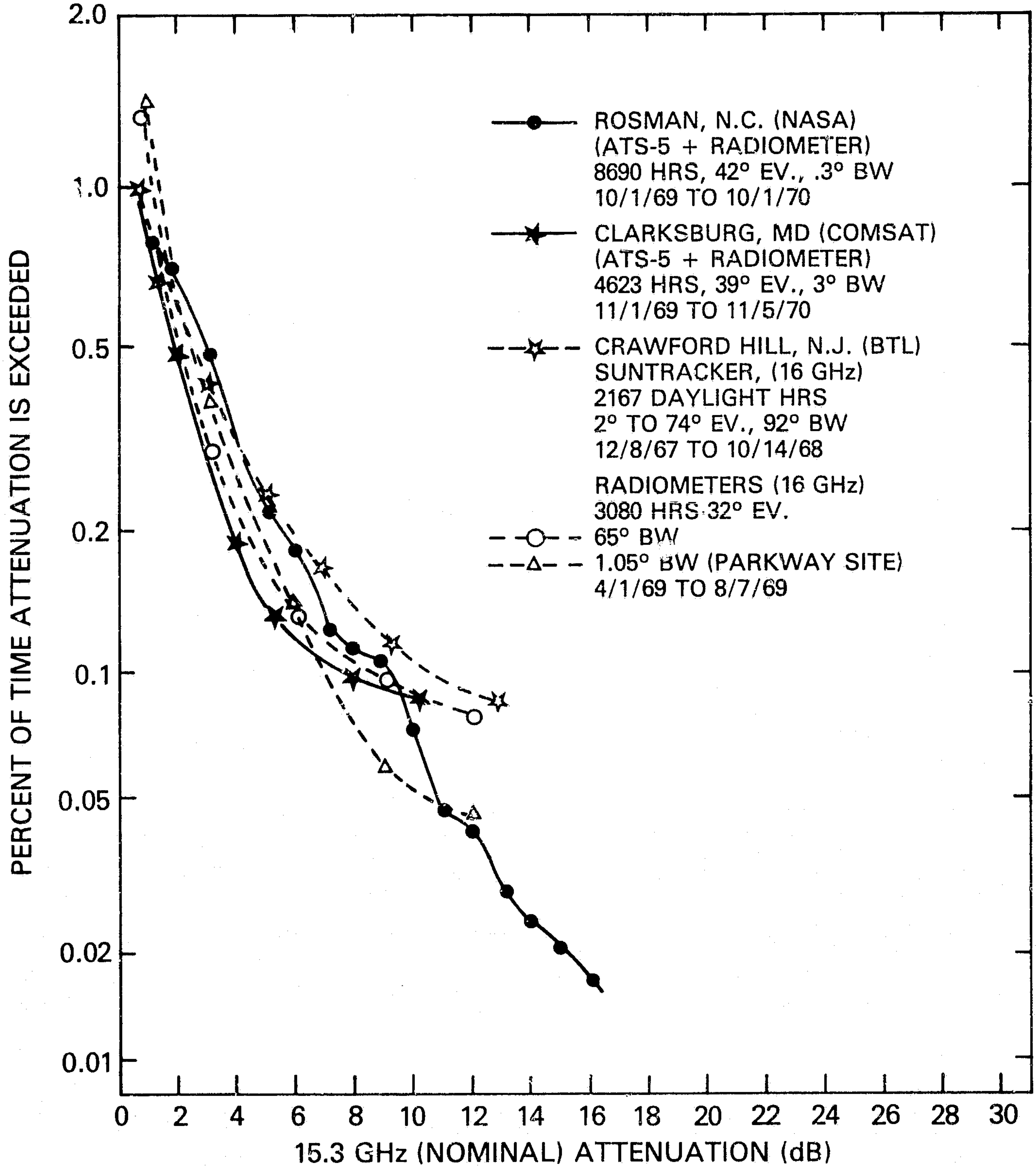

Figure 5.4-8 Summary of 15 GHz Measurements

5.4.3 19-20 GHz Data

Cumulative attenuation data in the 19 to 20 GHz range has been accumulated from both the ATS-6 and the COMSTAR beacons. In addition, the COMSTAR beacon has provided a source for direct measurement of depolarization.

The cumulative attenuation statistics at 19.04 and 20.0 GHz have been plotted in Figure 5.4-9. The Crawford Hill COMSTAR measurements (curve 2) included independent measurement of attenuation on nearly vertical (21 degrees from vertical) and nearly horizontal polarizations. Generally, horizontal and circularly polarized signals are attenuated more than vertically polarized signals. At 0.01% of the time, the COMSTAR measurements showed the horizontal attenuation to be about 2 dB greater than the vertical polarization (Cox, et.al - 1979a). The polarization dependence arises because of the shape and general orientation of the raindrops. Also shown are the effects of hurricane Belle on the annual cumulative statistics. Clearly, this single event significantly shifts the curve for the moderate values of attenuation associated with heavy, but not intense, rain rates.

5.4.4 28-30 GHz Data

The 28.56 GHz COMSTAR beacons and the 30 GHz ATS-6 beacon have provided excellent sources for attenuation measurements in the 30 GHz frequency region. The cumulative attenuation statistics for several locations are given in Figure 5.4-10. Note that as with the 20 GHz data, the Blacksburg, VA data shows a characteristic plateau at 0.001 percent. The reason for this plateau is unclear, but it may arise due to the local climatology of the ground station and the nearby hills.

5.4.5 Frequency Scaling of Attenuation Data

The relation between measured attenuations may be examined in several ways. The so-called statistical relation is obtained as a set of paired attenuations that are exceeded for equal amounts of time. These points may be obtained from the cumulative attenuation distributions. For the Crawford Hill measurements, for example, (Arnold, et al-1979) 19.5 dB attenuation at 19 GHz

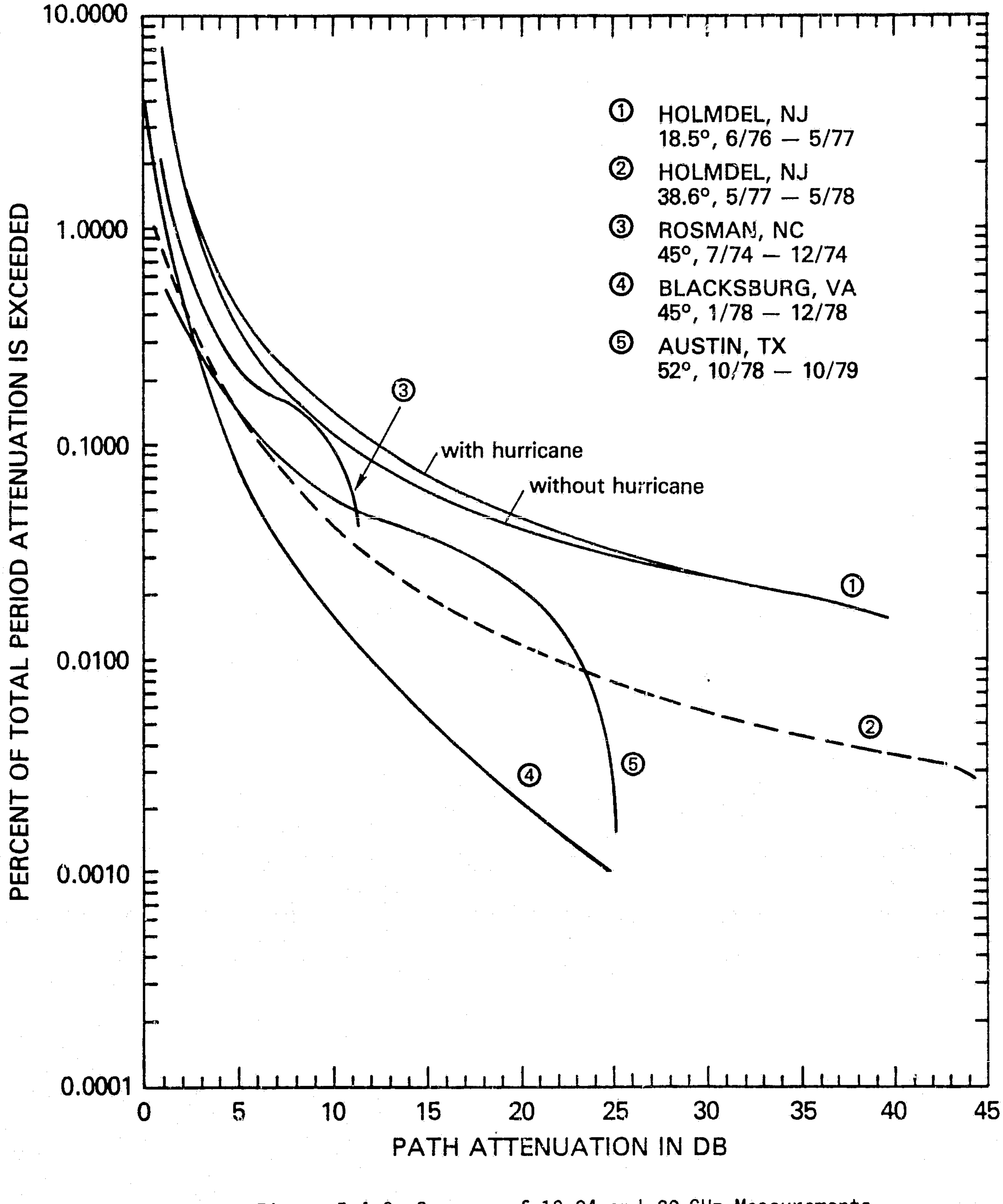

Figure 5.4-9 Summary of 19.04 and 20 GHz Measurements

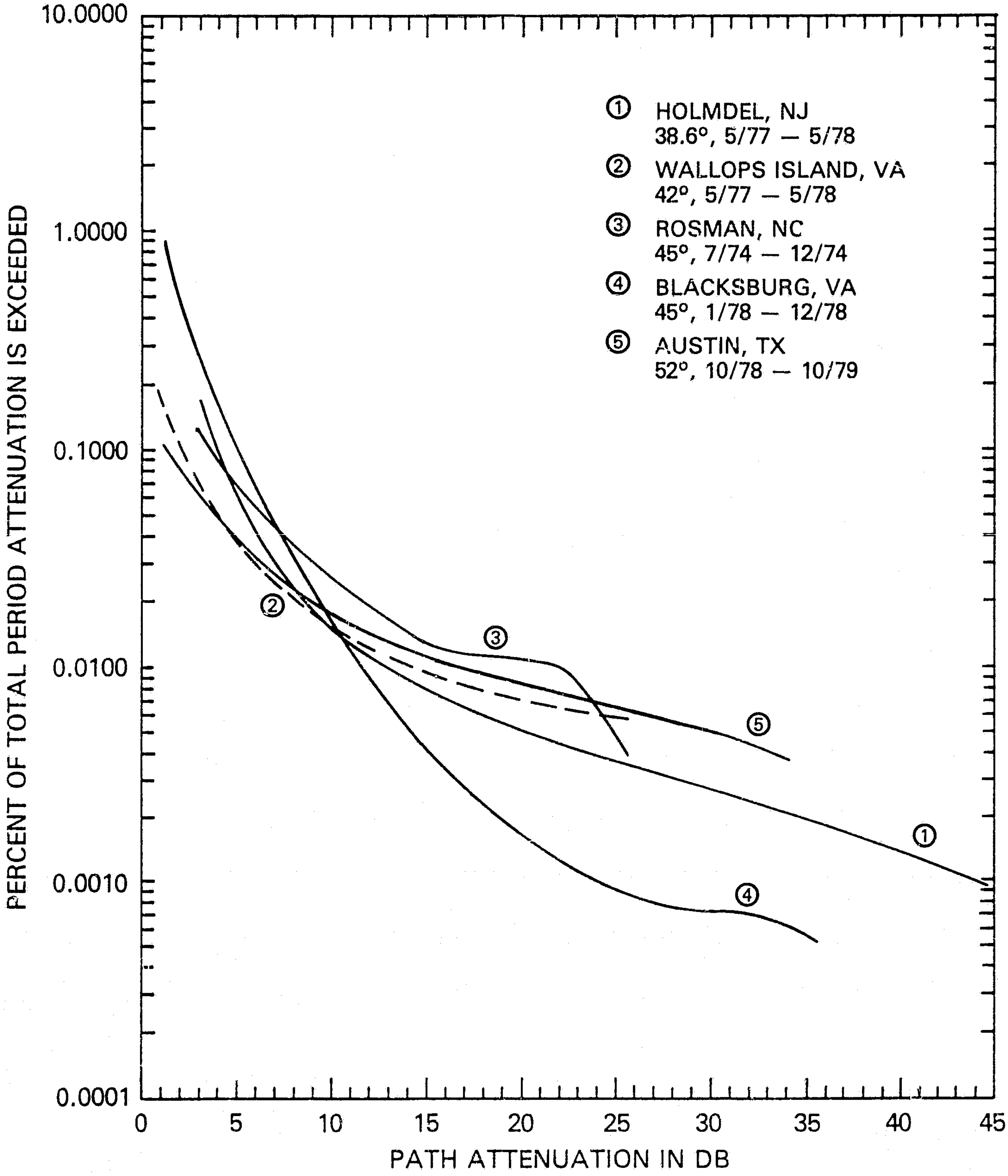

Figure 5.4-10 Summary of 28.56 and 30 GHz Measurements

and 40.3 dB at 28 GHz were both exceeded for 65 min. This statistical relation is plotted in Figure 5.4-11 as a series of open circles for 19 and 28 GHz data for Crawford Hill.

The instantaneous attenuation relation may be determined from simultaneous data recordings of attenuation at the two frequencies. This instantaneous relation is also shown in Figure 5.4-11. The dashed curve indicates the median 19 GHz attenuation observed for values of 28 GHz attenuation on the abscissa. The bars in the figure indicate the span between the 10% and 90% points in the distribution of 19 GHz attenuations observed for the 28 GHz attenuation values. The quantization is 0.5 dB for the 10% and 90% points and for the median. Note that, while these results are statistical in nature as well, the quantity considered is the instantaneous attenuation for the two frequencies. It is evident from the figure that the statistical relation and the median instantaneous relation are essentially identical.

The dotted line on Figure 5.4-11 is the line for $A_2 = (f_2/f_1)^2 A_1 = 2.25A_1$, where A_1 is the attenuation in dB at frequency f_1 = 19.04 GHz and A_2 is the attenuation in dB at frequency f_2 = 28.56 GHz. The relationships between the measured attenuations depart from a frequency squared relation particularly at high attenuation. A straight line, $A_2 = 2.1A_1$ fits the data closely up to A_1 20 dB, but the data depart from this line at still higher attenuation. This less than frequency squared attenuation dependence is consistent with the frequency dependence of Chu's theoretical attenuation coefficients (1974) in this frequency range. The further decrease in frequency dependence at higher attenuations is consistent with the same effect observed in the theoretical coefficients at higher rain rate since higher attenuation is associated with more intense rain.

In Figure 5.4-11, the increase in the spread between 10% and 90% points as attenuation increases is consistent with constant fractional fluctuation in the ratio of the attenuations at the two frequencies.

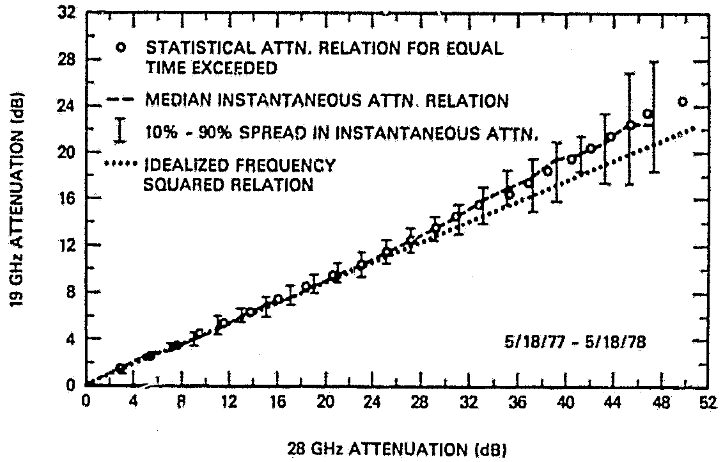

Figure 5.4-11. Relationships between 19 and 28 GHz attentuation for earth-space radio propagation.

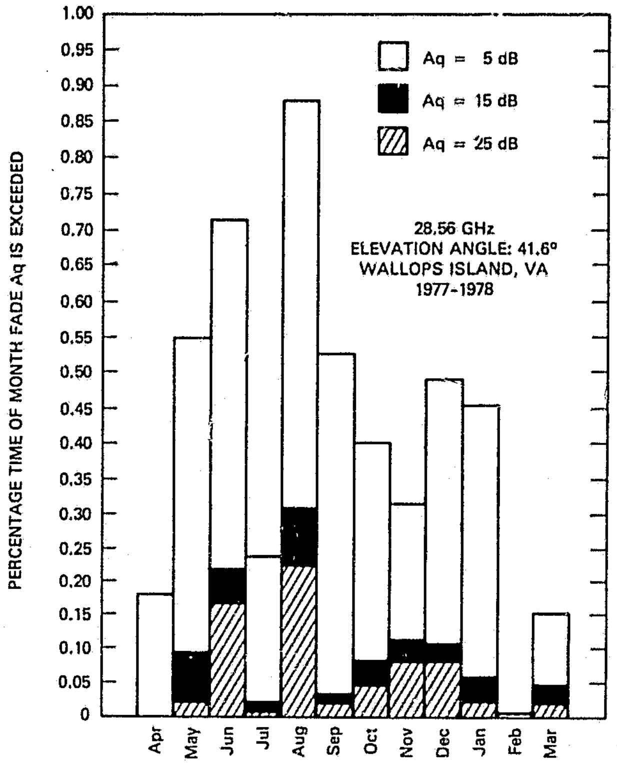

Figure 5.5-1. Histogram denoting percentage times for various months the fades of 5, 15, and 25 dB were exceeded.

5.5 TEMPORAL DISTRIBUTION OF FADES

Systems may be able to accommodate fades during certain months or periods of the day more readily than during other periods. To help assess the magnitude of these effects along the eastern U.S. coast, Goldhirsh (1979) has prepared histograms and cumulative distributions for various months and times.

5.5.1 Monthly Distribution of Attenuation

Figure 5.5-1 shows the percentage of time for each month in the period April 1977 to March 1978 that fades of 5, 15, and 25 dB were exceeded. These measurements were made at 28.56 GHz from the COMSTAR D2 satellite to Wallops Island, VA at an elevation angle of 41.6 degrees. The fades are more excessive during the summer months, except for July. This low value for July is not expected to be representative for that month and demonstrates how data from a single year can misrepresent the long-term average value.

Weather Bureau data may also be utilized to obtain this distribution by month, but this procedure may be inaccurate because the type of rain may vary significantly throughout the year. Some consideration to the amount of rainfall occurring in thunderstorms in a given month is needed to made these estimates more realistic. Ideally the rain rate distribution for each month would be required along with the attention models presented in Chapter 3.

5.5.2 Diurnal Distribution of Attenuation

Severe fades (those associated with thunderstorms) are most likely to occur during the late afternoon and early morning hours when tropospheric heat exchange is the greatest. This is confirmed by data taken at Wallops Island, VA from the 28.56 GHz COMSTAR beacon. Goldhirsh (1979) has presented the data in two formats. In Figure 5.5-2 the distribution averaged over four hour periods is presented, while in Figure 5.5-3 the cumulative distributions for the six four-hour time periods are displayed. These plots show basically the same data, except that the rain rate distribution can be inferred from Figure 5.5-3 more readily than in the histogram format. As described in Section 5.5.1, this data can be inferred from the Weather Bureau data, but some

Figure 5.5-2

Histogram denoting percentages of year the fade depths of 5, 15, and 25 dB were exceeded for six contiguous four-hour time slots of the day.

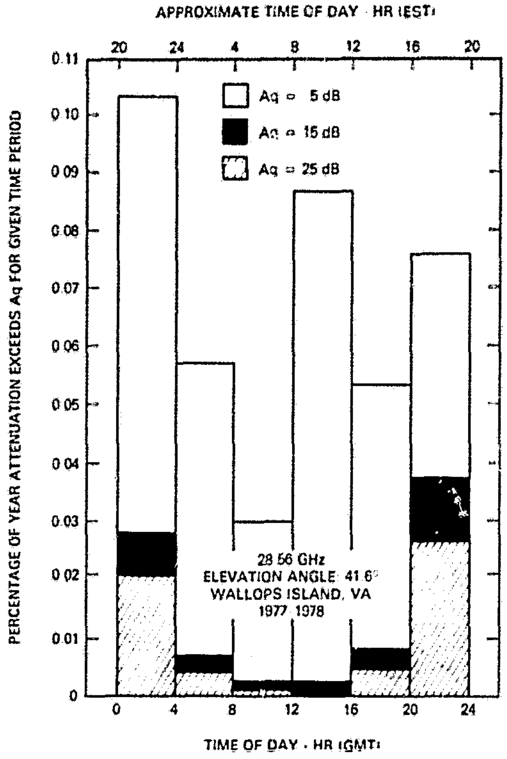

Figure 5.5-3

Cumulative distributions for six contiguous four-hour time slots of day for entire year period.

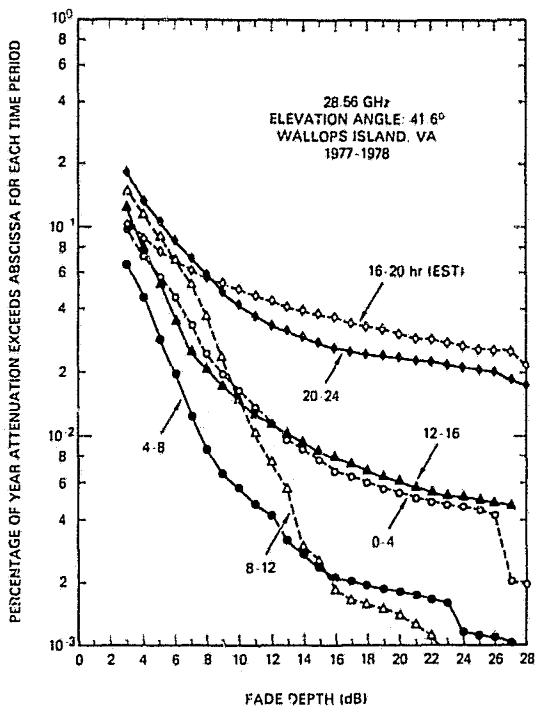

estimation of the rain rate distribution variation throughout the day is required for an accurate estimate. Generally this data is not available from Weather Bureau publications, but can be obtained from guage charts.

5.6 EXPERIMENTAL DEPOLARIZATION DATA

The crosspolarization discrimination not exceeded for a given percentage of time is approximated by a relation (Nowland, et al-1977)

$$XPD = \tilde{a} - \tilde{b} \log_{10} (CPA)$$

where CPA is the copolarized attenuation value in decibels exceeded for the same percentage of time. This suggests that the data be presented in a semilogarithmic format wherein each parameter is already a logarithm of another parameter. Therefore, in this Handbook we have replotted the results of others in order to present a uniform format of the data and to allow easy comparison with the CCIR analytic estimate (see Eq. 4.3-27).

5.6.1 19 GHz Data

Figure 5.6-1 and 5.6-2 present the 19 GHz cross-polarization data obtained by the Bell Laboratories experimenters at Crawford Hill, NJ (Arnold, et al-1979). The near vertical polarization appears to have slightly more cross-polarization discrimination than the horizontal polarization. However, both polarizations show less discrimination than the CCIR estimate. Therefore, in this case, the CCIR approximation appears to be optimistic.

5.6.2 28 GHz Data

The COMSTAR signal at 28 GHz has a fixed polarization, thus allowing measurements at only one orientation with respect to the raindrop anisotropy. The data replotted from Bell measurements (Arnold, et al-1979) is shown in Figure 5.6-3. Again, the CCIR approximation is over-optimistic when compared to the measured data.

C-3

Figure 5.6-1

19 GHz Cross-Polarization Measurements - Near Vertical Polarization

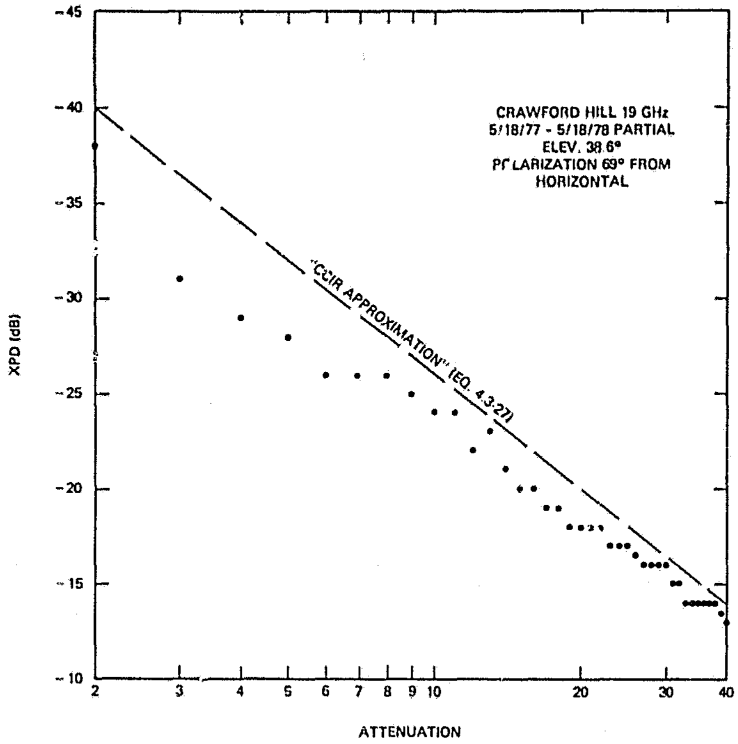

Figure 5.6-2

19 GHz Cross-Polarization Measurements - Near Horizontal Polarization

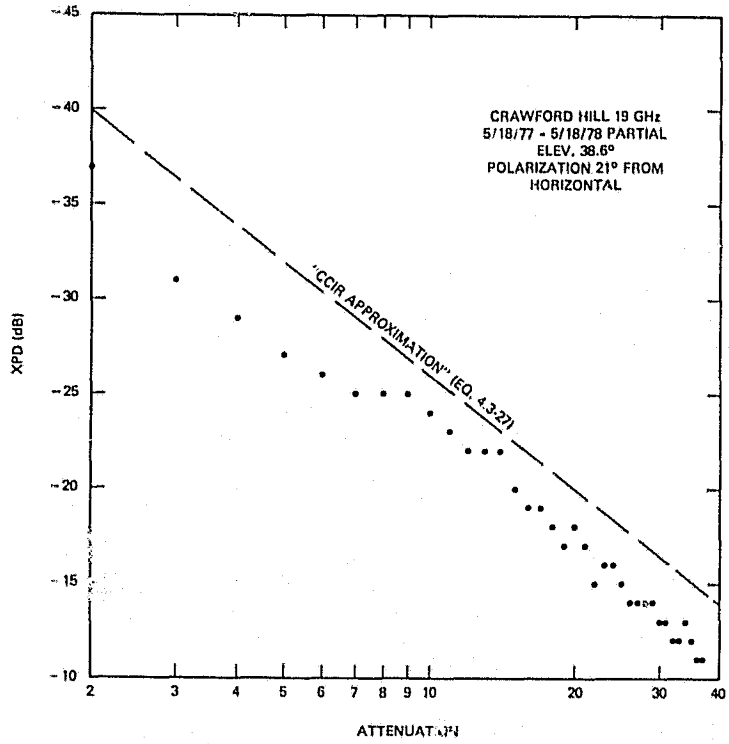

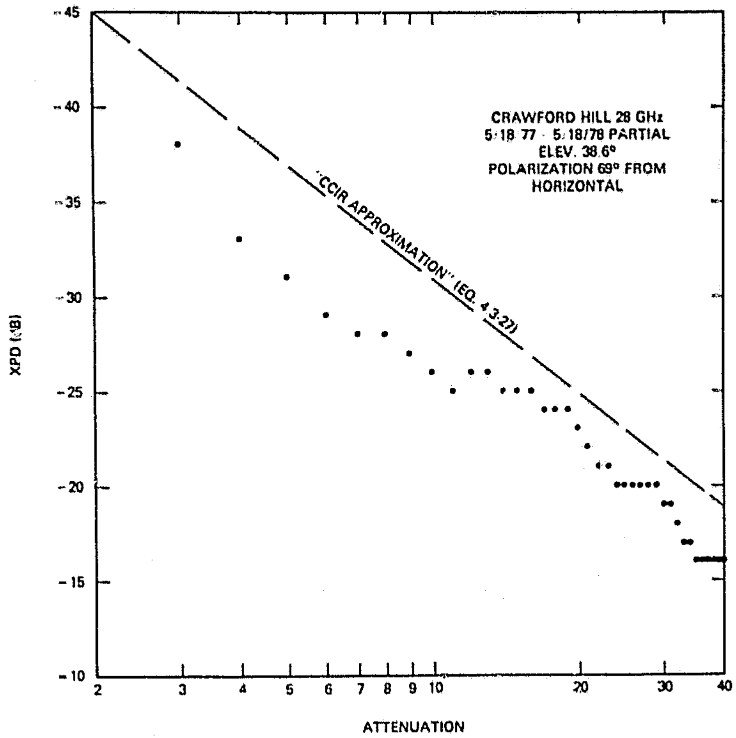

Figure 5.6-3
28 GHz Cross-Polarization Measurements

5.7 PHASE AND AMPLITUDE DISPERSION

Experimental measurements of the phase and amplitude dispersion in the lower troposphere made from the COMSTAR D2 satellite have been made at Crawford Hill, NJ (Cox, et al-1979b). The measurements were made across the 528 MHz coherent sidebands at 28 GHz and between the 19 and 28 GHz carriers which were coherent.

The nine-month Crawford Hill data set has been comprehensively searched for evidence of phase dispersion. For all propagation events, the change in average sideband to carrier phase is less than the measurement uncertainty of about 13° for attenuation up to 45 dB. Phase fluctuations are consistent with signal-to-noise ratios over the 45dB attenuation range. The change in average 19 to 28 GHz phase is on the order of 60° over a 30 dB attenuation range at 28 GHz. This average phase change appears to be due only to the average dispersive properties of the water in the rain along the path. There is no evidence of multipath type dispersion.

Attenuation in dB at 28 GHz is 2.1 times greater than that at 19 GHz for attenuations up to 29 dB at 19 GHz. The small spread observed in the relationship between 19 and 28 GHz attenuations is consistent with the absence of significant phase dispersion over the 528 MHz bandwidth.

5.8 REFERENCES

Arnold, H.W., D.C. Cox, H.W. Hoffman and R.P. Leck (1979), "Characteristics of Rain and Ice Depolarization for a 19 and 28 GHz Propagation Path from a COMSTAR Satellite," Conference Record, ICC 79, vol. 3, Boston, MA pp 40.5.1-6.

Bostian, C.W., et al (1979), "A Depolarization and Attenuation Experiment Using the COMSTAR and CTS Satellites," Virg. Poly. Inst. and State Univ., Annual Report, NASA Cont. NAS5-22577.

CCIR (1978a), Vol. 5, Recommendations and Reports of the CCIR, XIVth Plenary Assembly, Kyoto, Japan, ITU, Geneva.

CCIR (1978b), "Rain Attenuation Prediction," Document P/105-E, CCIR Study Groups, Special Preparatory Meeting (WARC-79), ITU, Geneva.

Chu, T.S. (1974), "Rain Induced Cross-Polarization at Centimeter and Millimeter Wavelengths," BSTJ, vol. 53, pp 1557-79.

Cox, D.C., H.W. Arnold and A.J. Rustako, Jr. (1979a), "Attenuation and Depolarization by Rain and Ice Along Inclined Radio Paths Through the Atmosphere at Frequencies Above 10 GHz," Conference Record, EASCON 79, Arlington, VA, vol. 1, pp 56-61.

Cox, D.C., H.W. Arnold and R.P. Lick (1979b), "Phase and Amplitude Dispersion for Earth-Space Propagation in the 20 to 30 GHz Frequency Rang," URSI Program and Abstracts, Spring Meeting, Seattle, Washington, June 18-22, p 253.

Crane, R.K. (1980), "Prediction of Attenuation by Rain," paper submitted to IEEE Trans. on Comm.

Crane, R.K. and D.W. Blood (1979), "Handbook for the Estimation of Microwave Propagation Effects - Link Calculations for Earth-Space Paths," ERT Tech. Rpt. No. 1, NASA Contract NAS5-25341.

Goldhirsh, J. (1979), "Cumulative Slant Path Rain Attenuation Statistics Associated with the Comstar Beacon at 28.56 GHz for Wallops Island, VA," IEEE, Trans. Ant. Prop., vol. AP-27, No. 6, pp 752-758.

Ippolito, L.J. (1978), "11.7 GHz Attenuation and Rain Rate Measurements With the Communications Technology Satellite (CTS)," NASA Tech. Memo. 80283, Greenbelt, MD.

Kaul, R., D. Rogers and J. Bremer (1977), "A Compendium of Millimeter Wave Propagation Studies Performed by NASA," ORI Tech. Rpt., NASA Contract NAS5-24252.

Nackoney, O.G. (1979), "CTS 11.7 GHz Propagation Measurements, Third Year's Data and Final Report," GTE Laboratories Report TR-79-471.2, Waltham, MA.

Nowland, W.L., R.L. Olsen and I.P. Shkarofsky, (1977), "Theoretical Relationship Between Rain Depolarization and Attenuation," Electronics Letters, vol. 13, No. 22, pp 676-7.

Rice, P.L. and N.R. Holmberg (1973), "Cumulative Time Statistics of Surface Point Rainfall Rates," IEEE Trans. Comm., vol. COM-21, pp 1131-1136.

Rustako, A.J., Jr. (1979), "Measurement of Rain Attenuation and Depolarization of the CTS Satellite Beacon at Holmdel, New Jersey," 1979 USNC/URSI Meeting, June 18-22, Seattle WA (abstract).

Vogel, W.J. (1979), "CTS Attenuation and Cross Polarization Measurements at 11.7 GHz," Univ. Texas Austin, Final Rpt., NASA Contract NAS5-22576.

CHAPTER VI

PREDICTION TECHNIQUES

6.1 INTRODUCTION

6.1.1 Purpose

This chapter provides a guide to prediction methods and related propagation results for the evaluation of earth-space paths operating above 10 GHz. The topics covered are:

Gaseous Attenuation
Rain Attenuation
Cloud, Fog, Sand and Dust Attenuation
Path Diversity
Signal Fluctuations and Low Angle Fading
Depolarization Effects
Bandwidth Coherence
Sky Noise

The techniques described here have been developed from recent ongoing NASA supported studies and from the relevant published literature. These techniques represent the state of knowledge of the adverse effects of the earth's atmosphere on reliable earth-space transmissions above 10 GHz.

This chapter provides propagation data in a format suitable for use by earth-space link system designers operating in the frequency range from 10 to 100 GHz in the United States and Canada. In this frequency range the troposphere can have a significant effect on the carrier-to-noise ratio of a propagating wave. Typically, the troposphere attenuates and depolarizes the carrier signal and adds broadband amplitude and phase noise to the signal. The resulting carrier-to-noise ratio reduction reduces the allowable data rate for a given bit error rate (digital systems) and the quality of transmission (analog systems). In the most severe cases the medium will significantly attenuate the carrier and destroy the transmission capabilities of the link (termed a link outage). The frequency of occurrence and average outage time per year are usually of most interest to system designers. Propagation studies to date now allow the predictions to be made with a high degree of certainty and have developed means to reduce the frequency and length of these outages.

6.1.2 Organization of This Chapter

This chapter is arranged in eight relatively independent sections covering the key topics related to the interaction of the troposphere and earth-space propagation paths. Each section presents a description of the effect(s) and an example calculation related to a typical communication system. Because these examples provide a concise guide to the calculations required, an index to the examples is given in Table 6.1-1.

6.1.3 Frequency Bands for Earth-Space Communication

Within the guidelines established by the International Telecommunication Union (ITU) for Region 2 (includes U.S. and Canada), the Federal Communications Commission (FCC) in the U.S. and the Department of Communications (DOC) in Canada regulate the earth-space frequency allocations. In most cases, the FCC and DOC regulations are more restrictive than the ITU regulations. Therefore, the FCC and DOC earth-space frequency bands are considered in this report.

Table 6.1-1. Guide to Propagation Examples

The services which operate via earth-space links are listed in Table 6.1-2. The definitions of each of these services are given in the Radio Regulations. The specific frequency allocations for these services are relatively fixed. However, some modifications can be expected at the 1979 World Administrative Radio Conference based on the recommendations of the FCC, DOC and others.

A review of the Radio Regulations indicates that most of the frequency spectrum above 10 GHz is assigned to the satellite services or the radio astronomy service. This does not mean that the FCC and DOC will utilize them, but it does highlight the potential for use of these frequency bands. Figure 6.1-1 shows those frequency segments not assigned for potential use by the services listed in Table 6.1-2.

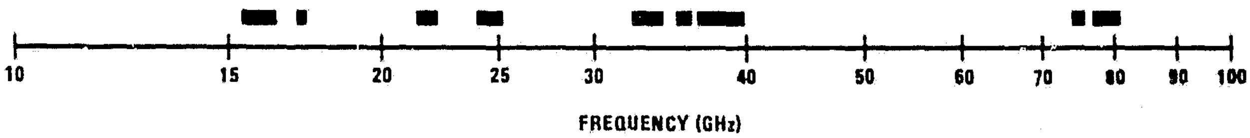

Figure 6.1-1. Frequencies NOT Potentially Available for Earth-Space Transmissions.

Table 6.1-2

Telecommunication Services Utilizing Earth-Space Propagation Links

Fixed Satellite
Mobile Satellite (military satellite)
Aeronautical Mobile Satellite
Maritime Mobile Satellite
Land Mobile Satellite
Broadcasting Satellite
Radionavigation Satellite
Earth Exploration Satellite
Meteorological Satellite
Amateur Satellite
Standard Frequency Satellite
Space Research
Space Operations
Radio Astronomy

6.1.4 Other Propagation Effects Not Addressed in This Chapter

6.1.4.1 Ionospheric Effects. The ionosphere generally has a small effect on the propagation of radio waves in the 10 to 100 GHz range. Whatever effects do exist (scintillation, absorption, variation in the angle of arrival, delay, and depolarization) arise due to the interaction of the radio wave with the free electrons, electron density irregularities and the earth's magnetic field. The density of electrons in the ionosphere varies as a function of geomagnetic latitude, diurnal cycle, yearly cycle, and solar cycle (among others). Fortunately, most U.S. ground station-satellite paths pass through the midlatitude (lowest) electron density region yielding only a small effect on propagation. Canadian stations may be affected by the auroral region electron densities which are normally higher. A more complete discussion of the effects is included in CCIR Volume VI (1978a).

A mean vertical one-way attenuation for the ionosphere at 15 GHz for the daytime is typically 0.0002 dB (Millman-1958), the amplitude scintillations are generally not observable (Crane-1977) and the transit time delay increase over the free space propagation time delay is of the order of 1 nanosecond (Klobuchar-1973). Clearly for most systems operating above 10 GHz these numbers are sufficiently small that other system error budgets will be much larger than the ionospheric contributions.

The one ionospheric effect which might influence wide bandwidth systems operating above 10 GHz is phase dispersion. This topic is discussed in Section 6.8.

6.1.4.2 Tropospheric Delays. Highly accurate satellite range, range-rate and position-location systems will need to remove the propagation group delay effects introduced by the troposphere. Extremely high switching rate TDMA systems may require these corrections in the future. The effects arise primarily due to the oxygen and water vapor in the lower troposphere. Typical total additional propagation delay errors have been measured to be of the order of 8 nanoseconds (Hopfield-1971).

Estimation techniques, based on the measurement of the surface pressure, temperature and relative humidity have been developed (Hopfield-1971, Bean and Dutton-1966, Segal and Barrington-1977) which can readily reduce this error to less than 1 nanosecond. In addition, algorithms for range (Marini-1972a) and range-rate (Marini-1972b) have been prepared to reduce tropospheric contributions to satellite tracking errors.

Since this topic is quite specialized and generally results in an additional one-way delay of less than 10 nanoseconds it is not addressed further in this report. An overview of this subject and additional references are available in CCIR Report 564-1 (1978).

6.2 PREDICTION OF GASEOUS ATTENUATION ON EARTH-SPACE PATHS

The mean attenuation of gases on earth-space paths in the 10 to 100 GHz frequency range has been theoretically modeled and experimentally measured. Above 20 GHz gaseous absorption can have a significant effect on a communication system design depending on the specific frequency of operation. Because of the large frequency dependence of the gaseous absorption, an earth-space communication system designer should avoid the high absorption frequency bands. Alternatively, designers of secure short-haul terrestrial systems can utilize these high attenuation frequency bands to provide system isolation.

6.2.1 Sources of Attenuation

In the frequency range from 10 to 100 GHz the water vapor absorption band centered at 22.235 GHz and the oxygen absorption lines extending from 53.5 to 65.2 GHz are the only significant contributors to gaseous attenuation. The next higher frequency absorption bands occur at 118.8 GHz due to oxygen and 183 GHz due to water vapor. The absorption lines are frequency broadened by collisions at normal atmospheric pressures (low elevations) and sharpened at high altitudes. Thus the total attenuation due to gaseous absorption is ground station altitude dependent.

6.2.2 Gaseous Attenuation

6.2.2.1 One-Way Attenuation Values Versus Frequency. The Zenith one-way attenuation for a moderately humid atmosphere (7.5 g/m^3 surface water vapor density) at various ground station altitudes (starting heights) above sea level is presented in Figure 6.2-1 and Table 6.2-1. These curves were computed (Crane and Blood, 1979) for temperate latitudes assuming the U.S. Standard Atmosphere, July, 45^o N. latitude. The range of values indicated in Figure 6.2-1 refers to the peaks and valleys of the fine absorption lines. The range of values at greater starting heights (not shown) is nearly two orders of magnitude (Leibe-1975).

Table 6.2-1
Typical One-Way Clear Air Total Zenith Attenuation Values, A_c'
(7.5 g/m^3 H_2O, July, 45^oN latitude, 21^oC)

Frequency	ALTITUDE				
	0km*	0.5km	1.0km	2.0km	4.0km
10 GHz	.055	.05	.043	.035	.02
15	.08	.07	.063	.045	.023
20	.30	.25	.19	.12	.05
30	.22	.18	.16	.10	.045
40	.40	.37	.31	.25	.135
80	1.1	.90	.77	.55	.30
90	1.1	.92	.75	.50	.22
100	1.55	1.25	.95	.62	.25

*1 km = 3281 feet

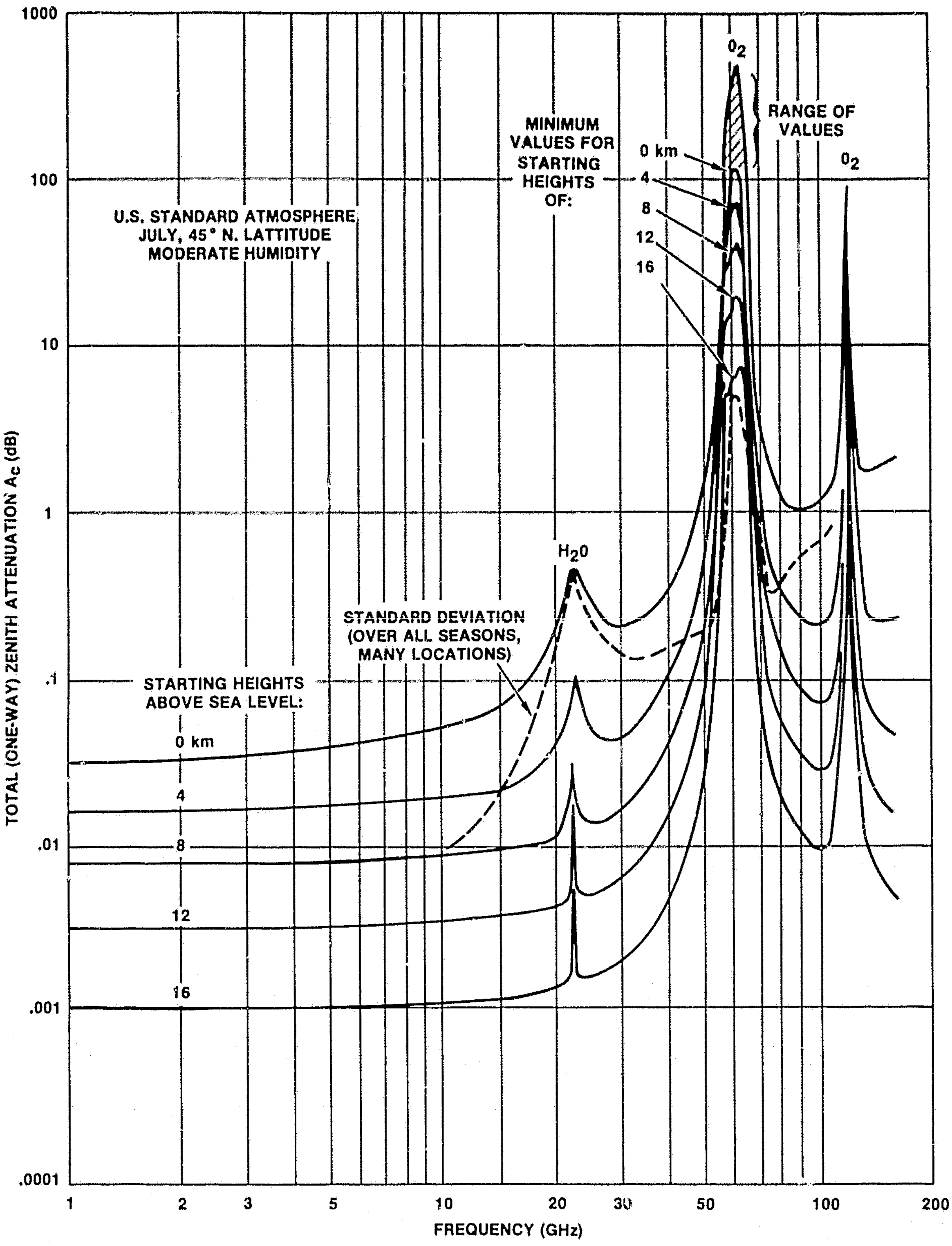

Figure 6.2-1. Total Zenith Attenuation Versus Frequency

Figure 6.2-1 also shows the standard deviation of the clear air zenith attenuation as a function of frequency. The standard deviation was calculated from 220 measured atmosphere profiles, spanning all seasons and geographical locations (Crane-1976).

6.2.2.1.1 Dependence on Ground Station Altitude. The compensation for ground station elevation can be done to first order by linearly interpolating between the curves in Figure 6.2-1. The zenith one-way attenuation for typical ground station altitudes, found in this way, is tabulated in Table 6.2-1 for easy reference.

6.2.2.1.2 Dependence on Water Vapor Content. The water vapor content is the most variable component of the atmosphere. Therefore, for arid or humid regions, a correction should be made based on the expected values of water vapor content when utilizing frequencies between 10 and 50 GHz. This correction to the total zenith attenuation is linearly related to the water vapor density at the surface ρ_o:

$$\Delta A_{c1} = b_\rho \; (\rho_o - 7.5 \text{ g/m}^3)$$

where ΔA_{c1} is an additive correction to the zenith clear air attenuation (given by Figure 6.2-1 and Table 6.2-1) that accounts for the difference between the actual surface water vapor density and 7.5 g/m^3. The coefficient b_ρ is frequency dependent and is given by Figure 6.2-2 (Crane and Blood, 1979).

The US and Canadian weather services generally measure relative humidity or the partial pressure of water vapor. The technique for converting these values to ρ_o is given in Section 6.2.5.

6.2.2.1.3 Dependence on Surface Temperature. The surface temperature T_o also affects the total attenuation because it affects the density of both the wet and dry components of the gaseous attenuation. This relation (Crane and Blood, 1979) is also linear:

$$\Delta A_{c2} = c_T \; (21^o - T_o)$$

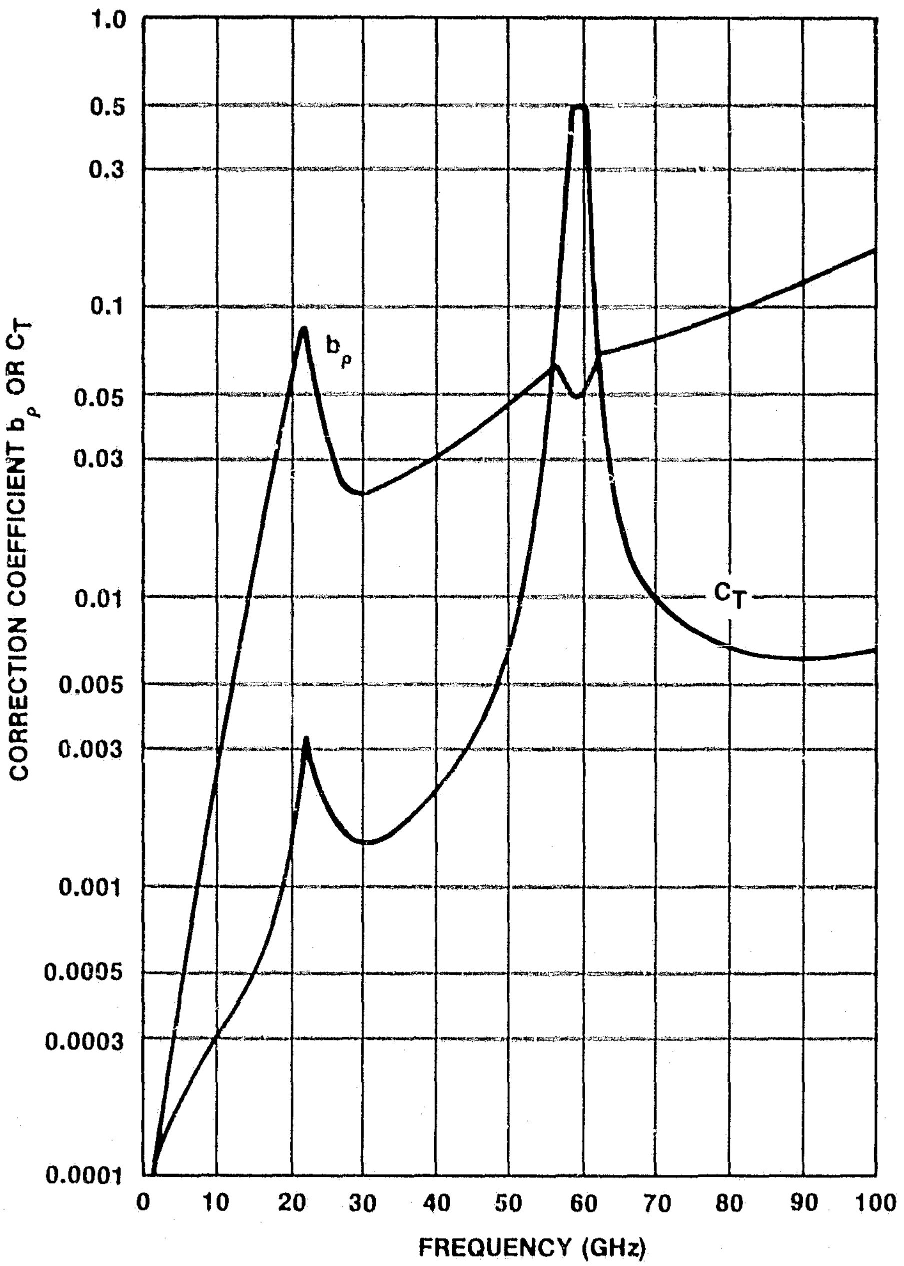

Figure 6.2-2 Water Vapor Density and Temperature Correction Coefficients

ΔA_{c2} is an additive correction to the zenith clear air attenuation. Frequency dependent values for c_T are given in Figure 6.2-2.

6.2.2.1.4 Dependence on Elevation Angle. For elevation angles greater than 5 or 6 degrees, the zenith clear air attenuation A_c is multiplied by the cosecant of the elevation angle θ. The total attenuation for arbitrary elevation angle is

$$A_c = A_c' \csc \theta$$

The standard deviation (see Figure 6.2-1) also is multiplied by the csc θ for arbitrary elevation angles.

6.2.3 Calculation of Gaseous Attenuation Values

Figure 6.2-3 shows the general technique for computing the mean clear air attenuation, given:

a) mean surface water vapor content,
b) surface temperature, and
c) earth-space elevation angle

Utilizing these techniques and surface data from the weather bureau, an estimate of the attenuation and the standard deviation of the attenuation can be made for elevation angles exceeding about 6 degrees. For lower elevation angles, reference to Crane and Blood, 1979, is suggested.

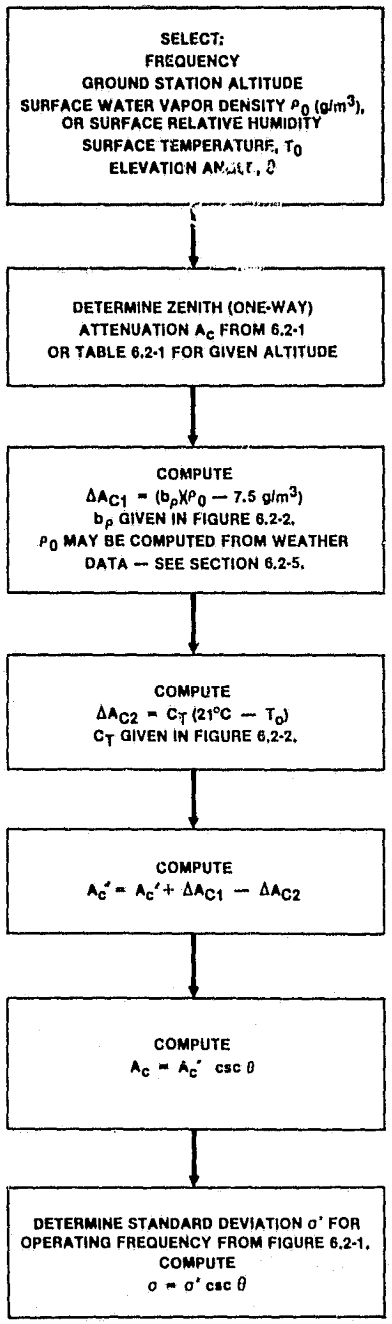

Figure 6.2-3. Technique for Computing Mean Clear Air Attenuation

6.2.4 An Example Calculation of Clear Air Attenuation: Rosman, NC.

Given:

Frequency	20 GHz
Altitude	880 m
Relative Humidity (R.H.)	60%
Temperature (T_o)	80^o F (26.7^oC)
Elevation Angle (θ)	47^o (to ATS-6)

1. Determine Total Zenith Attenuation, A_c':

   From Table 6.2-1, (interpolated), $A_c' = 0.20$dB

2a. Find Water Vapor Density, ρ_o:

   From Figure 6.2-4, Saturated Partial Pressure of Water Vapor at 80^oF, $e_s = 3448\ N/m^2$

   By formula of Section 6.2.5:

$$\rho_o = (0.6)\ 3448/[461\ (26.7 - 273)]$$
$$= 0.015\ kg/m^3$$
$$= 15\ g/m^3$$

2b. Compute Water Vapor Correction, ΔA_{c1}:

   From Figure 6.2-2, for frequency = 20 GHz, Correction Coefficient $b_\rho = 0.05$

   $\Delta A_{c1} = (0.05)\ (15\text{-}7.5) = 0.38$ dB

3. Compute Temperature Correction, ΔA_{c2}:

   From Figure 6.2-2, for frequency = 20 GHz, Correction Coefficient $c_T = 0.0015$

   $\Delta A_{c2} = (0.0015)\ (21\text{-}26.7) = -0.01$ dB

4. Compute Corrected Clear-Air Zenith Attenuation, A_c'':

   $A_c'' = 0.20 + 0.38 - 0.01 = 0.57$ dB

5. Compute Clear-Air Slant Attenuation, A_c:

   $A_c = 0.57 \csc 47^o = 0.57\ (1.37) = 0.78$ dB

6. Compute Standard Deviation, σ:
From Figure 6.2-1, for frequency = 20 GHz, $\sigma' = 0.2$ dB
$\sigma' = 0.2 \csc 47^{\circ} = 0.27$ dB

6.2.5 Conversion of Relative Humidity to Water Vapor Density

The surface water vapor density ρ_o (g/m^3) at a given surface temperature T_o may be found from the ideal gas law

$$\rho_o = (R.H.)e_s/[R_w(T_o+273)]$$

where R.H. is the relative humidity, e_s (N/m^2) is the saturated partial pressure of water vapor corresponding to the surface temperature T_o(^{o}C) and R_w=461 joule/kg^{o}K = 0.461 joule/g^{o}K. A plot of e_s in various units is given in Figure 6.2-4. For example, with

$$R.H. = 50\% = 0.5$$
$$T_o = 20^{o}C$$
$$e_s \approx 2400 \text{ n/m}^2 \text{ at } 20^{o}C \text{ from Figure 6.2-4}$$

then

$$\rho_o = 8.9 \text{ g/m}^3.$$

The relative humidity corresponding to 7.5 g/m^3 at 20^{o}C (68^{o}F) is R.H. = 0.42 = 42%.

6.3 PREDICTION OF CUMULATIVE STATISTICS FOR RAIN ATTENUATION

6.3.1 General Approaches

6.3.1.1 Introduction to Cumulative Statistics Cumulative statistics give an estimate of the total time, over a long period, that rain attenuation or rate can be expected to exceed a given amount. They are normally presented

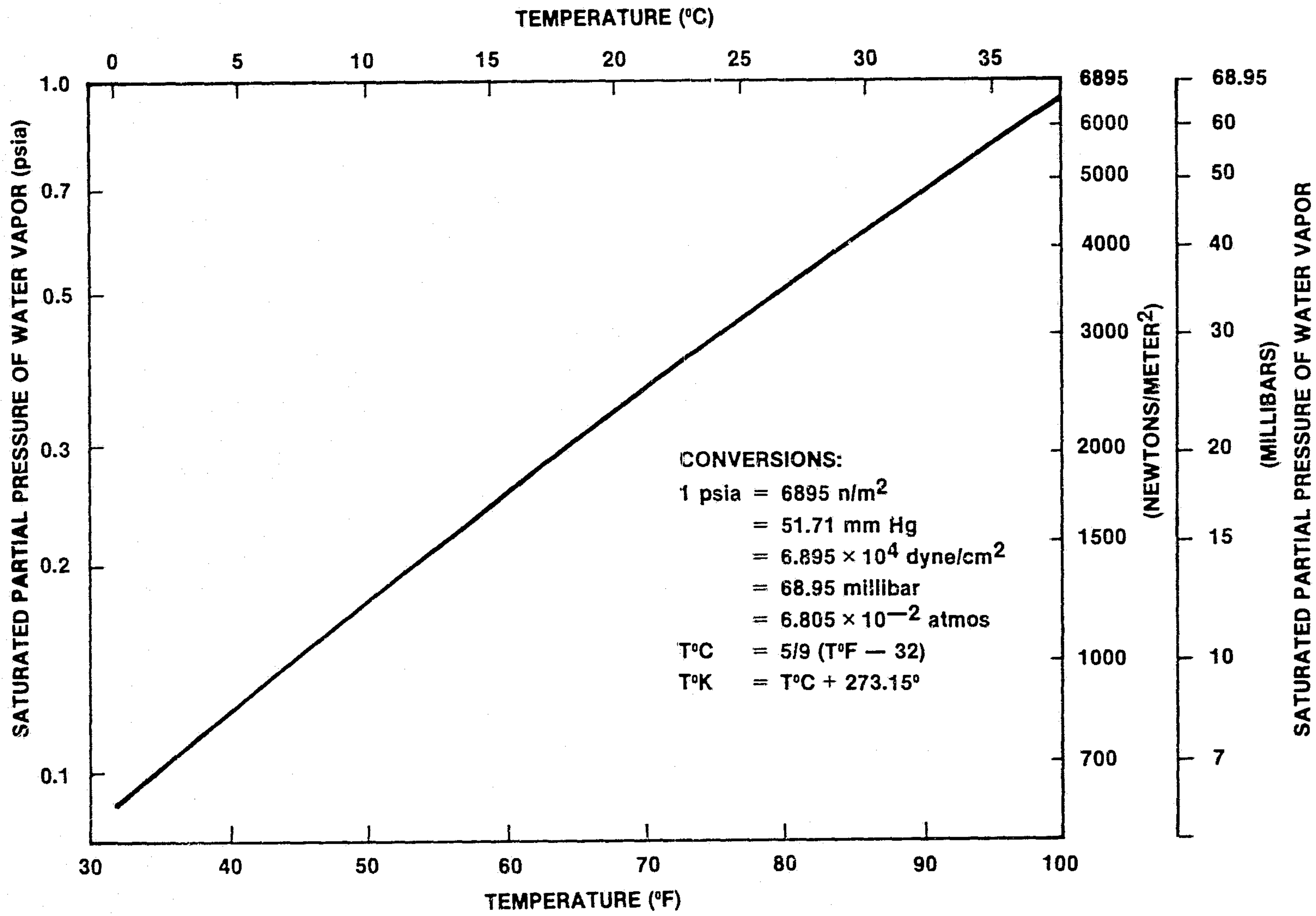

Figure 6.2-4 The Saturated Partial Pressure of Water Vapor Versus Temperature

with parameter values (rain rate or attenuation) along the abscissa and the total percentage of time that the parameter value was exceeded (the "exceedance time") along the ordinate. The ordinate normally has a logarithmic scale to most clearly show the exceedance times for large values of the parameter, which are often most important. Often, the percentage exceedance time is interpreted as a probability and the statistical exceedance curve is taken to be cumulative probability distribution function. Because of the general periodicity of meteorological phenomena, cumulative statistics covering several full years, or like periods of several successive years, are the most directly useful. (A technique exists, however, for extending statistics to apply to periods greater than those actually covered. This is described in Section 6.3.4.) Statistics covering single years or periods would be expected to exhibit large fluctuations from year to year, because of the great variability of the weather. In most geographic regions, data covering ten years or more is usually required to develop stable and reliable statistics.

Cumulative rain rate or attenuation exceedance statistics alone give no information about the frequency and duration of the periods of exceedance. Rather, only the total time is given. The nature of rain attenuation, however, is such that the exceedance periods are usually on the order of minutes in length. Different phenomena besides rain give rise to attenuation variations occurring on a time scale of seconds. These amplitude scintillations, as they are called, are not considered in this section, but are discussed in Section 6.6.

6.3.1.2 Procedures for Calculating Cumulative Rain Attenuation Statistics

The system designer needs reliable cumulative attenuation statistics to realistically trade off link margins, availability, siting and other factors. Needless to say, applicable millimeter-wave attenuation measurements spanning many years seldom exist. It is therefore necessary to estimate statistics, using whatever information is available.

An estimate of the rain attenuation cumulative statistics may be determined in several ways. The optimum way depends on the amount of rain and/or attenuation data available, and on the level of sophistication desired. However, it is recommended that the simplest calculations be carried out first to provide an approximation for the statistics and also to act as a check on the results of more sophisticated calculations.

The flow charts in Figures 6.3-1 and 6.3-9 will assist with deciding which calculation procedures are to be pursued. The steps are numbered sequentially to allow easy reference with the accompanying discussions in Sections 6.3.2, 6.3.3 and 6.3.4. These are the procedures given:

- Analytical Estimates (Section 6.3.2, Figure 6.3-1). Requires only Earth station location, elevation angle, and frequency.

- Estimates Given Rain Rate Statistics (Section 6.3.3, Figure 6.3-1). Requires cumulative rain rate exceedance statistics for vicinity of the Earth station location.

- Estimates Given Rain Rate and Attenuation Statistics (Section 6.3.4, Figure 6.3-9). Requires attenuation statistics which may be for frequency and elevation angle different from those needed.

6.3.1.3 <u>Other Considerations</u>. Generally the yearly cumulative statistics are desired. The worst-month or 30-day statistics are sometimes also needed, but are not derivable from the data presented here. Worst 30-day statistics are discussed in Section 6.3.7.

The attenuation events due to liquid rain only are considered here. Liquid rain is the dominate attenuation-producing species because its specific attenuation is considerably higher than snow, ice, fog, etc. The contribution of these other hydrometeors is estimated in later sections.

The cumulative statistics are appropriate for earth-space paths for geostationary or near-geostationary satellites with relatively stable orbital positions. The modifications required to develop statistics for low-orbiting satellites is unclear because of the possibly nonuniform spatial distribution of rain events arising from local topography (lakes, mountains, etc.). However, if one assumes these effects are of second-order, low orbiting satellites may simply be considered to have time-dependent elevation angles.

6.3.2 Analytic Estimates (Figure 6.3-1)

6.3.2.1 Discussion and Procedures. The following analytic estimation technique provides a quick and relatively precise technique for estimating the rain attenuation statistics. The technique is based on the modified Global Prediction Model (Crane and Blood- 1979). Only parts of the model relevant to the contiguous US and Canada, and elevation angles greater than 10^o, are presented here.

As inputs the model requires:

a) Ground station latitude, longitude and elevation

b) The earth-space path elevation angle

c) The operating frequency

As shown in Figure 6.3-1, start by selecting the appropriate rain rate climate region from Figure 6.3-2. Given the rain region, use the appropriate one-minute average surface rain rate curve shown in Figures 6.3-3a or b to obtain the cumulative rain rate distribution.

These distributions are also tabulated in Table 6.3-1 for common values of exceedance.

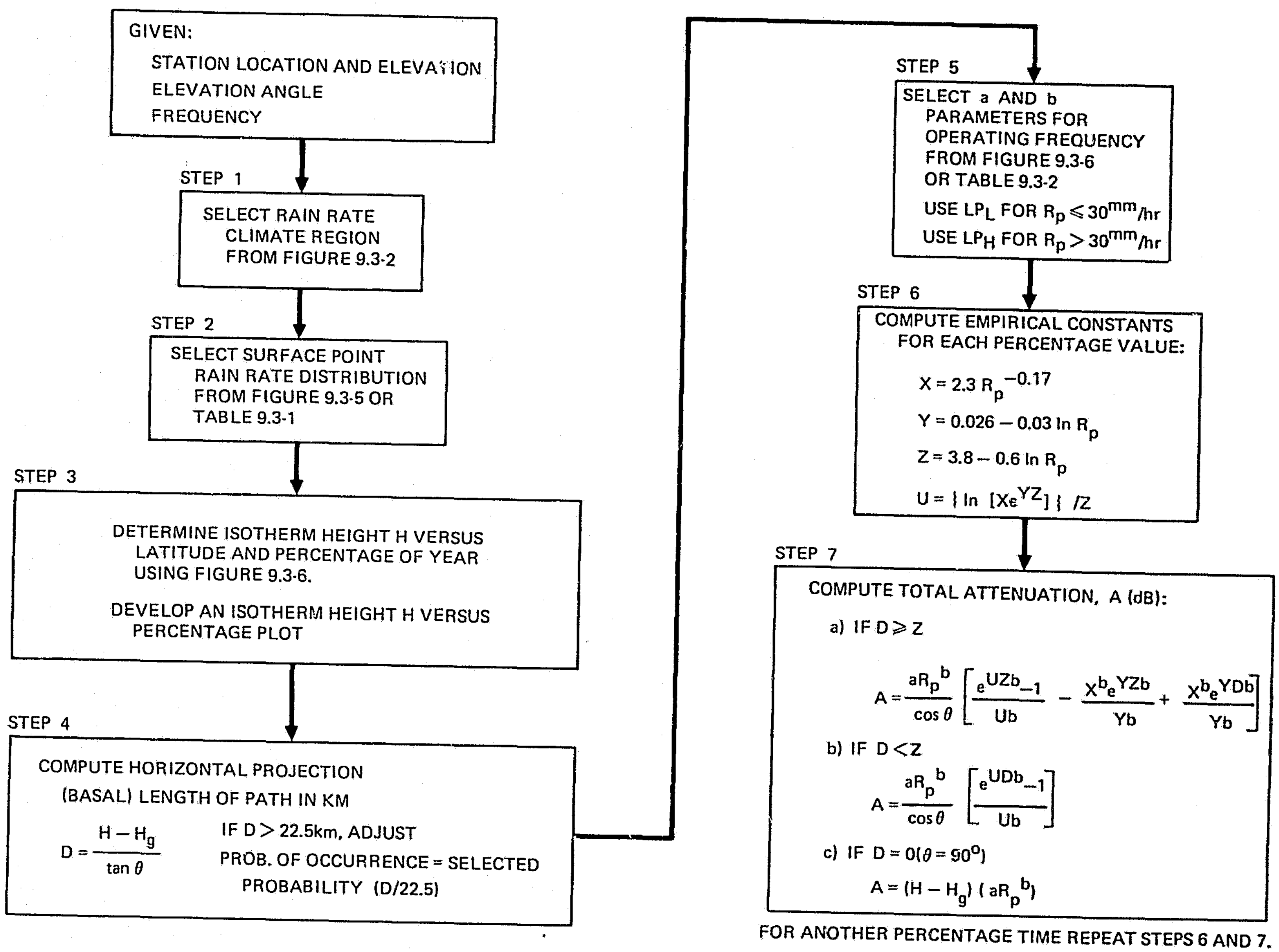

Figure 6.3-1. Analytic Estimate Procedure for Cumulative Rain Rate and Attenuation Statistics

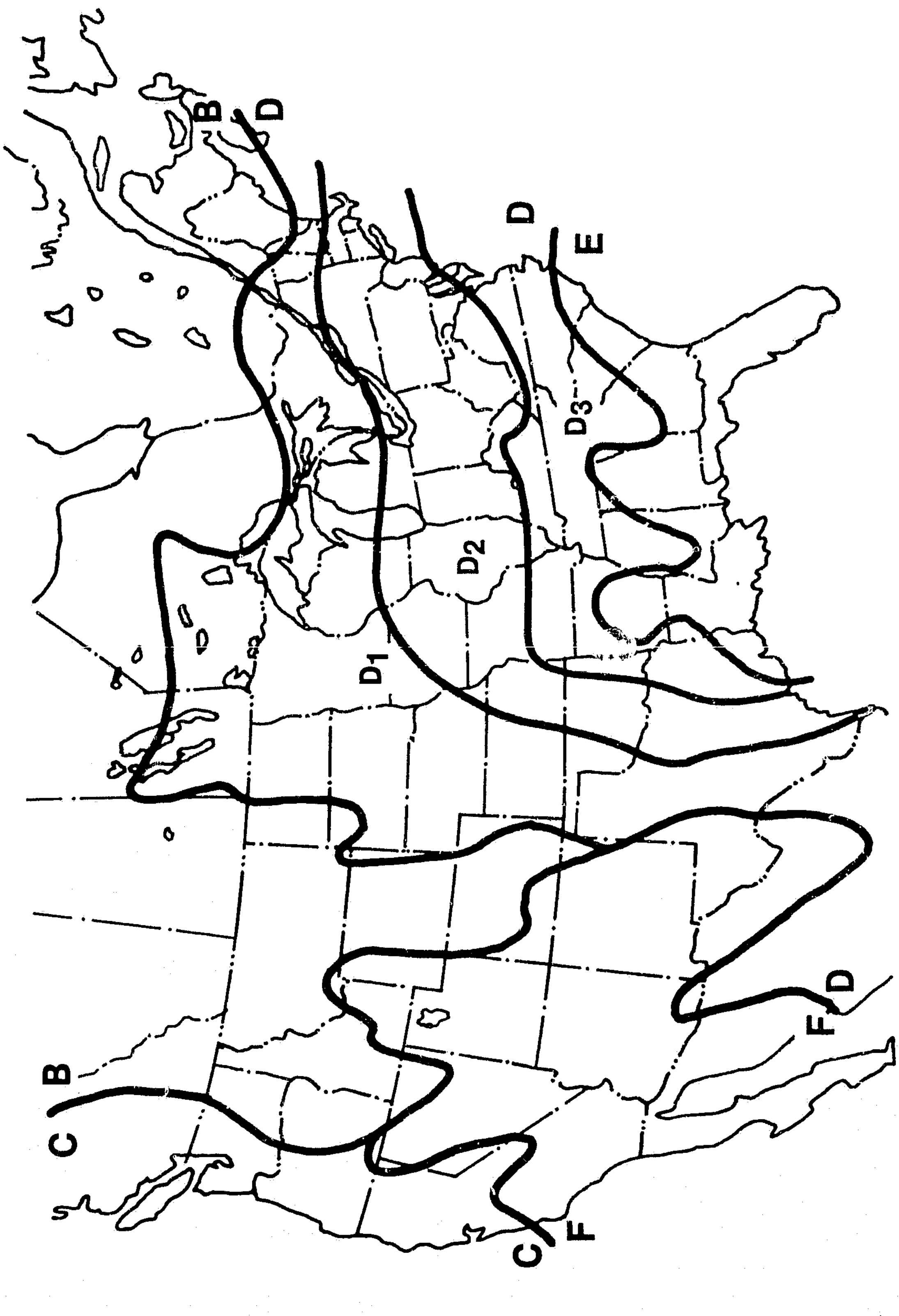

Figure 6.3-2 Rain Rate Climate Regions for Global Prediction Model

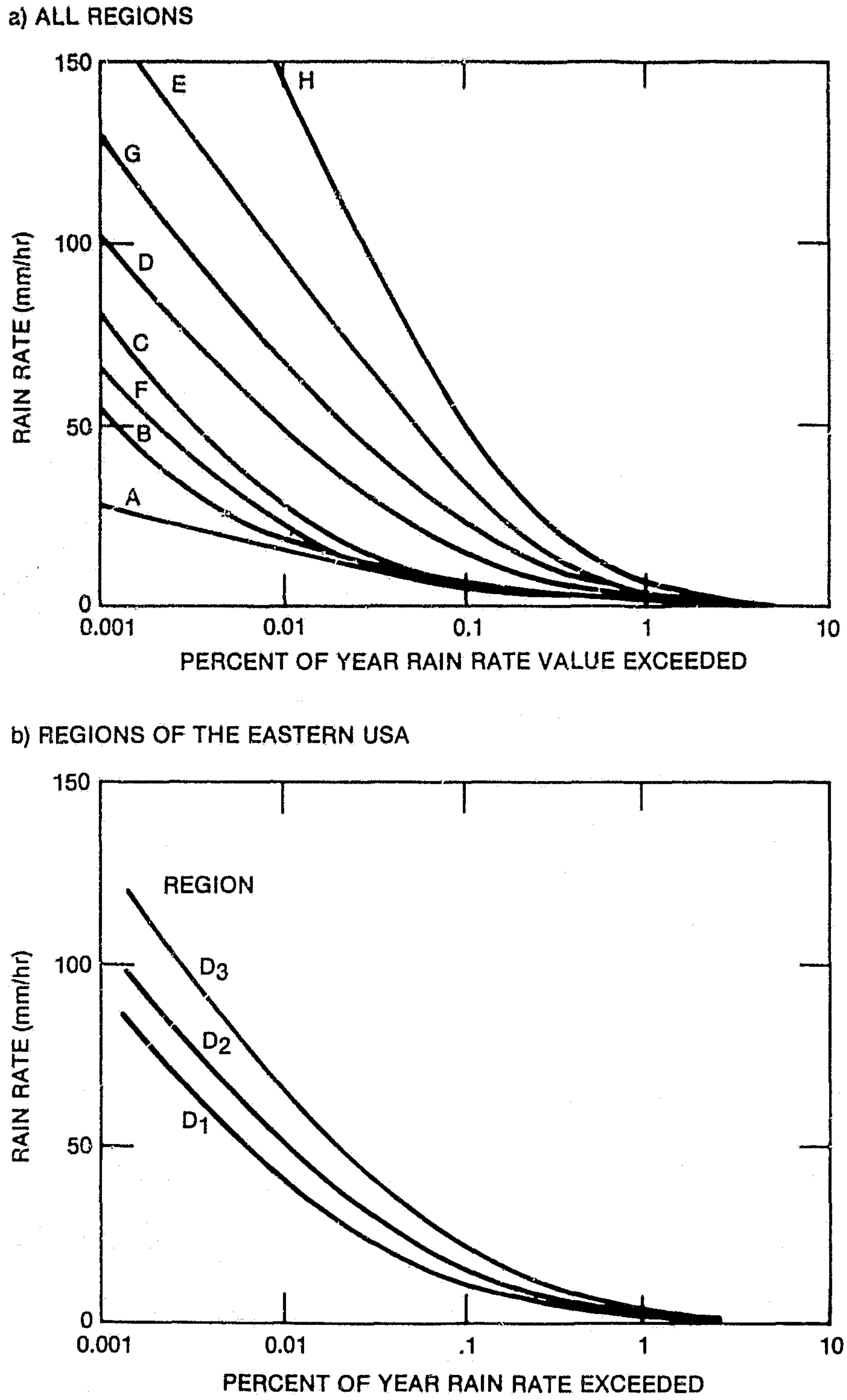

Figure 6.3-3 Rain Rate Distributions for Global Prediction Model Regions

Table 6.3-1

Point Rain Rate Distribution Values (mm/hr)

Versus Percent of Year Rain Rate is Exceeded

Percent of Year	Rain Climate Region:										Minutes Per Year	Hours Per Year
	A	B	C	D_1	D_2	D_3	E	F	G	H		
0.001	28	54	80	90	102	127	164	66	129	251	5.3	0.09
0.002	24	40	62	72	86	107	144	51	109	220	10.5	0.18
0.005	19	26	41	50	64	81	117	34	85	178	26	0.44
0.01	15	19	28	37	49	63	98	23	67	147	53	0.88
0.02	12	14	18	27	35	48	77	14	51	115	105	1.75
0.05	8	9.5	11	16	22	31	52	8.0	33	77	263	4.38
0.1	6.5	6.8	72	11	15	22	35	5.5	22	51	526	8.77
0.2	4.0	4.8	4.8	7.5	9.5	14	21	3.8	14	31	1052	17.5
0.5	2.5	2.7	2.8	4.0	5.2	7.0	8.5	2.4	7.0	13	2630	43.8
1.0	1.7	1.8	1.9	2.2	3.0	4.0	4.0	1.7	3.7	6.4	5260	87.66
2.0	1.1	1.2	1.2	1.3	1.8	2.5	2.0	1.1	1.6	2.8	10520	175.3

Since only the hydrometeors in liquid form attenuate the microwave energy significantly, the earth-space path up to the height H of the $0^{o}C$ isotherm dominates the attenuation. The height of the $0^{o}C$ isotherm varies with the season of the year and the latitude and the type of rain event. Figure 6.3-4 indicates the average isotherm height corresponding to various percentage exceedance values. For the convective events which occur during the summer and influence the 0.001 percent periods of the year, the mixing process extends th rain height above the $0^{o}C$ isotherm. The isotherm height shown in the figure for the 0.001 percent period has been adjusted upward to account for this.

Plot the values of the H versus the percentages and join the points by a smooth curve. Use this curve to estimate H at percentage values intermediate to 0.001, 0.002, and 0.01.

Compute the parameter D, the horizontal projection of the path (step 4), for each probability value desired.

If D > 22.5 km, which will occur for elevation angles of the order of 10 degrees of less, adjust the percentage values (probabilities) by the relation:

True Probability of Occurrence =
(Initial Probability of Occurrence) x (D/22.5 km).

This correction accounts for the effects of traversing multiple rain cells at low elevation angles.

Next (Step 5), select the a and b parameters in the aR^{b} specific attenuation relation from Table 6.3-2 or Figure 6.3-5 for the operating frequency. The values given have been recently derived for the Laws and Parsons drop size distributions and $0^{o}C$ raindrop temperature (Olsen, Rogers and Hodge-1978) and are recommended for this purpose. For rain rates of 30 mm/h or less the Laws and Parsons low rain rate values (labeled LP_L) are best, while for rain rates exceeding 30 mm/h the high rain rate (LP_H) values

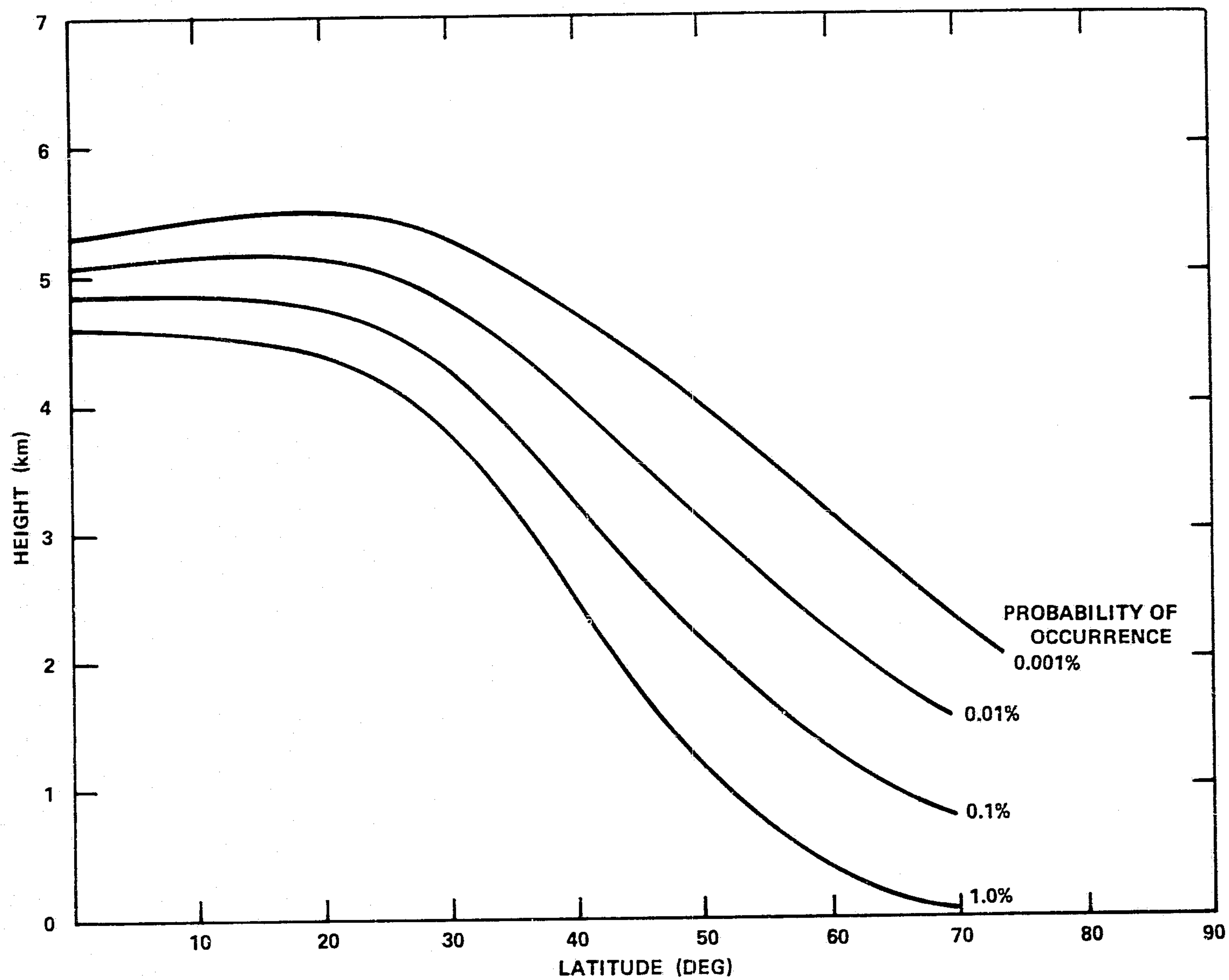

Figure 6.3-4 Latitude Dependence of the Rain Layer $0^{o}C$ Isotherm Height (H) as a Function of Probability of Occurrence

Table 6.3-2

Regression Calculations for a and b in aR^b (dB/km) as a Function of Frequency (Source: Olsen, Rogers and Hodge-1978)

FREQ. (GHz)	a		b	
	LP_L	LP_H	LP_L	LP_H
10	1.17×10^{-2}	1.14×10^{-2}	1.178	1.189
11	1.50×10^{-2}	1.52×10^{-2}	1.171	1.167
12	1.86×10^{-2}	1.96×10^{-2}	1.162	1.150
15	3.21×10^{-2}	3.47×10^{-2}	1.142	1.119
20	6.26×10^{-2}	7.09×10^{-2}	1.119	1.083
25	0.105	0.132	1.094	1.029
30	0.162	0.226	1.061	0.964
35	0.232	0.345	1.022	0.907
40	0.313	0.467	0.981	0.864
50	0.489	0.669	0.907	0.815
60	0.658	0.796	0.850	0.794
70	0.801	0.869	0.809	0.784
80	0.924	0.913	0.778	0.780
90	1.02	0.945	0.756	0.776
100	1.08	0.966	0.742	0.774

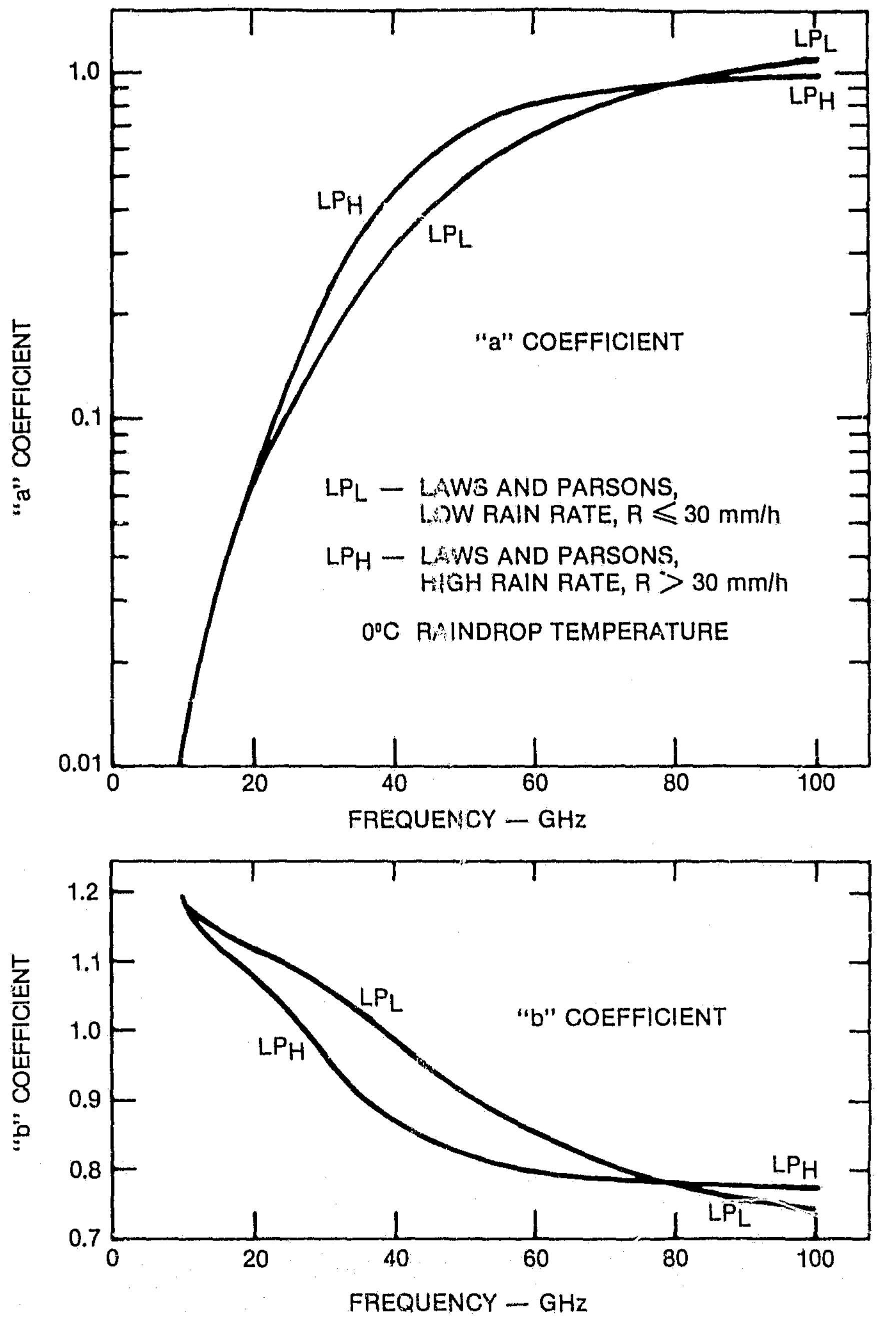

Figure 6.3.5 "a" and "b" Parameters in aR^b Relation Versus Frequency

are recommended. This 30 mm/h division between the LP_L and LP_H is not critical. The specific attenuation obtained using LP_L values is nearly the same as that using the LP_H values from 25 to 50 mm/h.

For the final calculations, compute the set of empirical constants X, Y, Z and U as shown in Step 6, and use them and the other parameters to compute the total rain attenuation A depending on the relative values of D and Z as shown in Step 7. Steps 6 and 7 are repeated for each of the selected values for percentage using the appropriate values for D, a, b, R_p, etc. The result is an analytic estimate for the cumulative rain attenuation statistics, i.e., percentage of time attenuation exceeds abscissa value. The use of a programmable calculator or computer is highly recommended for these calculations.

6.3.2.2 Example. The following information is given for the Rosman, NC Earth Station operating with the ATS-6 satellite.

Earth station latitude : 35^oN.
Earth station longitude: 277^oE.
Earth station elevation: 0.9 km

Antenna elevation Angle: 47^o

Operating frequency: 20 GHz

We wish to find an analytic estimate for the cumulative attenuation statistics using the procedure of Figure 6.3-1.

1. Select rain rate climate region for Rosman, NC:
   From Figure 6.3-2, Rosman is located in region D_3.

2. Select surface point rain rate distribution:
   From Table 6.3-1, region D_3 has the following distribution:

%	R_p
0.01	63
0.02	48
0.05	31
0.10	22
0.20	14
0.50	7
1.0	4

3. Determine isotherm height H:

From Figure 6.3-4, the following isotherm height estimates apply at 35^{o} latitude.

%	H
0.01	4.4 km
0.1	3.75
1.0	3.2

By plotting these, the following additional points may be interpolated

0.02	4.2
0.05	3.95
0.2	3.55
0.5	3.3

4. Compute D:

Using $\theta = 47^{o}$ and $H_g = 0.9$ km, we obtain

%	D
0.01	3.25 km
0.02	3.1
0.05	2.85
0.1	2.65
0.2	2.45
0.5	2.25
1.0	2.15

5. Select a and b:

For percentage values from 0.01 through 0.05, $R_p > 30$, so a and b are selected from the LP_H column of Table 9.3-2 at 20 GHz.

$$\left.\begin{aligned} a &= 0.0709 \\ b &= 1.083 \end{aligned}\right\} \text{ for } \% \leq 0.05$$

The LP_L column is used for the other percentages, since $R_p < 30$

$$\left.\begin{aligned} a &= 0.0626 \\ b &= 1.119 \end{aligned}\right\} \text{ for } \% > 0.05$$

6. Compute Empirical constants:

For example,

%	X	Y	Z	U
0.1	1.36	-0.067	1.95	0.091
0.2	1.47	-0.053	2.22	0.120
0.5	1.65	-0.032	2.63	0.158

7. Compute attenuation, A:

We note from step 6 that 0.2%, D is greater than Z. This also holds for percentages less than 0.1%. Thus the formula of Step 7 (a) is used to find the attenuation for % ≤ 0.1.

For % ≥ 0.5, D is less than Z, so the formula of Step 7 (b) applies. The attenuation values found in this way are plotted versus percentage exceedance in Figure 6.3-6. The figure includes statistics derived from 20 GHz attenuation measurements made at Rosman with the ATS-6 over a 6-month period.

6.3.3 Estimate Given Rain Rate Statistics

6.3.3.1 Discussion and Procedures. If the rainfall statistics can be reconstructed from Weather Service data or actual site measurements exist for a period of at least 10 years near the ground station site, these may be utilized to provide R_p versus percentage exceedance. The temporal resolution required of these measurements is dependent on the smallest percentage resolution required. I.e., if 0.001% of a year (5.3 minutes) statistics are desired, it is recommended that the rain rate be resolved to increments of no more than 1-minute to provide sufficient accuracy. This can be done utilizing techniques described in Chapter 2 of this handbook, but 5-minute data is more easily obtained.

The cumulative statistics measured near the ground station site replaces the activities in Steps 1 and 2 of Figure 6.3-1. The attenuation statistics are generated using the procedures in Steps 3 through 7 of Figure 6.3-1.

6.3.3.2 Example. Again we take the case of the 20 GHz ATS-6 link to Rosman, NC. We have cumulative rain rate statistics for Rosman for a six-month period as shown in Figure 6.3-7. (Data spanning such a short period should not be used to estimate long-term statistics. The use here is for demonstration purposes only.) We first select values of rain rate R_p corresponding to several values of percentage exceedance:

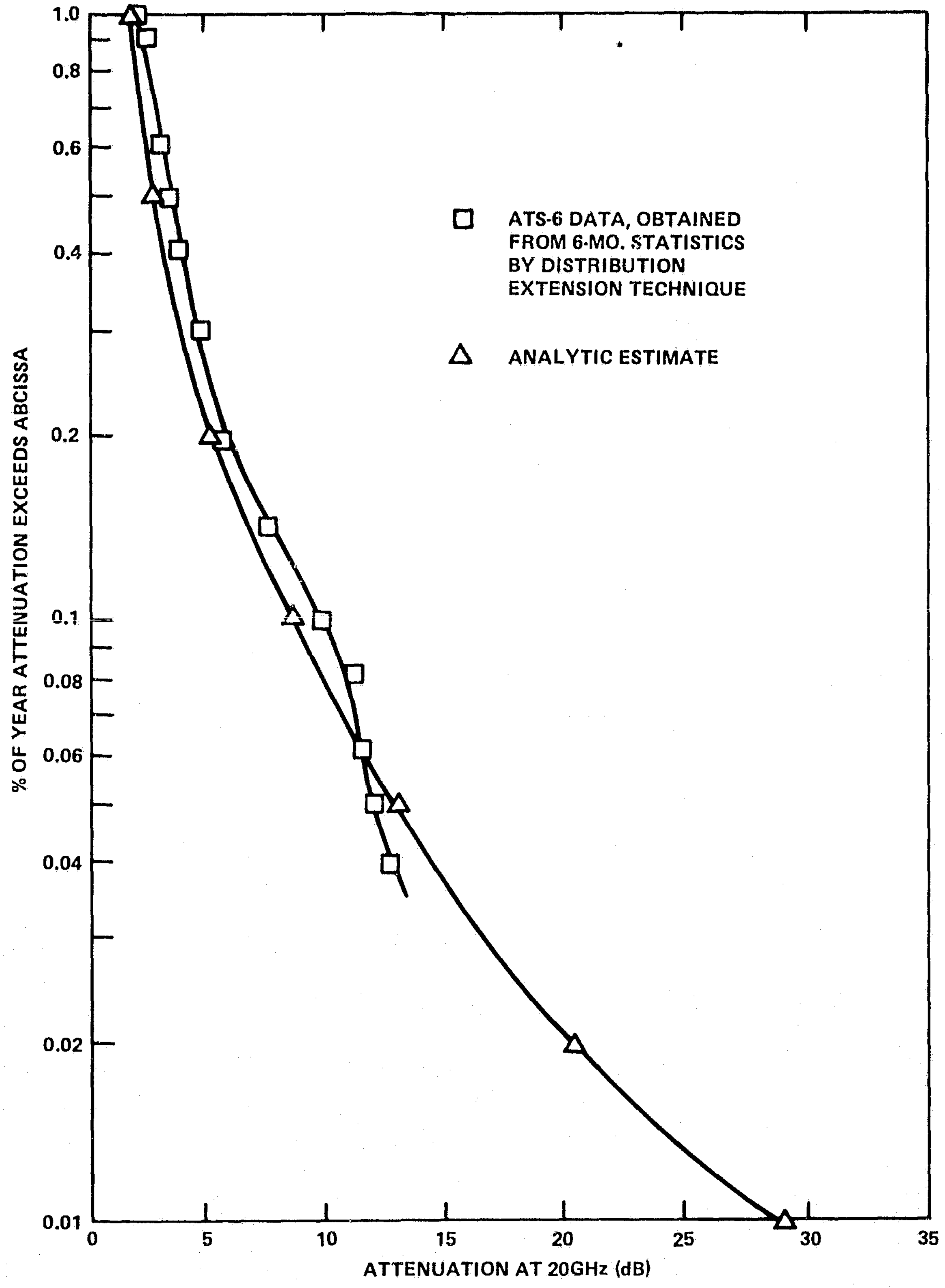

Figure 6.3-6 Analytic Attenuation Estimate and Actual Measurements

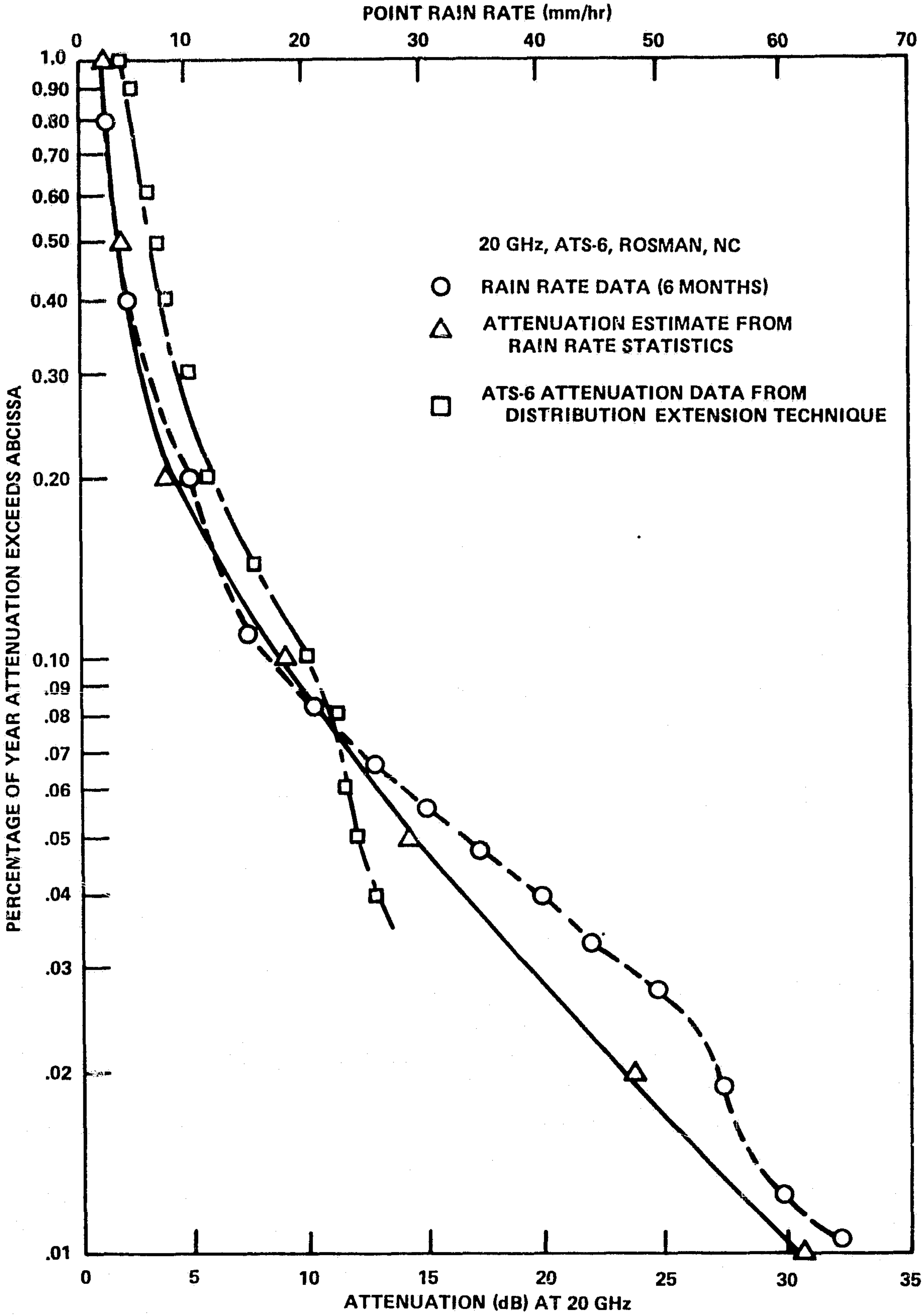

Figure 6.3-7 Attenuation Statistics Estimated Based on Measured Rainfall Statistics

%	R_p
0.01	66
0.02	55
0.05	34
0.10	16.5
0.20	10.5
0.50	4.5
1.0	2.3

We now proceed exactly as in the previous example, using these values of R_p instead of those in Table 6.3-1 or Figure 6.3-3. For the present case, the LP_L values of a and b are used for percentage values less than 0.1, and the LP_H values apply otherwise. The formula of Step 7(b) applies for percentages less than 0.1 and Step 7(a) is used otherwise.

The results of these calculations are shown in Figure 6.3-7, along with the measured attenuation statistics. This data is presented to demonstrate the technique. More accurate data, covering a longer period, is presented in Chapter 5.

6.3.4 Attenuation Estimates Given Limited Rain Rate and Attenuation Statistics

6.3.4.1 Discussion and Procedures. The system designer will virtually never find attenuation statistics spanning a number of years for his desired location, operating frequency and elevation angle. But by applying distribution extension and scaling procedures to the limited statistics available, the designer may make useful estimates of the statistics for the situation at hand.

Distribution extension allows one to take concurrent rain rate and attenuation measurements intermittently over a limited period of time, then convert the data into cumulative attenuation statistics covering the entire year. The conversion requires stable cumulative rain rate statistics for the site or a nearby weather station, and measurements taken over a statistically significant fraction of the year. Distribution extension is required in practice because it is sometime not worthwhile to make continuous attenuation measurements over extended periods. Rather, data is sometimes taken only during rainy periods.

Scaling is required to account for differences between the frequency and elevation angle applying to the available statistics, and those applying to the actual system under consideration. This scaling is based on empirical formulas which, to the first order approximation, depend only on the frequencies or the elevation angle and apply equally to all attenuation values. To a better approximation, however, the rain rate corresponding to the attenuation and other factors must be considered as well.

Figure 6.3-8 shows a generalized procedure for applying the distribution extension and scaling techniques described in this section.

6.3.4.2 Attenuation Distribution Extension. The technique is illustrated in Figure 6.3-9. The upper two curves represent cumulative rain rate and attenuation statistics derived from measurements taken over some limited period of time. The measurement time may consist for example, of only the rainy periods from April through September. The exceedence curves are plotted as functions of the percentage of the total measurement time. The lower solid curve represents the cumulative rain rate statistics, measured over an extended period at the same location as the attenuation measurements, or derived from multi-year rainfall records from a nearby weather station.

A curve approximating the long-term cumulative attenuation distribution (the bottom curve in Figure 6.3-9) is derived from the three upper curves by the following graphical procedure:

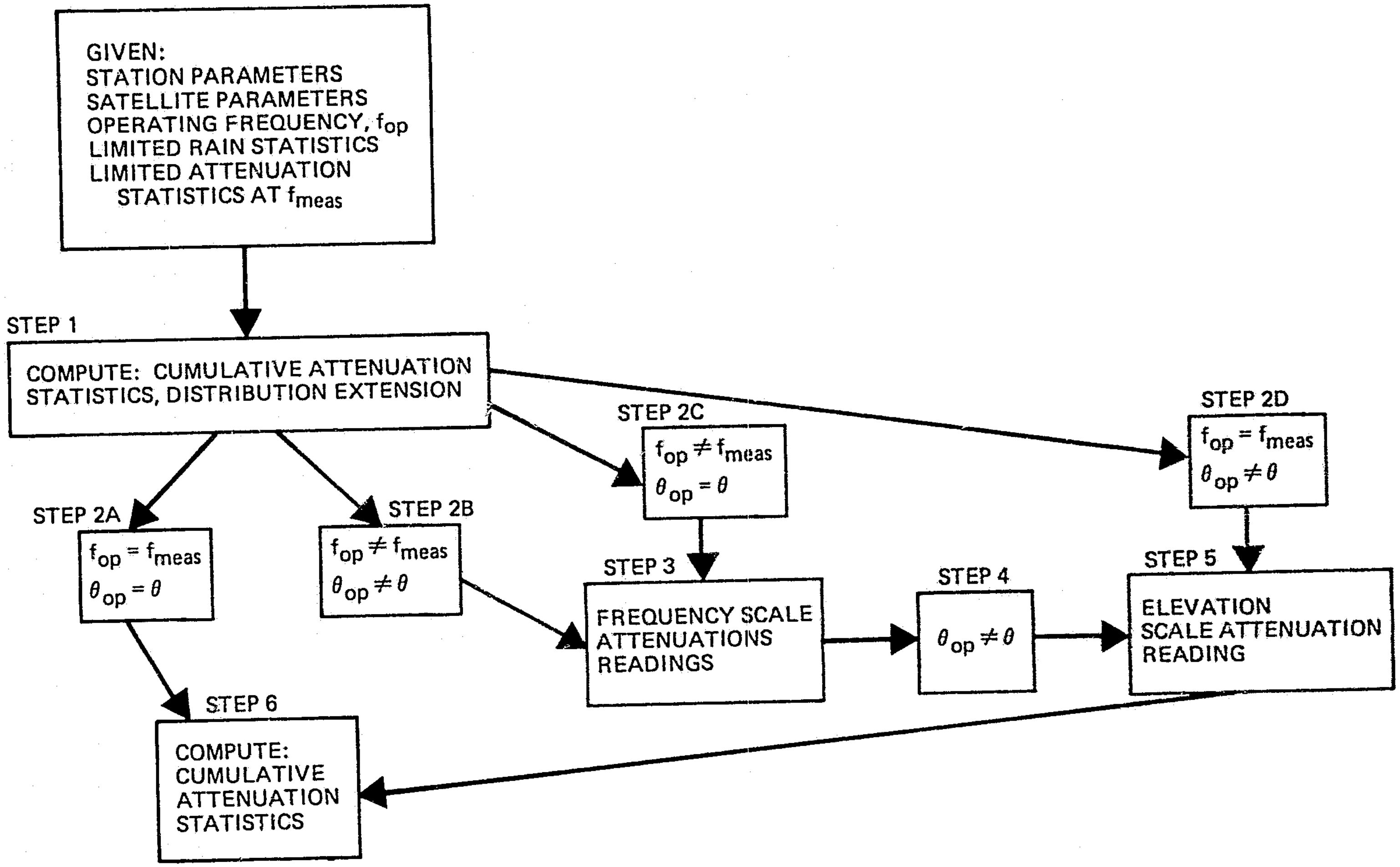

Figure 6.3-8 Procedure for Generation of Cumulative Attenuation Statistics Given Limited Rain Rate and Attenuation Statistics

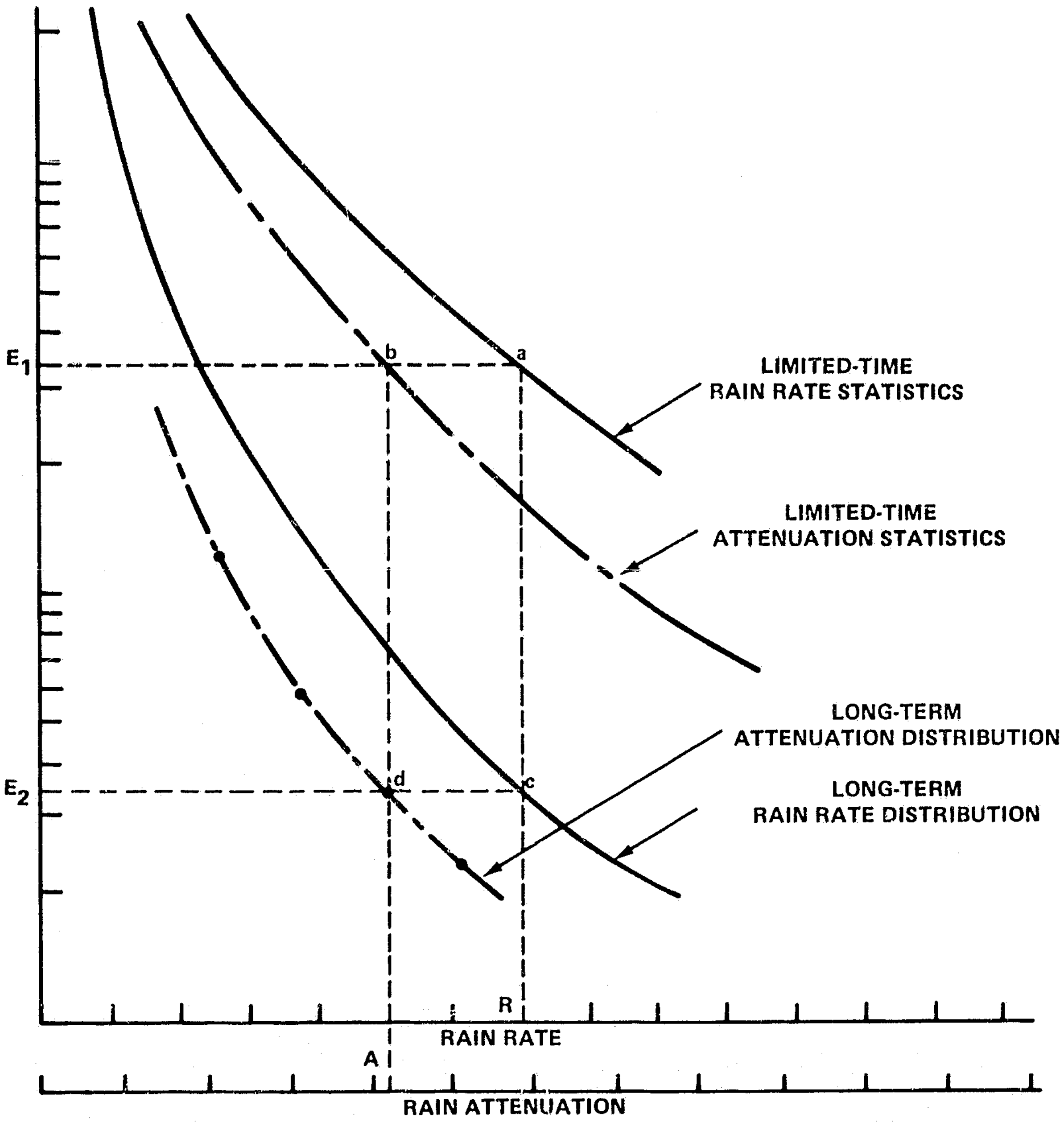

Figure 6.3-9 Construction of Cumulative Attenuation Statistics Using the Distribution Extension Technique

1. Select a percent exceedance value, E_1, and draw a horizontal line at that value intersecting the limited-time rain rate and attenuation distribution curves at points a and b, respectively.

2. At the rain rate value R corresponding to E_1, project a line down to intersect (at point c) the long-term rain rate curve at the exceedance value E_2.

3. At the attenuation value A corresponding to E_1, project a line down to the exceedance value E_2. This (point d) is a point on the long-term attenuation curve.

4. Repeat the process for several points and join them with a smooth curve.

Distribution extension in this manner assumes that the values of rain rate and attenuation remain the same as the measured values, on the average, for times of the year different than the measurement period. This is not necessarily so. The physical distribution of raindrops along the propagation path in a stratiform rain, for example, differs from the distribution in a mild convective storm. Both conditions could produce local rainfall at the same rate, but the attenuation produced could be quite different. Thus in regions where there is wide seasonal variation in how rain falls, distribution extension should be used with caution. The reliability of the extended distribution depends on how "typical" of the whole year the rainfall was during the measurement period. If the shapes of the limited-time and the long-term distribution curves are similar, the limited-time sample is statistically significant and the distribution extension will be valid.

6.3.4.3 Frequency Scaling. If frequency scaling of measured rain attenuation (Step 3 of Figure 6.3-8) is required, the specific attenuation scaling technique is recommended. In this technique the specific attenuation data (Olsen, Rogers and Hodge, 1978) given in Figure 6.3-5 and Table 6.3-2 is utilized to scale the attenuation A from frequency f_1 to frequency f_2.

Referring to the equation for rain attenuation in Step 7 of Figure 6.3-1, the result is

$$\frac{A_2}{A_1} = \frac{a_2}{a_1} R_p^{b_2-b_1} \cong \frac{a_2}{a_1} \text{(for } b_1 \cong b_2\text{)}$$

where

$$A_1 = A(f_1),\ A_2 = A(f_2),\ a_1 = a(f_1), \text{ etc.}$$

This is a fair estimate for small frequency ratios (e.g., less than 1.5:1), and moderate rain rates, but errors can be large otherwise. This is because the above equation implicity assumes that rainfall is homogeneous over the propagation path, which is usually not true. By assuming a simple Gaussian model for the rain rate with distance along the path, Hodge (1977) derived an expression for attenuation ratio that includes an inhomogeneity correction factor, and uses the high correlation between attenuation and peak rain rate to eliminate the rain rate:

$$\frac{A_2}{A_1} = \frac{a_2}{a_1}\left(\frac{A_1}{a_1}\sqrt{b_1/\pi}\right)^{b_2/b_1-1}\sqrt{b_1/b_2}$$

This yields a better fit to empirical data.

6.3.4.4 Elevation Angle Scaling. Step 5, the elevation angle scaling between the operational elevation angle θ_{op} and the measured data angle θ_{meas} is somewhat complex, since D is inversely proportional to cos θ. The first order, the cosecant rule is recommended, namely

$$\frac{A(\theta_2)}{A(\theta_1)} = \frac{\csc \theta_2}{\csc \theta_1} = \frac{\sin \theta_1}{\sin \theta_2}$$

If more detailed calculations are desired the full formulas in Figure 6.3-1 are utilized.

6.3.4.5 Example of Distribution Extension. Figure 6.3-10 shows an example of applying the distribution extension technique. The upper two curves are cumulative rain-rate and attenuation statistics derived from more than 600 total minutes of measurements over the July through December 1974 period. The bottom curve in the figure is the measured distribution of rain rate for the entire six-month period (265,000 minutes). Comparison of the two rain rate distributions shows that they are very similar in shape. This indicates that the rain rate measurements made during attenuation measurements are a statistically significant sample of the total rainfall, and that using the distribution extension technique is valid. The extended attenuation distribution, constructed as described in paragraph 6.3.4.2, is shown in the figure.

6.3.5 Fading Duration

System designers recognize that at some level of rain rate R_m the entire system margin will be utilized. The cumulative rain rate statistics indicate the percentage of time the rain rate exceeds R_m. In this section, a technique is presented for estimating an upper bound on the duration of the periods that the rain rate exceeds a given R_m. This is equivalent to the duration of fades exceeding the depth corresponding to R_m. Some limited experimental data is also presented.

6.3.5.1 Experimental Measurement of Fade Durations. Direct measurement of fade duration statistics are sparse (CCIR-1978, Rpts 426-2 and 564-1). The published results from measurements made in Europe (Slough, England) using sun-tracking radiometers with elevation angles varying from 5 to 62 degrees appear to be most complete (Davies-1973). These fade measurements, shown in Figure 6.3-11, were made at 19 and 37 GHz. At Slough a large proportion of the fades occurred during the winter months. In the US and Canada that seasonal distribution is unlikely to be the case (see below).

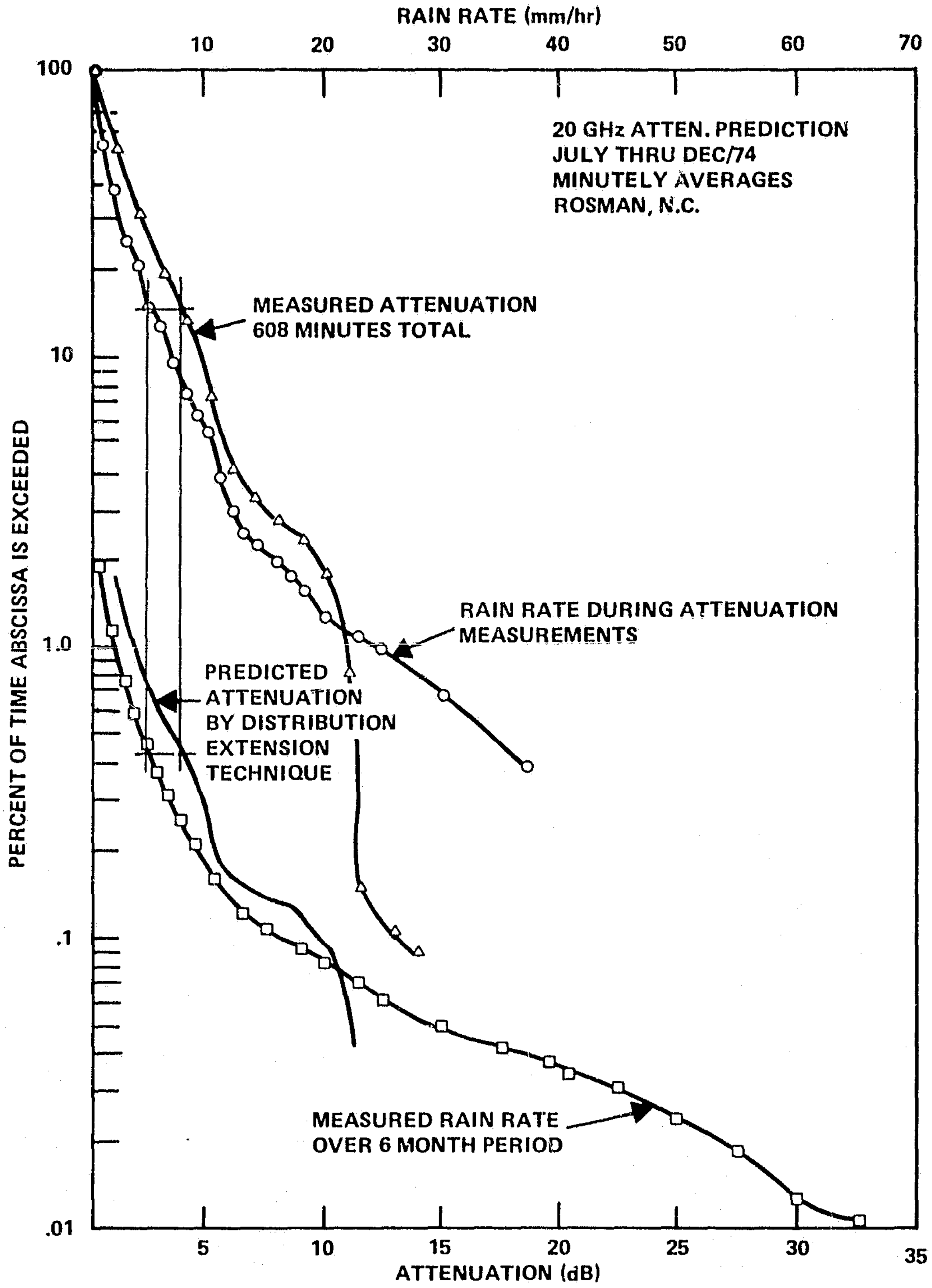

Figure 6.3-10 Example of Distribution Extension Technique

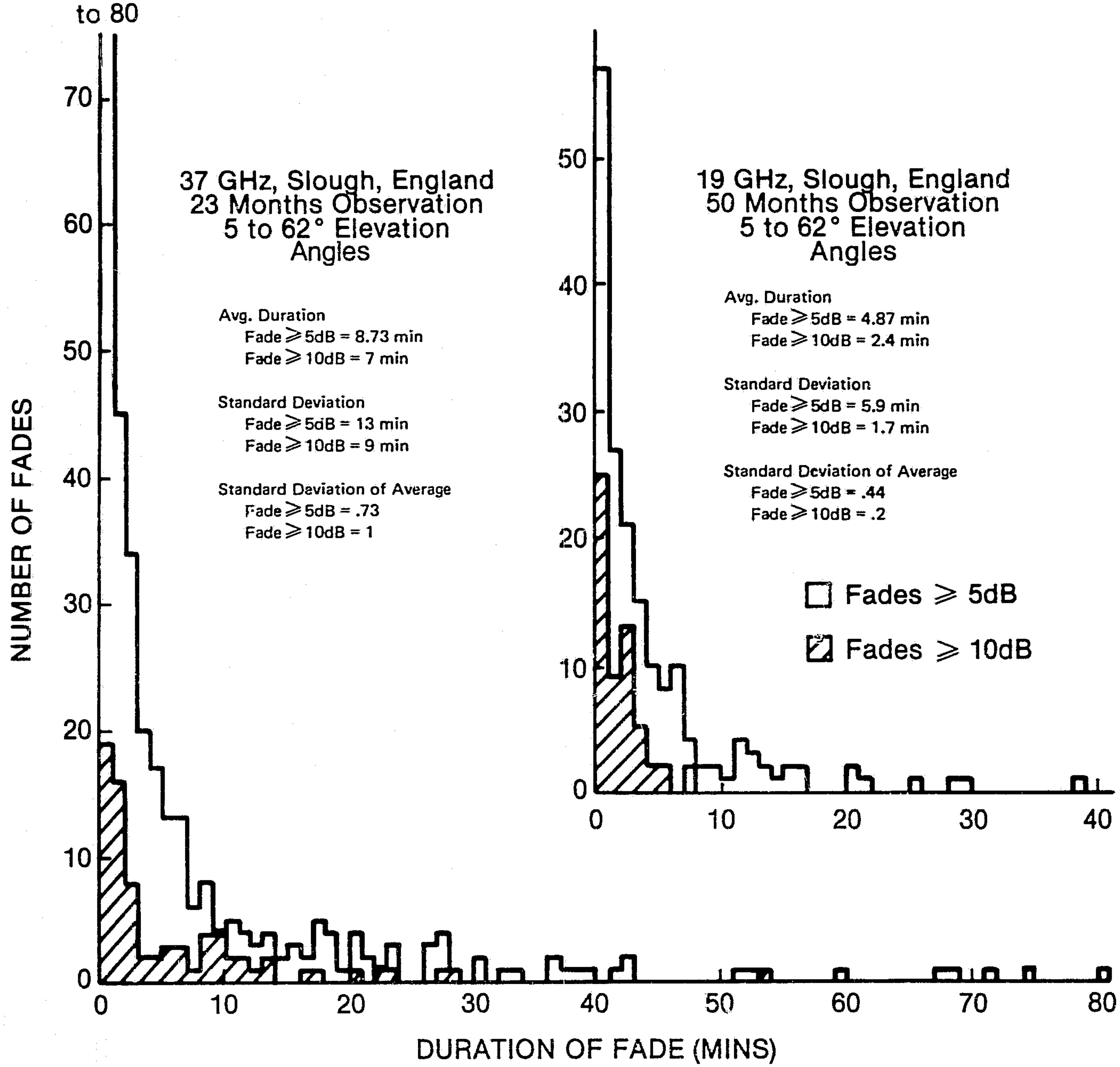

Figure 6.3-11 Histograms of Fades Greater than 5 and 10 dB at 19 and 37 GHz

Rogers and Hyde (1979) give fade duration histograms and diurnal distributions of fade duration for Etam and Lenox, West Virginia. Their data was based on 11.6 GHz sky noise temperature measurements made over a year's period.

Fading durations were also measured in the ESA experiments (CCIR-1978, Rpt 564-1). See Table 6.3-3. These results again include a range of elevation angles, between 20 and 45 degrees (Brussard-1977). The use of these distributions for fixed elevation angle design is not appropriate because of the lack of nighttime data and information required to generate a distribution for a fixed elevation angle. To date no suitable data base or technique of duration period prediction has been devised. However, based on a data base developed by the US and Canadian weather services, the average frequency of fades exceeding a given depth may be estimated.

6.3.5.2 Estimating Fade Duration Versus Frequency of Occurance. The US and Canadian weather services have published maximum rainfall intensity (rain rate) - duration - frequency curves which provide the point rain rates for several hundred locations on the North American continent (U.S. Dept. Comm.-1955 and Canada Atmos. Env.-1973). Two typical sets of curves for the

Table 6.3-3
Fade Duration At 11.4 GHz (ESA Radiometric Data)
Slough, England

Fade duration	Number of fades		Fraction of fading time	
	1 dB	3 dB	1 dB	3 dB
30 s	66	18	0.6%	1.4%
1 min	147	32	2. %	3.5%
2 min	210	50	4.5%	11. %
5 min	297	66	11.5%	15.5%
All fades	453	93	100 %	100 %

close-proximity cities of Baltimore, MD and Washington, D.C. are shown in Figure 6.3-12. The return periods are computed using the analysis of Gumbel (1958) since data is not always available for the 100-year return period. These curves are derived from the single maximum rain-rate event in a given year and are termed the annual series. For microwave propagation studies, curves that consider all high rain rate events are necessary. Such curves, called the partial-duration series, are not normally available, but empirical multipliers have been found for adjusting the annual series curves to approximate the partial-duration series (Dept. Commerce-1955). To obtain the partial-duration curve, the rain rates on the annual series curve for the desired return period are multiplied by the appropriate factors, given in Table 6.3-4.

The intensity-duration-frequency curves actually give the average rain rate over the duration period, whereas the instantaneous rain rate is of interest from a propagation standpoint. The curves therefore do not directly give the frequency versus duration of fades of a given depth. However, for short averaging periods (e.g., five minutes), the instantaneous rain rate would be expected to stay fairly close to the average rain rate, and would certainly never exceed it for the entire period. The curves then can be used to approximate the frequency of short-duration fades, and to place an upper bound on the frequency in any case.

TABLE 6.3-4
Multiplicative Factors to Convert
Annual to Partial-Duration Series

RETURN PERIOD	MULTIPLY ANNUAL SERIES RAIN RATE BY
2	1.13
5	1.04
10	1.01
25,50,100	1.00

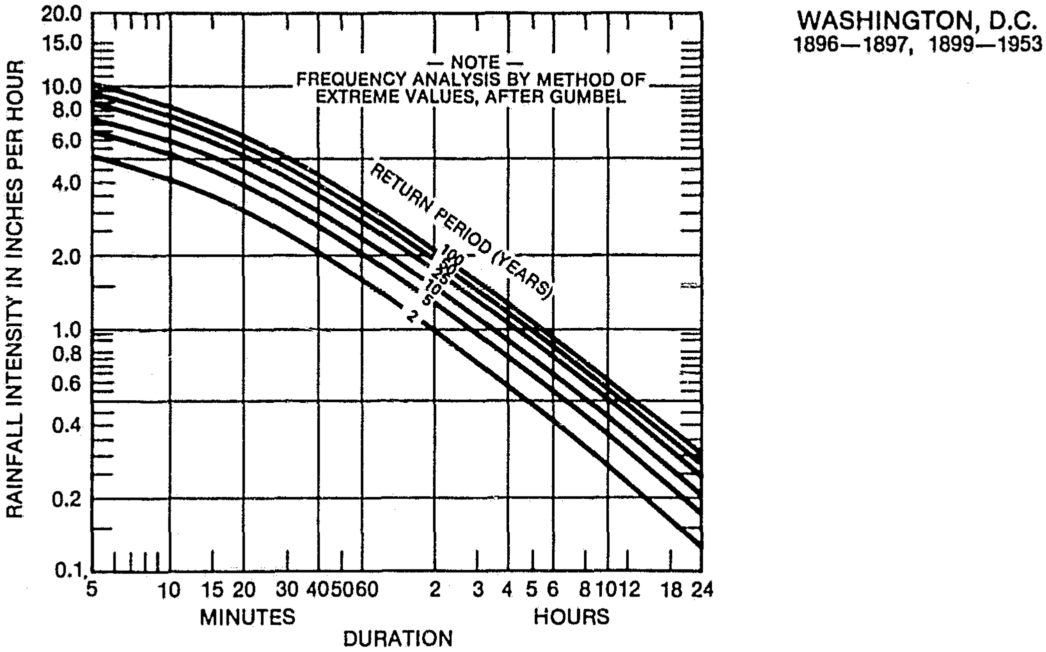

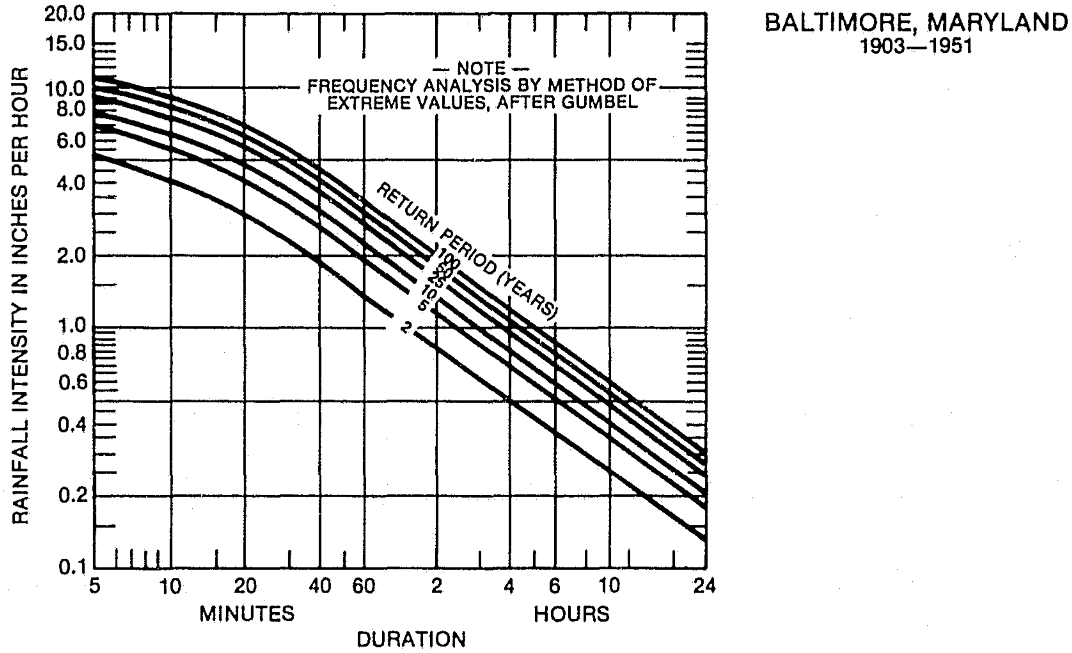

Figure 6.3-12. Typical Rain Rate-Duration-Frequency Curves From U.S. Weather Service, Annual Series

The minimum return period shown on Figure 6.3-12 is two years. It is desirable to be able to extrapolate to one year. This can be done using the Gumbel frequency analysis technique for extreme values. This has been accomplished graphically, for durations of 5 through 60 minutes as shown in Figure 6.3-13. The data used in the curves has been adjusted using the multipliers of Table 6.3-4 to correspond to the partial-duration series. For example, the rain rate expected in Baltimore in a 5-minute period once in 2 years is 5.2 x 1.13 = 5.9 inches per hour. Extrapolating to one year yields 4.8 inches per hour (122 mm/h). Similar calculations may be done for other duration periods to generate a 1-year return period curve for the partial-duration series.

The recommended technique for estimating the maximum fade period to be expected in a N-year rain event is described in Figure 6.3-14. Here the station parameters (latitude, longitude, etc.), operating frequency and link margin (after clear air attenuation is removed) are required inputs. By iteratively solving the attenuation equation in Figure 6.3-1 the maximum allowable point rain rate R_{pm} is obtained. The estimate of the maximum fade duration for the worst rain in 1,2,5,10 or more years is then obtained from data for the partial-duration series rain rate-duration-frequency curves (see Figure 6.3-13). For example, if the system maximum allowable rain rate R_{pm} is 5 inches/hour (125 mm/hr), a system in Washington, D.C. should on the average expect one maximum 5-minute fade each year, one maximum 10-minute fade every three years, etc.

6.3.5.3 Annual and Daily Temporal Distribution of Intense Rain Events. The temporal distribution of rain-induced fade events can be important to a designer since loss of a link during low utilization periods may be tolerable. Figure 6.3-15a shows the distribution, by season, of "record" rainfall events at 207 weather stations throughout the U.S. The events are measured in terms of depth-duration, which specifies the total number of inches of rain and the time over which it fell. The standard durations for comparison are shown in the figure, and range from 5 minutes to 24 hours. Figure 6.3-15b shows the distribution of the maximum events by the times when they start. It is clear that the short-duration events, having the most

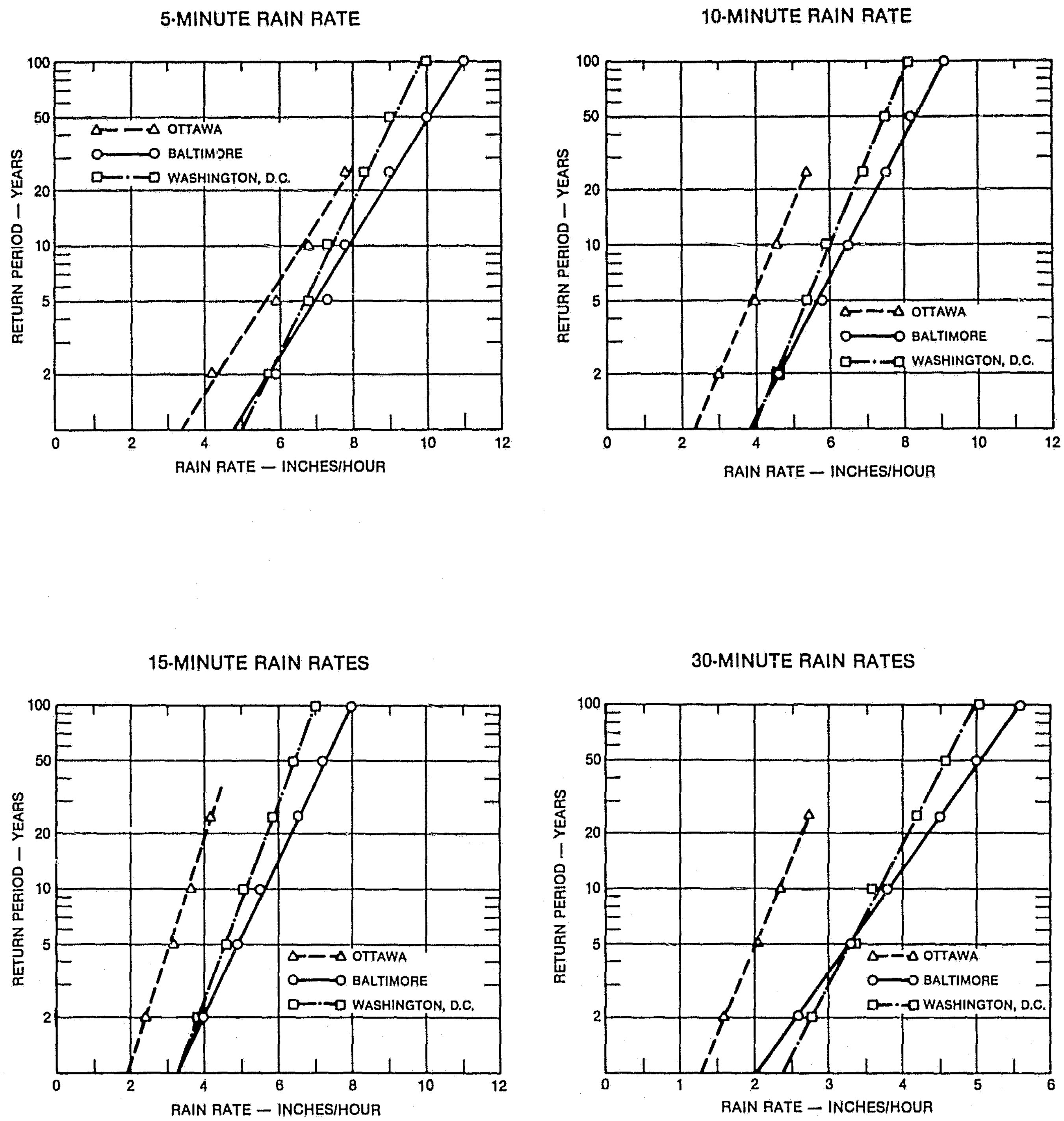

Figure 6.3-13. Extrapolated Partial-Duration Rain Rate-Duration-Frequency Curves

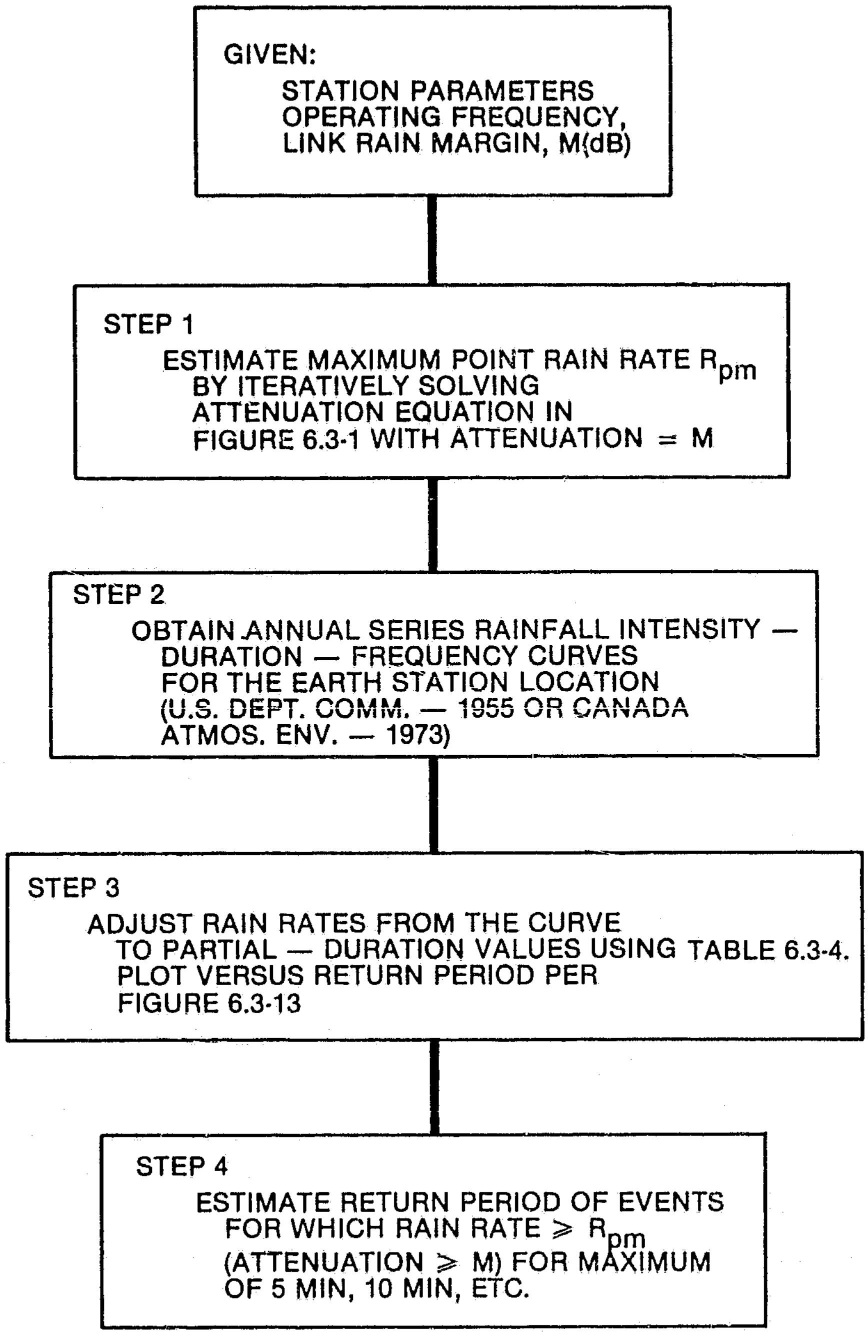

Figure 6.3-14. Technique for Estimating Frequency of Occurrence of Fades of Given Duration

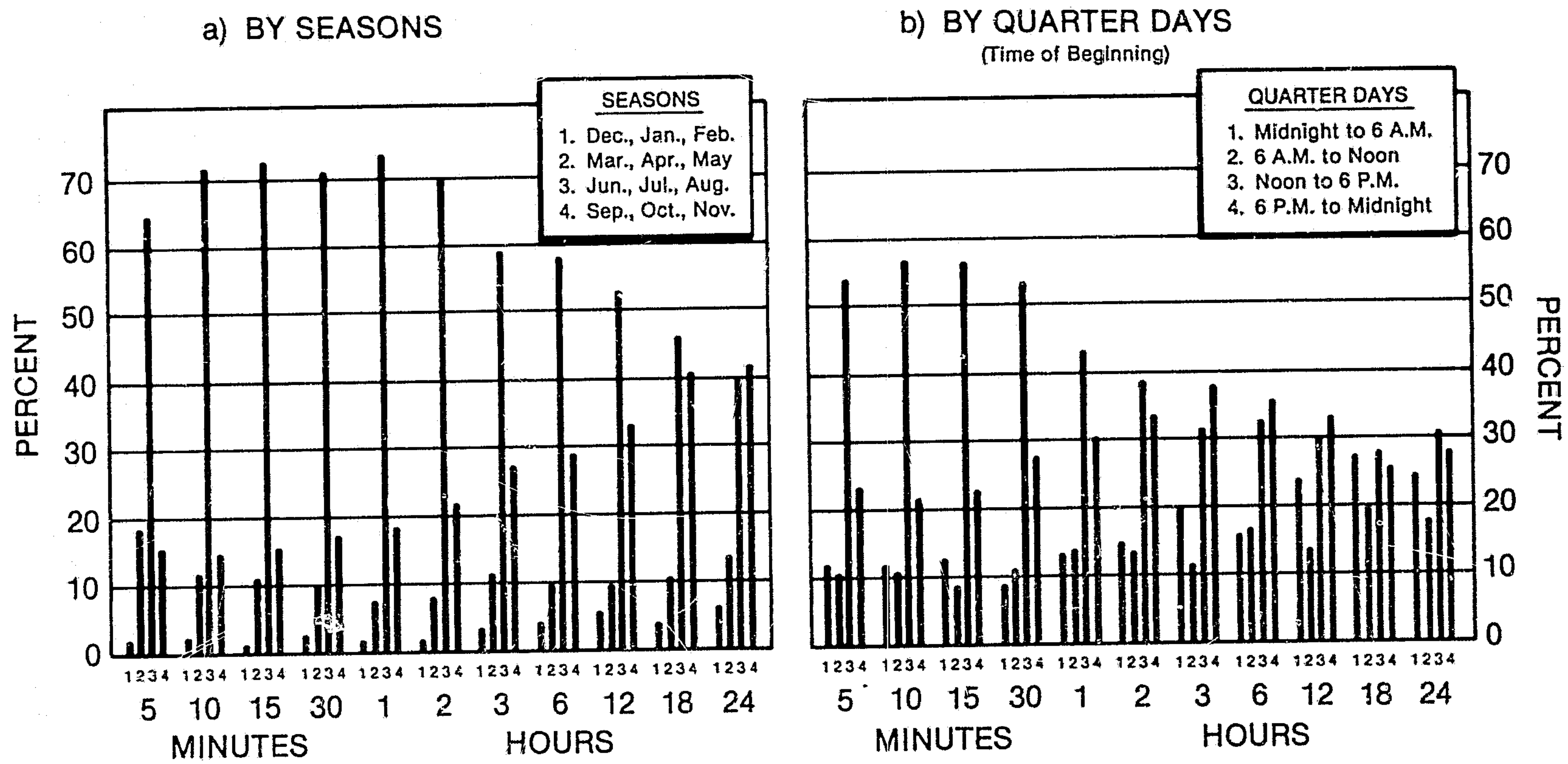

Figure 6.3-15 Distribution of Maximum Rainfall Occurrences at U.S. First-Order Stations (U.S. Dept. Comm.-1947)

intense rain (and the deepest fades) occur predominantly in the summer months and during the afternoon hours. There are regional variations, of course: throughout much of the west coast, summer rains are insignificant. In the midwest, nocturnal thunderstorms are common. The figure also shows that more than 40% of the record 24-hour rainfall events happen in the winter, when steady stratiform rains are the rule.

6.3.6 Rate of Change of Attenuation

Experimental data related to the rate-of-change of attenuation is relatively sparse. Apparently experimenters have not analyzed their measurements to obtain this information except during some extreme attenuation occurrences. Some measurements made at Rosman, NC of the CTS 11.7 GHz beacon showed a maximum rate-of-change of 2 dB/sec on April 24, 1977 (Ippolito-1979). This translates to change of rain rate from 50 mm/hr to 57 mm/hr in one second. Assuming this change in rain rate, the rate of change of attenuation would have been 4 dB/sec at 20 GHz.

More moderate rates, 0.1 dB/sec at 15 GHz, are the highest rates reported by Hodge (1974) and Strickland (1977).

6.3.7 Worst-Month Statistics

Worst-month statistics are of interest to those faced with designing a system to meet performance criteria expressed in terms of a percentage of any calendar month, or of any contiguous 30-day period. The system designer in this case needs to find the percentage of time that some threshold value of attenuation or rain rate will be exceeded within a given month. For every threshold value, there corresponds a month of the year having the highest percentage of time exceeding the threshold (i.e., the percentage exceedance). This is designated the "worst-month" for that threshold. The percentage exceedance in this month, to be expected once every year or every given number of years, is of most interest. For high rain rates, the worst-month would probably correspond to the period of highest thunderstorm intensity or frequency, whereas the worst-month for lower rain rates might be when most rainfall is of the steady, stratiform variety.

An exponential model has been devised (Crane and Debrunner-1978 and CCIR-1979, Rpt 723) for estimating the ratio of the percentage exceedance for a given threshold value in the worst-month to the average annual percentage exceedance for the same threshold. This exponential relationship is expected for statistics of rare events (Gumbel-1958).

Let X_{ij} be the percentage exceedance in month i corresponding to a threshold rain rate j. In a given year, there is for each value j a month h with the highest X_{ij}, denoted X_{hj}. The worst-month statistic is the value of X_{hj} that is equalled or exceeded, on average, once in N years where N (the return period) is specified. The probability that the worst month percentage exceedance is equal to or greater than X_{hj} is given by:

$$P(X_{hj}) = \frac{1}{12N}$$

The exponential model, which applies when X_{hj} is small, states:

$$P(X_{hj}) = C_{oj} \exp(-X_{hj}/C_{1j})$$

Inverting this equation yields:

$$X_{hj} = C_{1j} \left[\ln C_{oj} - \ln P(X_{hj})\right]$$

Figure 6.3-16 is a plot of monthly probabilities of exceeding preselected thresholds X_{ij} for 44 consecutive months of attenuation measurements. It clearly follows the straight-line relation of the model, with $C_{oj} = 0.19$ and $C_{1j} = 7.8 \times 10^{-4}$.

The ratio of the N-year worst-month percentage exceedance X_{hj} to Y_j, the average annual percentage exceedance for the same threshold j, is given by

$$Q_{jN} = \frac{X_{hj}}{Y_j} = \frac{\ln(12\,N\,C_{oj})}{C_{oj}}$$

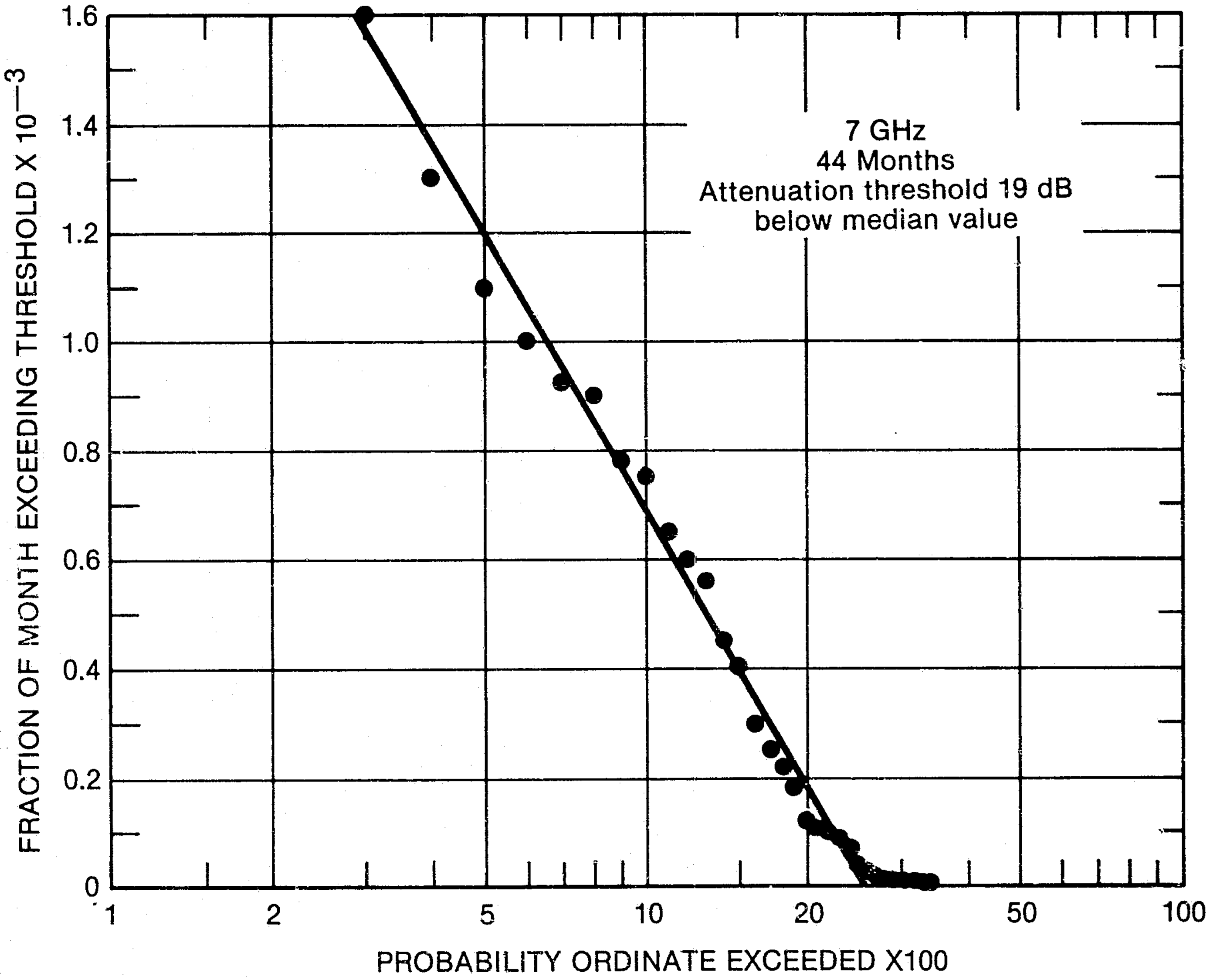

Figure 6.3-16 Probability of Attenuation Threshold Being Exceeded for the Indicated Fraction of Time Per Month (CCIR-1979, Rpt 723)

For the case of N=1 year, this is bounded by:

$$\frac{12}{m} \leq Q_{j1} \leq 12$$

Where M is the number of months in the year that intense rains typically fall. If $M < 3$, the exponential model should be questioned. The lower bound has been shown to be a fair estimate of Q_{j1} for rain rates with annual percentage exceedances in the .001% to .01% range.

An approximate procedure for generating the probability that the X_{hj} exceedance threshold will be exceeded during the worst month is shown in Figure 6.3-17. The process has three major steps. First, determine the worst month (30-day period); second, generate threshold X_{hj}'s associated with the link rain margin for N years, and; third, estimate the probability that the threshold for more than the specified number of minutes for the worst-month.

6.3.7.1 Determination of Worst Month. To determine the worst month, it is suggested that the frequency of thunderstorms (available from the U.S. Climatological Data Sheets or the Canadian Monthly Summary) be plotted per month. This is an approximate technique that assumes the most intense rain rates occur due to convective rain systems, and the thresholds of interest are at high rain rates. However, if more accuracy is desired, a detailed analysis of the hourly precipitation data may be done on a daily basis. The designer must determine if the time-consuming review of all these records is necessary.

6.3.7.2 Determination of X_{hj}. The system rain margin and other parameters will determine the threshold rain rate R_j above which the system will be inoperative or degraded. This value is obtained by iteratively solving the equation in Figure 6.3-1. From the hourly precipitation data for the worst month during N years for a nearby weather station, the days with heavy rain rates are determined and copies of the gauge recordings for these days are ordered. The highest rain rate during the month may be resolved to 15-minute resolution in the Hourly Precipitation Data sheet. However, this 15-minute

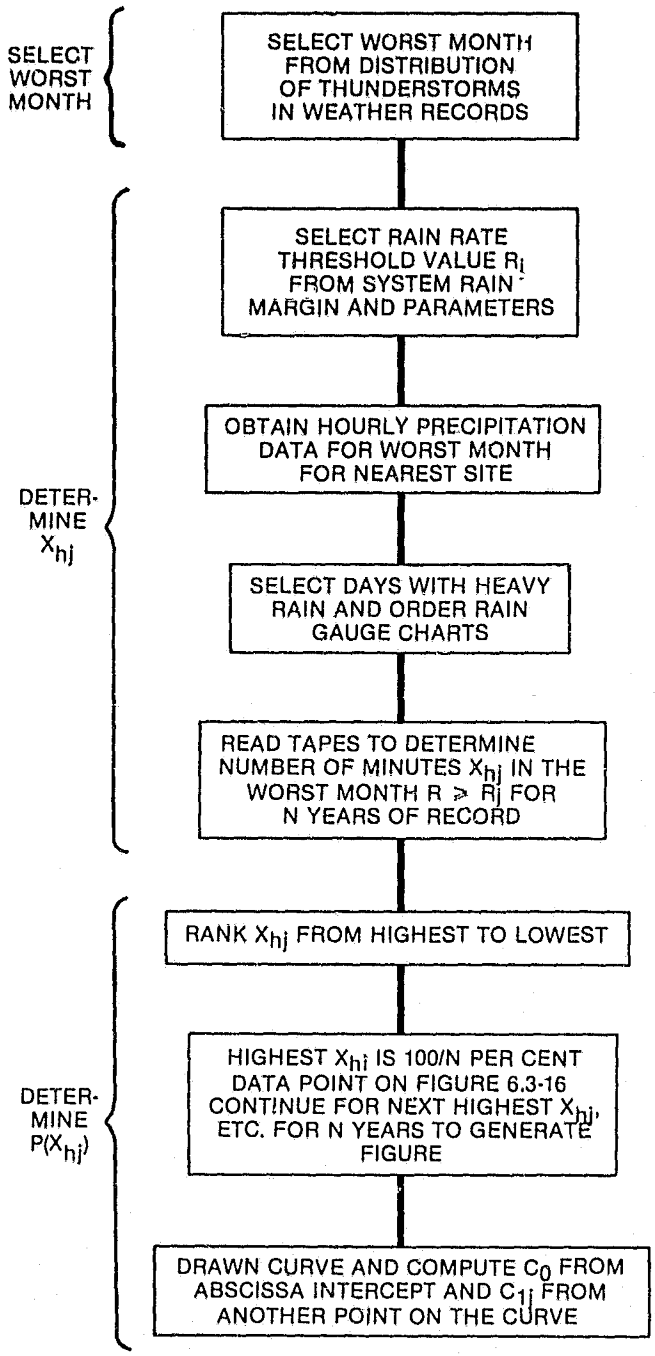

Figure 6.3-17. Technique for Computing the Probability a Worst-Month Estimate is Exceeded

value can only be extrapolated to an "instantaneous" rain rate by measuring the slope of the curve on the rain gauge. The same procedure of measuring the slope will be required for other rain events during the month. The accumulated number of minutes in the worst month when the instantaneous rain rate $R \geq R_j$ is X_{hj} for that year. The same procedure is repeated for the other N-1 years for the worst months only.

6.3.7.3 <u>Determination of $P(X_{hj})$</u>. To determine the probability of exceeding a particular X_{hj} the following procedure is suggested. Rank X_{hj} for N years (worst-months) from the highest to the lowest number of minutes. The highest X_{hj} occurs approximately 100/N percent of the time and represents one data point on Figure 6.3-16. The second highest value of X_{hj} occurs for approximately 100/N percent of the time and represents the second data point. This procedure is repeated for the N values of X_{hj}. A best-fit curve is drawn through these points (similar to the solid line in Figure 6.3-16) on semilog paper. The intersection of the curve with the abscissa is the constant C_{oj}, and C_{1j} is determined from another point on the curve. The resulting equation is:

$$P(X_{hj}) = C_{oj} \exp(-X_{hj}/C_{1j})$$

For the given threshold, this relation indicates the probability of exceeding X_{hj} during the worst month for any year.

6.4 CLOUD, FOG, SAND AND DUST ATTENUATION

6.4.1 <u>Specific Attenuation of Water Droplets</u>

The water droplets that constitute clouds and fog are generally smaller than about .01 cm in diameter. This allows the Rayleigh approximation to be used to calculate specific attenuation in clouds and fog for frequencies up to 100 GHz. Using this approximation, the specific attenuation α_c is, unlike the case of rain, independent of the droplet size distribution. It is proportional to the liquid water content ρ_ℓ:

$$\alpha_c = K_c \rho_\ell \, dB/km$$

is normally expressed in units of g/m^3. The attenuation constant K_c is a function of frequency and temperature and is given by Figure 6.4.1 (CCIR-1978, Rpt. 721). The curves given in the figure assume pure water droplets. The values for salt-water droplets, corresponding to ocean fogs and mists, are higher by approximately 25% at 20^{o}C and 5% at 0^{o}C (Koester and Kosowsky-1978).

6.4.2 Clouds

6.4.2.1 Water Content of Clouds. The liquid water content of clouds varies widely. For stratiform, or layered, clouds, the value was observed to most often fall in the range of 0.05 to 0.25 g/m^3. For the most dense of this type of cloud, stratocumulus, maximum values from 0.3 to 1.3 g/m^3 have been measured (Mason-1971). Cumulus clouds, especially the large cumulonimbus and cumulus congestus that accompany thunderstorms, have the highest values of liquid water content. Fair weather cumulus were found to have liquid water contents generally less than 1 g/m^3. Peak values exceeding 5 g/m^3 were found in cumulus congestus clouds by Weickmann and aufm Kampe (1953). They estimated an average value of 2 g/m^3 for cumulus congestus and 2.5 g/m^3 for cumulonimbus.

Clouds are not homogeneous masses of air containing evenly distributed droplets of water. Rather, the liquid water content can vary widely with location within a single cloud. On the average, the liquid water content in smaller cumulus congestus clouds increases fairly steadily with distance up from the base, then begins to drop off somewhere in the mid-to-upper parts. It also generally decreases with horizontal distance from the center toward the edges. Small-scale variations are also present, however. Sharp differences have been observed in localized regions on the order of 100 m across. One would expect fairly rapid local variation with time as well, due to the complex patterns of air movement taking place within

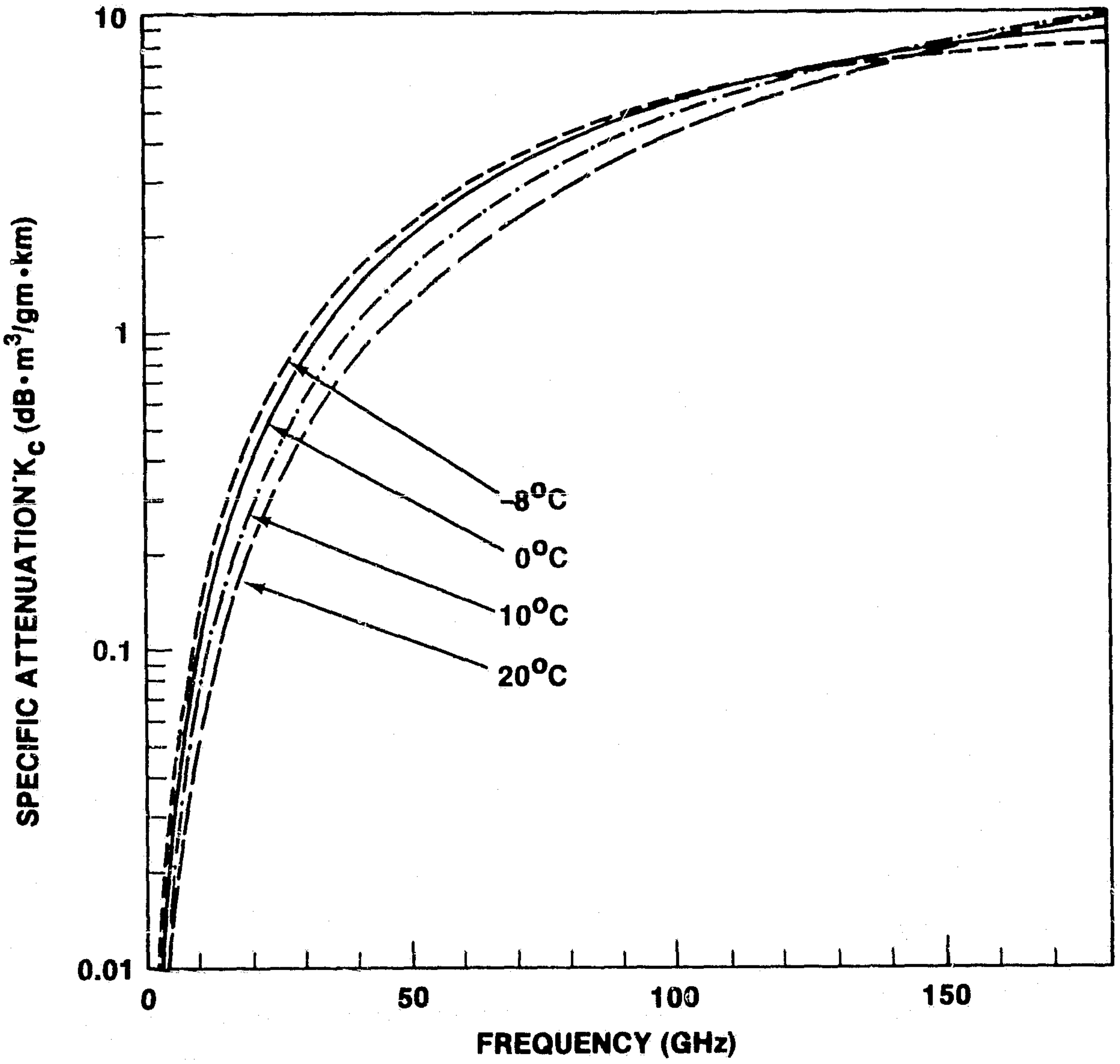

Figure 6.4-1 Attenuation Coefficient K_c Due to Water Droplets (from CCIR-1978, Rpt 721)

cumulus clouds. Updraft wind velocities greater than 10 m/s exist within cumulonimbus clouds (Rogers-1976).

6.4.2.2 Measured Attenuation of Clouds. Typical path lengths through cumulus congestus clouds probably fall between about 2 and 8 km. Using the estimated average liquid water content from above (2 g/m^3), and the attenuation coefficient from Figure 6.4.1, this implies an added path loss at 35 GHz of about 4 to 16 dB. Fortunately, this calculation grossly overestimates the actual attenuation that has been observed through these clouds. This appears to be generally true, as seen in Tables 6.4-1 and 6.4-2, which present measurements from two sources.

In Table 6.4-1, the gaseous attenuation, calculated for the measured surface relative humidity, is given for comparison. The cloud attenuation is in most cases 40% or less of the gaseous attenuation. For frequencies removed from the 35 and 95 GHz "windows," the cloud attenuation would be a smaller fraction of gaseous attenuation. In Table 6.4-1, the number of observations is rather small for all but two types of clouds. The numbers given should therefore not be given undue statistical significance. Also, in using both tables, one should bear in mind the great variability in size and state of development of the clouds observed.

The 35 and 95 GHz data of Table 6.4-1 or 6.4-2 may be roughly scaled in frequency, using the frequency dependence of attenuation coefficient from Figure 6.4-1. Scaling in this manner is quite approximate, as is seen from Table 6.4-1. The ratio of attenuation coefficients at 35 and 95 GHz varies between about 3.9 for -8^{o}C to 6.3 for 20^{o}C. The ratio of average cloud attenuations measured at those frequencies is, from the table, 3.4 for stratocumulus, 2.8 for cumulus, and 6.9 for cumulonimbus. In another series of measurements on individual fair weather cumulus clouds (Lo, et al-1975) this ratio was usually between 3.7 and 5.5.

Table 6.4-1
Zenith Cloud Attenuation Measurements,
From Lo, Fannin and Straiton (1975)

Cloud Type	Number of Observations	Mean Cloud Attenuation (dB)		Mean Gaseous Attenuation (dB)	
		35 GHz	95 GHz	35 GHz	95 GHz
Altocumulus	7	.02	.23	.38	1.93
Altostratus	2	.15	.30	.34	1.73
Stratocumulus	22	.18	.61	.43	2.14
Stratus	8	.13	.12	.42	2.14
Nimbostratus	5	.14	.11	.44	2.32
Cumulus	20	.12	.34	.41	2.12
Cumulonimbus	6	.34	2.36	.40	2.07

Table 6.4-2
Zenith Cloud Attenuation Measurements,
From CCIR (1978, Rpt. 721)

Cloud Type	Cloud Attenuation (dB)	
	95 GHz	150 GHz
Stratocumulus	0.5 - 1	0.1 - 1
Small, Fine Weather Cumulus	0.5	0.5
Large Cumulus	1.5	2
Cumulonimbus	2 - 7	3 - 8
Nimbostratus (Rain Cloud)	2 - 4	5 - 7

There appears to be a large discrepancy between tables 6.4-1 and 6.4-2 in the attenuation of nimbostratus clouds at 95 GHz. The large values of Table 6.4-2 may be due to the inclusion of precipitation in the path, however, because the presence of nimbostratus clouds would usually be accompanied, sooner or later, by precipitation at the ground station, the higher values of attenuation would be expected. This does not necessarily apply to cumulonimbus clouds, however. Because of the large vertical development and limited horizontal extent of these clouds, a typical (30-40^0 elevation angle) propagation path may be intercepted by them without significant rainfall at the ground station.

6.4.2.3 Estimating Cloud Attenuation. There is little experimental data for cloud attenuation, and virtually no long term statistics. Fortunately, the additional attenuation due to clouds appears to be only a fraction of that due to clear air for most types of clouds, and a smaller fraction of that due to rain. The greatest amount of cloud attenuation in the absence of precipitation seems to be caused by cumulonimbus clouds, which accompany thunderstorms. The cloud attenuation accompanying a thunderstorm may be a prologue or epilogue of the greater attenuation of the thundershower, or may be experienced without the accompanying rainfall. The relative frequency of these three possibilities would, on the average, depend upon the azimuth of the ground station beam compared with the prevalent direction of travel of local thunderstorm activity. Considering the current limited state of theoretical analysis and experimental data, the best course of action that can be recommended to system designers is to consider these factors and to adjust attenuation statistics appropriately.

6.4.3 Fog

6.4.3.1 Water Content of Fog. Fog results from the condensation of atmospheric water vapor into water droplets that remain suspended in air. Fog is characterized by optical visibility, which is defined as the distance over which a black target against the sky horizon background can just be discerned by the human eye. The international definition of fog is satisfied when visibility is less than one kilometer (Koester and Kosowsky-1970).

There are two main types of fog, differing in the locale and method of formation. Advection fog is coastal fog that forms when warm, moist air moves over colder water. The liquid water content of advection fog does not normally exceed 0.4 g/m^3. Radiation fog forms inland at night, usually in valleys and low marshes, and along rivers. Radiation fog can have a liquid water content up to 1 g/m^3. Empirical relations have been found (Koester and Kosowsky-1970) between the liquid water content, ρ_ℓ, and the visibility, V(km):

$$\rho_\ell = (18.35\ V)^{-1.43} \quad \text{for advection fog}$$

$$\rho_\ell = (42.0\ V)^{-1.54} \quad \text{for radiation fog}$$

6.4.3.2 Attenuation of Fog. The specific attenuation of fog (in dB/km) is estimated using the curves in Figure 6.4-1. The 10^oC curve is recommended for the summer, and the 0^oC curve should be used for other seasons. Typical liquid water content values for both types of fog vary between about 0.1 and 0.2 g/m^3. The specific attenuation of this, assuming a temperature of 10^o, would be about 0.08 to 0.16 dB/km at 35 GHz, or 0.45 to 0.9 dB/km at 95 GHz. (See Figure 6.4-1.) In a typical fog layer 50 m thick, a path at a 30^o elevation angle would be in the fog only 100 m, producing less than 0.1 dB of attenuation at 95 GHz. This suggests that fog attenuation would, in most cases, be negligible.

6.4.3.3 Estimating Fog Attenuation. Fog attenuation need not be a design consideration unless the ground station is located in an area where fog often reaches extremes of density or depth, and the antenna elevation angle is low. Because radiation fog can be an extremely localized phenomenon, a history of observations at the ground station site may be necessary. Lacking this, records from a nearby airport would be useful.

6.4.4 Sand and Dust Attenuation

Sand and dust scatter electromagnetic energy and their effect may be evaluated via Mie scattering. To date simulated measurements have been carried out in the laboratory (Ahmed and Auchterlouis-1976). At 10 GHz and concentrations of sand and dust less than 10^{-15} g/m^3 the measured specific attenuation was less than 0.1 dB/km for sand and 0.4 dB/km for clay. Severe storms have concentrations exceeding these values.

Blowing sand and dust storms occur in some regions of the U.S. These are recorded by the Weather Service as part of the Local Climatological Data (LCD) at the 291 stations. Ground stations needing this information should review the data recorded by a nearby LCD recording station.

The vertical extent of these sand storms is unknown, but it seems unlikely that high concentrations would exceed 1 km. The path length is expected to vary between 1/2 and 3 km, generally resulting in a total additional attenuation due to sand of the order of 1 dB or less. No measured satellite beacon link data is available to confirm these results.

6.5 PREDICTION OF PATH DIVERSITY FOR EARTH-SPACE PATHS

6.5.1 The Diversity Concept

6.5.1.1 Path Diversity. Rain attenuation often degrades earth-space paths operating above 10 GHz so seriously that the requirements of economical design and reliable performance cannot be achieved simultaneously. To overcome this problem, Hogg (1968) proposed the use of path diversity on earth-space paths to achieve the desired level of system reliability at a reasonable cost compromise. This proposal was based on the hypothesis that rain cells and, in particular, the intense rain cells that cause the most severe fading are rather limited in spatial extent. Furthermore, these rain cells do not occur immediately adjacent to one another. Thus, one might expect that the probability of simultaneous fading on two paths to spatially separated earth terminals would be less than that associated with either individual path. This hypothesis was tested first by Wilson (1970) using radiometric noise emission measurements to determine the rain attenuation on separated paths and by Hodge (1974a) using actual earth-space paths. These and other ensuing experiments have clearly demonstrated that path diversity is an effective technique for improving system reliability in the presence of rain attenuation.

A typical path diversity earth terminal configuration is shown in Figure 6.5-1 along with the definitions which will be used in the later discussions. The parameters are defined as follows:

AZ = azimuth of earth-space path (degrees)
EL = elevation of earth-space path (degrees)
d' = separation between earth terminals (km)
β' = orientation of earth terminal baseline (degrees $0 \le \beta < 180$)
ϕ = major axis of predominant rain cell orientation (degrees $0 \le \phi < 180$)

6.5.1.2 Other Diversity Concepts. Six alternative approaches (Brandinger-1978 and Engelbrecht-1979) have also been suggested as techniques for improving reliability in the presence of rain attenuation. The first, angle diversity, uses one ground site with more than one earth-space path to satellites located in separated orbital positions; thus, the paths are oriented along different azimuths. If a rain cell is located on one path at some distance from the terminal, the result will be quite similar to that for path diversity; however, if a rain cell is located near the terminal, little improvement results. This approach is not as effective as path diversity but may find utility in cases where multiple satellites are available.

The second approach, frequency diversity, is based on the frequency dependence of rainfall attenuation. In this case channel assignments both

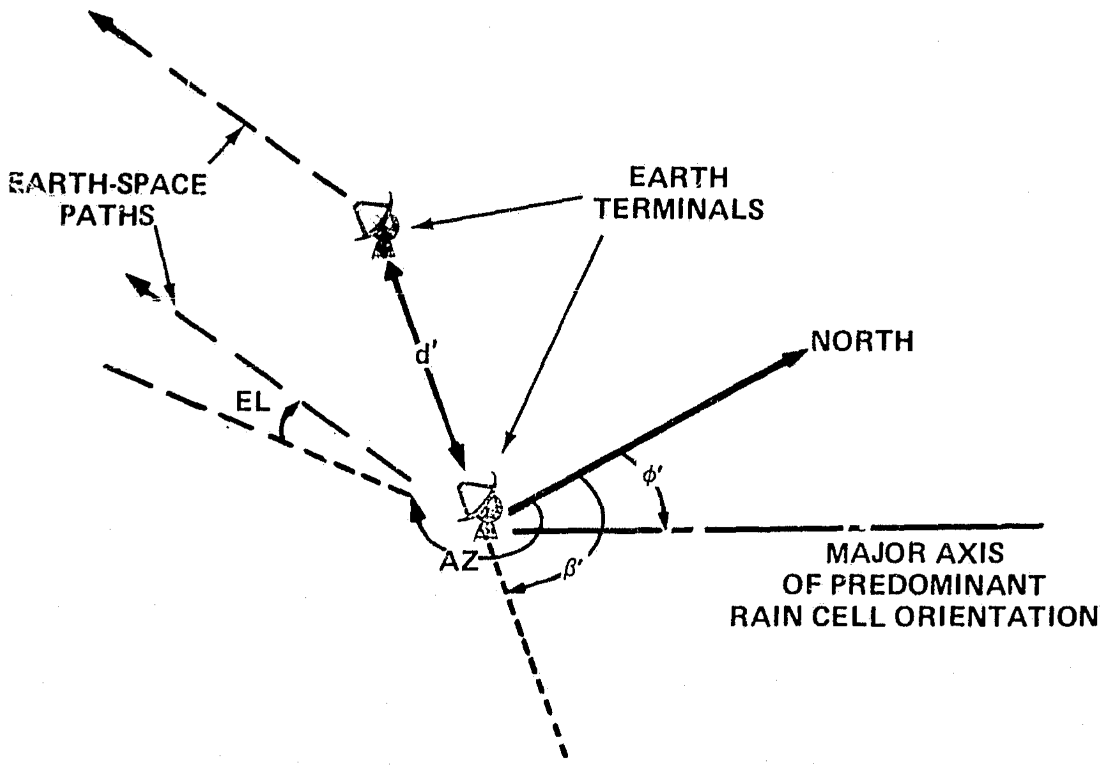

Figure 6.5-1. Path Diversity Configuration and Parameters

above and below 10 GHz are incorporated in the same system. Thus, in the event of rainfall, high priority traffic is diverted to the lower frequency which is less susceptible to rain attenuation. Thus, the channel capacity is adaptively reduced to maintain reliability for a portion of the traffic. This is equivalent to assigning all high priority traffic to a lower frequency and tolerating a lower reliability channel above 10 GHz.

The remaining four approaches are (Engelbrecht-1979):

1) transmitter power diversity
2) signal bandwidth diversity
3) transmission delay or temporary data storage diversity
4) spacecraft antenna gain diversity.

Transmitter power diversity involves adjusting the ground station (uplink) power to maintain the power level at the satellite. On the satellite, this requires increasing the down-link power to overcome the highest attenuation observed by any one of the ground stations it serves simultaneously.

Bandwidth diversity trades off signal power in accordance with the channel capacity relation involving the signal bandwidth.

Transmitter delay diversity is possible when real-time operation is not mandatory. In this case data is temporarily stored during the fade and transmitted later.

Spacecraft antenna gain diversity utilizes an adaptive spacecraft antenna to compensate for the temporal and spatial fade variations. Clearly this technique involves sophisticated antenna hardware aboard the spacecraft.

To date only path diversity has been experimentally verified by propagation researchers, but system designers may well want to consider any combination of all of the diversity options. Obviously complexity and additional cost play a major role in the ultimate decision to use any diversity technique. These factors are not considered further in this document.

6.5.2 Diversity Gain and Diversity Advantage

In order to characterize the performance of a diversity system, it is convenient to establish a descriptive parameter for this purpose. Two such parameters have been proposed and utilized in the literature; they are diversity gain, G_D, and diversity improvement, I.

Let us consider the distribution of rain attenuation, i.e., excess path attenuation, fade depth, or attenuation above the clear sky level, exceeded on a single path, A(T), for a given percentage of time, T; and the rain attenuation, $A_{div}(T)$, exceeded jointly on two separated paths for the same percentage of time as shown in Figure 6.5-2. Diversity gain, G_D, (Hodge-1974a) may be defined as the difference between the rain attenuation exceeded on a single path and that exceeded jointly on separated paths for a given percentage of time, i.e.,

$$G_D(A) = A(T) - A_{div}(T) \tag{6.5-1}$$

Diversity advantage, I, (Wilson and Mammel-1973) may be defined as the ratio of the percentage of time exceeded on a single path to that exceeded jointly on separated paths for a given rain attenuation level, i.e.,

$$I(A) = \frac{T(A)}{T_{div}(A)} \tag{6.5-2}$$

Diversity gain may be interpreted as the reduction in the required system margin at a particular percentage of time afforded by the use of path diversity. Alternatively, diversity advantage may be interpreted as the factor by which the fade time is improved at a particular attenuation level due to the use of path diversity.

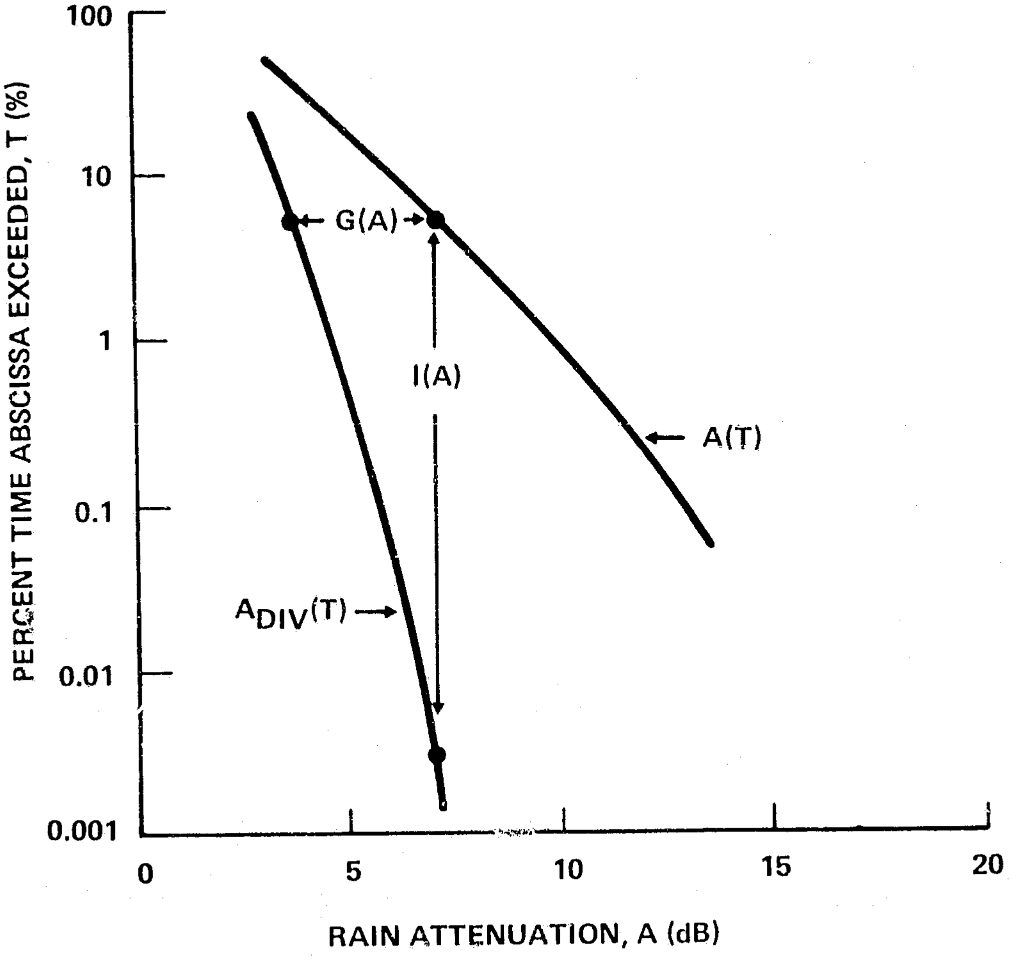

Figure 6.5-2 Hypothetical Rain Attenuation Distribution

In the preceding discussion, it has been implicitly assumed that the fade distributions associated with each individual earth terminal were identical. However, in actual practice this is seldom the case. These distributions may differ because the measurement period is not long enough for the spatial rainfall distribution to become uniform; in this case the differences between the distributions are an indication of the uncertainty of the measurement. Alternatively, local climatological variations may give rise to real differences between distributions measured only a few kilometers apart; very little is known definitively about this latter effect. In general, however, since there is little or no basis to give greater weight to one distribution over another, the definitions given in eqs. 6.5-1 and 6.5-2 should be generalized for experimental data analysis to:

$$G_D(A) = A_{ave}(T) - A_{div}(T) \qquad (6.5\text{-}3)$$

$$I(A) = \frac{T_{ave}(A)}{T_{div}(A)} \qquad (6.5\text{-}4)$$

where $A_{ave}(T)$ is the average of the single terminal fade depth exceeded for the percentage time, T, and $T_{ave}(A)$ is the average of single terminal percentages of time exceeded at the fade level A.

6.5.3 Diversity Experiments

The experimental diversity results available in the literature are summarized in Table 6.5-1. This table includes the results reported for each of the four methods -- direct measurement of satellite beacons, radiometric measurement of the sky temperature, radar measurements of rain structures and radiometric measurements of solar emission. In each case the reference is cited along with the location of the experiment, the frequency, station separation distance, baseline orientation, path azimuth, and path elevation. In cases where multiple measurements are reported, the range of the appropriate parameters is indicated.

REFERENCE	LOCATION	FREQ.	SEPARATION	BASELINE	AZ	EL
I. SATELLITE EXPERIMENTS						
Hodge (1974)	Columbus, Ohio	15.3 GHz	4.0-8.3 km	159-164°	210°	38°
Hodge (1976b)	Columbus, Ohio	20-30	13.2-14.0	33-151°	197°	40°
Vogel, et al (1976)	Austin, Texas	30	11.0	0°	172°	53°
Hyde (1976)	Boston, Mass.	18	6.7-35.2	74-93°	212°	36°
	Columbus, Ohio	18	5.1-38.9	91-95°	196°	42°
	Starkville, Miss.	18	8.3-40.0	105°-113°	190°	51°
Westinghouse (1975)†	Washington, DC area	20-30	27.9-75.8	Several	≈206°	≈40°
II. RADIOMETER EXPERIMENTS						
Wilson (1970)	Crawford Hill, N.J.	16	3.2-14.4	135°	226°	32°
Wilson & Mammel (1973)	Crawford Hill, N.J.	16	11.2-30.4	135°	226°	32°
Gray (1973)	Crawford Hill, N.J.	16	19.0-33.0	45-135°	226°	32°
Funakawa & Otsu (1974)	Kokubunji, Japan	35	15.0	---	180°	45°
Hall & Allnutt (1975)	Slough, England	11.6	1.7-23.6°	20-106°	198°	30°
Allnutt (1975)	Slough, England	11.6	1.7-23.6°	20-106°	198°	30°
Strickland (1977)	Quebec, Canada	13	18.0	11°	122°	19°
	Ontario, Canada	13	21.6	1°	116°	16°
Bergmann (1977)	Atlanta, Georgia	17.8	15.8-46.9	141-146°	228°	38°
	Denver, Colorado	17.8	33.1	86°	197°	43°
III. RADAR EXPERIMENTS						
Goldhirsh & Robison (1975)	Wallops Island, Va.	13-18	2-20	0-180°	0-360°	45°
Goldhirsh (1975)	Wallops Island, Va.	13-100	2-20	0-180°	0-360°	45°
Goldhirsh (1976)	Wallops Island, Va.	18	2-20	0-180°	0-360°	45°
Hodge (1978)	Montreal, Quebec	13	4-42	0-180°	122-240°	19-40°
IV. SUNTRACKER EXPERIMENTS						
Wulfsburg (1973)	Boston, Mass.	35	11.2	158°	---	---
Funakawa & Otsu (1974)	Kokubunji, Japan	35	15.0	---	---	---
Davies & Croom (1974)	Slough, England	37	10.3	67°	---	---
Davies (1976)	Slough, England	37	10.3-18.0	67-110°	---	---

† Long-Baseline Site Diversity Experiment

Table 6.5-1. Summary of Diversity Experiments

6.5.4 Path Diversity Design Factors

6.5.4.1 Separation Distance. Diversity gain depends strongly upon the earth terminal separation distance, d'. The diversity gain increases rapidly as d' is increased over a small separation distance, i.e., up to about 10 km; thereafter the gain increases more slowly until a maximum value is reached, usually between about 10 and 30 km (Fig. 6.5-3). This maximum value is generally quite close to that value associated with uncorrelated fading at the individual earth terminals.

In contrast to the uncorrelated case, one may argue that correlated fading may occur for paths separated by distances associated with typical rain cell separation distances. Such an effect may be inferred from the rainfall statistics of Freeny and Gabbe (1969); however, these statistics are associated with point rainfall rates rather than path average rainfall rates. Again, no definitive report of this effect has been published to date.

6.5.4.2 Baseline Orientation. The perpendicular separation between parallel paths is greatest when the earth terminals are located on a baseline perpendicular to the projections of the paths on the earth's surface. This arrangement minimizes the possibility of both paths passing through the same rain cell. Nevertheless, the dependence of diversity gain on baseline orientation is quite weak except, possibly, for very short separation distances.

The baseline orientation problem is further complicated if spatial anisotropy of the rain cells, i.e., a preferred direction of rain cell elongation, is known to exist in the region of interest. In this case, a baseline orientation perpendicular to the preferred axis of rain cell orientation would be desirable if the direction of the propagation path were ignored.

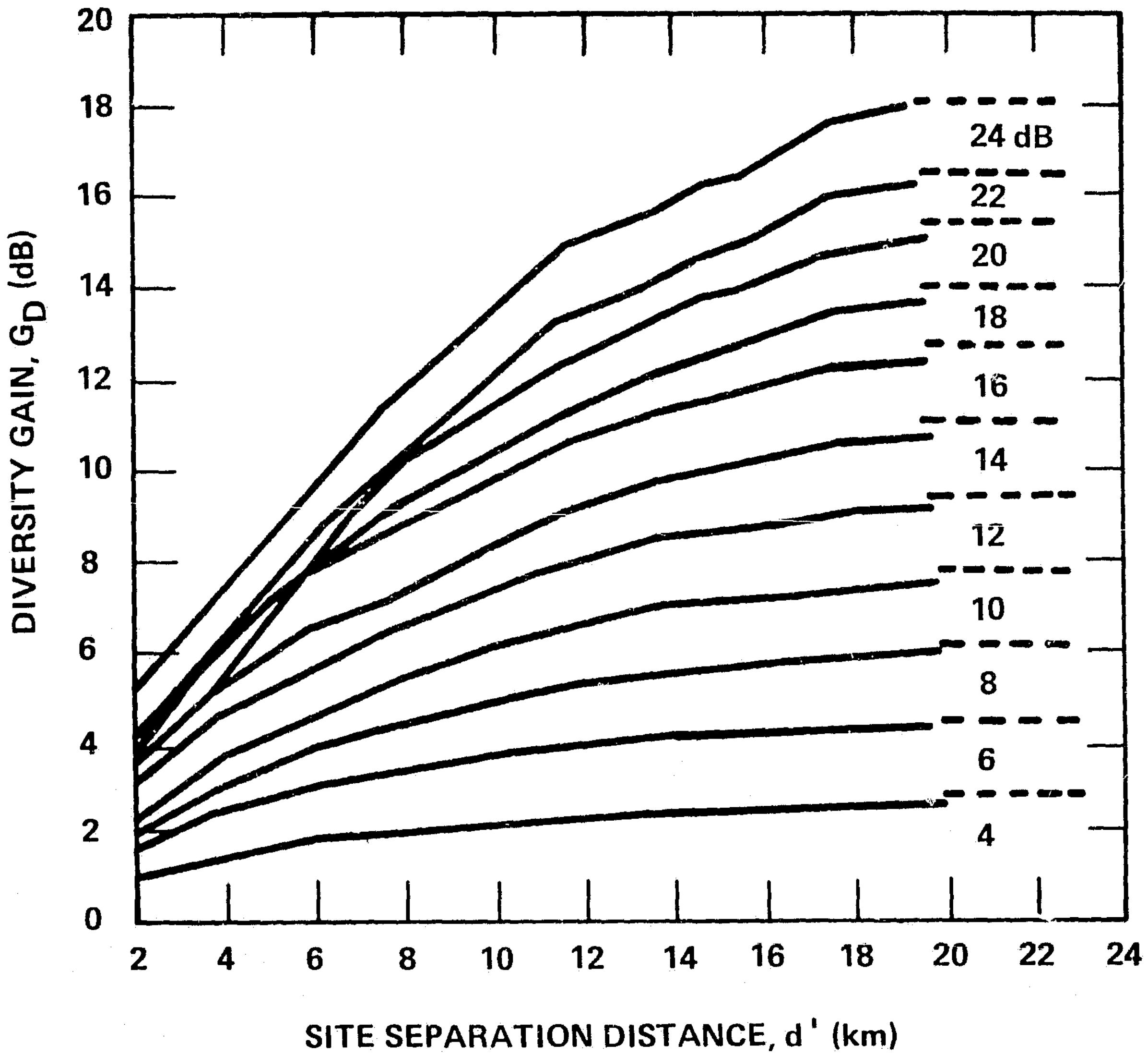

Figure 6.5-3. Diversity Gain, G, versus Separation Distance, d, f = 18 GHz. (Horizontal Dashed Lines Represent Optimum Levels (Goldhirsh and Robison-1975)

Considering both factors together, it appears that the most desirable baseline orientation is that which bisects the larger of the two angles between the projection of the propagation path and the preferred axis of rain cell orientation.

6.5.4.3 Path Elevation Angle. The separation distance required to achieve a given level of diversity gain increases as the path elevation angle decreases (Hodge-1978). This is due to the increased likelihood of path intersections with rain cells at lower elevation angles. This effect is coupled to the problem of rain cell anisotropy and path azimuth as noted below.

6.5.4.4 Path Azimuth Angle. For synchronous satellites the path azimuth and elevation angles are not independent, and, thus, the dependence of diversity performance on these variables cannot be fully separated. If all rain cells were isotropic, one would expect no variation in diversity performance with azimuth angle other than that associated with the elevation angles. However, when rain cell anisotropy is considered, there appears to be a weak improvement in diversity performance for path azimuths in the southerly compass quadrant that does not contain the preferred axis of rain cell orientation.

6.5.4.5 Link Frequency. Experimental measurements to data have shown no significant dependency of diversity gain on the link frequency (Goldhirsh and Robison-1975) over the 10-30 GHz frequency. Certainly the probability of a given attenuation level being exceeded on a single path is strongly frequency dependent. However, diversity gain is a conditional statistic based upon the difference between single terminal and diversity attenuation levels. However, for link frequencies above 30 GHz, attenuation on both paths simultaneously can be sufficient to create an outage. Therefore, extrapolation beyond 30 GHz is not recommended.

6.5.4.6 Anisotropy of Rain Cells Along a Front. There is a tendency for convective rain cells associated with frontal activity to occur in bands nearly perpendicular to the direction of movement of the front. The direction of motion of the cells within such a band tends to be along or slightly ahead of the direction of the front, and, furthermore, the more intense cells tend to elongate in their direction of motion (Harrold and Austin-1974). Thus, two types of anisotropy are evident. The first is associated with the elongation of individual cells and is related to the probability of parallel paths passing through the same cells. The second is associated with the statistics of the vector separation between rain cells and is associated with the probability of parallel paths simultaneously intersecting two different rain cells. Fortunately, these two preferred orientations are nearly parallel, and thus the same corrective action is required in each case. Namely, the baseline orientation should be nearly perpendicular to these preferred directions.

6.5.4.7 Local Climatology. To a first order of approximation it is commonly assumed that the probabilities of rain cell occurrence are uniformly distributed over rather large regions of the earth's surface. This assumption may be invalidated by the presence of any one of the following features: mountains, large valleys, large bodies of water, or urban heat "islands". These features can give rise to nonuniform spatial distributions of rain cell probabilities.

Spatial distributions of rainfall accumulation are readily available in the meteorological literature; however, it is not currently known whether the use of these data is applicable to the question of earth terminal siting. For example, it may be argued that these rainfall accumulations are dominated by low rainfall rates and thus do not reflect the spatial distributions of intense rain cells which dominate the occurrence of high attenuation levels on earth-space paths.

6.5.4.8 Switching Rates. The fading rate on a single path is relatively slow. The highest rates reported are on the order of 0.1 dB/sec. at 15 GHz (Hodge-1974a, Strickland-1977) and 2 dB/sec. at 11.7 GHz (Ippolito-1979). This implies that the decision and switching process for diversity paths may be quite slow and should pose no significant problem in the system design.

6.5.4.9 Connecting Link. The implementation of a path diversity system must incorporate a connecting link between the two earth terminals. If this link is closed, i.e., waveguide, coax, etc., its performances will be independent of meteorological variables and will not directly influence the reliability improvement provided by the use of path diversity. If, however, the connecting link operates above 10 GHz in the atmosphere, the joint fading statistics of the connecting link with the earth-space paths must be considered. This degrading effect appears to be small except for cases of very long baselines or baseline orientations parallel to the earth-space propagation paths. (Ferguson and Rogers-1978)

6.5.4.10 Multiple Earth Terminals. Substantial link reliability improvements result from the use of two earth-space propagation paths. Thus one may conjecture that further improvement might result from the addition of additional diversity paths. Determination of diversity gain for N diversity terminals shows that most of the gain is realized for two terminals with very little further increase in gain for additional terminals (Hodge-1974b).

6.5.5 An Empirical Model

6.5.5.1 Description of the Model. The data available from early diversity experiments in New Jersey and Ohio (Hodge-1974a, Wilson-1970, Wilson and Mammel-1973, Gray-1973) were used to develop an empirical model for the dependence of diversity gain on separation distance, d', and single site attenuation, A (Hodge-1976a). The resulting model was of the form

$$G_D = a'(1-e^{-b'd'}) \qquad (6.5\text{-}5)$$

where the coefficients a' and b' depended upon the single site attenuation according to

$$a' = A - 3.6\ (1-e^{-0.24A}) \qquad (6.5\text{-}6)$$

$$b' = 0.46\ (1-e^{-0.26A}) \qquad (6.5\text{-}7)$$

These results were nominally applicable to baseline orientations of 135^{0}, i.e., NW-SE, elevation angles of 35^{0}, azimuth angles of 220^{0}, and link frequencies of 15 GHz. The model reproduced all of the available data at the time within 0.75 dB as shown in Fig. 6.5-4. The variation of the coefficients a' and b' are shown in Fig. 6.5-5.

The empirical relation should not be utilized for attenuation in excess of 15 or 20 dB, since it appears to reach an unphysical limit for large attenuation values such as those associated with frequencies above 30 GHz. Consider the following relation for the link margin:

$$M' = M_o' - A + G \tag{6.5-8}$$

where M' is the link margin at any time and M_o' is the zero-rain link margin. In the limit where A becomes large

$$M' \simeq M_o' - 3.6 - (A-3.6)e^{-0.46d'} \tag{6.5-9}$$

neglecting terms similar to $e^{-0.24A}$, etc. Thus for even moderate separation distances, $d \geq 10$ km

$$M' \simeq M_o' - 3.6 \tag{6.5-10}$$

which says that the link only degrades 3.6 dB for any level of attenuation.

Rewriting Eq. 6.5-9 for A yields the amount of attenuation on the reference link allowable for a given M_o' and M',

$$A = 3.6 + (M_o'-M'-3.6)e^{+0.46d'} \tag{6.5-11}$$

Solving this for M_o' = 20 dB, M'_{min} = 10 dB for a low error rate and d = 10 km, yields

$$A_{max} = 3.6 + (20-10-3.6)e^{0.46d'} \tag{6.5-12}$$

$$\simeq 640 \text{ dB!}$$

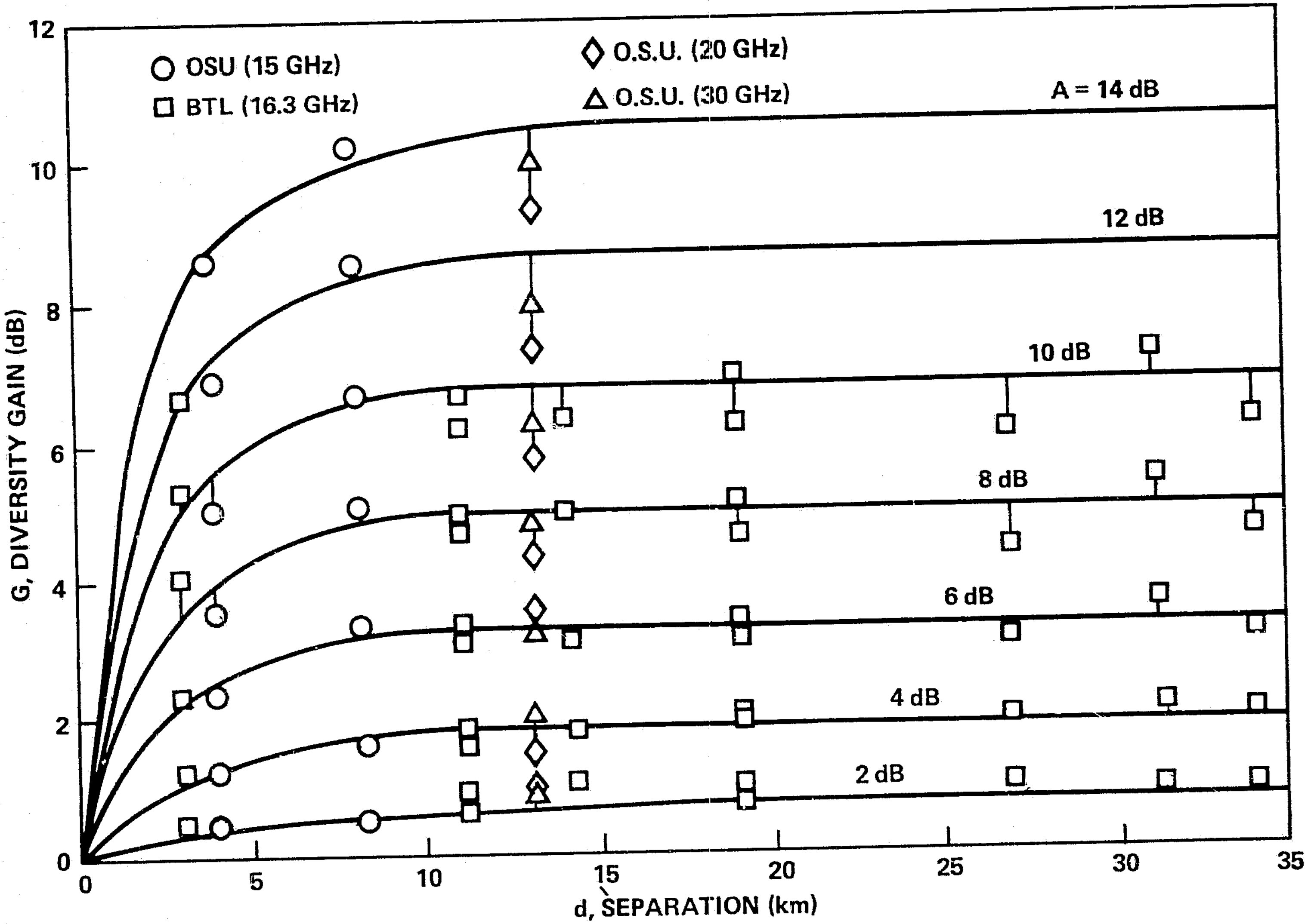

Figure 6.5.4 Diversity Gain Versus Separation Distance

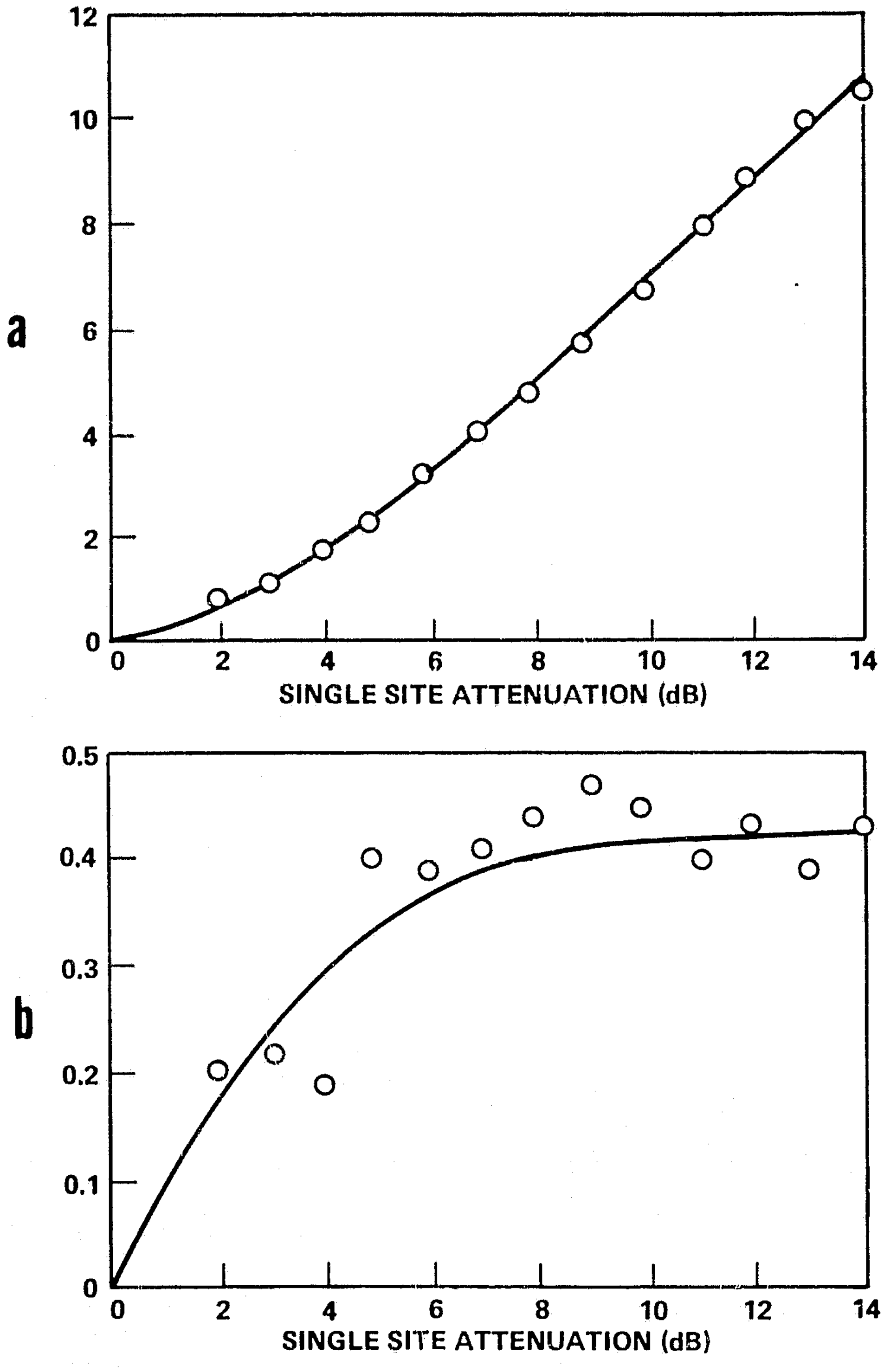

Figure 6.5-5 Variation of Empirical Model Coefficients with Fade Depth (Hodge-1976)

Clearly this is a physically unrealizable number. A term must be added to Eq. 6.5-11 and then into 6.5-5 to avoid this situation. The form of this term is now under study.

6.5.5.2 Example of the Empirical Model. The experimental results in Figure 6.5-4 do demonstrate that the diversity gain does appear to apply up to the 8 to 10 dB level in the 10 to 30 GHz frequency range. Using this fact, the cumulative attenuation statistics for a hypothetical ground station system of two identical stations separated by 10 to 15 km at Rosman, N.C., would yield statistics significantly better than one station. These are shown in Figure 6.5-6 based on the attenuation data obtained by the distribution extension technique in Section 9.3. The diversity gain is the difference in attenuation levels for a given percentage of exceedance. For example, at A = 10 dB the diversity gain is approximately 6.7 dB (see Figure 6.5-6). The diversity advantage (defined in Figure 6.5-2) would be about 4.8 at A = 3.3 dB.

6.6 PREDICTION OF SIGNAL FLUCTUATIONS AND LOW-ANGLE FADING ON EARTH-SPACE PATHS

The amplitude, phase, and angle-of-arrival of a microwave signal passing through the troposphere vary due to inhomogeneities in the refractivity (clear air). The effects occur on time scales shorter than a minute and on spatial scales shorter than a kilometer. At low elevation angles, the amount of troposphere traversed is significant, and so, below approximately 10 degree elevation angles, low-angle fading must be considered.

6.6.1 Antenna Aperture Effects

The effects of tropospheric turbulences and the antenna can not be totally decoupled because, of course, the measurements and operating systems utilize antennas. The antenna aperture processes the incident wavefront with its spatial and temporal fluctuations into a received signal with only temporal variations.

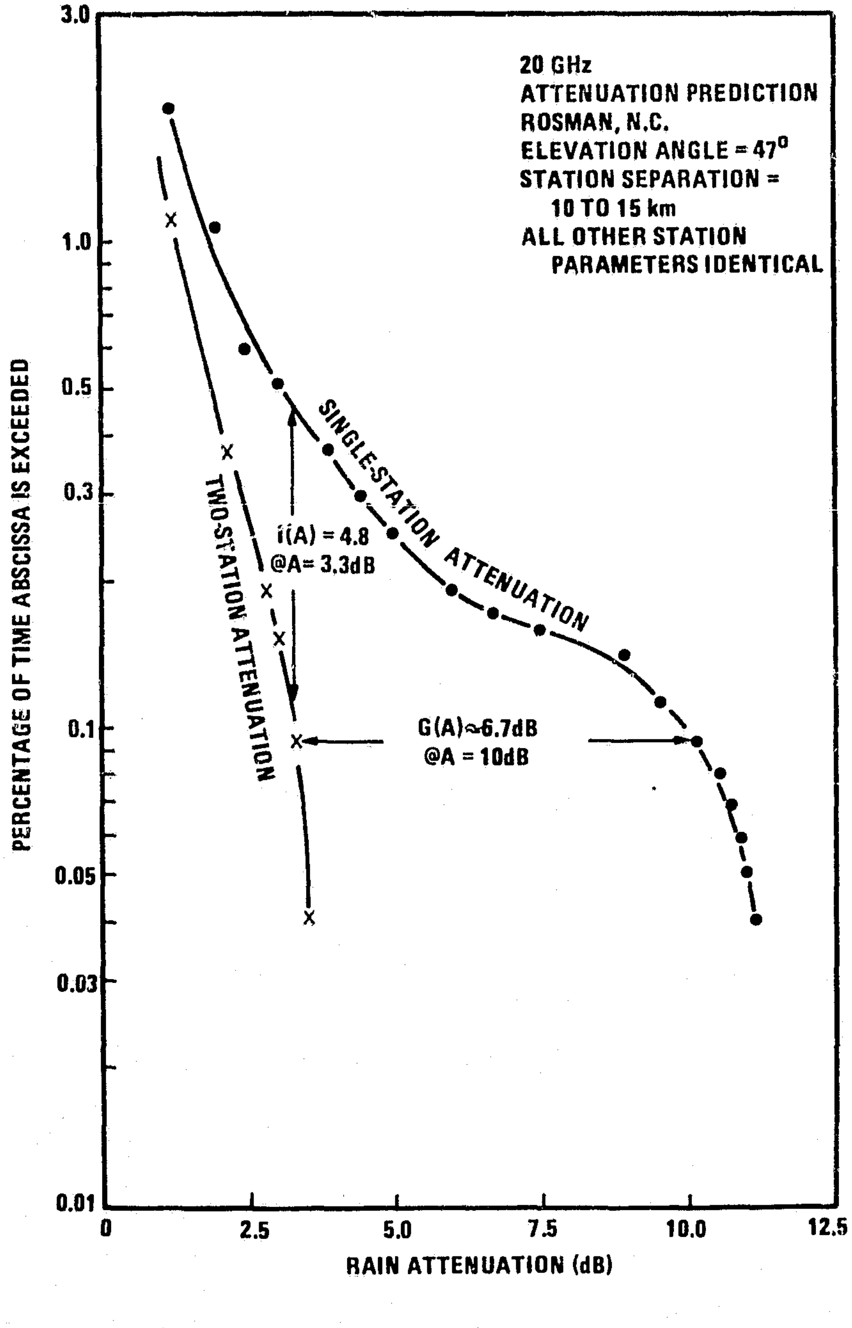

Figure 6.5-6 Path Diversity Gain Statistics for Rosman, N.C.

Wavefront tilt due to inhomogeneities and gradients in the refractivity appear to the antenna as an angle-of-arrival variation. Average elevation angle ray bending is usually 10 times more pronounced than azimuthal ray bending. However, wave tilt fluctuations tend to be randomly distributed in angle relative to the slant path propagation direction, at least when the majority of the path is above the regime of surface effects (surface effects extend upwards several hundred meters).

Fluctuations occurring on spatial scales smaller than the size of the aperture are often referred to as wavefront ripple. This phase incoherence results in an instantaneous gain loss or degradation.

The fluctuations described herein apply to the ground station downlink because its antenna is in close proximity to the turbulent medium. An uplink satellite path will suffer fluctuation gain degradation only due to scattering of energy out of the path. Because of the large distance traversed by the wave since leaving the troposphere, the wave arrives at the satellite antenna as a plane wave (no ripple) and with only minute angle-of-arrival effects. Interference to satellites on the geostationary arc can occur due to the refraction and diffraction of radio relay links oriented toward the satellite (see CCIR-1978, Rpt. 393-2).

6.6.2 Amplitude Fluctuations

6.6.2.1 Overview. The phenomena of amplitude and angle-of-arrival fluctuations combine to form received signal amplitude fluctuations. For many cases of propagation one or more of these effects may often be neglected. For example, a receiving system which employs an antenna with a wide beamwidth will not experience angle-of-arrival-induced amplitude fluctuations for most elevation angles. However, such simplification is not always possible. The theory of wave propagation and scattering in random media allows a combination of the turbulence induced effects to be performed in the context of weak fluctuations along a line-of-sight path. The work of Ishimaru (1978), which defines coherent and incoherent field components as a plane wave propagates through a random medium, provides a method of combining amplitude and angle-of-arrival effects into a model of received signal amplitude fluctuation. A model utilizing the concept of incident plane wave decomposition (see Figure 6.6-1) has been proposed by Theobold and Hodge (1978).

6.6.2.2 <u>Variance of Received Signal Amplitude.</u> The assumption of weak turbulence, i.e., log-amplitude variance $\sigma_x^2 < 0.5$, is invoked for a plane wave incident on a region of turbulence, propagating a distance L_t (km) and impinging on circular aperture of diameter d_a (meters). The antenna is assumed to have a Gaussian pattern function with half-power beamwidth B (degrees). If v_d is the received signal amplitude voltage, an expression for signal variance relative to average power is

$$S^2 = 10 \log_{10} \left(\frac{<V_d^2> - <V_d>^2}{<V_d>^2} \right)$$

$$= 10 \log_{10} \left(\frac{I_c \sigma_1^2 + \dfrac{I_i B^2}{5.55\sigma_2^2 + B^2} - I_i \left(\dfrac{B^2}{2.77\sigma_2^2 + B^2} \right)^2}{I_c + I_i \left(\dfrac{B^2}{2.77\sigma_2^2 + B^2} \right)^2} \right)$$

where

$$I_i = 1 - \exp [-L_t/L_o]$$

$$I_c = (1 - I_i) / (1 + \sigma_1^2)$$

$$\sigma_1^2 = \text{amplitude variance} \simeq \sigma_x^2$$

σ_2^2 = angle-of-arrival variance (deg^2)

L_t = path length

L_o = a function of density and cross-section of scattering along the path.

Measurements at The Ohio State University of the ATS-6, 20 and 30 GHz beacons as the satellite underwent synchronous orbit transition were used to derive empirical constants for this model with an effective turbulence height, h_t, of 6 km (typical), r_e = mean earth radius = 6377 km, θ = elevation angle, and L_t = path length.

$$L_t = \left[h_t + 2r_e h_t + (r_e \sin\ )^2\right]^{1/2} - r_e \sin\theta$$

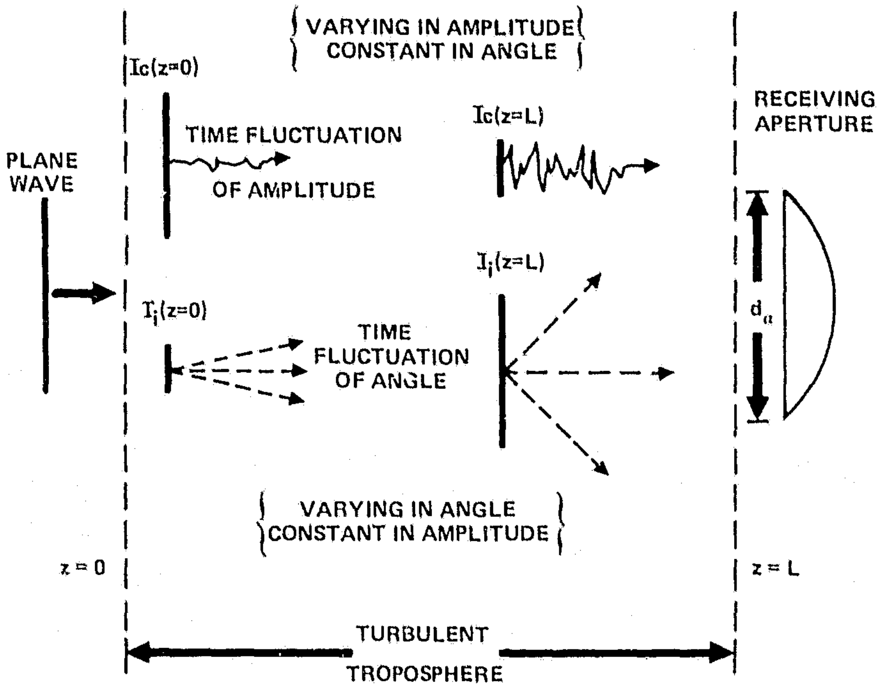

Figure 6.6-1. Decomposition into Coherent and Incoherent Components

The constants were

$$L_o = 180 \text{ km}$$

$$\sigma_1^2 = 2.6 \times 10^{-7} f(\text{GHz})^{7/12} L_t(\text{km})^{11/6}$$

$$\sigma_2^2 = 5.67 \times 10^{-6} L_t(\text{km})^{1.56} d_a(\text{m})^{-1/3}$$

A plot of the variance measurement, S^2, expressed in dB, is shown in Figure 6.6-2 for four representative frequencies for a 4.6 m diameter aperture. S^2 is plotted as a function of elevation angle and equivalent path length for a 6 km high region of turbulence.

Figure 6.6-2 represents the average S^2 as derived from the O.S.U. empirical constants. However, since both σ_1^2, and σ_2^2 may be represented in closed form as a function of C_n^2 (Tatarski-1961), instantaneous, diurnal, or seasonal values for S^2 may be found from this model given an estimate of the appropriate C_n^2.

6.6.2.2.1 Applicability of the Model. The empirical constants which were found from observed data are applicable for the prediction of average turbulence-induced propagation effects in a temperature climate, during the warmer seasons of the year, and under non-precipitating clear-air conditions. It is necessary to derive local estimates of C_n^2 for the model if these conditions are not the same.

6.6.2.2.2 Distribution of Amplitude Variance. It is known that peak-to-peak variations of 30 N-units in the refractive index are expected on a time scale of days and hours (Theobold-1978). Corresponding fluctuations in received signal amplitude variance expressed in dB would be expected to be about 20 dB peak-to-peak for a fluctuation of 30 N-units out of an average of 345. Figure 6.6-3 shows a representative case of average amplitude variance at 30 GHz for a 4.6 m diameter aperture as a function of elevation angle. Curves for plus or minus 10 dB variation in C_n^2 about the average are shown for comparison.

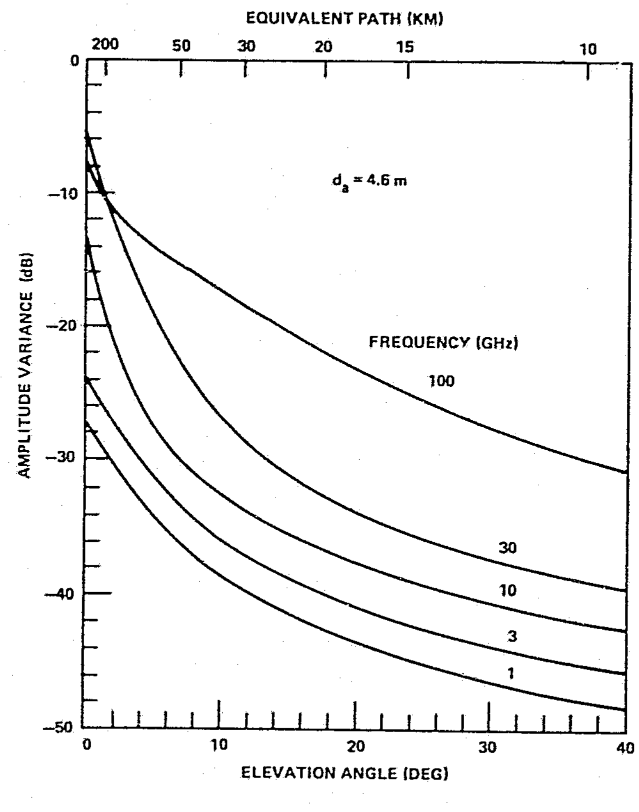

Figure 6.6-2 Amplitude Variance for a 4.6m Diameter Aperture for 1 to 100 GHz

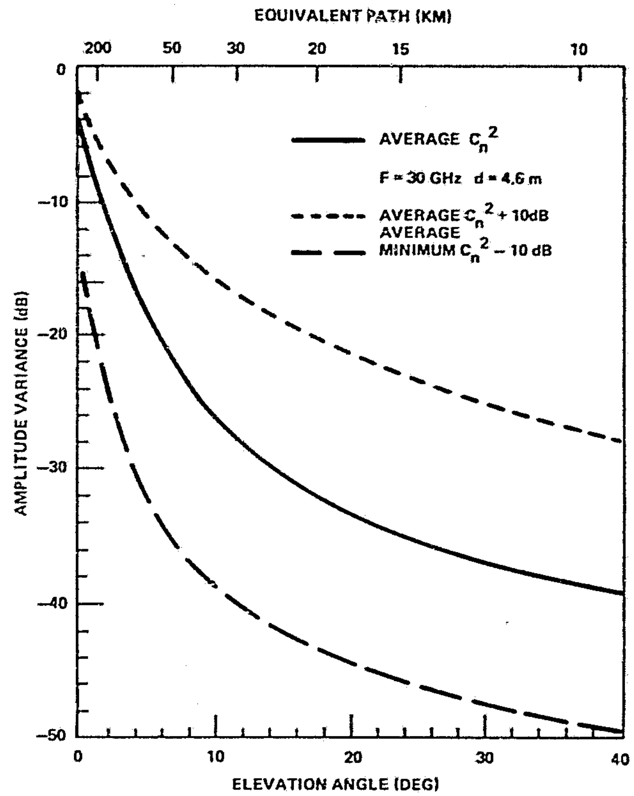

Figure 6.6-3 Effect of 20 dB Peak-to-Peak (30 N-units) Variation of C_n^2 on Amplitude Variance

A more exact representation of the expected distribution of amplitude variance may be obtained given measured statistics of variance variability about the average. Figures 6.6-4a and b present probability distribution functions of variance differences for 2 and 30 GHz earth-space signals measured over a period of 26 days. The satellite was undergoing transition in elevation from 0.38^{o} to 45^{o} and the mean variance was removed as a function of elevation angle. The 90% confidence limits of 14.6 and 14.7 dB, respectively, are in good agreement with the statistics of expected refractive index variation.

6.6.2.2.3 Power Spectral Density. The formulation of the structure of the power spectral density of turbulence-induced amplitude fluctuations has been derived from classical turbulence theory (Tatarski-1961). The theoretical spectrum of amplitude fluctuations in a medium characterized by a real refractive index is found to roll off as $f_f^{-8/3}$, or -26.6 dB/decade, in fluctuation frequency f_f. This behavior is not a function of operating frequency, as long as the wavelengths is small or on the order of the smallest refractive inhomogeneities. Deviation from this slope will occur due to non-stationarity of the scintillation process.

The spectral slope was calculated for time records of 102.4 seconds at 2 and 30 GHz on the ATS-6 CW beacons as the satellites moved in elevation angle from 0.38 to 25 degrees (Baxter and Hodge-1978). Spectral slope was found to be essentially independent of equivalent path length and measured statistics were well centered about the theoretical value of -26 dB/decade. Figures 6.6-5a and b present the probability distribution functions of the 2 and 30 GHz spectral slopes, respectively. Figure 6.6-6 presents the worst-case confidence limits of distribution of spectral slope from an average -26.6 dB/decade, for 50% and 90% of total time. Such an estimate may be used to directly find the expected fading rates and spectral components due to turbulence-induced amplitude scintillation. The data represents clear air statistics over a period of 26 days.

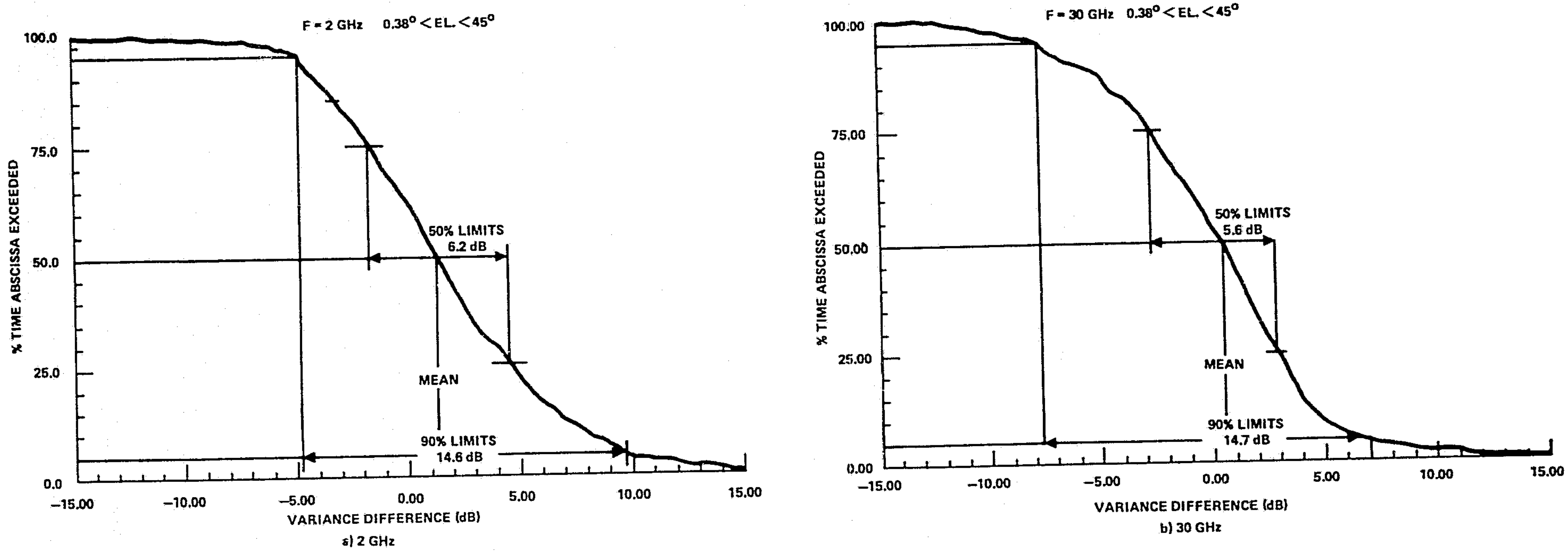

Figure 6.6-4 Distribution of Amplitude Variance from that Predicted from Average Turbulence-Induced Fluctuation Theory

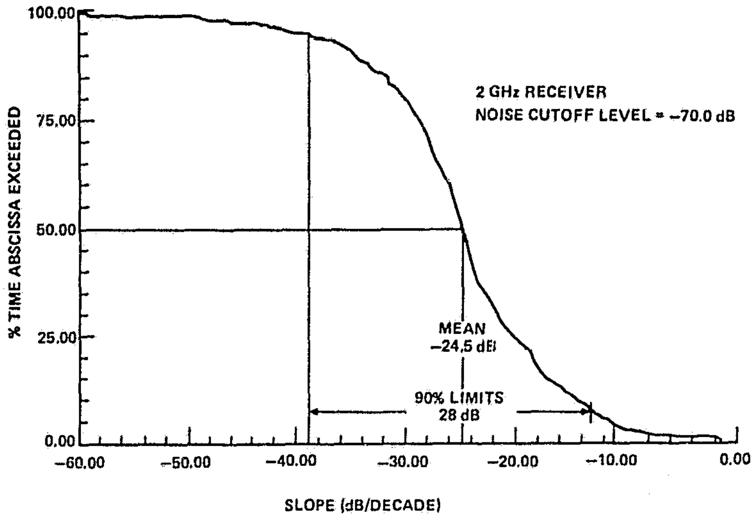

a) 2 GHz RESULTS

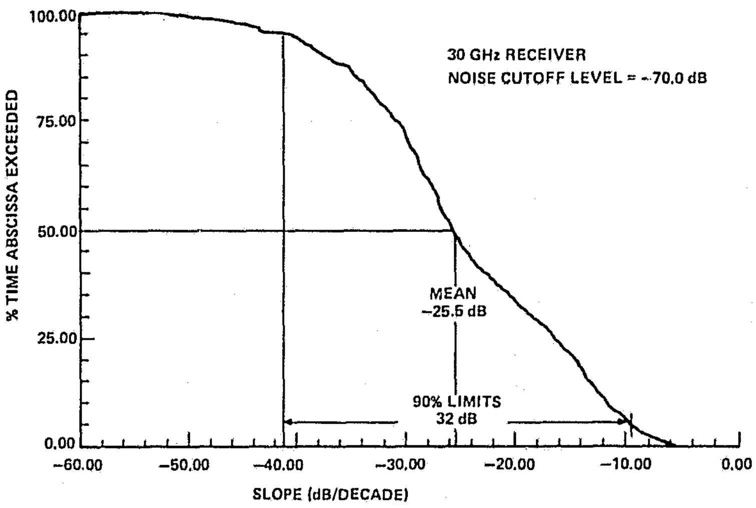

b) 30 GHz RESULTS

Figure 6.6-5 Probability Density Function of Spectral Slope

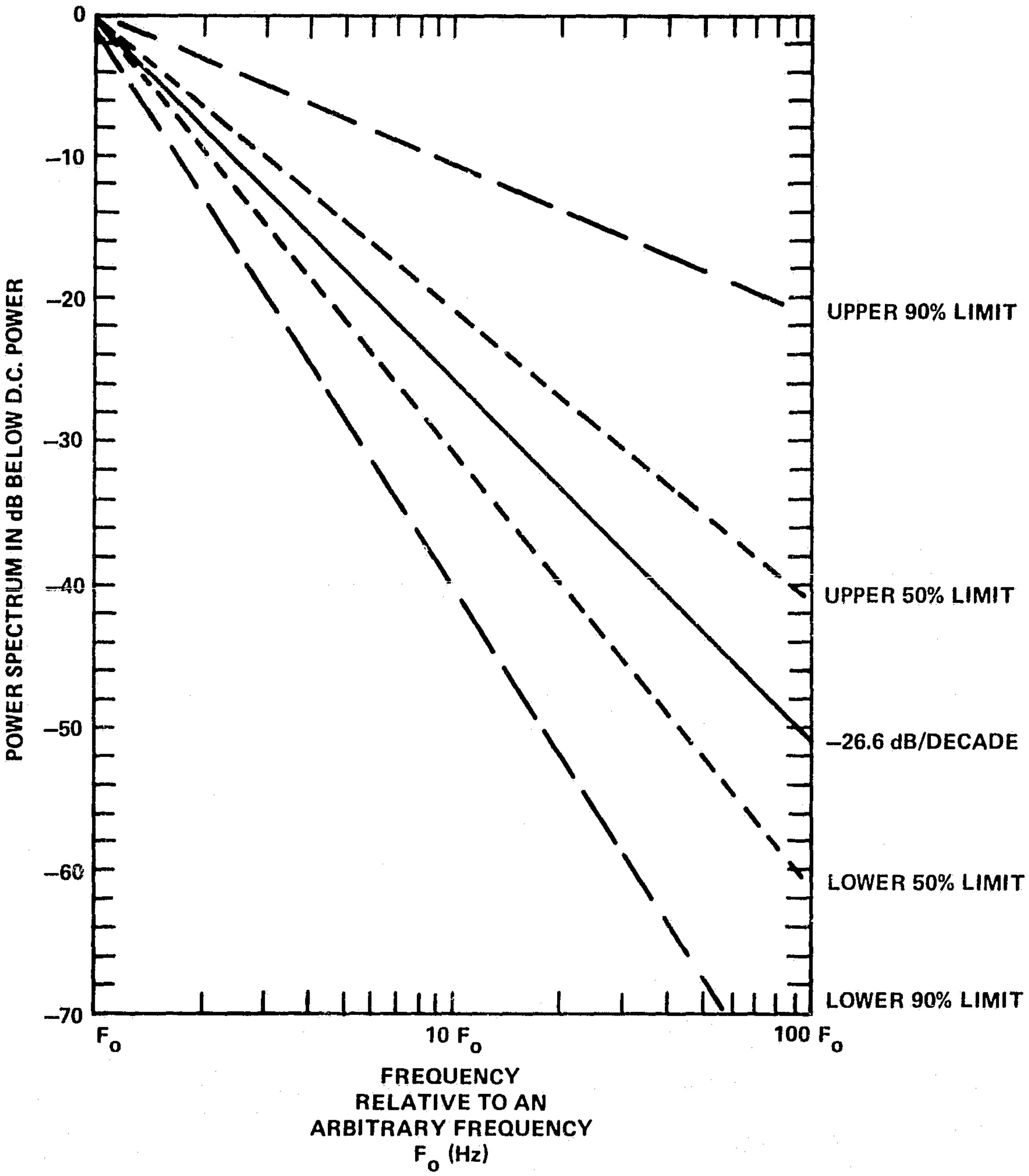

Figure 6.6-6 Confidence Limits of Distribution of Spectral Slope from Average -26dB/decade

6.6.2.2.4 Estimation of Gain Degradation. The mode for received signal amplitude variance has also been used to derive an expression for gain reduction, R, defined by (Theobold and Hodge - 1978)

$$R = 10 \log_{10} \frac{\langle v_d^2 \rangle}{\langle v_d^2 \rangle |_{\text{no angle fluctuations}}}$$

$$R = 10 \log_{10} \frac{I_c + I_i \left[\dfrac{B^2}{2.77\, \sigma_2^2 + B^2} \right]^2}{I_c + I_i}$$

where the constants are the same as those defined for the variance expression, S^2. This value for R may then be combined with atmospheric gas loss in order to obtain an estimate of average received signal level for an earth-space path. Figure 6.6-7 presents an example of predicted signal levels for 2, 7.3 and 30 GHz for antenna beam widths of 1.8^{o}, 0.3^{o}, and 0.15^{o}, respectively. Also included are measured signal levels, relative to zenith, from the ATS-6 2 and 30 GHz (Devasirvatham and Hodge-1977) transmissions and TACSATCOM 7.3 GHz (McCormick and Maynard-1972) beacons as the satellites were moving in elevation angle.

6.6.2.3 <u>Low Angle Scintillations/Fading</u>. At low elevations (typically less than 10 degrees) scintillations and fades occur due to refractive effects and multipath effects in the troposphere. In addition for stations utilizing antennas with significant sidelobe levels intercepting the ground, classic multipath is possible and should be considered. However, the effects reported here are generally thought to not include the effects of ground-reflected multipath.

Because no unified theory for low-angle fading exists, the design of future systems must be done by similarity. As more data becomes available and more systems require low elevation angle operation, undoubtedly a low-angle fading theory will be developed.

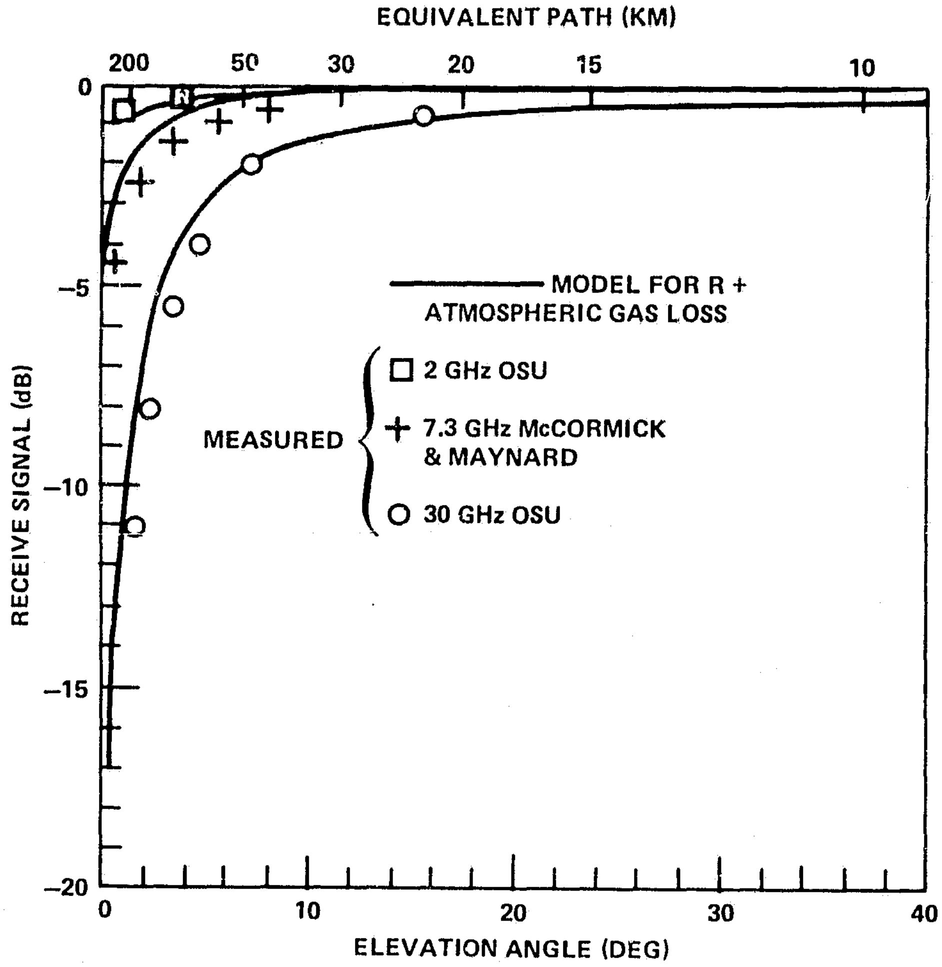

Figure 6.6-7 Predicted and Measured Signal Level as a Function of Elevation Angle

6.6.2.3.1 Presentation of Selected Experimental Results. A concise summary of the magnitude of the low-angle fading effects measured in a variety of locations is given in Table 6.6-1 (CCIR-1978, Rpt 564-1). These results are typical of the magnitude of the effect, however to date no comprehensive model attempts to explain these effects. A typical plot of the signal amplitude variance at 20 and 30 GHz as observed in Columbus, Ohio between 42 and 2 degrees is shown in Figure 6.6-8 (compare with Figure 6.6-2). Because the distribution suggested a cosecant behavior, a minimum mean-square-error curve was fit to the data as noted in Figure 6.6-8.

Experimental measurements of the fade durations at 6 GHz for fades from 0 to 21 dB below the long term median are shown in Figure 6.6.9 (Strickland, et al-1977). These measurements were made at Eureka, Canada during the month of July 1974 when the moisture content (N-value) is above the yearly average. This data is probably typical of continental air mass data. The frequency and elevation angle scaling factors for this data are not thoroughly confirmed, but the Tatarski (1961) model appears to model experimental results (CCIR-1978, Rpt 718). The variance appears to scale proportional to frequency according to the relation:

$$\text{variance} = 42.25\left(\frac{2\pi}{\lambda}\right)^{5/6}\int C_n^{2}(p)\, p^{5/6}\, dp$$

where p is the distance along the path.

The cumulative distribution for the rate of change of signal amplitude between 0.4 second samples was found to be identical for positive and negative-going signals (Strickland, et al-1977). The measured distribution is given in Figure 6.6-10, but again the frequency and elevation angle scaling factors are unknown.

Table 6.6-1. Fading Data Predominantly Due to Scintillation From Satellites at Low Angles of Elevation

Location	Satellite	θ (degrees)	Fading data
United Kingdom; Martlesham, Suffolk	ATS-6; 30 GHz	6.5 3.3 2.4	6.5 (dB) (peak-to-peak) 10 (dB) (peak-to-peak) 18 (dB) (peak-to-peak) } Maximum in turbulent windy conditions
		0.3–1.2	Occasional deep fades of 20 dB
United Kingdom; Birmingham	ATS-6; 30 GHz	1–2	Slow enhancements and sudden fades of 20 dB
USA; Virginia [Stutzman *et al*, 1975]	ATS-6; 20 GHz	9 4.7–5.1 4.5	2–3 dB Before and after light rain 2–7 dB Hazy conditions 8–15 dB Partly cloudy conditions
USA; Ohio	ATS-6; 2 and 30 GHz	2.8 0.38	3 dB at 2 GHz 15 dB at 30 GHz 7 dB at 2 GHz 20 dB at 30 GHz } Maximum effect in cumulus clouds
USA; Massachusetts	IDCSP; 7 GHz	10 3	0.03–0.2 dB r.m.s. 10 dB r.m.s. was observed occasionally in summer. Elevation angle fluctuations of up to 0.01° at 3° elevation and 0.002° at 10° elevation (r.m.s values in 5-min period).
Canada; Eureka [Strickland *et al*, 1977]	Anik II; 4 and 6 GHz	1	Data similar at the two frequencies. Fades of 11 and 20 dB predicted for 1% and 0.1% of worst month.
United Kingdom; Goonhilly [Harris, 1977]	Indian Ocean Satellite; (INTELSAT IV) 4 and 6 GHz	6.5	3 dB (peak-to-peak) exceeded for 0.3% of time on 4 GHz down-link, in a 9-month continuous measurement.
USA; Maryland [Ippolito, 1976]	ATS-6; 20 and 30 GHz	2.5–9	1.5 dB (peak-to-peak) at 9°, increasing to 11 dB at 2.5° at 30 GHz. Values at 20 GHz about 40–70% of those at 30 GHz. Occasional deep fades during light rain.

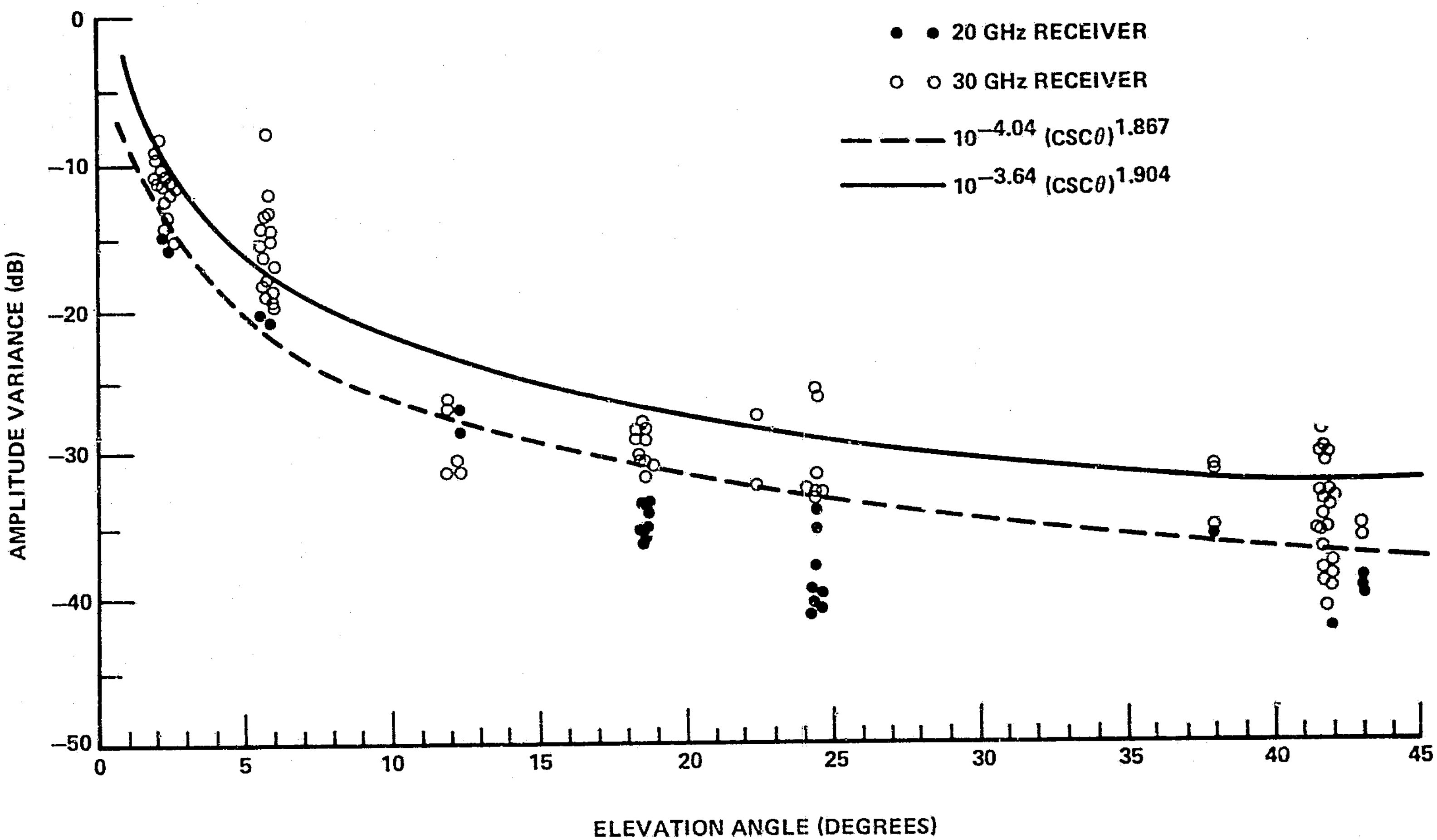

Figure 6.6-8 Measured Amplitude Variance Versus Elevation Angle (Columbus, Ohio)

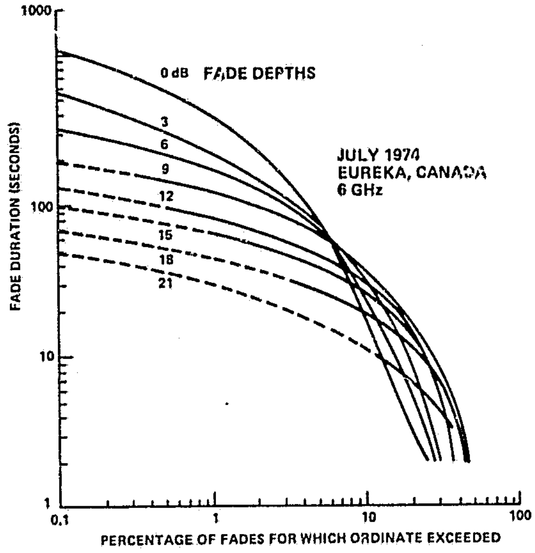

ns

Figure 6.6-9 Cumulative Distributions of Fade Durations at 6 GHz

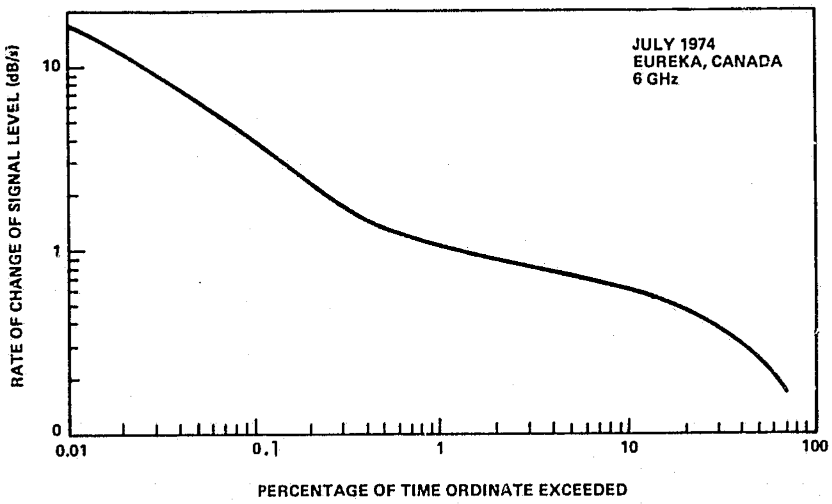

Figure 6.6-10 Cumulative Distribution of Rate of Change of 6 GHz Signal

6.6.3 Phase Variations

Phase variations arise due to the variable delay as the wave passes through a medium with variable refractivity and also due to wavefront ripple introduced by the "lumpy" medium. The former is termed phase delay fluctuations, while the latter effect is called phase scintillations.

6.6.3.1 Estimation of Phase Delay Fluctuations on Earth-Space Paths. An expression for the rms phase fluctuation for a finite circular aperture antenna of diameter d_a,

$$\sigma_\phi = \left(1 - \frac{d_a^2}{4\ell^2}\right)\left(2L_t\ell\,\overline{\Delta N^2}\right)^{1/2} \frac{2\pi \times 10^{-6}}{\lambda}$$

has been presented by Muchmore and Wheelon (1955). The derivation employs a ray theory approach and assumes an exponental spatial correlation for the turbulence scale. σ_ϕ is in radians, ℓ is the scale length of the turbulent eddy, L_t is the path length through the turbulence, λ is wavelength, and $\overline{\Delta N^2}$ is the mean-square fluctuation in the refractivity N. When using this expression, one should only assume values of ℓ and $\overline{\Delta N^2}$ such that

$$5\text{m} \le \ell\overline{\Delta N^2} \le 500\text{m}.$$

The results of using this relation at the limiting values of $\ell\overline{\Delta N^2}$ for 3 and 10 GHz are presented in Figure 6.6-11. Typical values of ℓ are 60 meters and $\overline{\Delta N^2} = 1/2$. This model indicates that the phase delay fluctuations increase linearly with frequency and become significantly less if the antenna diameter approaches the scale length.

Another technique for estimating these phase delay fluctuations based on the monthly variance of the surface refractivity and estimates of the frequency spectrum of the delay fluctuation have been made by Nusple, et al (1975).

6.6.3.2 Estimate of Phase Ripple Effects on Earth-Space Paths. Accompanying the amplitude scintillations of a plane wave propagating through tropospheric turbulence are transverse phase ripple variations. According to the theory of Tatarski (1961) the mean-square phase variation over a distance ρ_ϕ transverse to the propagation path is:

$$D_\phi(\rho_\phi) = K_\phi C_{no}^2 (2\pi/\lambda)^2 L_t \rho_\phi^{5/3}$$

where λ is wavelength, L_t is the propagation path length through the region of turbulence, and C_{no} is the surface structure constant. The constant K is equal to 2.91 for the exponential C_n^2 model (Tatarski-1961) and equal to 4.57 from Ohio data (Theobold and Hodge-1978). This expression may be used to estimate the expected mean-square phase variation between two points separated by a distance ρ_ϕ normal to the direction of propagation, given an estimate of C_{no}.

Clearly, this phase incoherence appears as an apparent antenna gain degradation. Measurements made with a 22 m diameter antenna at 5 degrees elevation angle and 4 and 6 GHz indicate a 0.2 to 0.4 dB degradation (Yokoi, et al-1970). A 7 meter diameter antenna at 5 degrees elevation angle and 15.5 and 31.6 GHz yielded a gain degradation of 0.3 and 0.6 dB, respectively (Yamoda and Yokoi-1974). This effect is clearly most pronounced for large antennas, high frequencies and elevation angles below 5 degrees (CCIR-1978, Rpt. 664-1).

6.6.4 Angle-of-Arrival Variation

The average ray bending (mean deviation from the geometric or vacuum line-of-sight) along a slant path has been estimated by a linear relation to the surface refractivity (Crane-1976a and CCIR-1978, Rpt. 718). Below the apparent fluctuations of the angle-of-arrival are estimated. Because they are assumed to arise solely due to refractive effects the variations are symmetrical about the direction of propagation and the fluctuation frequency is of the order of the time for the turbulence length to pass through the beam.

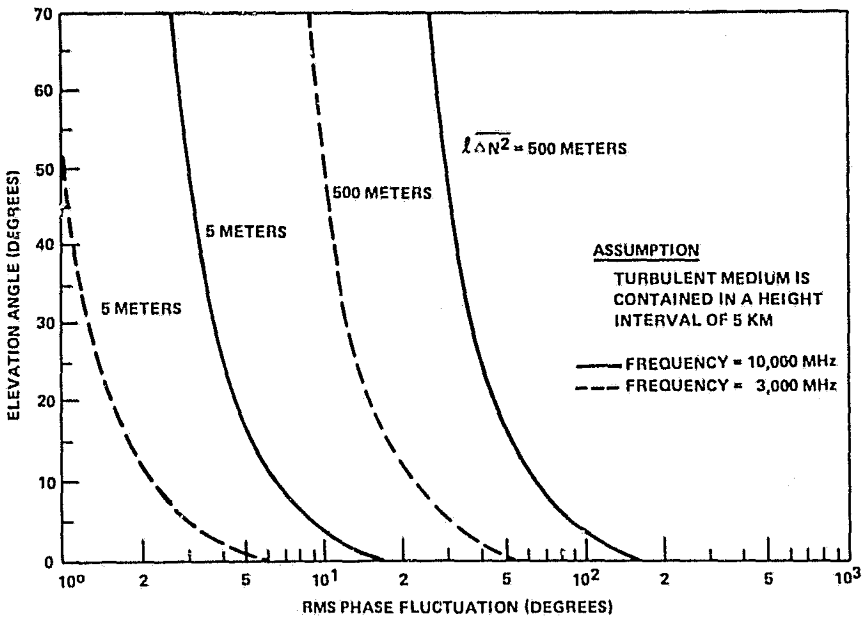

Figure 6.6-11. R.M.S. Phase Fluctuations for an Earth-Space Path

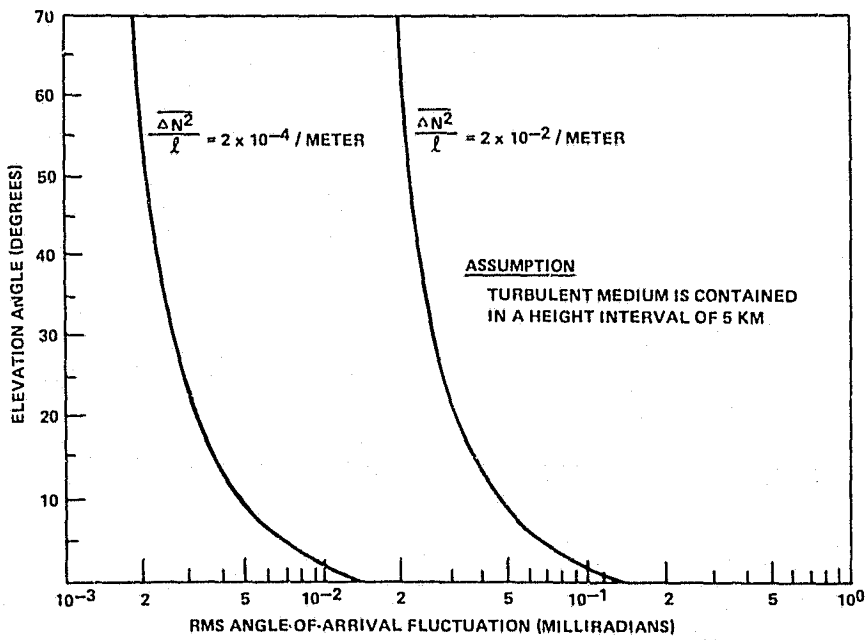

Figure 6.6-12. R.M.S. Angle-of-Arrival Fluctuations for an Earth-Space Path

The Muchmore and Wheelon expression for the rms angle-of-arrival fluctuation in radians is

$$\sigma_\theta = \left[\frac{2\sqrt{\pi}\, L_\ell\, \overline{\Delta N^2}}{\ell} \right]^{1/2} \times 10^{-6}$$

where all parameters are as previously defined. A Gaussian correlation function for the scale of turbulence was assumed and one should impose the limits

$$2 \times 10^{-4} m^{-1} \leq \overline{\Delta N^2}/\ell \leq 2 \times 10^{-2} m^{-1}$$

Figure 6.6-12 is an example for this expression, within the stated range of $\Delta N^2/\ell$, for an earth-space propagation path through a turbulent region of height 5 km. Note that σ_θ^2 is directly proportional to path length and independent of operating frequency. Also, σ_θ decreases with increasing eddy size, ℓ, while phase fluctuation σ_θ increases with increasing eddy size.

Estimates (CCIR-1978, Rpt. 564-1) indicate that the short-term variations in the angle-of-arrival may be of the order of 0.02 degrees (0.37 milliradians) at 1 degree elevation. This is higher than the theory predicts (see Figure 6.6-12), but the effect does decrease rapidly with increasing elevation angle. Crane (1976) reports values of σ_θ within the bounds of Figure 6.6-12 for 7 GHz measurements made at varying elevation angles with a 37 m diameter antenna.

Generally, for beamwidths greater than 0.01 degree and elevation angles above 10 degrees, the angle-of-arrival fluctuations are masked by other fluctuations.

6.6.5 Fading and Gain Degradation Design Information

6.6.5.1 Fade Distribution Function Estimation. The estimates of gain reduction and signal variance parameters, R and S^2, have been presented. These quantities may be incorporated into distribution functions which are of the form used in link design. They represent the long term average fade statistics due to clear air amplitude and angle-of-arrival fluctuations. The estimates of R and S^2 may be more closely matched to local and seasonal conditions if a local estimate of C_n^2 is available. A hypothetical low elevation angle fade distribution is presented in Figure 6.6-13. The abscissa is referenced to the signal level received in the absence of turbulence, i.e., including free space loss and gaseous absorption. The point at which the signal level is R dB is also the mean of the received signal; thus, one point on the fade distribution is established. The fade distribution for turbulence-induced fluctuations is assumed to be log-normal, with mean and median being equal. The fade distributions resulting from the Ohio State University ATS-6 30 GHz beacon measurements (Devasirvatham and Hodge-1977) indicate that this log-normal assumption is valid for elevation angles above approximately 2^o. A similar observation was made concerning the 7.3 GHz fade distribution above 4^o elevation angle observed by McCormick and Maynard (1972).

A fade distribution may now be produced using this assumption of linearity. Referring to Figure 6.6-13, it was noted that the point at which the received signal level is R dB represents the mean signal level. For a normal distribution, the mean is plotted at the 50% time abscissa exceeded point, indicated by 1 in the figure. One standard deviation to the right of the mean on a normal distribution occurs at the 15.9% time abscissa exceeded level. It may be easily shown that the standard deviation of received signal level, expressed in dB and denoted $\sigma_{v_{dB}}$, may be written in terms of the signal variances S^2. This point, $\sigma_{v_{dB}}$, to the right of R, is denoted by 2 in the figure. A straight line drawn between points 1 and 2 now approximately represents the fade distribution, referenced to the mean signal level in the absence of turbulence induced fluctuations. This distribution was based on small fluctuation arguments and should be employed as a lower bound when estimating a particular fade distribution.

Deviation of this fade distribution from the expected form will occur at small time percentages. Additional fading due to precipitation, abnormal

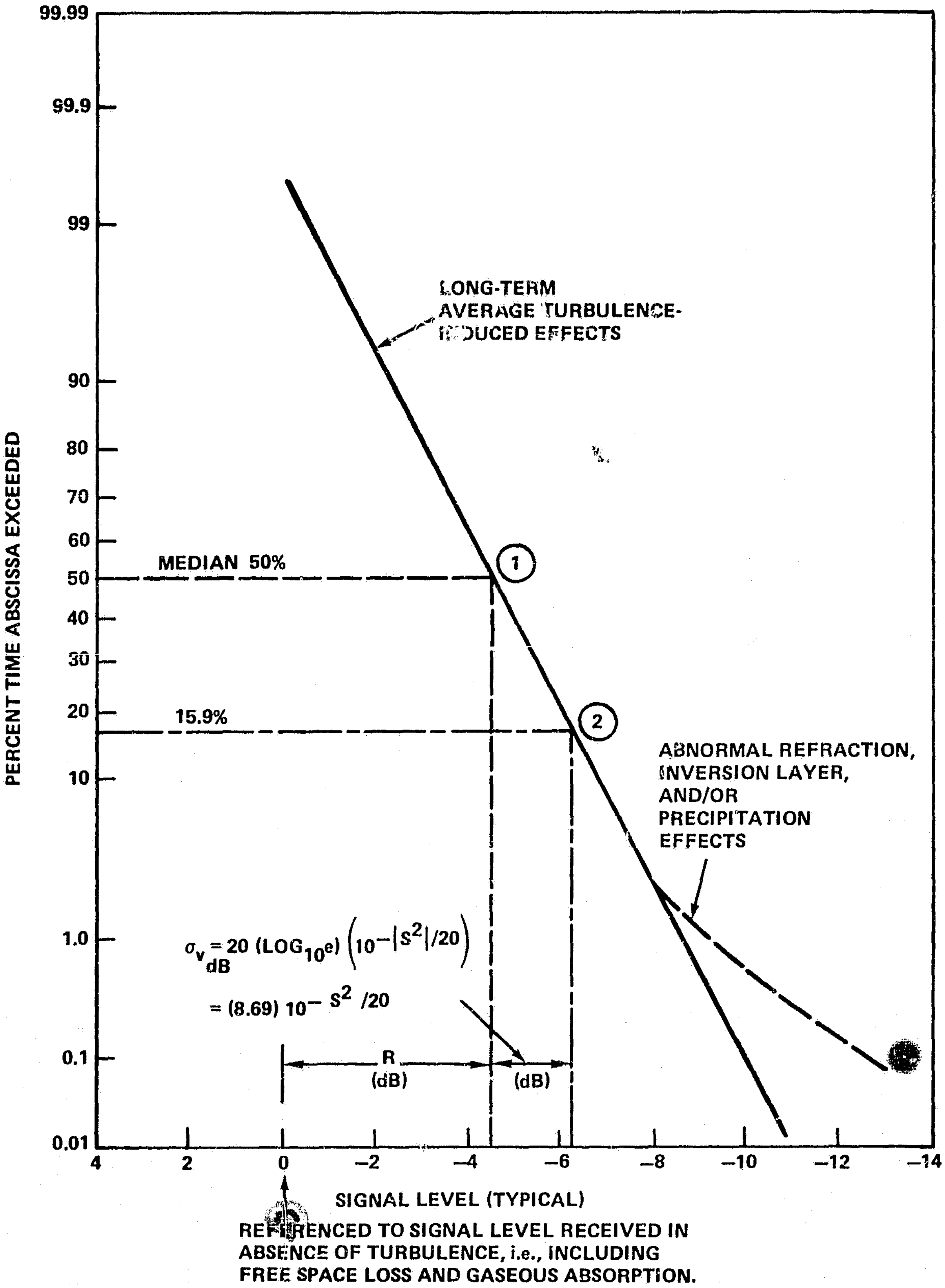

Figure 6.6-13. Hypothetical Fade Distribution Function for Low Elevation Angles

refraction, or inversions in the atmosphere will cause greater fade depths for the small time percentages. However, the turbulence effects, which are always present, are still dominant for larger time percentages. For high elevation angles, i.e., short path lengths, S^2 will be very small and the line drawn through points 1 and 2 will be virtually vertical.

However, the precipitation effects at the lower percentages will still be present for short path length cases and will become the dominant feature of the fade distribution.

6.6.5.2 Gain Degradation Design Information.

6.6.5.2.1 Estimation of Domains. The effects of amplitude and angle-of-arrival fluctuations are, of course, most prominent for very long path lengths and/or very narrow beamwidths. One may estimate whether or not gain degradation need be considered in a path design if elevation angle (or equivalent path length) and antenna beamwidth are known. Figure 6.6-14 presents regimes of average gain degradation between 0.5 and 3 dB and where they must be considered as a function of elevation angle and antenna beamwidth.

Realized gain, or expected gain less gain degradation, is plotted as a function of antenna beamwidth (for any frequency) or equivalent aperture diameter at 30 GHz in Figure 6.6-15. All equivalent aperture diameters are presented for an antenna aperture efficiency of 0.6. The curve representing zero path length L_t is simply the common gain approximation $G = 41253/B^2$, where B is in degrees. Realized gain curves for path lengths of 50 to 300 km are plotted using the model. Equivalent earth-space path elevation angles assuming a 6 km high homogeneous atmosphere are presented in parentheses.

Notice that gain degradation due to turbulence-induced fluctuation is negligible for beamwidths wider than about 0.7^o for all path lengths. Degradation effects then gradually increase as beamwidth narrows from 0.7^o to 0.05^o and at any particular beamwidth are approximately directly proportional, in dB, to path length. As beamwidth narrows beyond 0.05^o, a saturation effect occurs and the degradation becomes constant for any one path length.

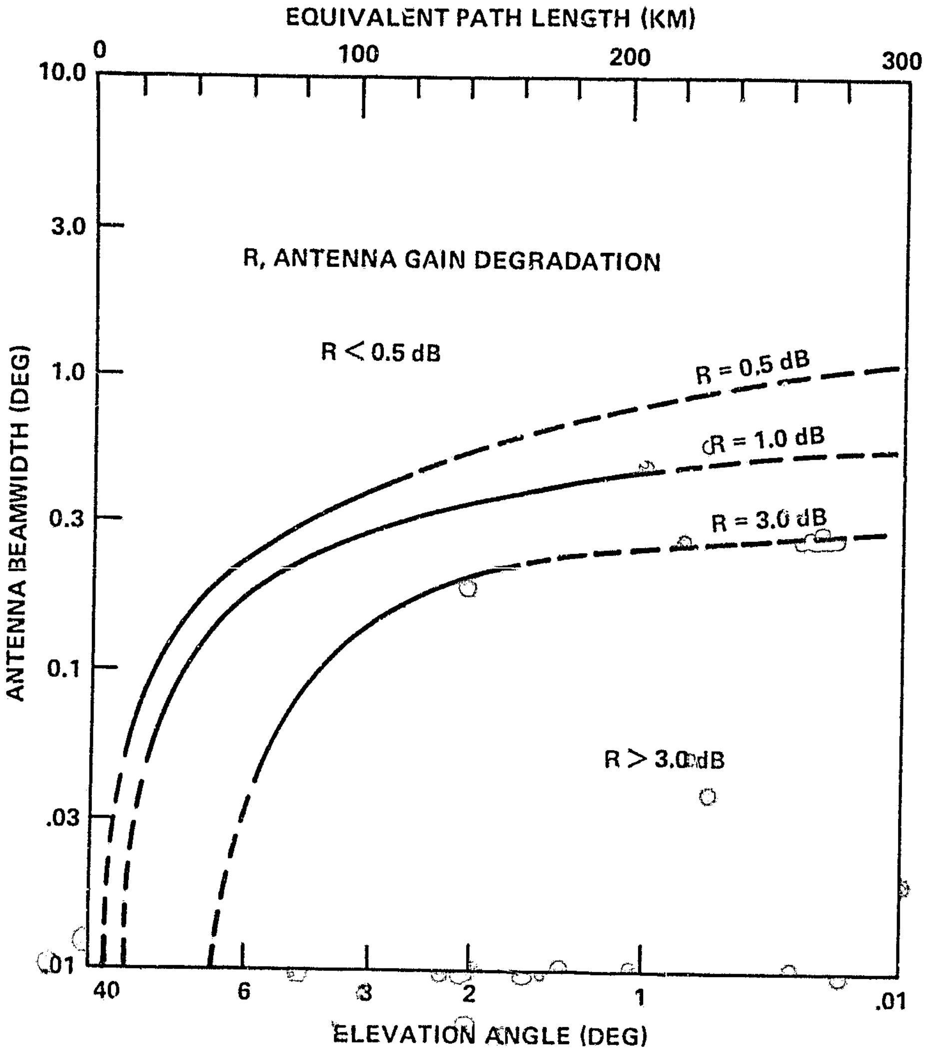

Figure 6.6-14 Gain Degradation Regimes as a Function of Beamwidth and Elevation Angle

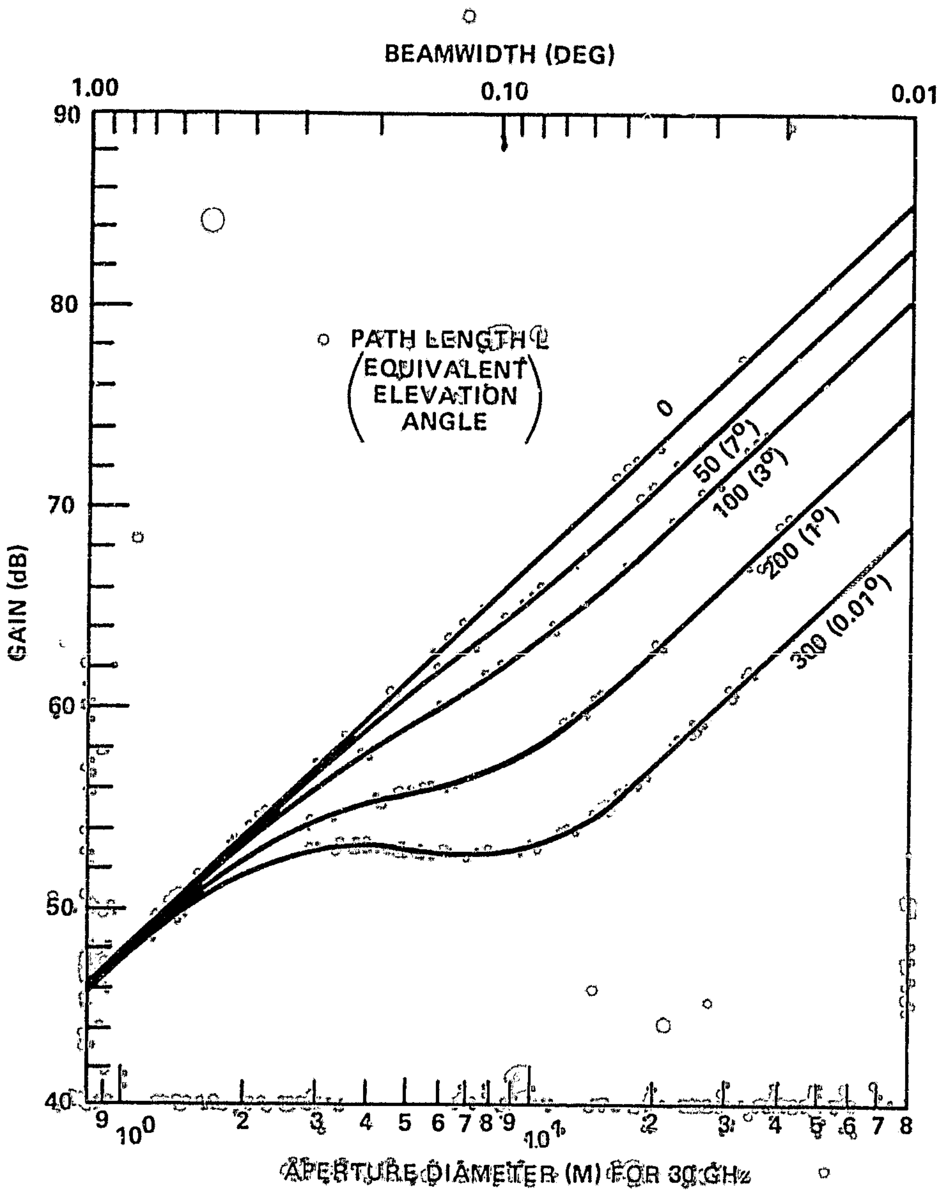

Figure 6.6-15 Realized Gain versus Beamwidth or Aperture Diameter at 30 GHz

All design figures of Section 6.6.5 represent estimates for clear air effects in a temperate climate during daytime and in the warmer months of the year. If a local value of C_n^2 is known, more accurate values of R and S^2 may be obtained. If local statistics of C_n^2 are known, statistics of R and S^2 may be obtained.

6.6.5.2.2 Spatial Diversity. Paths operating at very low elevation angles with narrow beamwidth antennas may experience unacceptable fading due to scintillation and multipath effects. The required reliability may be regained by the use of spaced site diversity. A site separation greater than 300 m transverse to the propagation path has been suggested (CCIR-1978, Rpt 564-1) as necessary to alleviate severe turbulence-induced effects. In effect, separation on the order of or larger than the scale size of the largest inhomogeneities in refractive index along the propagation path, and especially near the surface where refraction is greatest, results in decorrelation of the instantaneous signal fluctuations and hence improved performance.

The aperture effects of large antennas may be circumvented if several phase-locked antennas, each with relatively wide beamwidth, are employed in an array to achieve the desired system gain. Of course, overall fade margins will be on the order of that for a single element, but angle-of-arrival effects are eliminated. In addition, such an array alleviates the need to mechanically track a geosynchronous satellite, as is necessary with large aperture, narrow beamwidth antennas.

6.6.6 An Example Computation of Signal Fluctuations and Gain Degradation

In this section examples of the parameters described in Section 6.6 are worked out for a hypothetical ground station located at Columbus, Ohio with a 4.6m (15 ft) diameter parabolic antenna observing a 28.56 GHz COMSTAR beacon at 10 degrees elevation angle. Actually, the COMSTAR satellites are not at that low an angle, but in order to demonstrate the effects of gain reduction this value has been arbitrarily selected.

6.6.6.1 Amplitude Fluctuations. The variance of the received signal amplitude is calculated using the expression in Section 6.6.2.2. The full half-power beamwidth B in degrees is $70\ \lambda/d_a = 70\ c/fd_a = (70)(3\times10^8 m/sec)/(28.56\times10^9 sec^{-1})(4.6m) = 0.16$ degrees. The path length of the turbulence L_t is computed from $h_t = 6$ km, $r_e = 6377$ km and $\theta = 10$ degrees using the equation

$$L_t = \left[h_t^2 + 2r_e h_t + (r_e \sin\theta)^2\right]^{1/2} - r_e \sin\theta = 34 \text{ km}$$

The other constants are:

$$L_0 = 180 \text{ km}$$

$$\sigma_1^2 = 1.18 \times 10^{-3}$$

$$\sigma_2^2 = 8.35 \times 10^{-4}$$

$$I_i = 0.17$$

$$I_c = 0.83$$

and the signal variance relative to the average power is

$$\sigma^2 = 10 \log_{10} \frac{9.79 \times 10^{-4} + 0.14398 - 0.14297}{0.83 + 0.14}$$

$$= 10 \log_{10} (2.03 \times 10^{-3}) \simeq -27 \text{ dB}$$

Note that this agrees well with the results in Figure 6.6-2. Reference to Tatarski (1961) would have allowed evaluation in terms of C_n^2 rather than the formulation by Theobold and Hodge (1978) utilized here.

Reference to Figure 6.6-4b indicates that 50% of the time the S^2 would be between -24 and -30 dB, while 90% of the time S^2 would be between -20 and -34 dB.

The power spectrum density of the fluctuations decreases at 26.5 dB/decade (see Figure 6.6-6). If one considers some lower frequency cutoff for the amplitude fluctuations (say 0.1 Hz) the fluctuation power at 1 Hz is on the average 26.5 dB below the value of 0.1 Hz. Only 10% of the time will the 1 Hz fluctuation power be only 10 dB below the 0.1 Hz fluctuation power. Clearly, most of the fluctuation power for clear air fluctuations is at the low frequencies (less than 1 Hz).

6.6.6.2 Phase and Angle-Of-Arrival Variations. Phase fluctuations are estimated from the model of Muchmore and Wheelon (1955) presented in Section 6.6.3. Data quoted in Muchmore and Wheelon indicate typical values for $\ell \approx$ 60m $\cong$ 200 feet and $\overline{\Delta N^2} = 1/2$. Thus $\ell \overline{\Delta N^2} = 30$ meters.

For a finite circular antenna (see Section 9.6) of 4.6 m diameter, the rms phase delay fluctuation is 0.85 radians = 48 degrees. For a $C_{no} = 10^{-14}$, the phase ripple fluctuation across the antenna is very small.

The estimate of the angle-of-arrival fluctuations in radians (see Section 9.6.4) is calculated to be 3.2×10^{-5} radians = 1.8×10^{-3} degrees. This is a small number compared to 0.16 degree half-power beamwidth of the antenna. Also note that the limits on $\overline{\Delta N^2}/\ell = 8.3 \times 10^{-3} m^{-1}$ are not exceeded.

6.6.6.3 Prediction of the Average Received Signal Gain Reduction. The average received signal reduction is calculated using the same parameters required for calculation of the amplitude fluctuations. Using the relation in Section 6.6.2.2.4

$$R = 10 \log_{10} \frac{(0.83 + 0.17(0.84))}{1.0} = 0.12 \text{ dB}$$

Thus during clear weather this COMSTAR beacon will on the average be 0.12 dB below the value calculated considering clear air attenuation only. This same value could be estimated from Figure 6.6-15.

The long-term average distribution in Figure 6.6-13 is now constructed from R and S^2. The point 2 (15.9% point) is found to be $20(\log_{10}e)\ 10^{-|S^2|/20} = 0.39$ dB which is the standard deviation of the receiver voltage taken from a square law detector.

6.7 PREDICTION OF DEPOLARIZATION ON EARTH-SPACE PATHS

6.7.1 Introduction

Depolarization refers to that effect wherein an earth-space wave's polarization is altered in the troposphere. Depolarization is also referred to as cross-polarization. For linearly polarized waves a vertically (horizontally) polarized wave will, after passing through a media, have a horizontally (vertically) polarized component in addition to the initial wave. For circularly polarized waves a RHCP (LHCP) wave will develop into an elliptical wave. For frequency reuse systems based on polarization isolation this coupling reduces isolation and increases "cross-talk."

6.7.1.1 Sources of Depolarization. Depolarization on earth-space paths has been observed due in the presence of

- rain
- ice
- snow
- multipath
- refractive effects

These hydrometeor and scattering effects generate depolarization because of their asymmetry. For example, as raindrop sizes increase their shape departs from spherical and becomes an oblate spheroid with an increasingly pronounced flat bottom. For large drop sizes a concave depression develops (Pruppacher and Pitter-1971). Polarized microwave energy scattered from these particles can easily be converted into an orthogonal polarization.

6.7.1.2 Measures of Depolarization. The measurement of depolarization by propagation researchers usually has been done utilizing orthogonally-polarized feeds on a single antenna while observing singly-polarized satellite signals. This parameter is called the cross-polarization discrimination (XPD) or cross-polarization ratio (XPR) defined as (Bostian, et al-1977)

$$\text{XPD} = \frac{\text{power output from the co-polarized port}}{\text{power output from the cross-polarized port}}$$

$$= (\text{XPR})^{-1}$$

For perfect transmitting and receiving antennas and a perfect medium this isolation could become infinite, but with practical components some leakage is always present. Definitions and example calculations of depolarization terms have been well documented in a tutorial report by Stutzman (1977).

Unfortunately, the system designer desires the cross-polarization isolation (XPI) term defined as

$$\text{XPI (dB)} = \text{co-polarized signal power (dB)} - \text{cross-polarized signal power (dB) on the same channel}$$

Fortunately, for most levels of attenuation observed, $\text{XPI} \approx \text{XPD} = (\text{XPR})^{-1}$ (Watson and Arbabi-1973).

6.7.1.3 Depolarization Measurements. Most experimental depolarization data has been obtained from the 11.7 GHz right-hand circularly polarized Communications Technology Satellite (CTS) beacon and the 19.04 and 28.56 GHz linear polarized AT&T COMSTAR satellite beacons.

6.7.2 Rain Depolarization

6.7.2.1 Depolarization Versus Attenuation Relations. Correlation of depolarization with rain rate has not been too successful because of the many parameters required for these calculations. However, experimentally and analytically (Nowland, et al-1977) it has been observed that rain-induced depolarization can be related to total attenuation by the formula

$$XPD = \tilde{a} - \tilde{b} \log_{10} (A)$$

where XPD is the cross-polarization discrimination in dB and A is the total attenuation in dB due to rain (not including the clear air attenuation).

6.7.2.1.1 CCIR Approximation. The CCIR (1978, Rpt. 564-1) has found that the following approximation appears to be in reasonable agreement with existing theory and available data. The relation is

$$XPD = 30 \log_{10}(f) - 40 \log_{10} (\cos \theta) - 20 \log_{10}(\sin 2\tau) - 20 \log_{10}(A). \quad (6.7\text{-}1)$$

where f = frequency in GHz

θ = elevation angle

τ = polarization tilt angle with respect to horizontal ($\tau = 45^{0}$ for circular polarization)

This relation is valid for

$1dB \leq A \leq 15dB$

$10dB \leq CPD \leq 40dB$

$8\ GHz \leq f \leq 40\ GHz$

$10^{o} \leq \tau \leq 80^{o}$

$10^{o} \leq \theta \leq 60^{o}$

6.7.2.1.2 VPI & SU and Univ. of Texas Results. The Virginia Polytechnic Institute and State University (VPI&SU) have analyzed their CTS (11.7 GHz) and COMSTAR (16.04 and 28.56 GHz) beacon depolarization data in two manners. The first technique is to compare the measured cumulative XPD with the measured cumulative rain attenuation statistics. These results are termed the statistic depolarization results. The second technique pairs "instantaneous" (half-minute) intervals of data for both parameters and smooths the data to obtain $\tilde{a}$ and $\tilde{b}$.

The results of these two techniques for 11.7 GHz data both from VPI&SU and the University of Texas (C.W. Bostian, et al-1979) are shown in Figure 6.7-1. Clearly these results indicate a wide spread of values have been obtained to date even though they are averaged over an entire year. The attenuation has been truncated at 5 dB because of the effects of ice depolarization (see Section 6.7.3).

VPI&SU has also related the XPD to attenuation for each month of 1978 for which 5 dB or greater fades occurred. These $\tilde{a}$ and $\tilde{b}$ results are shown in Table 6.7-1 for the number of half-minute samples indicated. The R-squared term is a measure of the goodness of the fit. The wide variations noted are similar to those observed by other investigators.

Additional data from the University of Texas at Austin (Vogel - 1979) incorporating exceedance values is presented in Figure 6.7-2. These curves show the 10%, 50% (median) and 90% expectation of exceeded isolation for each attenuation. For example at 5 dB (meaning $4\ dB \leq A \leq 5\ dB$) the XPD exceeded 23 dB for 90%, exceeded 28 dB for 50% and exceeded 33 dB for 10% of the data. The logarithmic fit to these three curves is

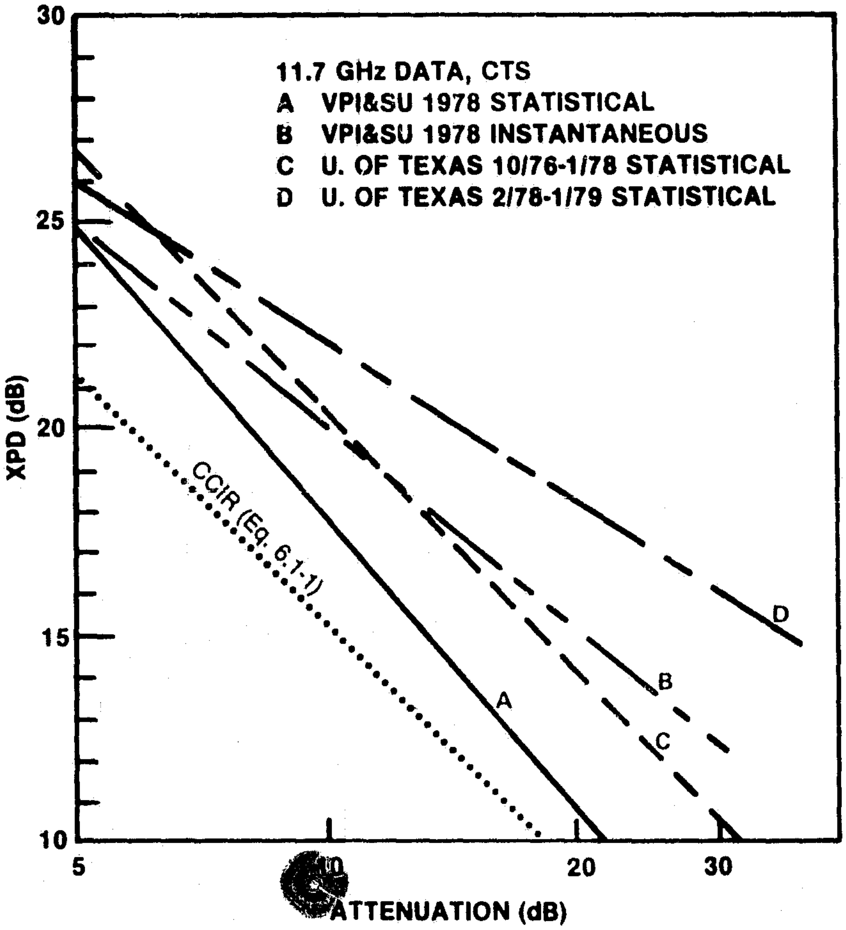

Figure 6.7-1 Cross-Polarization Discrimination versus Attenuation for Statistical and Instantaneous Data

$XPD = \tilde{a} - \tilde{b} \log_{10} A$ $5 < A < 30$ dB VPI&SU 1978 CTS DATA

MONTH	$\tilde{a}$	$\tilde{b}$	R^2	NO. OF 1/2 MINUTE INTERVALS
JAN	30.79	2.62	.00	22
MAR	51.18	38.18	.63	309
MAY	49.01	27.93	.90	30
JUNE	38.42	17.53	.56	38
JULY	42.23	21.94	.80	74
AUG	47.31	25.99	.47	28
SEPT	64.20	51.93	.32	50
NOV	27.59	4.11	.04	7
YEAR	36.29	16.22	.36	574

Table 6.7-1. Least-Mean Square Fits of Depolarization Coefficients by Month

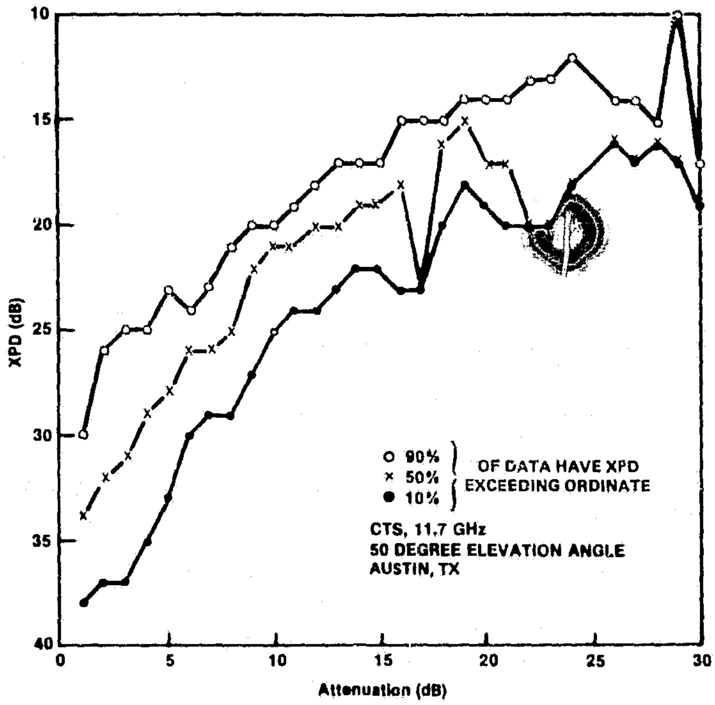

Figure 6.7-2. Twelve Month Isolation Versus Attenuation Data

10% : XPD - 42.9 - 17.5 $\log_{10}A$
50% : XPD - 35.8 - 13.4 $\log_{10}A$
90% : XPD - 31.5 - 12.6 $\log_{10}A$

for the 11.7 GHz CTS beacon at 50 degrees elevation angle.

6.7.2.2 Frequency Scaling Depolarization Measurements. The Virginia Polytechnic Institute and State University (Bostian, et al-1978, 1979a) has also made simultaneous measurements of the depolarization at 19 GHz vertical and horizontal and 28.56 GHz using the COMSTAR beacons. Their preliminary results for 1977 and 1978 are given in Table 6.7-2.

Table 6.7-2
Cross-Polarization Discrimination Versus Attenuation
(Least-Mean-Square Fits)

Blacksburg, VA		Elevation Angle = θ
Period	Frequency/Polarization	$XPD = \tilde{a} - \tilde{b} \log_{10}(A)$
Aug 1977	11 GHz, RHCP (CTS, θ = 33°)	$XPD = 44.7 - 22.6 \log_{10}(A)$
CY 1978	11 GHz, RHCP (CTS)	$XPD = 36.3 - 16.2 \log_{10}(A)$
Aug 1977	19 GHz, vertical (COMSTAR, θ = 44°)	$XPD = 47 - 24.5 \log_{10}(A)$
Sept 1977	19 GHz, horizontal (COMSTAR)	$XPD = 37.1 - 20.0 \log_{10}(A)$
CY 1978	19 GHz, vertical (COMSTAR)	$XPD = 43.9 - 16.6 \log_{10}(A)$
Aug 1977	28 GHz, vertical (COMSTAR)	$XPD = 36.4 - 15.4 \log_{10}(A)$
CY 1978	28 GHz, vertical (COMSTAR)	$XPD = 31.2 - 7 \log_{10}(A)$

The analysis of Nowland, et al (1977a) may be utilized to show the expected frequency dependence of the coefficients $\tilde{a}$ and $\tilde{b}$ in $XPD = \tilde{a} - \tilde{b} \log_{10}(A)$. Using Equations 11 and 12 of Nowland, et al (1977a) and many of the constants in the paper, the solid curve was derived in Figure 6.7-3. The dashed curve was derived using the effective path length

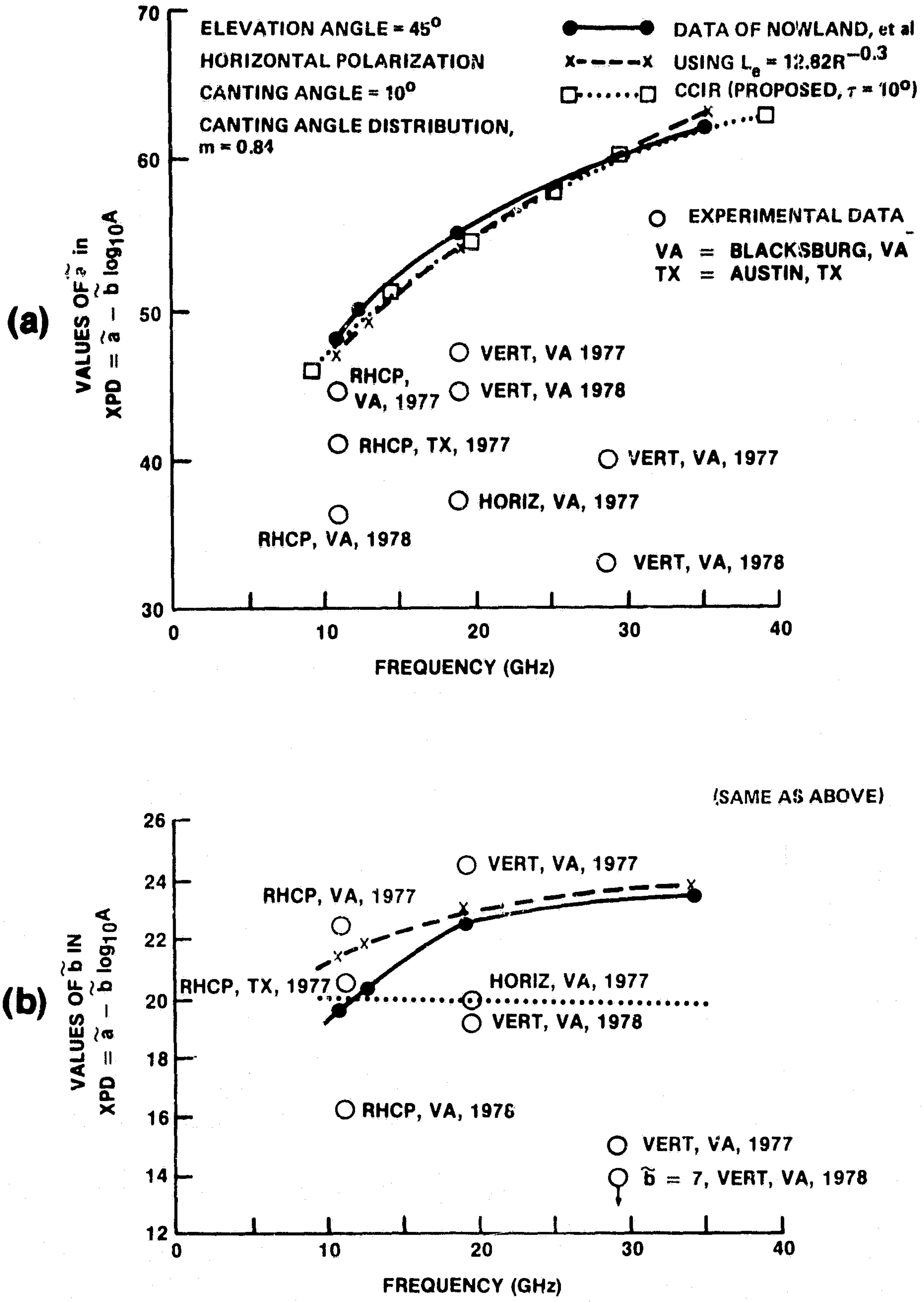

Figure 6.7-3 Frequency Dependence of the Coefficients in the Cross-Polarization Discrimination Relation

$L_e = 12.82\ R^{-0.3}$ and the specific attenuation in Section 6.3. Several experimental data points are shown, but these do not correlate well with the theory (possibly because of the polarization dependence of $\tilde{a}$). The important results of these figures are that a increases with increasing frequency, while $\tilde{b}$ appears to be relatively constant. In the relation $XPD = \tilde{a} - \tilde{b}\ \log_{10}(A)$ this would imply that the XPD increases with increasing frequency, but because of the rapid increase in A with frequency, XPD will actually decrease for increasing frequency and moderate rain rates.

Chu (1979a) has found a linear relation between the XPD and frequency throughout the 3 to 30 GHz frequency range. Specifically the approximation is

$$XPD\ (2f_1) = XPD\ (f_1) - 6\ dB$$

for a given level of attenuation. And,

$$XPD\ (2f_1) = XPD\ (f_1) + 6\ dB$$

for a given value of 5-minute average rain rate at the ground station. The reason for these differences is, of course, the frequency dependence of the attenuation. Bostian (1979b) confirms this linear relation between the XPD (f_1) and XPD(f_2) from his monthly COMSTAR data for 1978, but, the value XPD(f_2)/XPD(f_1) varies from month to month.

6.7.2.3 Elevation Angle Dependence of Depolarization. In U.S. and Canada depolarization measurements have been obtained at elevation angles from 24.6 degrees in Ottawa (McEwan-1977) to 49° at Austin, Texas (Vogel-1978). The general dependence of XPD versus A on elevation angle θ can be obtained from the theoretical results of Nowland, et al (1977a). Note that both the coefficient $\tilde{a}$ and the total attenuation A depend on elevation angle.

The elevation angle dependent results of Nowland, et al (1977b) 11.7 GHz (experimental data) are shown in Figure 6.7-4. Clearly the $\tilde{a}$ coefficient is elevation angle dependent, however the experimental data does

(a)

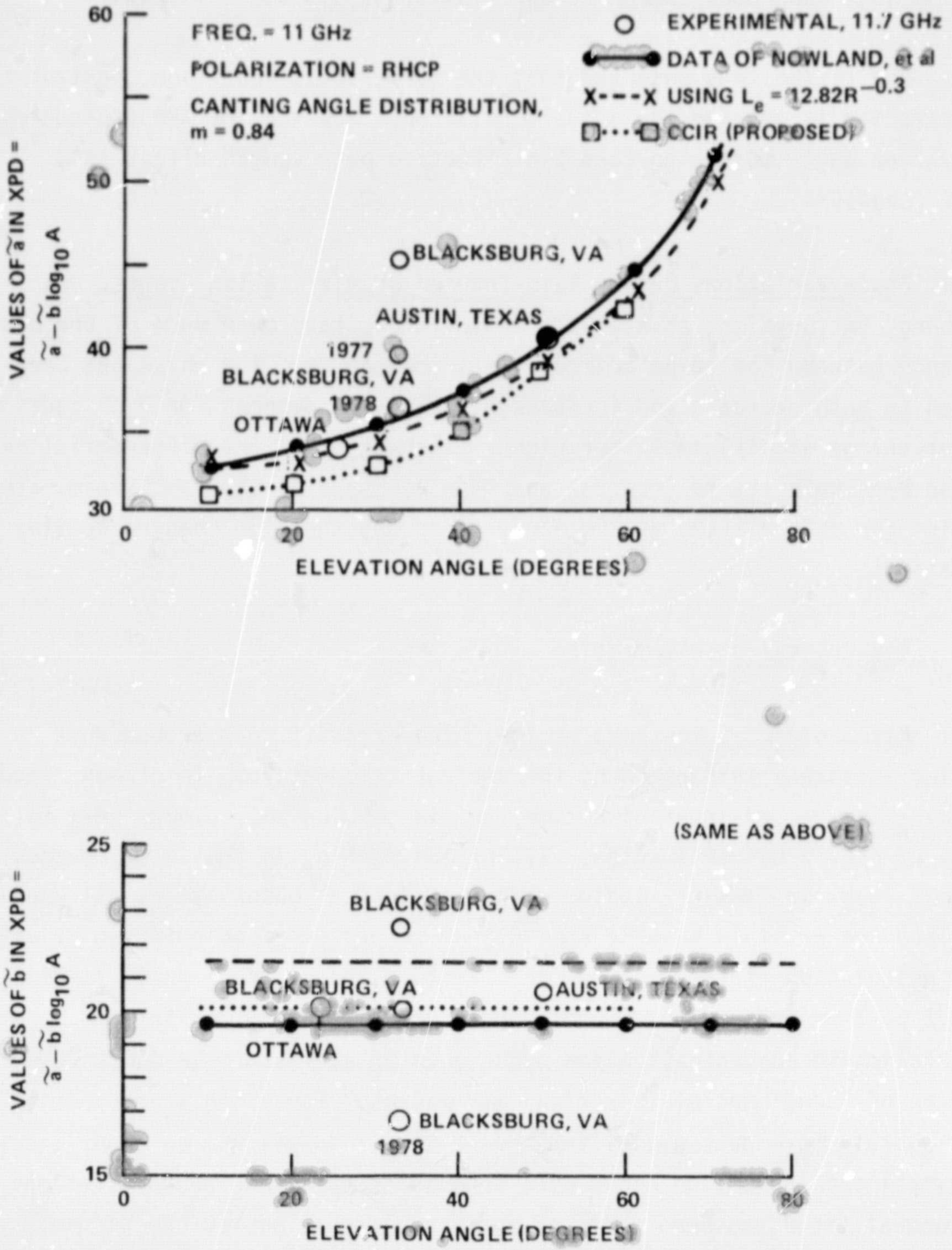

(b)

Figure 6.7-4 Elevation Angle Dependence of the Coefficients in the Cross-Polarization Discrimination Relation not confirm this fact. The $\tilde{b}$ coefficient appears to be nearly independent of elevation angle and does appear to agree with the limited data base.

Chu (1979b) has observed that the different propagation constant for depolarization is governed by a $\cos^2\theta$ relation. However the XPD dependence on elevation angle must also take the effective path length effect into account (Chu-1974).

6.7.2.4 Phase Variations During Rain-Induced Depolarization Events. At Blacksburg, VA (Bostian, et al-1977) measurements have been made of the phase difference between the co-polarized signal components. The phase has been observed to both decrease and increase by about 150 degrees for 3 dB fades and then not change significantly for higher attenuations. The differential phase has also been observed to increase and then decrease in the same storm. The mechanism for this plateau at 150 degrees and why the sign changes remains unexplained.

6.7.3 Ice-Crystal Depolarization

6.7.3.1 Meteorological Presence of Ice. Ice crystals form around dust particles in shapes influenced by the ambient temperature. In cirrus clouds they may exist for an indefinite time, but in cumulonimbus clouds they follow a cycle of growth by sublimation, falling and melting in the lower reaches of the cloud (Bostian-1979). Radio, radar and optical observations all confirm that cloud ice crystals possess some degree of preferred orientation related to the orientation of the electrostatic field. The crystals range in size from 0.1 to 1 mm and concentrations range from 10^3 to 10^6 crystals/m^3. The variation in concentration and occurrence of events may be due to the variation of "seed" nuclei in various air masses. For example continental air masses contain more dust nuclei than maritime air masses and so occurrences of ice-crystal depolarization occur more frequently at inland ground stations. This general trend has been observed between observations at the Virginia Polytechnic Institute and State University (inland, most frequent), University of Texas at Austin (intermediate) and Bell Telephone Laboratories (maritime, least frequent).

6.7.3.2 Ice-Crystal Depolarization Measurements. Ice particles well above the height of the melting layer may have significant cross-polarization effects even for small values of attenuation (typically below 3 to 5 dB at 11.7 GHz). This effect is believed to contribute to the poor correlation between the excess attenuation and the cross-polarization discrimination at these low values of attenuation.

In Austin, TX (Vogel-1978, 1979) ice depolarization was associated with either thunderstorms during the summer months or with clouds in the presence of polar air masses during the winter. An example of the percentage of time that XPD was less than or equal to the abscissa given that the excess attenuation was less than or equal to 1 dB is shown for the 18 month period from 12 June 1976 to 31 January 1978 and the period February 1978 to January 1979 in Figure 6.7-5. This curve shows that during 1976-78 45 per cent of the time that the XPD was less than or equal to 35 dB, there was less than 1 dB of attenuation; 24 per cent of the time that the XPD $\leq$ 30 dB the A $\leq$ 1 dB and 12 per cent of the time that XPD $\leq$ 25 dB the A $\leq$ 1 dB. In contrast, using the rain depolarization relation; for 1 dB yields a XPD $\leq$ 40 dB. Therefore systems requiring 30 dB or more XPD should expect a significant number of depolarization events due to ice.

Also, it has been observed (Shutie, et al-1978) that at 30 GHz ice crystals yield a constant value (typically 90 degrees) of the relative phase angle between the crosspolar and copolar signals as a function of XPD as shown in Figure 6.7-6. The corresponding polar plot for a heavy rain event is shown in Figure 6.7-7. In this case the XPD was reduced by signal attenuation and the signal to noise ratio of the relative phase measurement decreased as the XPD decreased. This effect appears to increase the scatter of the phase angle with decrease in XPD.

English investigators have also noted that rapid changes in relative phase and XPD are observed in thunderstorms and are associated with realignment of the ice crystal orientation by the electrostatic fields. In electrically-active storms, these electrostatic fields discharge rapidly

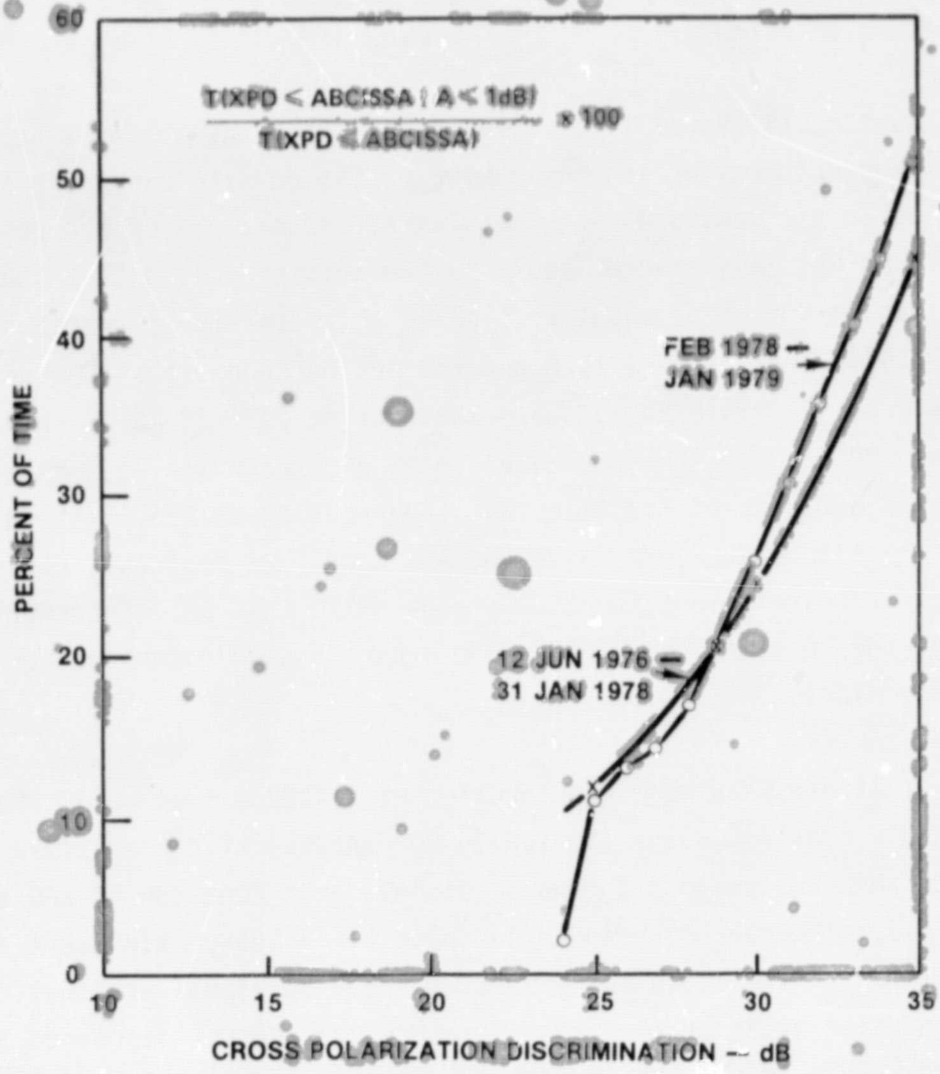

Figure 6.7-5 Contribution of Ice Depolarization to all Depolarization Events

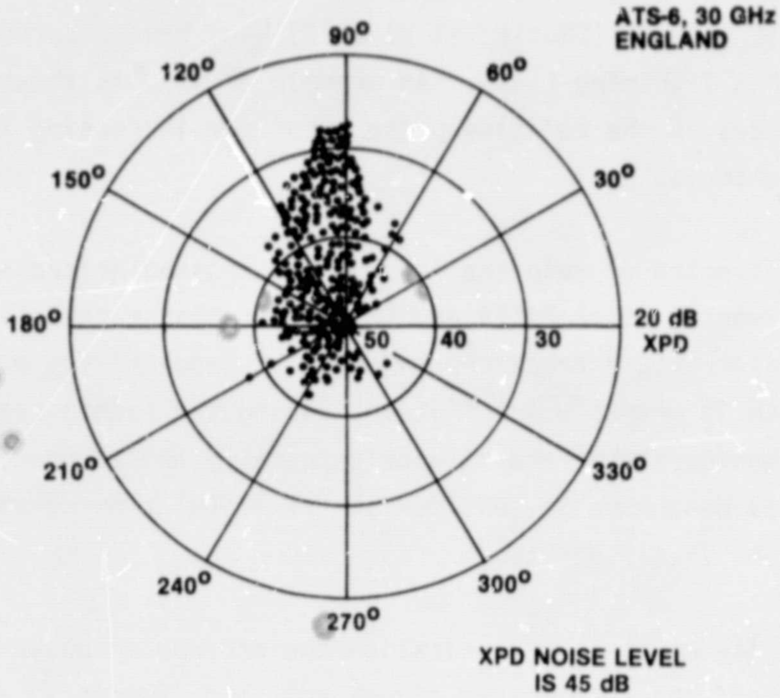

Figure 6.7-6 Polar Plot of the Cross Polarization Discrimination Arising From an Ice Cloud

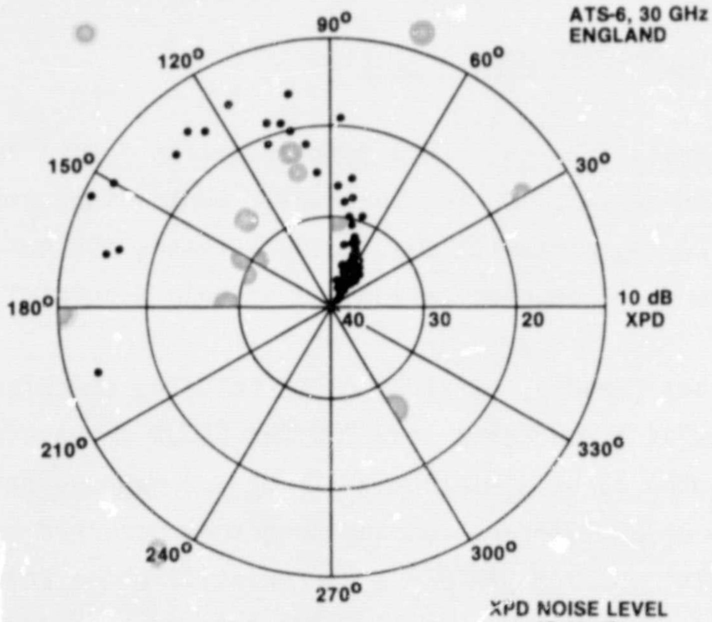

Figure 6.7-7 Polar Plot of the Cross Polarization Discrimination Arising From a Heavy Rain Event

resulting in rapid relative phase shifts of 180^{o} and rapid decreases in XPD of 27 dB in 20 seconds (Shutie, et al-1977) have been observed at the occurrence of a lightning flash. An example of this is shown in Figure 6.7-8 where the spikes in the relative phase occur for increasing XPD and result in large phase changes.

The spectra of rain and ice-induced crosspolarized signals have been analyzed (Hayworth, et al-1977) and it appears that a cancellation system with a 10 Hz bandwidth would track the majority of depolarizing events. However this bandwidth is probably insufficient during the sudden realignment of ice crystals in thunderstorms and in nonelectrically active precipitation. A suggestion has been made to consider use of a dual time constant system to accommodate all likely events.

For ice crystal depolarization the crosspolar phase shift is usually $\pm$ 90 degrees of the copolarized signal and so differential attenuation dominates the XPD variations. This effect was displayed in Figure 6.7-6. However depending on the frequency, rain-induced XPD variations predominantly shift the phase near 20 GHz and below and induce differential attenuation from 20 to 60 GHz (Hogg and Chu-1975).

6.7.4 Other Sources of Depolarization

6.7.4.1 Snow Depolarization. Snow depolarization occurs during both the winter and summer months. During the summer months snow exists above the 0^{o}C isotherm. During winter as the isotherm lowers the thickness of the snow increases and the depolarization due to rain decreases.

In Canada (Hendry, et al-1976) tests using circularly polarized diversity radars at frequencies near 2.9 GHz (10.4 cm wavelength) and 16.7 GHz (1.8 cm wavelength) at an elevation angle of 3.2 degrees have diagnosed storms during both summer and winter. During June snow occurred during a storm from 2.6 to 8.2 km altitude and yielded a differential phase shift of 0.36 deg/km at 2.9 GHz. Winter data taken at 16.7 GHz gave more variable results of 0.16 to 1.17 deg/km for moderate to heavy snowstorms ranging in altitude from 70 m to 2.6 km. The mean value of differential phase shift was 0.69 deg/km at 16.7 GHz.

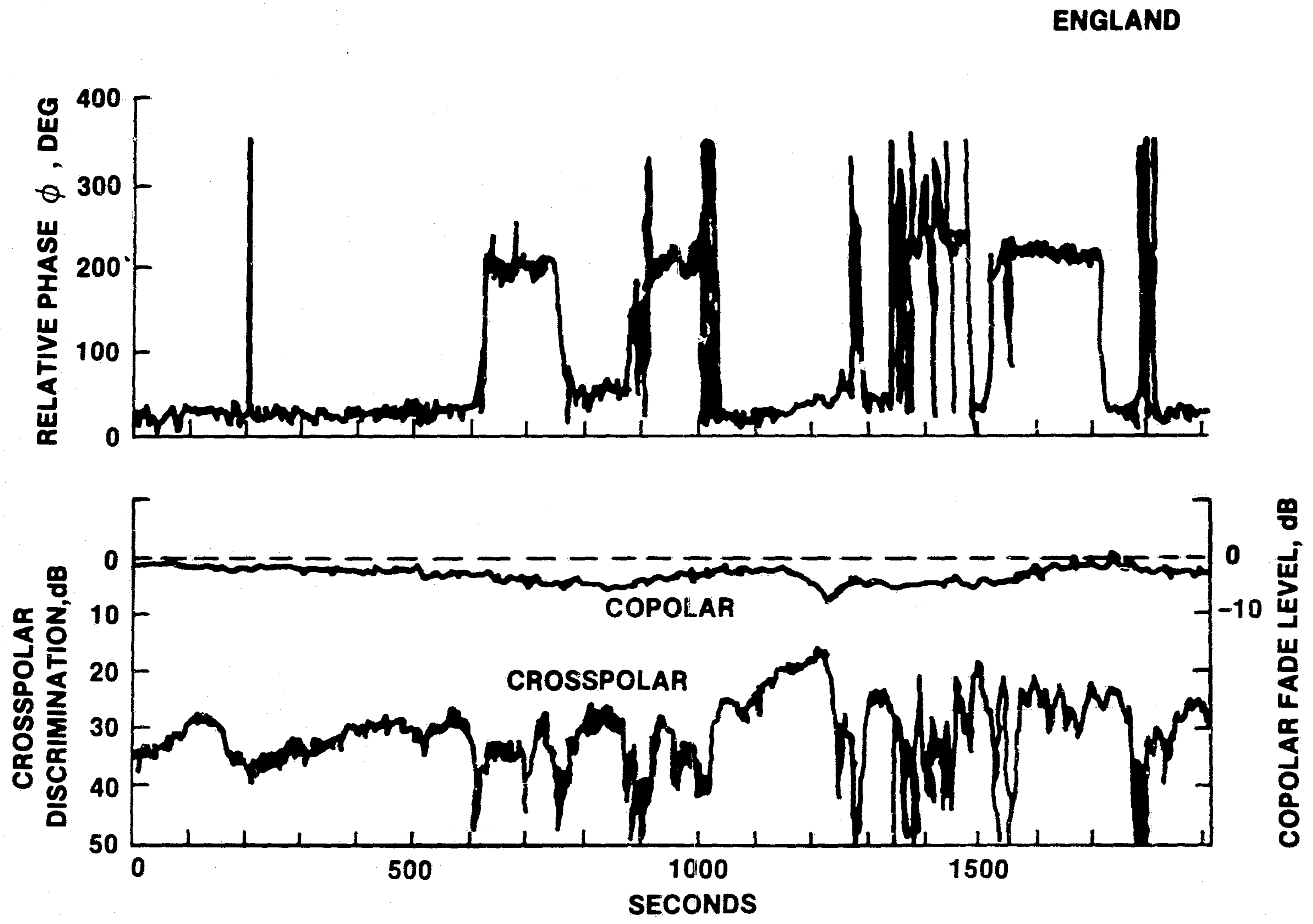

Figure 6.7-8 Phase, Copolar Fade and Crosspolar Discrimination for an Electrically Active Thunderstorm (15th July 1976)

6.7.4.2 Multipath Depolarization. A sharp antenna cross-polarization diagram can allow an oblique indirect ray to produce a significant cross-polar component. This condition is usually associated with low elevation angle events where the sidelobes are receiving energy from the oblique ray. Measurements have been made on terrestrial links at 11 GHz (Watson, et al-1973) and 22 GHz (Turner-1973).

The magnitude of the indirect signal reflected from the earth can be roughly estimated from the data in Lord and Oliver (1946) taken near 3 GHz. Generally the ground-scattered wave amplitude is at least 20 dB below the direct wave.

6.7.4.3 Refractive Effects. Variations in the radio refractivity (dielectric constant of tropospheric layers) can cause rotation of the polarization plane of the rays refracting through the layers. This condition will occur for layers which are not perpendicular to the vertical plane containing the transmitter and receiver as described by LeFrancois, et al (1973).

6.7.5 Prediction of Depolarization Statistics

In most cases depolarization arises due to two sources: rain and ice. The statistics of depolarization events can be estimated using the methodology shown in Figure 6.7-9. For rain depolarization the starting point is the cumulative rain attenuation statistics computed or measured via techniques described in Section 6.3. For example, the cumulative attenuation statistics for Rosman, NC while observing the 20 GHz ATS-6 satellite beacon are shown in Figure 6.7-10. This data was obtained by the distribution extension technique described in Section 6.3.

Since the ATS-6 was nearly vertically polarized (within 20 degrees of vertical) the formula

$$XPD = 47 - 24.5 \log_{10}(A)$$

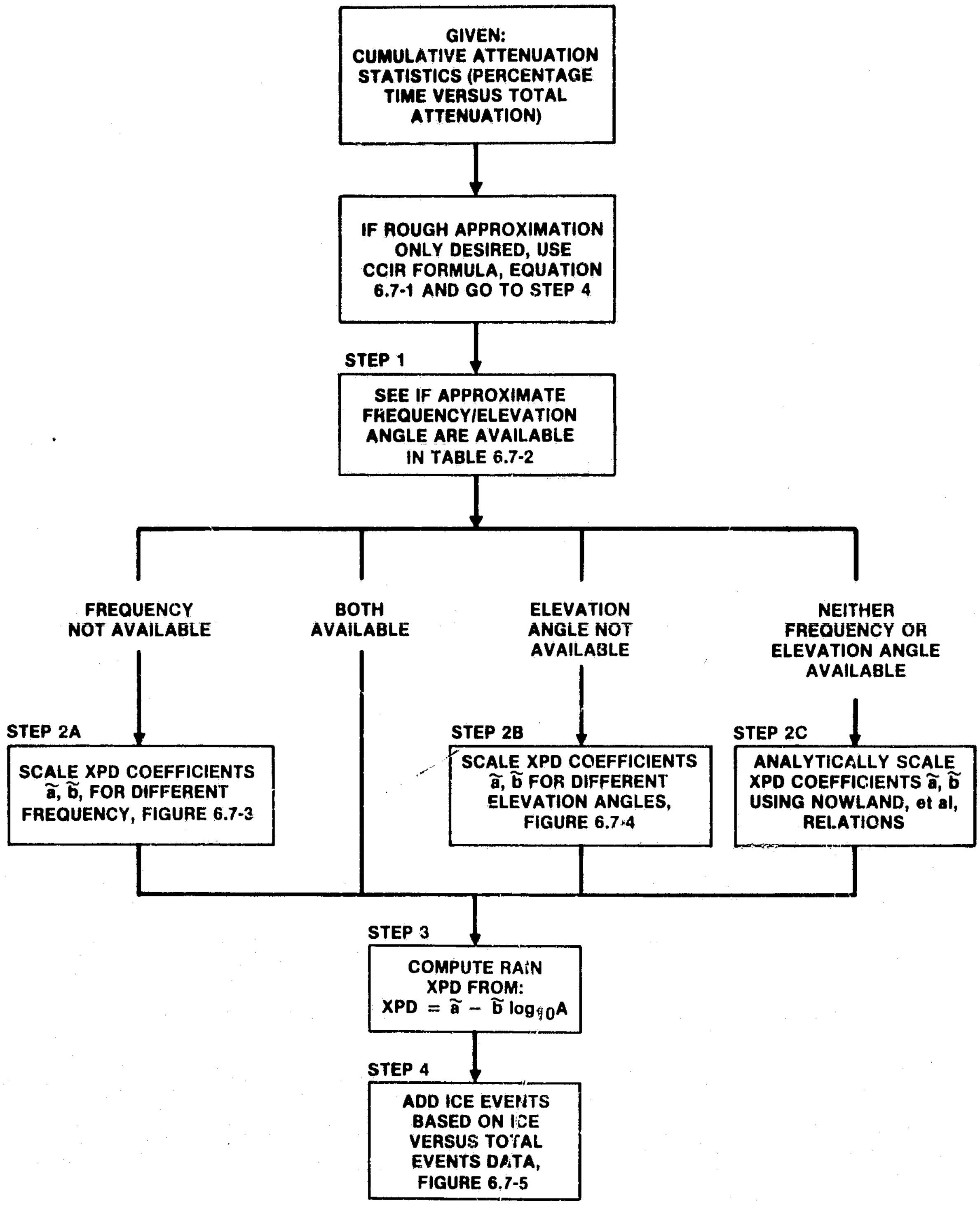

Figure 6.7-9. Technique for Prediction of Depolarization Statistics

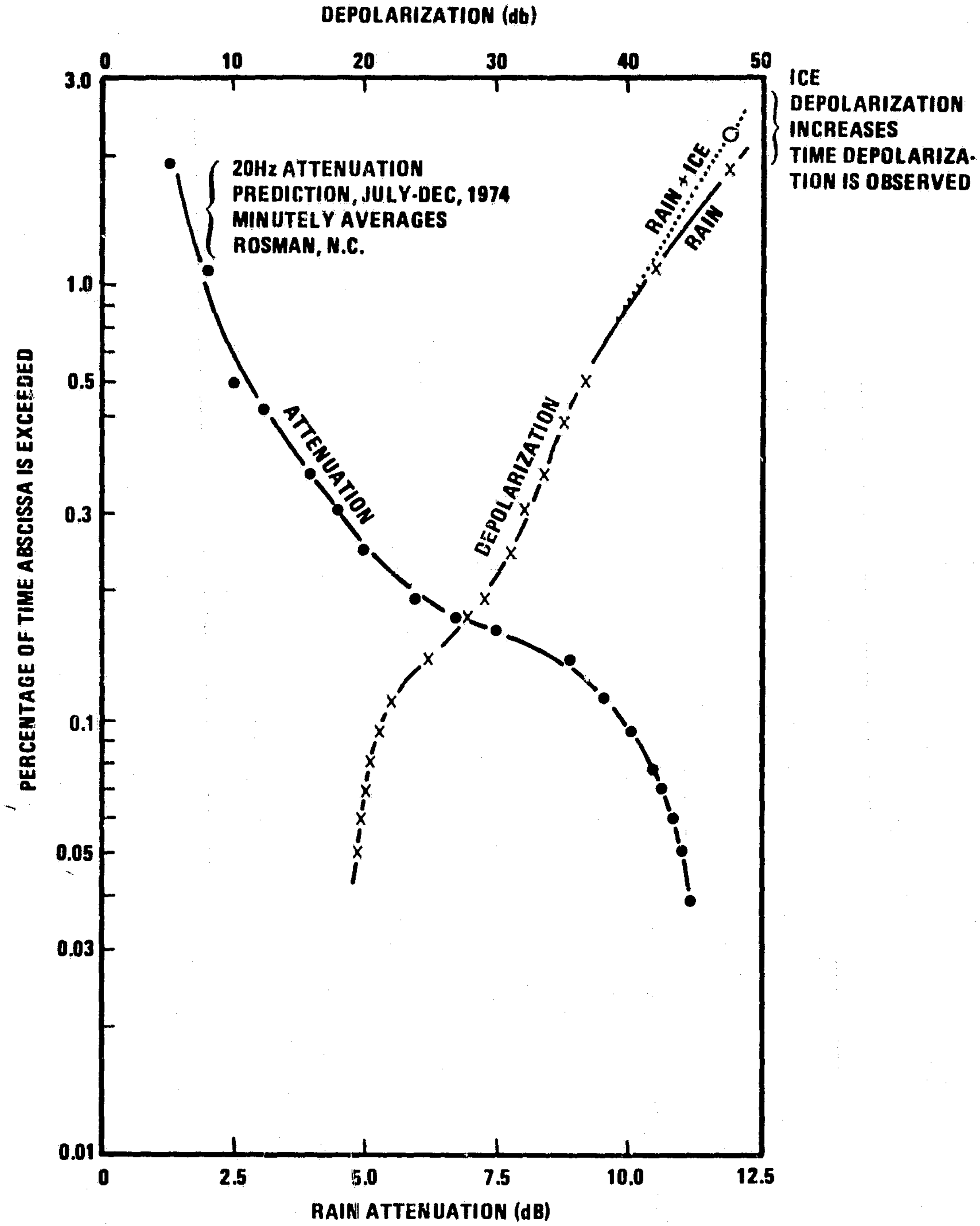

Figure 6.7-10 Attenuation and Depolarization Statistics for Rosman, N.C.

is selected from Table 6.7-2. At this point, two techniques exist for correcting this formula for frequency and elevation angle. If a large frequency or elevation angle scaling were required, the suggested approach would be to use the equations of Nowland, et al (1977). However, since no frequency scaling is required and since the elevation angle to ATS-6 from Rosman is 47 degrees compared to the Blacksburg, VA elevation angle to COMSTAR of 44 degrees, no scaling is needed. If the effect of polarization needs to be considered, the equations of Nowland, et al (1977) or CCIR (1978, Rpt 564-1) must be used.

Within the accuracy of the required statistics the relation

$$XPD\ (dB) = 47 - 25\ \log_{10}(A)$$

will be utilized. Substituting the attenuation values for a given percentage of the year (from Figure 6.7-5) into this relation yields the XPD statistics for rain shown in Figure 6.7-10. Based on these results the CPD will exceed 20 dB during 99.9% of the year.

However, for low attenuation levels (high XPD's), ice will introduce depolarization. A crude estimate of this effect can be made based on the data in Figure 6.7-5. Namely, when $A \leq 1$ dB about 30% more XPD events occur due to ice and rain, than just rain alone. This translates the data point in Figure 6.7-10 corresponding to A = 1 dB from about 0.18 percent of the year to (1.3)(0.18%) = 0.23% of the year (indicated by a 0 in Figure 6.7-10). Thus the XPD curve is raised up for low values of attenuation. For attenuations above 3 dB the rain plus ice depolarization plots are essentially all rain effects.

Note that one could have added in the effect of ice depolarization by translating the corresponding rain and ice XPD's. This is probably less accurate because high values of XPD are equipment dependent. Therefore an average value of 30% ice contribution was selected rather than converting each value of XPD using data shown in Figure 6.7-5. This correction is based on very preliminary results from a single geographic location and should be added only to show a trend, since the absolute value is probably in error.

6.8 ADDITIONAL PROPAGATION FACTORS RELATED TO SYSTEM DESIGN

6.8.1 Contents of this Section

Several other factors affect trans-tropospheric transmissions from satellites. Among these are

- Dispersion
- Sky and extraterrestrial noise

When the dispersion of the propagating medium is sufficiently high, the phase and/or amplitude of wide-bandwidth transmissions may be selectively altered. The tropospheric effects have been predicted and measured to be small, but ionospheric dispersion may be significant below 10 GHz. Therefore, in this section the ionospheric effects on the path are considered.

Measurements are underway with the COMSTAR satellites at 28.56 ± 0.264 GHz by Bell Laboratories. Results of these measurements are only now becoming available. They indicate that dispersion is not a problem at 28 GHz. The first available data was obtained from the ATS-6 satellite and is presented here.

The absorbing gases and hydrometeors in the troposphere are a source of broadband incoherent noise. This is normally expressed as a sky temperature T_s observed by the receiving system, such that the noise power is $P_{NOISE} = kT_sB_n$ where k = Boltzmann's constant = 1.38×10^{-23} joule/degree and B_n is the noise bandwidth (equivalent to the bandwidth of a rectangular filter whose noise ouput is the same as the receiver's actual bandwidth limiting filter). The other sources of noise are extraterrestrial sources (primarily the sun) and ground noise entering the antenna sidelobes at low elevation angles.

The above noise sources are observed by ground station antennas. Satellite antennas pointed at a ground station observe noise radiated by the earth and cloud tops.

Note that precipitation in the path both reduces the system carrier strength and raises the background noise level, resulting in a reduced carrier-to-noise ratio. The increase in noise level (noise temperature) is particularly significant in low-noise receiver front ends, where the resultant noise figure during a precipitation event could be increased by 2 dB or more.

6.8.2 Tropospheric Effects on Bandwidth Coherence

6.8.2.1 Amplitude Variations.

6.8.2.1.1 Theoretical Results. Theoretical estimates of the degradation of pulse shapes through rain have indicated that only minor effects are observed. The calculations (Crane-1967) indicated that pulse distortion does not become significant until total rain attenuations of the order of 100 dB are encountered. Since current link margins do not allow such high attenuations, the link will fail due to signal attenuation before the pulse shape affects transmission.

However, if required, calculations of the amplitude dispersion are possible for both clear air and rain attenuation based on the data and formulas in Section 6.3 of this report.

For rain the frequency dependence of the specific attenuation (dB/km) is

$$\frac{\partial \alpha}{\partial f} = \frac{\partial (aR^b)}{\partial f} = \alpha \left[\frac{1}{a} \frac{\partial a}{\partial f} + (\ln R) \frac{\partial b}{\partial f} \right]$$

where, for example, for the frequency range from 8.5 to 25 GHz (Olsen et al-1977)

$$\frac{\partial a}{\partial f} = 1.02 \times 10^{-4} f^{1.42}$$

$$\frac{\partial b}{\partial f} = -0.11 f^{-1.0779}$$

For example, at 20 GHz and R = 25 mm/hr,

$$a = 5.93 \times 10^{-2}$$

$$b = 1.12$$

$$\frac{\partial a}{\partial f} = 7.18 \times 10^{-3}$$

$$\frac{\partial b}{\partial f} = -4.36 \times 10^{-3}$$

$$\alpha = 2.18 \text{ dB/km}$$

so

$$\frac{\partial \alpha}{\partial f} = 0.23 \text{ dB/(km-GHz)}$$

or a typical effective path length $L_e = 6$ km,

$$\frac{\partial (\alpha L_e)}{\partial f} = L_e \frac{\partial \alpha}{\partial f} = 1.39 \text{ dB/GHz}$$

6.8.2.1.2 Experimental Results. The ATS-6 beacons at 20 and 30 GHz were both capable of being modulated with ±180, ±360, ±540 and ±720 MHz sidetone signals. Typical selective fading events across the 1.44 GHz bands are shown in Figures 6.8-1 and 6.8-2, respectively (WEC-1977). These are four-second averages taken on day 270 of 1974 just before the onset of a fade event

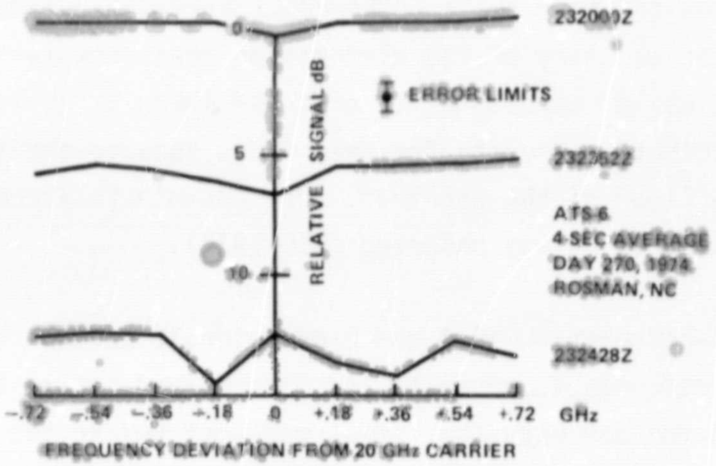

Figure 6.8-1 Selective Fading Near 20 GHz

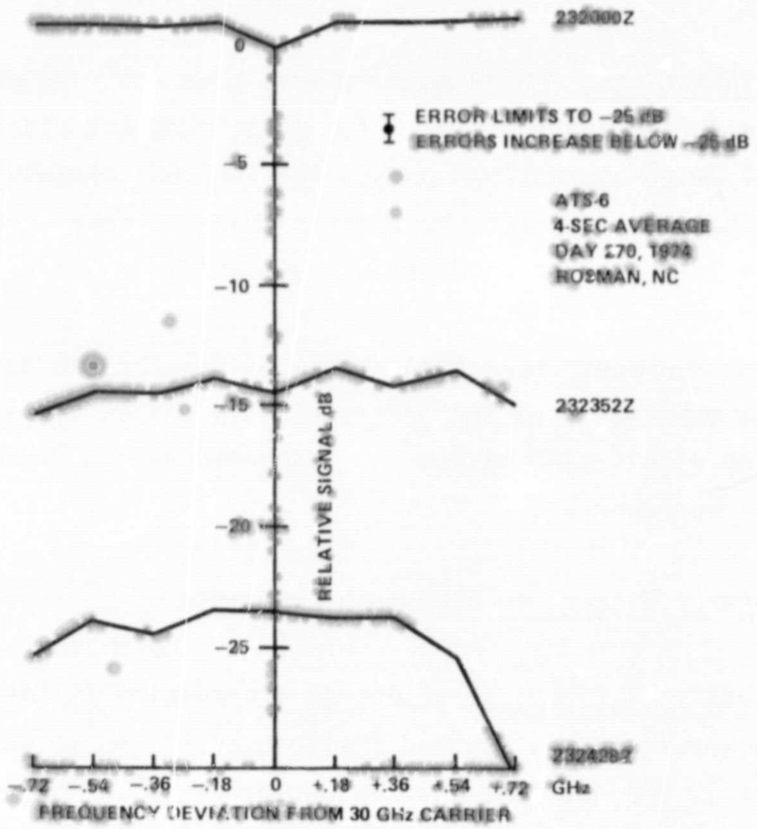

Figure 6.8-2 Selective Fading Near 30 GHz

(230000Z), at the beginning of the fade event (232352Z), and before receiver lock was lost during the fade event (232428Z). Except for fade depths in excess of 20 dB, the accuracy of the attenuation measurements is ±1 dB. These rain fade results, while representative of those taken at Rosman, do not appear to be sufficiently accurate for deep fades because the signal levels approach the noise floor of the receiver. For one-minute averages, no measurable selective fading was observed (WEC-1977).

The cross-correlation of 4 and 6 GHz signals due to low angle fading in the Canadian arctic was found to be low (Strickland, et al-1977). During a 2.5 hour period on the day when the fading was most severe the correlation coefficient was 0.34 since the 6 GHz signal experienced 55% more fades than the 4 GHz signal. This would indicate a dispersion was present, but the mechanism for this effect is tropospheric refraction and not rain. Frequency selective fading may be significant at low elevation angles.

6.8.2.2 Phase Variations. Phase measurements have not yielded significant results for frequencies above 10 GHz. The phase coherent sidetone signals on ATS-6 showed only minor variations across the 1.44 GHz bandwidths. These variations were most evident for the shorter (one and four second) averaging periods compared to the one-minute period (WEC-1977).

Phase measurements have been attempted for the one degree elevation angle satellites observed from the arctic (Strickland et al-1977). Unfortunately, no significant fade events occurred and no differential phase variations were recorded.

6.8.3 Ionospheric Effects on Bandwidth Coherence

6.8.3.1 Amplitude Variations. Ionospheric attenuation is inversely proportional to the frequency squared (Millman-1958) and is generally less than 0.001 dB at 15 GHz and an elevation angle $\theta = 90^{\circ}$. The variation is approximately related to cosecant θ. The attenuation is therefore usually less than 0.01 dB above 10 GHz.

6.8.3.2 Phase Variations. The group delay due to the free electrons in the ionosphere is (Klobuchar-1973)

$$\Delta\tau = 40.3\ N_e/cf^2$$

where N_e is the total electron content in electrons/m^2, $c = 3\times10^8$ m/sec and f is in Hertz. This delay is equivalent to a phase delay (in radians)

$$\Delta\tau = \frac{\Delta\phi}{2\pi f}$$

so that

$$\Delta\phi = (2\pi)(40.3)N_e/(cf)$$

For a typical value of $N_e = 10^{17}\ m^{-2}$, the total phase delay at 11.7 GHz is only 7.21 radians. The frequency dependence of this is only

$$\frac{\partial(\Delta\phi)}{\partial f} = -\frac{2\pi(40.3)\ N_e}{cf^2}$$

$$= -\ 6.2 \times 10^{-10}\ \text{radian/Hertz}$$

$$= -0.62\ \text{radian/GHz}$$

$$\approx -35\ \text{degrees/GHz.}$$

For higher frequencies, the rate of change of phase with frequency decreases.

6.8.4 Sky Noise Observed by Ground Stations

6.8.4.1 Tropospheric Contribution to Sky Noise. The effective sky noise due to the troposphere is primarily dependent on the attenuation at the frequency of observation. For sky radiometers an empirical equation has been derived (Wulfsberg-1964):

$$A\ (dB) = -10 \log_{10} \frac{T_m - T_s}{T_m}$$

where T_s is the sky noise temperature, T_m is the mean absorption temperature of the attenuating medium and A is the specific attenuation times the effective path length. Temperatures are in degrees Kelvin. The value

$$T_m = 1.12 \text{ (surface temperature in } ^oK) - 50^oK$$

has been empirically determined (Wulfsberg-1964). As T_s increases toward T_m, the radiometer tends to saturate. For typical values of minimum temperature resolution, $(\Delta T)_{rms}$, the radiometer can only accurately measure to 10 or 15 dB attenuation levels.

Inverting this relation yields the resulting sky temperature for a given path attenuation A (in dB) of

$$T_s = T_m \left[1 - 10^{(-A/10)}\right]$$

This relation may now be utilized for estimation of the sky temperatures using the data in Section 6.3 of this report for the attenuation A.

6.8.4.1.1 Clear Air Sky Noise. The sky noise contributed by water vapor and oxygen may be computed from the clear air attenuation. A typical set of curves (CCIR, Rpt 720-1978) as a function of elevation angle θ is shown in Figure 6.8-3. Here the ground station is assumed to be at sea level, pressure at one atmosphere (1013.6 millibars), surface temperature at 20^oC and water vapor density at 10 gm/m^3 (R.H. = 58%).

As an example, for a 20 GHz downlink at 10 degrees elevation angle, $T_s = 150^oK$.

6.8.4.1.2 Sky Noise Due to Rain. The value of sky noise increases significantly during rain events. When the total attenuation approaches 10 to 15 dB the sky noise temperature is nearly T_m.

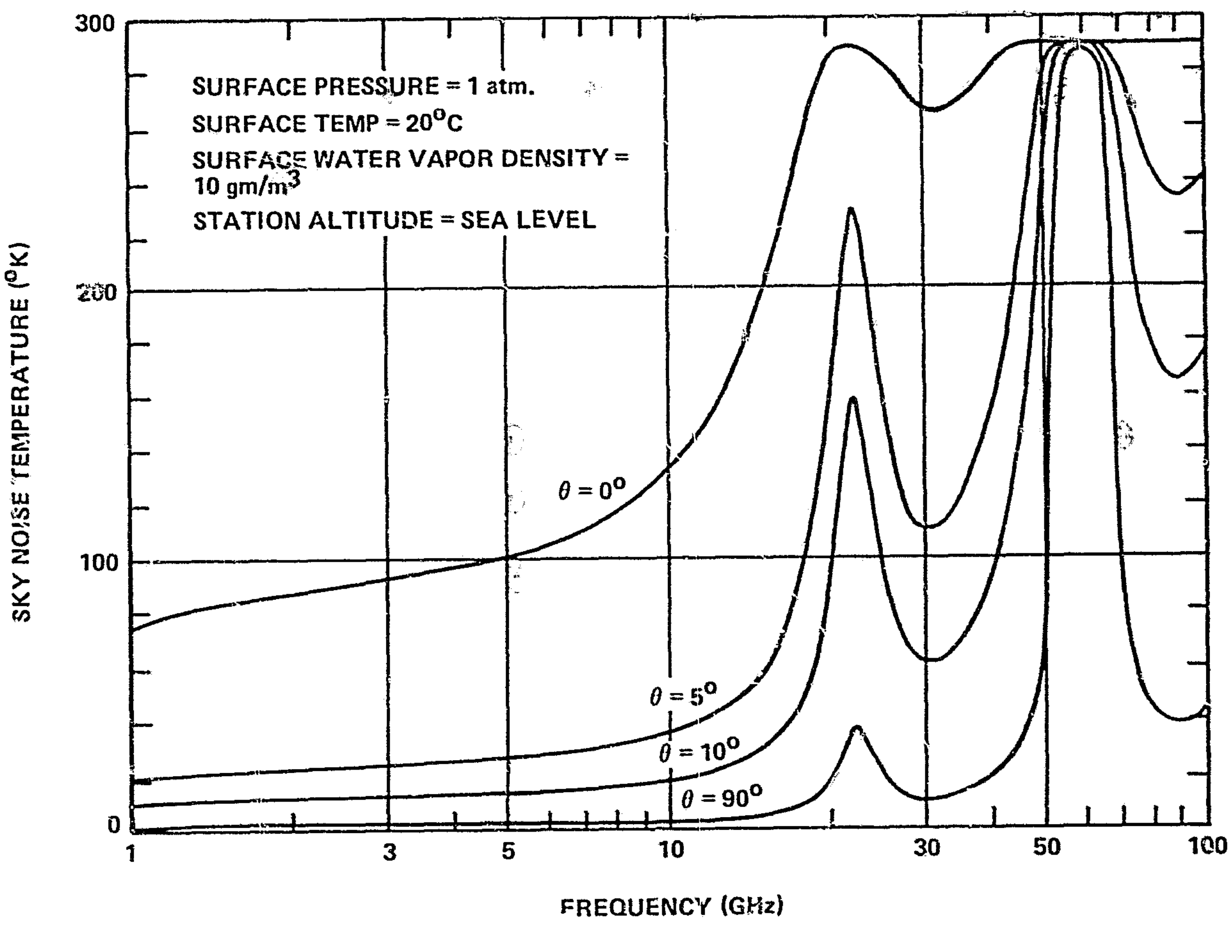

Figure 6.8-3 Sky Noise Temperature Due to Clear Air

Actual values of T_s may be obtained using the attenuation calculation techniques in Section 6.3. For example, to compute the cumulative statistics of T_s, first compute the cumulative attenuation statistics due to rain, and then use the Wulfsberg relation (above) to convert attenuation to apparent sky noise temperature. An example of this process has been done for Rosman, NC at 20 GHz. The results are given in Table 6.8-1.

The sky noise temperature (see last column of Table 6.8-1) will degrade the overall system noise figure of the receiver system. For example, for a receiver with a 4 dB noise figure, the resultant noise figure for the rain rate corresponding to 0.01% of the year will be 5.4 dB, i.e., an increase of 1.4 dB.

6.8.4.1.3 Sky Noise Due to Clouds, Fog, Sand and Dust. The major contributor to the sky noise temperature is the medium with the highest attenuation. Generally, clouds will present higher attenuations than fog, sand or dust. For example, for cumulus clouds with no precipitation the water density will be approximately 0.5 g/m^3. For the Rosman example described earlier (20 GHz),

$$A = K_c \rho_\ell \ t_c \csc \theta$$

where t_c is the thickness of the clouds (typically 2 kilometers). Using typical numbers

$$\begin{aligned} A &= (0.4 \text{ dB m}^3/\text{gm km})\ (0.5 \text{ gm/m}^3)\ (2 \text{ km}) \csc (47^o) \\ &= 0.55 \text{ dB} \end{aligned}$$

The corresponding sky noise contribution is then

$$T_s = T_{mc} \left[1 - 10^{-(0.55/10)}\right]$$

Letting T_{mc} equal the temperature of the cloud should be conservative (i.e., $T_{mc} = 0^oC = 273^oK$). The result is only 32^oK. Clearly, rain represents a much more significant contributor to the sky noise temperature than clouds.

TABLE 6.8-1

CUMULATIVE STATISTICS OF SKY TEMPERATURE

DUE TO RAIN FOR ROSMAN, N.C. AT 20 GHz

$T_m = 275^0K$

PERCENT OF YEAR	POINT RAIN RATE VALUES	AVERAGE RAIN RATE	TOTAL RAIN ATTENUATION*	SKY NOISE TEMPERATURE†
0.001	102 mm/hr	89 mm/hr	47 dB	275°K
0.002	86	77	40	275
0.005	64	60	30	275
0.01	49	47	23	274
0.02	35	35	16	269
0.05	22	24	11	252
0.1	15	17	7	224
0.2	9.5	11.3	4.6	180
0.5	5.2	6.7	2.6	123
1.0	3.0	4.2	1.5	82
2.0	1.8	2.7	0.93	53

NOTES:

* At 20 GHz the specific attenuation $A = 0.06\ R_{ave}^{1.12}$ dB/km and for Rosman, N.C. the effective path length is 5.1 km to ATS-6.

† For a ground temperature of 17°C = 63°F the $T_m = 275^0K$.

6.8.4.1.4 Total Sky Noise Temperature Arising from Several Contributors. The sky noise temperatures from several sources do not add linearly. Rather, the attenuation from each contributor must be added and the total result substituted into the sky noise versus attenuation relation. For example, for the Rosman ground station observing the ATS-6, the clear air attenuation is 1.2 dB yielding a T_s (clear air) = 66^{o}K. From Table 1 for 0.2% of the year (105 minutes) the rain induced sky temperature due to clear air and rain is 203^{o}K which is significantly less than the sum of each contributor (246^{o}K). During rain conditions the cloud contributions should also be added, but these will generally be even a smaller contribution than the clear air attenuation.

6.8.4.2 Extraterrestrial Sources of Sky Noise

6.8.4.2.1 Solar Noise. The sun generates very high noise levels when it is collinear with the Earth station-satellite path. For geostationary satellites, this occurs near the equinoxes, for a short period each day. The power flux density generated by the sun is given as a function of frequency in Figure 6.8-4 (Perlman, et al-1960). Above about 20 GHz, it is practically constant at -188 dBW/Hz-m^2 for "quiet sun" conditions.

Reception of solar noise can be viewed as an equivalent increase in the antenna noise temperature by an amount T_s. T_s depends on the relative magnitude of the antenna beamwidth compared with the apparent diameter of the sun (0.48^{o}), and how close the sun approaches the antenna boresight. The following formula, after Baars (1973), estimates T_s when the sun, or another extraterrestrial noise source, is centered in the beam.

$$T_s = \frac{1 - \exp[-(D/1.2\theta)^2]}{f^2 D^2} \log^{-1} \frac{S + 250}{10}$$

where D = apparent diameter of the sun, deg

f = frequency, GHz

S = power flux density, dBw/Hz-m^2

θ = antenna half-power beamwidth, deg

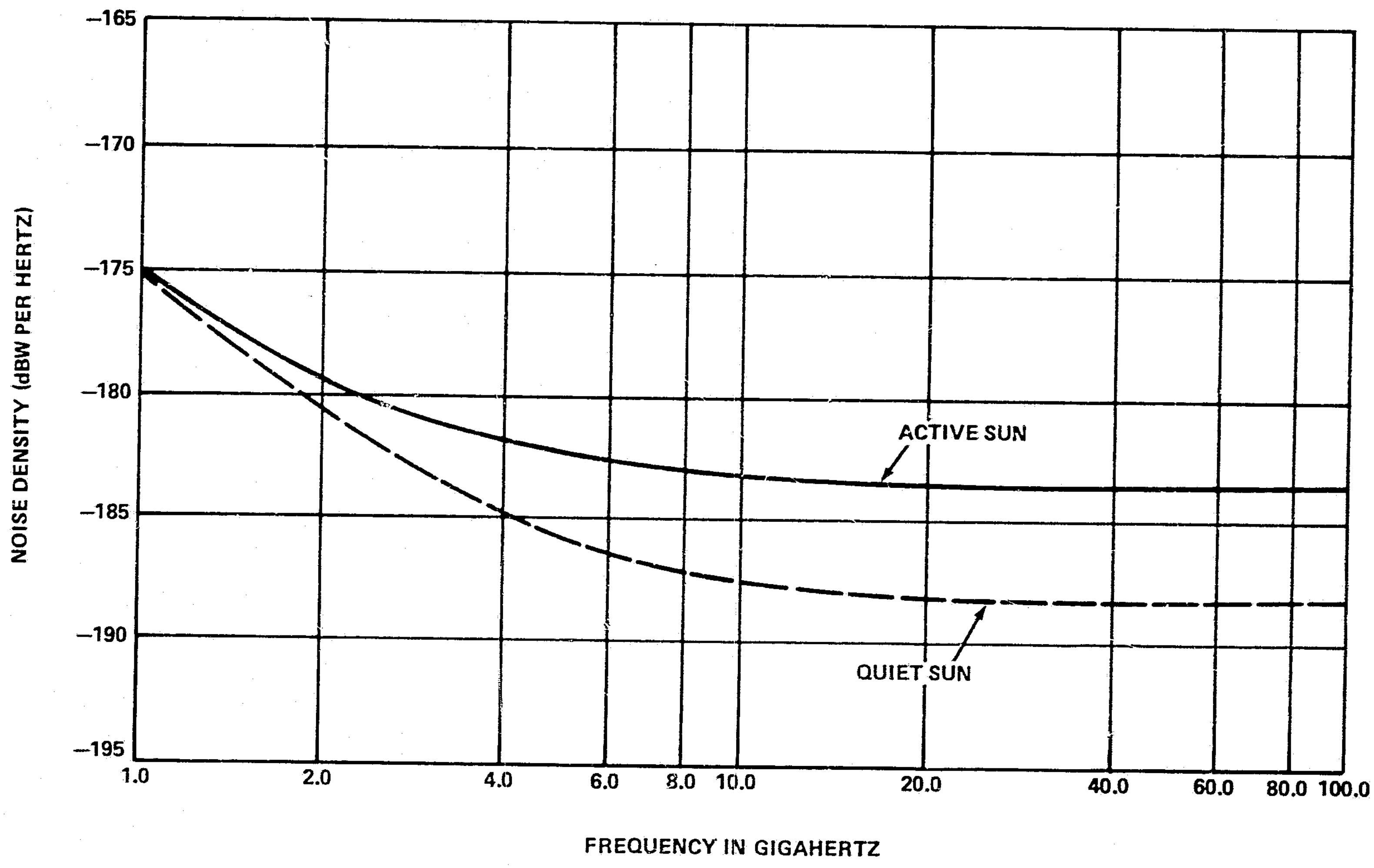

Figure 6.8-4 Values of Noise From Quiet and Active Sun. Sun Fills Entire Beam (Perlman, et al-1960)

For an Earth station operating at 20 GHz with a 2 m diameter antenna (beamwidth about 0.5^o), the maximum increase in antenna temperature that would be caused by a ("quite") sun transit is about 8100 ^oK, according to the formula.

The sun's flux has been used extensively for measuring tropospheric attenuation. This is done with a sun-tracking radiometer, which monitors the noise temperature of an antenna that is devised to automatically remain pointed at the sun.

6.8.4.2.2 Lunar Noise. The moon reflects solar radio energy back to the Earth. Its apparent size is approximately 1/2 degree in diameter, like the sun. The noise power flux density from the moon varies directly as the square of frequency, which is characteristic of radiation from a "black body." The power flux density from the full moon is about -202 dBW/Hz-m^2 at 20 GHz. The maximum antenna temperature increase due to the moon, for the 20 GHz 2m antenna considered earlier, would be only about 320^o. Because of the phases of the moon and the ellipticity of its orbit, the apparent size and flux vary widely, but in a regular and predictable manner. The moon has been used in measuring Earth station G/T (Johannsen and Koury-1974).

6.8.4.2.3 Radio Stars. The strongest radio stars are ten times weaker than the lunar emission. The strongest stars (Wait, et al-1974) emit typically -230 dBW/Hz-m^2 in the 10 to 100 GHz frequency range. Three of these strong sources are Cassiopeia A, Taurus A and Orion A. These sources are sometimes utilized for calibration of the ground station G/T. During the calibrations the attenuation due to the troposphere is usually cancelled out by comparing the sky noise on the star and subtracting the adjacent (dark) sky noise. Thus the attenuation-induced sky noise cancels out.

6.8.5 Noise Observed by Satellite-Borne Receivers

Receiving (uplink) antennas aboard spacecraft observe the warm earth or the earth's cloud cover. This represents a noise source competing with the uplink signal from the ground station.

Measurements of the brightness temperature of the earth measured with the electrically-scanned microwave radiometer aboard Nimbus-5 at 19.35 GHz have demonstrated brightness temperature differences of 160^oK when comparing water (130^oK) and land (290^oK) (Webster, et al-1975). Clouds appear to have a temperature near 270^oK (0^oC). Because of the high percentage of clouds and ocean areas on the earth, a full earth coverage antenna will observe approximately 270^oK. However, when observing a ground based temperature zone ground station a 300^oK brightness temperature is not uncommon. The noise temperature of the receive antenna, when the Earth fills its beam, is increased by an amount equal to the radiation efficiency of the antenna times the average brightness temperature seen in the pattern.

6.9 REFERENCES

Ahmed, I.Y. and L.J. Auchterlouie (1976), "Microwave Measurements of Dust Using an Open Resonator," Electronics Letters, Vol. 12, No. 17, p. 445.

Allnutt, J.E. (1976), "Slant Path Attenuation and Space Diversity Results using 11.6 GHz Radiometers," Proceedings IEE, Vol. 123, p. 1197.

Baars, J.W.M. (1973), "The Measurement of Large Antennas with Cosmic Radio Sources," IEEE Trans. Ant. Prop., Vol. AP-21, No. 4, pp. 461-474.

Bean, B.R. and E.J. Dutton (1966), "Radio Meteorology," National Bureau of Standards Monograph 92.

Bergmann, H.J. (1977), "Satellite Site Diversity: Results of a Radiometer Experiment at 13 and 18 GHz," IEEE Trans. Ant. Prop., Vol. AP-25, p. 483.

Bostian, C.W. (1979), private communication.

Bostian, C.W., S.B. Holt, Jr., S.R. Kauffman, E.A. Manus, R.E. Marshall, W.L. Stutzman and P.H. Wiley (1977), "Rain Depolarization and Attenuation Measurements at 11.7, 19.04 and 28.56 GHz: A Description of the Experiment and Some Preliminary Results," URSI Comm. F Proc., April 28 - May 6, La Baule, France, pp. 403-408.

Bostian, C.W., W.L. Stutzman, E.A. Manus, P.H. Wiley, R.E. Marshall and P. Santago (1979), "Summary of 1978 Attenuation and Depolarization Measurements Made With the CTS (11.7 GHz) and COMSTAR (19.04 and 28.56 GHz) Beacons," Invited Paper for the USNC/URSI Special Sessions on Propagation Above 10 GHz, Jume 18-20, Seattle, Washington.

Brandinger, P. (1978), "Propagation Requirements for 30/20 GHz System Design," 1978 Spring URSI Meeting, Washington, D.C.

Brussard, G. (1977), "Rain Attenuation on Satellite-Earth Paths at 11.4 and 14 GHz," URSI (Commission F), Symposium Proc., April 28 - May 6, LaBaule, France.

CCIR (1978), Propagation in Non-Ionized Media, Vol. V, XIV Plenary Assembly, Kyoto, Japan.

CCIR (1978a), Propagation in Ionized Media, Vol. VI, XIV Plenary Assembly, Kyoto, Japan.

Canada Atmospheric Environment (1973), Short Duration Rainfall Intensity-Duration-Frequency Graphs, Downsview, Ontario, Canada.

Chu, T.S. (1974), "Rain-Induced Cross-Polarization at Centimeter and Millimeter Wavelengths," Bell Syst. Tech. Jrnl., Vol. 58, No. 8, pp. 1557-1579.

Chu, T.S. (1979a), private communications.

Chu, T.S. (1979b), "Microwave Depolarization of an Earth-Space Path," URSI Meeting Abstracts, Seattle, Washington, June 18-20, p. 254.

Crane, R.K. (1967), "Coherent Pulse Transmission through Rain," IEEE Trans. Ant. Prop., Vol. AP-15, p. 252.

Crane, R.K. (1976), An Algorithm to Retrieve Water Vapor Information from Satellite Measurements, NEPRF Tech-Rept. 7-76, Final Report, Project No. 1423, Environmental Research & Technology, Inc., Concord, Mass.

Crane, R.K. (1976a), "Refraction Effects in the Neutral Atmosphere," Astrophysics, Part B. Radiotelescopes, Vol. 12 of Methods of Experimental Physics, M. C. Weeks, ed., Academic Press, N.Y.

Crane, R.K. (1977), "Ionospheric Scintillations," Proc. IEEE, Vol. 65, pp. 180-199.

Crane, R.K. and D.W. Blood (1979), Handbook for the Estimation of Microwave Propagation Effects-Link Calculations for the Earth-Space Paths, Environmental Research & Technology, Inc., Concord, Mass., report to NASA/GSFC under Contract NAS5-25341.

Crane, R.K. and W.E. DeBrunner (1978), "Worst-Month Statistics," Electronics Letters, Vol. 14, No. 2, pp. 38-40.

Davies, P.G. (1973), "Slant-path Attenuation at Frequencies above 10 GHz," IEE Conf. Pub. No. 98, pp. 141-149.

Davies, P.G. (1976), "Diversity Measurements of Attenuation at 37 GHz with Sun-Tracking Radiometers in a 3-site Network," Proceedings IEE, Vol. 123, p. 765.

Davies, P.G. and D.L. Croom (1974), "Diversity Measurements of Attenuation at 37 GHz with Solar-Tracking Radiometers," Electronics Letters, Vol. 10, p. 482.

Devasirvatham, D. and D.B. Hodge (1977), "Amplitude Scintillations on Earth-Space Propagation Paths at 2 and 30 GHz," The Ohio State University ElectroScience Lab., Tech. Rpt. 4299-4.

Engelbrecht, R.S. (1979), "The Effect of Rain on Satellite Communications Above 10 GHz," RCA Review, Vol. 40, p. 191.

Ferguson, A. and R.R. Rogers (1978), "Joint Statistics of Rain Attenuation on Terrestrial and Earth-Space Propagation Paths," Radio Science, Vol. 13, p. 471.

Freeny, A.E. and J.D. Gabbe (1969), "A Statistical Description of Intense Rainfall," Bell System Technical Journal, Vol. 48, p. 1789.

Funakawa, K. and Y. Otsu (1974), "Characteristics of Slant Path Rain Attenuation at 35 GHz Obtained by Solar Radiation and Atmospheric Emission Observations," Journal de Recherches Atmospherique, Vol. 8, p. 339.

Goldhirsh, J. (1975), "Prediction Methods for Rain Attenuation Statistics at Variable Path Angles and Carrier Frequencies Between 13 and 100 GHz," IEEE Trans. Ant. Prop., Vol. AP-23, p. 786.

Goldhirsh, J. (1976), "Path Attenuation Statistics Influenced by Orientation of Rain Cells (1976)," IEEE Trans. Ant. Prop., Vol. AP-24, p. 792.

Goldhirsh, J. and F. Robison (1975), "Attenuation and Space Diversity Statistics Calculated from Radar Reflectivity Data of Rain," IEEE Trans. Ant. Prop., Vol. AP-23, p. 221.

Gray, D.A. (1973), "Earth-Space Path Diversity: Dependence on Base Line Orientation," 1973 G-AP/URSI Meeting, Boulder, Colorado.

Gumbel, E.J. (1958), Statistics of Extremes, Columbia Univ. Press, New York, New York.

Hall, J.E. and J.E. Allnutt (1975), "Results of Site Diversity Tests Applicable to 12 GHZ Satellite Communications," IEE Conference Publication No. 126, Satellite Communication Systems Technology, London.

Harrold, T.W. and P.M. Austin (1974), "The Structure of Precipitation Systems - A Review," Journal de Recherches Atmospherique, Vol. 8, p. 41.

Hendry, A., G.C. McCormick and B.L. Barge (1976), "Ku-Band and S-Band Observations of the Differential Propagation Constant in Snow," IEEE Trans. Ant. Prop., Vol. AP-24, No. 4, pp. 521-525.

Hodge, D.B. (1974a), "Path Diversity for Reception of Satellite Signals," Journal de Recherches Atmospherique, Vol. 9, p. 443.

Hodge, D.B. (1974b), "A 15.3 GHz Satellite-to-Ground Path Diversity Experiment Utilizing the ATS-5 Satellite," Radio Science, Vol. 9, p. 1.

Hodge, D.B. (1976a), "An Empirical Relationship for Path Diversity Gain," IEEE Trans. Ant. Prop., Vol. AP-24, p. 250.

Hodge, D.B. (1977), "Frequency Scaling of Rain Attenuation," IEEE Trans. Ant. Prop., Vol. AP-25, pp. 446-447.

Hodge, D.B. (1978), "Path Diversity for Earth-Space Communication Links," Radio Science, Vol. 13, p. 481.

Hodge, D.B., D.M. Theobold, and R.C. Taylor (1976b), "ATS-6 Millimeter Wavelength Propagation Experiment," Ohio State University, ElectroScience Laboratory, Rept. 3863-6.

Hogg, D.C. (1968), "Millimeter Wave Communication through the Atmosphere," Science, Vol. 159, p. 39.

Hogg, D.C. and T.S. Chu (1975), "The Role of Rain in Satellite Communications," Proc. IEEE, Vol. 63, No. 9, pp. 1307-1331.

Hopfield, H.S. (1971), "Tropospheric Effect on Electromagnetically Measured Range: Prediction from Surface Weather Data," Radio Science, Vol. 6, pp. 357-367.

Hyde, G. (1976), "Data Analysis Report - ATS-F Comsat Millimeter Wave Propagation Experiment," Comsat Laboratories, Clarksburg, Maryland.

Ippolito, L. J. (1979), private communication.

Ishimaru, A. (1978), Wave Propagation and Scattering in Random Media, Single Scattering and Transport Theory, Vol. 1, Academic Press, New York, N.Y.

Johannsen, K.G. and A. Koury (1974), "The Moon as a Source for G/T Measurements," IEEE Trans. Aerosp. Elect. Syst., Vol. AES-10, No. 5, pp. 718-727.

Klobuchar, J. A. (1973), "Total Electron Content Studies of the Ionosphere," Air Force Cambridge Research Laboratories Technical Report AFCRL-TR-73-0098, Bedford, Mass.

Koester, K.L. and L.H. Kosowsky (1970), "Attenuation of Millimeter Waves in Fog," Fourteenth Radar Meteorology Conference, November 17-20, Tuscon, Arizona.

Koester, K.L. and L.H. Kosowsky (1978), "Millimeter Wave Propagation in Ocean Fogs and Mists," Proceedings IEEE Ant. Prop. Symposium.

LeFrancois, G.L., Martin and M. Rooryck (1973), "Influence de la Propagation Sur la Valeur de Decouplage de Deux Polarisations Orthogonales," Ann. des Telecomm., Vol. 28, July-August, in French.

Liebe, H.J. (1975), "Molecular Transfer Characteristics of Air Between 40 and 140 GHz," IEEE Trans. Microwave Theory and Techniques, MTT-23, No. 4.

Lo, Lai-Inn, B.M. Fannin and A.W. Straiton (1975), "Attenuation of 8.6 and 3.2 mm Radio Waves by Clouds," IEEE Trans. Ant. Prop., Vol. AP-23, No. 6.

Lord, L.H. and R. Oliver (1946), "An Experimental Investigation of the Reflection and Absorption of Radiation of 9-cm Wavelength," Proc. Phys. Soc., Vol. 58, pp. 265-280.

Marini, J.W. (1972a), "Correction of Satellite Tracking Data for an Arbitrary Tropospheric Profile," Radio Science, Vol. 7, pp. 223-231.

Marini, J.W. (1972b), "Tropospheric Range-Rate Tracking Data Correction," NASA/Goddard Space Flight Center, Doc. X-551-72-277.

Mason, B.J. (1971), The Physics of Clouds, Clarendon Press, Oxford, pp.119-121.

McCormick, K.S. and L.A. Maynard (1972), "Measurements of S. H. F. Tropospheric Fading Along Earth Paths at Low Elevation Angles, "Electronics Letters, Vol. 8, No. 10.

McEwan, N.J., P.A. Watson, A.W. Dissanayake, D.P. Haworth and V.T. Vakili (1977), "Crosspolarization from High Altitude Hydrometeors on a 20 GHz Satellite Radio Path," Electronics Letters, Vol. 13, pp. 13-14.

Millman, G.H. (1958), "Atmospheric Effects on VHF and UHF Propagation," Proc. IRE, Vol. 46, pp. 1492-1501.

Muchmore, R.B. and A.D. Wheelon (1955), "Line-of-Sight Propagation Phenomena - I. Ray Treatment," Proc. IRE. Vol. 43, pp. 1437-1449.

Nowland, W.L., R.L. Olsen and I.P. Shkarofsky (1977a), "Theoretical Relationship Between Rain Depolarization and Attenuation," Electronics Letters, Vol. 13, No. 22, pp. 676-677.

Nowland, W.L., I.I. Strickland, J. Schlesak and R.L. Olsen (1977b), "Measurements of Depolarization and Attenuation at 11.7 GHz by Using the Communications Technology Satellite," Electronics Letters, Vol. 13, No. 24, pp. 750-751.

Nusple, P.P., N.G. Davies and R.L. Olsen (1975), "Ranging and Synchronization Accuracies in a Regional TDMA Experiment," Proc. Third Intl. Digital Satellite Comm. Conf., Kyoto, Japan.

Olsen, R.L., D.V. Rogers and D.B. Hodge (1978), "The aR^b Relation in the Calculation of Rain Attenuation," IEEE Trans. Ant. Prop., AP-26, pp. 318-329.

Perlman, S., W.J. Russel, Jr., and F.H. Dickson (1960), "Concerning Optimum Frequencies for Space Vehicle Communications," IRE Trans. Mil. Elect., Vol. MIL-4, Nos. 2-3, pp. 184-192.

Pruppacher, H.R. and R.L. Pitter (1971), "A Semi-empirical Determination of the Shape of Cloud and Rain Drops," J. Atmos. Science, Vol. 28, pp. 86-94.

Radio Regulations, International Telecommunication Union, Geneva.

Rogers, R.R. 1976, A Short Course in Cloud Physics, Chapter 12, Pergamon Press, London.

Segal, B. and R.E. Barrington (1977), Tropospheric Refractivity Atlas for Canada, Dept. of Communications, CRC Report No. 1315-E, Ottawa.

Shutie, P.F., J.E. Allnutt and E.C. MacKenzie (1977), "Depolarization Results at 30 GHz Using Transmissions from the ATS-6 Satellite," Proc. URSI, Symposium on Propagation in Non-Ionized Media, La Baule, France, April 28 - May 6, pp. 367-369.

Shutie, P.F., E.C. MacKenzie and J.E. Allnutt (1978), "Relative Phase Measurement at 30 GHz Between Copolar and Induced Crosspolar Signals Produced by Ice Particles on a Satellite-to-Ground Link,"Electronics Letters, Vol. 14, No. 4, pp. 105-107.

Strickland, J.I. (1974), "Radar Measurements of Site Diversity Improvement During Precipitation," Journal de Recherches Atmospherique, Vol. 8, p. 451.

Strickland, J.I. (1977), "Radiometric Measurements of Site Diversity Improvement at Two Canadian Locations," Proceedings, URSI Commission F Symposium, 28 April - 6 May, LaBaule, France.

Strickland, J.I., R.I. Olsen and H.L. Werstiuk (1977), "Measurements of Low Angle Fading in the Canadian Arctic," Ann. Telecomm., Vol. 32, Nos. 11-12, pp. 530-535.

Stutzman, W.L. (1977), "Mathematical Formulations and Definitions for Dual Polarized Reception of a Wave Passing Through a Depolarizing Medium (A Polarization Primer)," Virginia Polytechnic & State Univ., prepared under NASA Contract NAS5-22577.

Tatarski, V.I. (1961), Wave Propagation in a Turbulent Medium, McGraw-Hill Book Co., New York, N.Y.

Theobold, D.M. (1978), "Tropospheric Refraction," report prepared for ORI, Inc. under NASA Contract NAS5-23438.

Theobold, M.D. and D.B. Hodge (1978), "Gain Degradation and Amplitude Scintillation Due to Tropospheric Turbulence," The Ohio State University ElectroScience Lab., Tech. Rpt. 784229-6, Revision 1.

Thompson, M.C., Jr., L.E. Woods, H.B. Janes and D. Smith (1975), "Phase and Amplitude Scintillations in the 10 to 40 GHz Band," "IEEE Trans. Ant. Prop., Vol. AP-23, pp. 792-797.

Turner, D.J.W. (1973), "Measurements of Cross-Polar Discrimination at 22 and 37 GHz," IEE Conf. Proc. No. 98.

U.S. Dept. of Commerce (1947), Tech. Paper No. 2, "Maximum Recorded United States Point Rainfall," Washington, D.C.

U.S. Dept. of Commerce (1955), Tech. Paper No. 25, "Rainfall Intensity-Duration-Frequency Curves," Washington, D.C.

Vogel, W.J. (1978), CTS Attenuation and Cross-Polarization Measurements at 11.7 GHz, Final Report, Elect. Eng. Res. Lab., Univ. Texas at Austin, prepared under NASA Contract NAS5-22576.

Vogel, W.J., A.W. Straiton, B.M. Fannin and N.K. Wagner (1976), "Attenuation Diversity Measurements at 20 and 30 GHz," Radio Science, Vol. 11, p. 167.

Vogel, W.J., A.W. Straiton and B.M. Fannin (1977), "ATS-6 Ascending: Near Horizon Measurements Over Water at 30 GHz," Radio Science, Vol. 12, September-October, pp. 757-765.

Wait, D.F., W.C. Daywitt, M. Kanda and C.K.S. Miller (1974), A Study of the Measurement of G/T Using Casseopeia A, National Bureau of Standards, Rept. No. NBSIR 74-382.

Watson, P.A. and M. Arbabi (1973), "Cross-polarization Isolation and Discrimination," Electronics Letters, Vol. 9, No. 22, pp. 516-517.

Watson, P.A., F. Goodall and M. Arbabi (1973), "Linear Cross-Polarization and Attenuation Measurements at 11 and 36 GHz," IEE Conf. Proc. No. 98.

Webster, W.J., Jr., T.T. Wilheit, T.C. Chang, P. Gloersen and T.J. Schmugge (1975), "A Radio Picture of the Earth," Sky and Telescope, Vol. 49, No. 1, pp. 14-16.

Weickmann, H.K. and H.J. Kaumpe (1953), "Physical Properties of Cumulus Clouds," Journal of Meteorology, Vol. 10.

Westinghouse Electric Corporation (1975), "ATS-6 Millimeter Wave Propagation Experiment - Final Data Analysis Report," Baltimore, Md., prepared under NASA/GSFC Contract NAS5-20904.

Wilson, R.W. (1970), "A Three-Radiometer Path Diversity Experiment," Bell System Technical Journal, Vol. 49, p. 1239.

Wilson, R.W. and W.L. Mammel (1973), "Results from a Three Radiometer Path Diversity Experiment," Proceedings of Conference on Propagation of Radio Waves at Frequencies above 10 GHz, London, p. 23.

Wulfsberg, K.H. (1964), "Apparent Sky Temperatures at Millimeter-Wave-Frequencies," Phys. Science Res. Paper No. 38, Air Force Cambridge Res. Lab., No. 64-590.

Wulfsburg, K.N. (1973), "Path Diversity for mm-wave Earth-to-Satellite Links, Radio Science, Vol. 8, p. 1.

Yamada, M. and H. Yokoi (1974), "Measurements of Earth-Space Propagation Characteristics at 15.5 and 31.6 GHz Using Celestial Radio Sources," Elect. and Comm. in Japan, Vol. 57-B, p. 2.

Yokoi, H., M. Yamada and T. Ogawa (1970), "Atmospheric Attenuation and Scintillation of Microwaves from Outer Space," Astronomical Society, Japan, Vol. 22, pp. 511-524.

CHAPTER VII

APPLICATION OF PROPAGATION PREDICTIONS TO EARTH/SPACE TELECOMMUNICATIONS SYSTEM DESIGN

7.1 INTRODUCTION

A function of the satellite communication system designer, or system engineer, is to interface between the source of system requirements (i.e., the user) and the sources of performance data. Stated in terms of the present problem, the system engineer uses propagation and other technical data to achieve a system design that will meet the requirements specified by the user. These requirements are specified in terms of a gross quantitative need (e.g., number of channels), a quantitative expression of performance (e.g., percent of time available), and, sometimes, more qualitative expressions (e.g., "highly reliable"). Even though both the propagation data and the requirements are often expressed in terms of cumulative probability distributions, it is not always straightforward to relate one distribution to the other. The correspondence between a given propagation phenomenon and system performance may be complex. The purpose of this chapter is to relate propagation data to system performance parameters. It should allow the system engineer to perform the analyses telling how well requirements are met by a given system design, thereupon enabling the system engineer to modify that design if necessary. First (in Section 7.2), the various ways of specifying performance criteria for different kinds of systems are discussed, then (in Section 7.3) a general procedure for system design is presented and demonstrated.

There are engineering disciplines for which true synthesis procedures exist, but the design of complex systems with interactive elements is usually not a true synthesis. Instead, iterative analyses are performed, starting with a preliminary design choice, until the refined design can be shown by analysis to meet the requirements. The application of this philosophy of system design or synthesis to satellite communications is summarized here and detailed in Section 7.3.

The system design procedure is based on criteria that take the form of discrete cumulative probability distribution functions of performance. The steps necessary to go from this set of performance requirements and propagation statistics to a system design are (see Figure 7.1-2):

INITIAL PHASE

1) Establish system performance requirements (discrete distribution of baseband/digital performance)

2) Apply modulation equations to convert system performance requirements to discrete distribution of the received composite CNR

3) Prepare initial design with parameters sized according to free space propagation conditions (apply power budget equations).

DESIGN SYNTHESIS AND TRADE OFF PHASE

4) Employ

   a) Composite CNR distribution from step 2)
   b) System architecture
   c) Multiple Access equations
   d) Availability sub-allocation philosophy

   to develop distribution functions for CNR on each path.

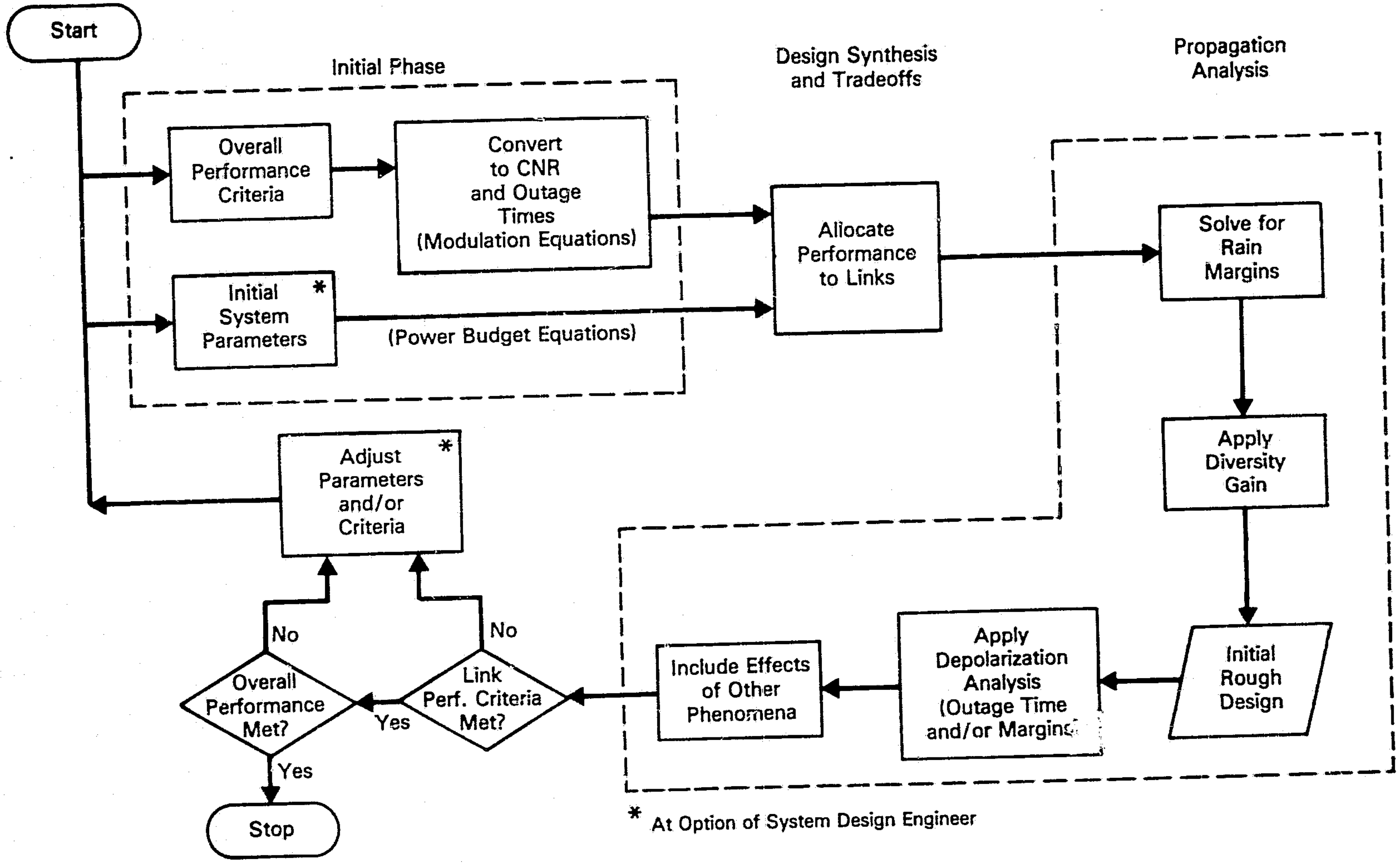

Figure 7.1-1 System Design Process

PROPAGATION ANALYSIS AND ITERATION PHASE

5) Compute rain margins, as reduced by diversity gain, for each path.

6) Adjust system parameters according to margins given by 5). This gives a preliminary design at the feasibility concept level.

7) Apply depolarization analysis to adjust margins and/or increase the outage time values (% of time for the worst-performance level of the distributions).

8) Consider other propagation effects such as cloud and fog attenuation, signal fluctuations, and antenna gain degradations and add margin to design as necessary.

9) Adjust system parameters to include all additive margins. Analyze system performance, first at the path level, then on the end-to-end performance level.

10) If performance meets requirements closely, stop. Otherwise, adjust design and repeat analysis. If design cannot be made to meet requirements, consider changing requirements.

Performance criteria typically deal with baseband quality, or digital error rates, whereas the power budgets relate physical system parameters to CNR (or equivalents such as S/N, E_b/N_o, C/kT, etc.). Therefore, the baseband or digital performance criteria must be functionally related to CNR by means of modulation performance equations.

Gross design is performed by means of elementary power budget analysis and free-space (or clear air) propagation characteristics. Basic choices are made at this point, such as selection of modulation and multiple access techniques. It is assumed that the reader is familiar with these techniques and power budget analysis (Northrop-1966). This analysis establishes a relationship between basic system parameters and the signal- or carrier-to-noise ratio (CNR) on a given transmission path.

The system performance requirements, which apply to end-to-end performance, are suballocated to various system components. Most important, the relationship of the end-to-end communication performance to that of each of the links must be determined. For example, the actual received CNR is a composite which may include both uplink and downlink noise contributions. The end-to-end availability involves availabilities of each path.

Since rain induced attenuation is the most severe propagation effect for the frequencies of interest, the next step in the procedure is to calculate a rain margin. If the system uses site diversity, some of this rain margin may be offset by "diversity gain." The remaining margin is then applied to the initial system parameters. Typically, the margin is applied as an increase in power; but it is also possible to increase antenna gains or modify the modulation parameters. At this point, a rough design has been achieved. This level of detail and accuracy may be sufficient if the objective is only to determine system feasibility. For more accurate results, the effects of other propagation phenomena must be considered. Except for depolarization, these effects are generally additive in terms of margin. Loss in crosspolarization isolation (usually termed "depolarization") can be accommodated as an additive term whenever the interference component is small relative to thermal noise and other interference sources. Thus, small degradations such as those due to depolarization from ice are treated as part of the system margin computation*. The more severe degradations in cross polarization such as those caused by rain cannot be counteracted by margin increases. These events will usually be severe enough to cause an outage. Therefore, in systems employing cross polarization isolation, the depolarization phenomenon may reduce or limit the system availability.

Having thus adjusted the system parameters and the performance analyses, the system design engineer can determine whether performance

---

* It is not necessary to add margins on a worst case basis. Where large margins have already been included for rain, the ice depolarization event can be assumed to "share" the same margin.

criteria are met, first for the individual link, and then for the overall system. If so, the design process is essentially completed*. If not, the system parameters and/or the performance criteria are modified, and the analysis procedure is repeated. To some, the idea that the criteria are subject to change is disturbing. Within physical (and economic) constraints, it is preferable to modify only the technical system parameters. But there may be cases where the initial performance goals are unrealistic. For example, it simply may not be worth the expense of a large increase in EIRP in order to get a circuit availability of 99.99% for small earth terminals at 44 GHz.

Section 7.2 addresses system performance criteria, while paragraphs 7.3.1 through 7.3.3 are introductions to general system design procedures. The experienced communication system engineer will probably be familiar with the material covered in these paragraphs, and may therefore skip them without loss of continuity, and concentrate on paragraphs 7.3.4 through 7.3.6, which are addressed to the main issue at hand, namely the specific application of propagation data.

7.2 COMMUNICATION SYSTEM PERFORMANCE CRITERIA

7.2.1 Introduction

Criteria for communication system performance represent attempts to quantify the "reliability or "quality" of the service. Two methods, applying different probabilistic notions, are generally used. The first method is to regard some indicator of communication quality (e.g., CNR) as a random variable and specify values of its inverse cumulative distribution function, or the probability that a given value is exceeded. With the second method of specifying performance criterion, the quality indicator is taken as a random process, and some statistic of this time-varying process is used. A typical statistic in this case might be the median, mean, or "three-sigma" duration of

---

* A fine-tuning iteration may be desirable if the design exceeds requirements.

the periods during which the value stays below a given threshold. If a period during which the CNR is below some threshold is regarded as an "outage," then the criterion would specify outage duration statistics.

The first type of performance criterion, which will be termed availability criterion, is generally specified as the percentage of time that a threshold value is exceeded (or not exceeded), rather than a probability. This is natural, since what we can measure is percentage of time, and not probability. (Ergodicity allows these to be assumed equivalent). Availability criteria are in wide use, and the bulk of long-term performance data analysis has been done from an availability standpoint. However, such criteria and data do not give any information about the time-variation of performance. In many situations, it is desirable to know something about how fast the performance may change. Some temporal information is given by a slightly modified availability criterion, in which a time period is specified. For example, the criterion could state that a given level of noise will not be exceeded for more than a certain percentage of any month. However, the connection between such a criterion and any quantitative temporal description is obscure.

The second type of performance criterion, which expressly describes the temporal behavior, such as mean outage duration, will be termed outage statistics. Beside the outage duration, such statistics might include the distribution function for the time until the next outage, given that an outage is just over. Or they might probabilistically describe diurnal or seasonal performance variations. In the limit, such statistics would give the autocorrelation function or the spectral density of the process. As yet, the available data does not cover a long enough time span to be statistically reliable. We will therefore confine our attention primarily to performance criteria that specify availability, rather than outage statistics.

There are several sources of performance criteria. Among the more generally accepted standards are those promulgated by the International Radio Consultative Committee (CCIR). Telecommunication systems for U.S. commercial use conform to standards similar but not identical to the CCIR's. These criteria are expressed in terms of a baseband noise level (analog) or an error rate degradation (digital) not to be exceeded more than some small percentage of the time in any month (typically, .001 to 0.3%). The Defense Communications Agency has more recently advanced (Kirk and Osterholz-1976 and Parker-1977) criteria based on the probability of occurrence of outage on a five minute call (voice channels), or the error free block probability for a 1000 bit block (data channels).

7.2.2 Digital Transmission Performance

7.2.2.1 Short Term Bit Error Rate. The primary measure of circuit or transmission quality for digital systems is the bit error rate (BER). Semantically, we use "bit" error rate because the overwhelming majority of digital communications systems transfer binary data streams.* Bit error rate usually applies over a moderately short term, and normally does not incorporate "errors" or outages of duration longer than a few tens of bits.

For most digital systems, the bit error probability can be expressed as a function of the energy-per-bit to noise power spectral density ratio (E_b/N_o). These relationships are available for the theoretical performance of commonly used modulation and coding systems from any good communication theroy reference (e.g., Schwartz, et al-1966 and Spilker-1977). The theoretical BEP vs. E_b/N_o relations usually assume white, Gaussian noise. In the presence of non-white or non-Gaussian noise, or interference, these relations are not accurate. It is now becoming common to express the performance of actual systems in terms of the E_b/N_o rather than CNR. E_b/N_o is numerically equal to the ratio of signal power to noise power within a (noise) bandwidth equal in hertz to the digital bit rate in bits per second. (Note that bit rate is not in general the same as symbol rate.) For example, the (theoretically ideal) performance of binary PSK modulation requires an E_b/N_o of 9.6 dB for a BER of 10^{-5}.

---

* We should also distinguish between bit error rate, which defines the actual performance, and must be measured by averaging over a sequence of bits communicated, and the bit error probability (BEP), which is a theoretical concept that can apply even to a single bit.

In the case of digital systems used to accommodate fundamentally analog requirements (e.g., PCM voice channels) there exists a threshold error rate at which circuit quality is considered unacceptable. This threshold value then determines the point at which an "outage" exists. Because error rate is a sensitive function of E_b/N_o, circuit quality degrades quite drastically when E_b/N_o falls below the value corresponding to the threshold error rate. Degradation is not "graceful."

7.2.2.2 Data System Performance. Data communications systems rarely transmit uniform, homogeneous, continuous bit streams. Rather, the data is often formatted in blocks or packets. In many cases, then, the performance requirement is specified in terms of the probability of an error free block, which might typically contain 1000 or more bits. If the only type of transmission imperfection is the randomly occuring bit error process, then the block error performance can be calculated from the bit error rate: Probability of error free block of n bits = $P(\geq 1,n) = (1 - BER)^n$. However, the block error performance may be influenced by the probability of longer outages, losses of synchronization, and the like, which are not usually included in the BER.

In systems used to transfer well-defined messages, other performance criteria may be required. In the most general case where a block is composed of many messages, the system performance requirements could include a message performance criterion, a block transmission performance criterion and a bit error rate. Note that consistency among the various criteria is mandatory. For example, a block error performance of 99% (i.e., 99 out of 100 blocks are error free) for 1000-bit blocks could not be achieved when the bit error rate is 10^{-4}.

In data communications systems where real time delivery is not critical, the concept of throughput is often used. It is implicit that the system involves a return channel path over which acknowledgements and/or requests for retransmission are made. The throughput is defined (Brayer - 1978) as the ratio of the number of information bits transmitted (K) to the total number of bits (including overhead and re-transmissions), n, before the block is accepted. The throughput is approximately

$$K\left[1-P(\geq 1,n)\right]/n$$

This approximation for throughput as a function of block error rate applies only when the return channel is error free. Brayer (1978) makes a case for using message delivery delay as the most important criterion, rather than throughput itself. However, they are related closely.

In summary it can be seen that throughput and block error rate are directly related. Bit error rate contributes a major, but not always the only, portion of the block error rate. In communication system design, the (short term) bit error rate or bit error probability is taken as a parameter of analysis and preliminary design. Final performance estimates must, however, take into account both the nominal BER performance, and some consideration of outages. The qualitative relationships among the various criteria are shown in Figure 7.2-1. Notice that the fundamental, or user-requirement- oriented, criteria are on the right side of the diagram, yet the correct logical path for analysis is from left to right. Thus, analysis is employed to demonstrate that a set of system and environmental conditions will meet the performance requirements.

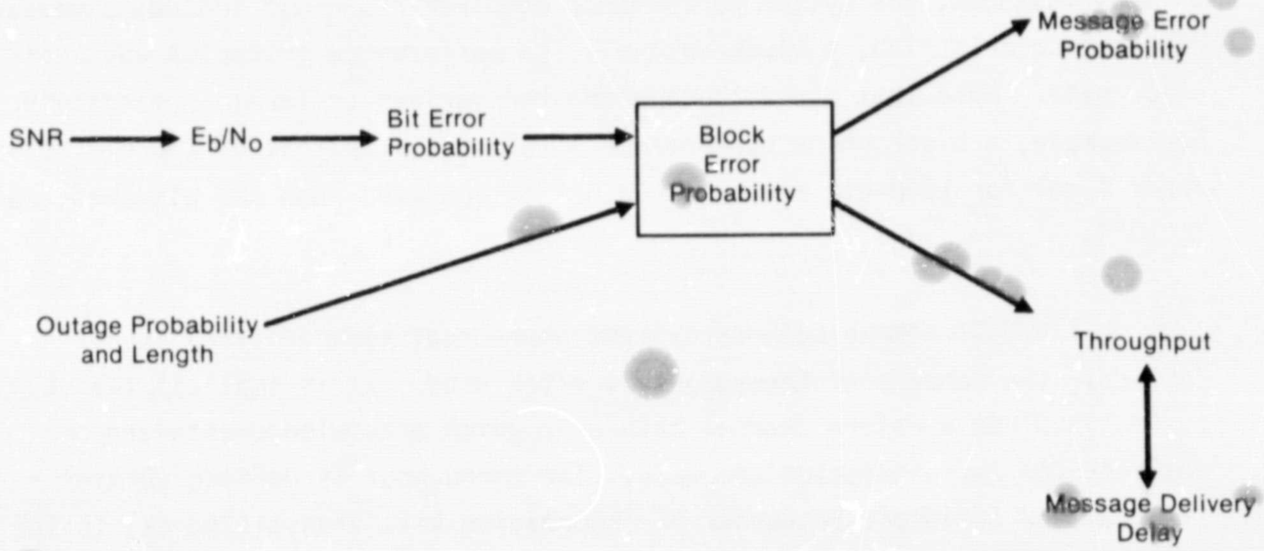

Figure 7.2-1 Data System Performance

7.2.3 Analog Transmission Performance

The establishment of performance criteria for analog systems is a complex issue. Transmission system criteria are usually defined on an end-to-end, reference circuit basis. If the satellite system is only a portion of this end-to-end path, a sub-allocation must be made to the satellite segment. Also, when the system is used for relay of multichannel voice trunks, the conversion from baseband (voice channel) performance criteria to the radio frequency criteria (i.e., C/N) involves assumptions about channel loading and modulation parameters. For example, for an FDM-FM system, the noise in picowatts, psophometrically weighted (pWOp), in a voice channel is (GTE-1972)

$$pWOp = 10 \exp \left\{ 1/10 \left[- C - 48.1 + F - 20 \log (\Delta f / f_{ch}) \right] \right\}$$

where

- C = RF input power in dBm
- F = receiver noise figure, dB
- Δf = peak deviation of the channel for a 1 kHz test tone signal
- f_{ch} = center frequency of the channel in the baseband

Similar equations apply to single channel FM voice and FM video, and to other modulation structures.

pWOp is one of many noise measures in use. Specifically,

dBrnc (dB above reference noise, C-message weighting. Reference noise is equivalent in power to a 1,000 hertz tone at -90 dBm.)

dBa (dB above reference noise-adjusted, F1A weighting. Reference noise adjusted is equivalent in power to a 1,000 hertz tone at -85 dBm.)

pWp (picowatts of noise power, psophometrically weighted.)

dBmp (psophometrically weighted noise power in dB, with respect to a power level of 0 dBm.)

These units represent absolute values of noise. By appending a "0" to each (e.g., pW0p), the same units serve as measure of noise relative to 0 level signal (i.e., 0 dBm). Then the following approximate conversions apply (GTE-1972):

$$\text{dBrncO} = 10 \log_{10}\text{pW0p} + 0.8 = \text{dBaO} + 6.8 = \text{dBm0p} + 90.8 = 88.3 - S/N$$

In general, most standards involve long term nominal objectives and short term or worst case threshold values. Below this threshold, an "outage" exists. FM links are often engineered so that the receiver FM threshold value of C/N is at or within a few dB of that value which gives the absolutely minimum acceptable performance. That is, the receiver RF performance threshold and the baseband (acceptable) performance threshold are matched.

As an example of a long-term performance objective, the latest CCIR position (reflected in Recommendation 353-3, CCIR-1978) is that 10,000 pW0p one-minute mean noise power should not be exceeded more than 20% of any month. The old U.S. criterion for long intertoll trunks required 20,000 pW0p or less nominal (in the absence of a fade). In the case of television signals, various criteria require a weighted baseband S/N of from 50 to 59 dB to exist under nominal conditions.

Noise performance requirements for small percentages can be thought of as "outage" conditions. The CCIR recommendation is that 1,000,000 pW0 (unweighted) measured with a 5 ms. integration time, exist not more than 0.01% of any year. An intermediate requirement is also established: that 50,000 pW0p one-minute mean power not be exceeded for more than 0.3% of any month. In the U.S., a criterion of 316,000 pW0p for .02% of the time is often employed. DCA standards similarly require that 316,000 pW0p not be exceeded for more than 2 minutes in any month nor for one minute in any hour. Video threshold requirements are typically in the 33 to 37 dB weighted signal to noise ratio range.

Criteria are under constant revision. Indeed, there are arguments suggesting that new applications require specialized criteria. Current criteria, developed for terrestrial systems or for satellite communications systems below 10 GHz, may not be applicable for millimeter wave systems where the statistics differ appreciably.

Note that outage criteria, such as the one DCA has promulgated (probability of outage on a five minute call), are very different from nominal or long-term availability criteria. Because propagation outages in the frequency range of interest typically have durations on the order of magnitude of minutes, it is not straightforward to relate availability statistics to outage probability statistics. Some approximations may be made from rain statistical data and limited data on fade depth vs. duration, but more theoretical and experimental work appears to be necessary before such outage criteria can be reliably applied in design. In this Handbook, therefore, we have found it necessary to emphasize availability criteria. Where duration data is available, it may be employed as a subsidiary, or second order, check on whether system requirements are met.

7.2.4 Summary of Nominal Criteria and Their Application

The nominal performance criteria for digital and analog systems are substantially different. However, these can be related by analysis to corresponding values of CNR, which communication engineers prefer to work with. There is, usually, a long term or nominal performance standard, as well as some definition of short term event behavior (outage criterion). With data systems, the long and short term phenomena may be statistically combined, so that it is possible to define combined performance criteria. These similarities, differences, and relationships are shown in Table 7.2-1.

7.2.5 Additional Performance Criteria

In some applications, more specific control of the transmission quality is necessary and criteria such as those cited above are inadequate.

Table 7.2-1

Performance Criteria and Relationships

System	Fundamental Quality Parameter	Nominal (Long Term) Performance	Short-Term (Outage) Criterion	Combined Criterion
Analog	Baseband noise or signal to noise	Mean or Median CNR	CNR equalled or exceeded except for p%	—
Digitized Analog	Baseband quality ⟷	Bit Error Rate ⟷ CNR	Same as above	—
Data	Error free block probability	Bit Error Rate ⟷ CNR	Outage probability	Error free block probability Throughput Delivery Delay

In these situations a number of linear and nonlinear distortion parameters may be specified. Most of these relate to the system (hardware) components. It appears that the only significant distortion parameter introduced by the propagation path is phase fluctuation (scintillation)*. Small amounts can be accommodated in the power budget analysis as equivalent S/N or E_b/N_o degradations. (By "small amounts," we mean values which lead to no more than, say, 1 dB in equivalent S/N degradation.) On the other hand, large phase scintillations that occur infrequently will add to the outage time calculation, providing:

1) these events are not concurrent with the predominant cause of outage, namely amplitude fades (attenuation), and

2) the rate of phase variation is high enough that it will not be tracked by a digital system, or be filtered out in an analog system.

---

* A possible exception is dispersion at frequencies near the absorption bands, but these bands will usually be avoided.

7.3 DESIGN PROCEDURE

7.3.1 Introduction

The procedure presented in this Section is a general one, applicable to satellite communication systems of conventional design and application. Special purpose systems, unusual variants, or unusual system architectures will require modifications to the procedure. For example, those systems which employ adaptive power control or adaptive antenna beam control fall into the "unusual" category.

The procedure is based on time percentage availability or outage as the primary and initial design criterion. Emphasis on this approach is necessitated by the fact that the largest amount of reliable propagation data is presented in time percentage terms. Where other criteria are important, different procedures may be necessary. But even where other criteria are employed, it is expedient to perform initial gross sizing calculations according to time percentage criteria.

As previously noted, the system design process is not a true synthesis. It consists rather of iterative analyses. The designer begins with some rough "guesstimates" of parameters such as earth terminal antenna size, satellite RF power, along with a set of system requirements (coverage area or locations, capacity, connectivity, and service criteria). By employing analytic (not synthetic) procedures, the designer determines whether the initial parameters and the requirements/criteria are consistent. If not, additional iterations are made, with adjustments either to the parameters or to the requirements. This last point is not trivial: if there is a large disparity between calculated system performance and the requirements, it may be necessary to consult with the source of the requirements and agree to a change (e.g., lower capacity or availability). The final system design parameters should always be verified in as many variables as possible according to available data. Thus, although the initial design may have been performed using an availability criterion, it may be of interest and importance to predict outage duration statistics, if the necessary data are available.

7.3.2 Path Performance Versus Overall Channel Performance: Availability Allocation

The typical satellite communication application involves two or four distinct links. For example, a telephone trunk system between Los Angeles (LA) and New York (NY) will involve these links:

LA to Satellite
Satellite to NY
NY to Satellite
Satellite to LA

If the performance requirements for this example specify the availability of a duplex telephone circuit between NY and LA, the system designer may be faced with a difficult problem. In general, finding the simplex, duplex, or (worst of all) system-wide availability with multiple earth terminal locations is a problem of considerable statistical complexity. Significantly, this problem is unique to satellite systems, and is particularly aggravated at the higher frequencies. Terrestrial line-of-sight and scatter microwave communications systems represent a simpler problem, since they do not span large distances in a single hop. Also, symmetry applies in these systems. Statistical assumptions made and procedures developed for terrestrial systems, and for satellite systems below 10 GHz, may not be adequate for the applications to which this Handbook is directed.

Some sort of availability allocation is necessary, since most of the propagation data and procedures for applying them are oriented towards single path availability. The composite availability calculations involved are similar to multiple and redundant part reliability calculations. Each application will involve its own special considerations in the allocation process. Often, a worst case philosophy is applied in an attempt to simplify the problem. The following factors are relevant:

- One end (terminal location) often has considerably worse rain statistics than the other.

- Satellite systems are limited in downlink power; uplink power margin at the earth terminal is more readily obtainable.*

- Uplink and downlink effects are quantitatively similar <u>except</u> for widely separated uplink/downlink frequencies (e.g., 30/20, 43/20), where attenuation factors in particular can differ substantially.

- The uplink and downlink connecting to a given earth terminal have highly correlated propagation outage statistics.

- The propagation effects on paths between the satellite and two different earth terminals are uncorrelated.

Because of the variety of system concepts and frequency bands possible, general rules for allocation of availability cannot be given. The following may be of help in many cases of interest:

- In a one-way (simplex) system, availability can be suballocated or split between the up and downlink with considerable freedom.

  Frequently, however, the downlink is the dominant (weaker) link. In other words, the working assumption is that the uplink non-availability is an order of magnitude smaller than the downlink's.

- For a two-way (duplex) system, one of the following simplifications may be applied:

  - One end has much worse rain statistics than the other. Then, this duplex circuit can be treated as two simplex circuits with the majority of the outages on that end. On each of these simplex circuits, either the uplink <u>or</u> the downlink, whichever is worse, dominates the availability.

---

*A very important exception involves mobile or portable terminals.

Assume initially that uplink margin is liberally available. The duplex link availability is then determined by the composite availability of both downlinks (or, the circuit outage time is the sum of the outages of each of the two downlinks).

Because the designer is forced by the procedure to iterate the design, errors introduced by simplifying assumptions made during the availability suballocation phase are corrected when performance verification analyses are made. For example, suppose the initial downlink design parameters were selected under the assumption that ample uplink margin exists, and that the uplink parameters were chosen to be as good as possible within economic constraints. In the final performance computation, the slightly less than perfect availability of the uplink is factored into the overall availability. Any shortfall relative to requirements can then be met by a small adjustment to the downlink parameters, in the next iteration of the design.

7.3.3 Summary of Procedures for Application of Propagation Data

The system design procedure presented here is based on criteria that take the form of discrete cumulative probability distribution functions of performance. In practice, three, two, or just one point on this distribution are given, for example, 99.9% probability that the baseband signal to noise ratio exceeds 20 dB. The worst (lowest probability) point of this set is usually considered to be the outage point or the non-availability threshold. In addition, a statement might be made about the time characteristics of the outage events, for example, the maximum acceptable value for the average duration. These criteria are usually for the baseband (e.g., voice channel) noise performance, or for the digital channel performance (e.g., error rate). The steps necessary to go from this set of requirements and propagation statistics to a system design are (see Figure 7.3-1):

INITIAL PHASE

1) Establish system performance requirements (discrete distribution of baseband/digital performance)

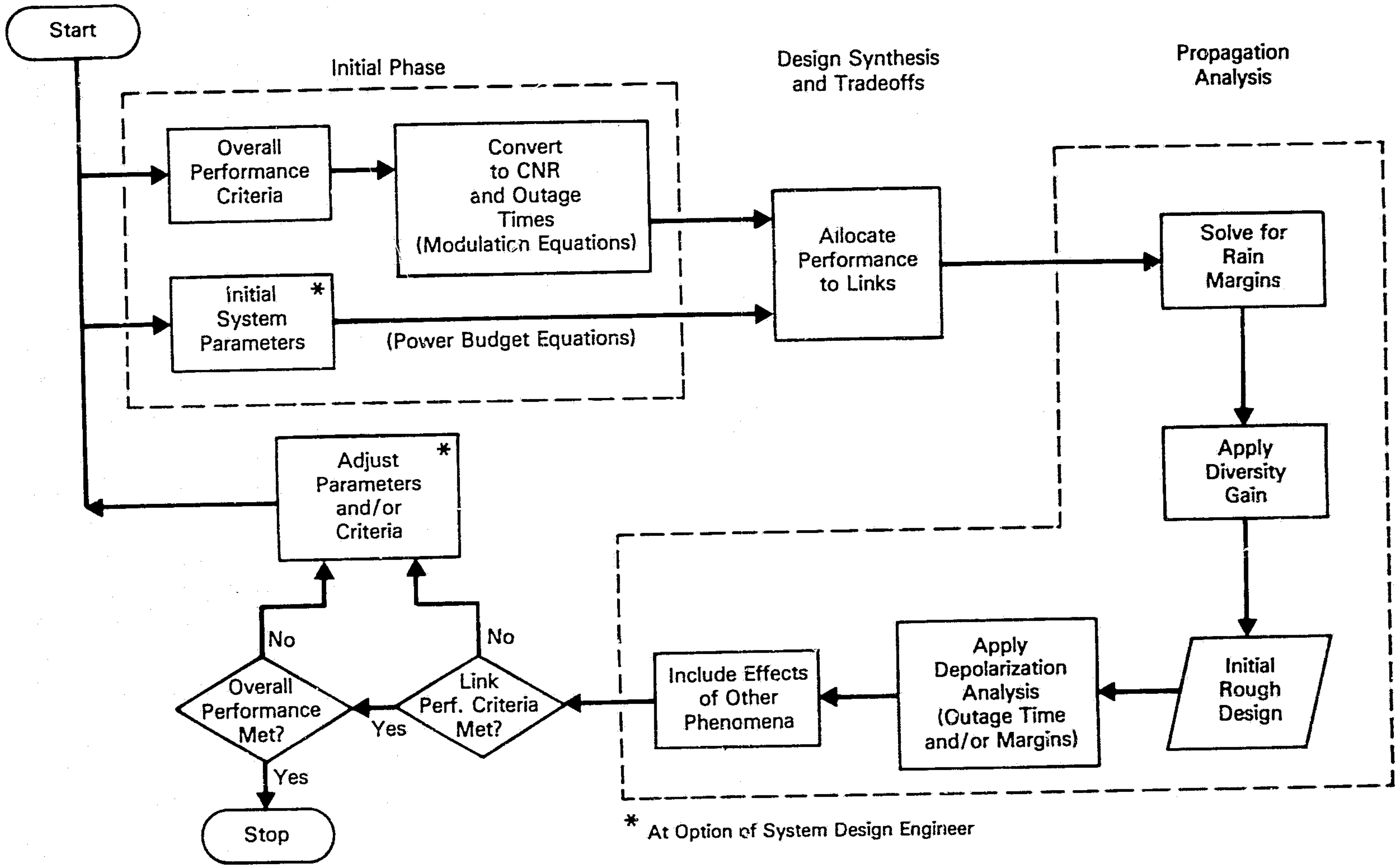

Figure 7.3-1 System Design Process

2) Apply modulation equations to convert system performance requirements to discrete distribution of the received composite CNR

3) Prepare initial design with parameters sized according to free space propagation conditions (apply power budget equations).

DESIGN SYNTHESIS AND TRADEOFF PHASE

4) Employ

   a) Composite CNR distribution of 2)
   b) System Architecture
   c) Multiple Access Equations
   d) Availability sub-allocation philosophy

   to develop distribution functions for CNR on each path.

PROPAGATION ANALYSIS AND ITERATION PHASE

5) Compute rain margins, as reduced by diversity gain, for each path.

6) Adjust system parameters according to margins given by 5). This gives a preliminary design at the feasibility concept level.

7) Apply depolarization analysis to adjust margins and/or increase the outage time values (% of time for the worst-performance level of the distributions).

8) Consider other propagation effects, adding margin to design as necessary.

9) Adjust system parameters to include all additive margins. Analyze system performance, first at the path level, then on the end-to-end performance level.

10) If performance meets requirements closely, stop. Otherwise, adjust design and repeat analysis. If design cannot be made to meet requirements, consider changing requirements.

These steps will be considered in more detail in the remainder of this chapter. The most difficult step is 4) above. It is not possible to define a step-by-step "cookbook" procedure for this phase of the design process.

As indicated above, these steps may be grouped into three major phases. It is in the third phase that propagation phenomena and data are explicitly considered. Since the emphasis of this Handbook is propagation, a detailed exposition of the first two phases is not appropriate. However, some discussion is required because both performance criteria and the system engineering are profoundly influenced by the pronounced propagation effects which apply above 10 GHz.

7.3.4 Specifics of Application, Initial Phase

The initial phase contains three steps:

1) performance requirements
2) conversion to received CNR requirement
3) initial design choices

These steps can best be illustrated by means of examples. Consider the following:

a) A digital transmission system required to have a one-way bit error rate of 10^{-6} at least 80% of the time, and a degraded mode bit error rate of 10^{-4} no more than 1% of the time

b) An analog, duplex telephone trunking system which is required to have no more than 10,000 pWOp under "nominal" conditions ($\geq$ 80% of the worst month), and $\leq$ 100,000 pWOp except for 0.3% of the time. An outage occurs if 500,000 pWOp are exceeded.

The second and third steps are performed in parallel. Conversion from the basic performance criteria to receiver CNR requirements involves application of modulation equations. To apply the equations, the type of modulation* and other system parameters such as total link capacity need to have been selected. For the above two examples:

1) The digital system is considered to operate at a link data rate of 40 Mbps, employing quaternary phase shift keying (QPSK) and Rate 3/4 convolutional encoding with Viterbi decoding. This combination is assumed to operate with an E_b/N_0 of 10.3 dB for a BER of 10^{-4}, and 12 dB for 10^{-6}. Then the corresponding CNR's measured in a 53.3 MHz (4/3 x 40 = 53.3 = symbol rate) bandwidth are 9 dB and 10.7 dB. Alternatively, the C/kT (or P_r/N_0) values are 86.3 and 88 dB-Hz, respectively.

2) The analog system is assumed to use FDM-FM with 120 channels and CCIR pre-emphasis characteristics. The following is a simplified version of the FM modulation performance equation:

$$(C/kT)_{dB} = 125.9 - 20 \log (\Delta f/f_{ch}) - 10 \log (pWOp)$$

From this, and typical parameters, the required values of C/kT are:

pWOp	C/kT	%
10,000	84.1	80
100,000	74.1	99.7
500,000	67.1	N/A (defines outage)

---

* "Modulation" is used in a generic sense here, to include coding, baseband processing, and the like.

Note however that the FM equation only applies above "threshold". The threshold values of C/kT must also be determined. Since this system has a bandwidth of about 62 dB-Hz, the threshold values of C/kT and the threshold C/kTB are related:

$$(C/kTB)_{dB} = C/kT - 62$$

Thus, if this system is implemented with a conventional FM receiver of 12 dB C/kTB threshold, a C/kT of 74 dB will be at threshold, and this becomes the outage point. With an extended threshold demodulator (6 dB threshold), the 500,000 pW0p outage noise level and the demodulator threshold occur at about the same point, which is desirable.

To complete the first phase of design, it remains only to select other, not yet defined, system parameters, such as the total number of channels, the coverage area, and so on. Many of these are determined by overall system requirements. However, power budget equations can be used to relate the values of C/kT computed in the previous step to physical system parameters. In decibel form, the basic transmission power budget equation is:

$$C/N = P_t + G_t + G_r - L_{fs} - L_1 - L_{rain} - k - 10 \log_{10} B(T_r + T_{sky})$$

where:

P_t	=	satellite transmitter power, dBW
G_t	=	satellite antenna gain, dBi
G_r	=	ground receiving terminal antenna gain, dBi
L_{fs}	=	free space path loss, dB
L_1	=	attenuation losses which are constant, especially gaseous absorption, dB
L_{rain}	=	attenuation from rain, dB
k	=	Boltzmann's constant, $dBW\text{-}K^{-1}\text{-}Hz^{-1}$

B	=	bandwidth, Hz
T_r	=	receiving terminal noise temperature, K
T_{sky}	=	sky noise temperature, K

In these first phase iterations, one assumes L_{rain}=0dB, L_1=0dB, T_{sky}=0 K or some small clear air value. Note that $(P_t + G_t)$ is the satellite EIRP, and that $(G_r - 10 \log T_r)$ is often given as a single parameter, the terminal's Figure of Merit or G/T.

For the digital example system, let us make the following assumptions about system requirements and characteristics:

1) 12 GHz downlink L_{fs} = 205 dB
2) satellite EIRP (per downlink channel) = 40 dBW
3) Earth terminal noise temperature T_r = 300 K

The values of C/N required in this system are 9 dB (≥99% of the time) and 10.7 dB (≥80% of the time). Let us solve for the required antenna gain assuming that the 10.7 dB, or 80% availability, value applies under free space propagation:

$$10.7 = 40 + G_r - 205 + 228.6 - 77.3 - 24.8$$

$$G_r = 49.2 \text{ dBi}$$

which corresponds to a 3-meter antenna. Note that the C/N threshold for "degraded" operation is only 1.7 dB lower than the nominal value. Therefore it is expedient to perform further design calculations only for the 99% point.

For the analog example system, assume the following initial parameters:

1) 20 GHz downlink L_{fs} = 210 dB
2) Earth terminal G/T = 40 dB/K
3) satellite antenna gain = 36 dBi

The nominal (≥80% of the time) C/kT is required to be 84.1 dB-Hz in a 62 dB-Hz bandwidth, or S/N = 22.1 dB. So the power budget equation becomes:

$$22.1 = P_t + 36 + 40 - 210 - 228.6 - 62$$
$$P_t = -10.5 \text{ dBW}$$

This preliminary value has little significance, by itself. If the other parameters (G_t and G/T) are "frozen", then any margin needed in the system will have to come by increases in P_t. Such tradeoffs will be made later in the design process.

7.3.5 Design Synthesis and Tradeoff Phase

A general theory and a methodology for this phase does not exist at this time; further study is needed. Although the translation of overall performance objectives into individual link objectives has been studied and resolved for line of sight systems (Parker-1977 and GTE-1972), and for satellite systems at lower frequencies (CSC-1971), the mathematical tractability for those cases depended on the assumptions that fading statistics are log-normally distributed, and very deep fades are extremely rare. These assumptions do not hold for the present problem. We will not treat this matter in detail here. The examples will be used to illustrate the types of simplifications which typically are made for satellite systems operating above 10 GHz.

At this point in the design procedure we have two functionally related parameters: a required composite C/N value, and the percentage of time for which this C/N applies. There may be several points of this function (the cumulative probability distribution function of C/N) specified. At some small percentage of time, the system is considered to be unavailable. At some larger percentge of time, a form of "degraded" operation might be defined, corresponding to a higher C/N value than the outage C/N.

For both outage time calculations and C/N, there are two important factors which must be considered in satellite communications systems:

- Simplex versus Duplex Service.
  On duplex links, an outage is caused by an outage in either direction. Composite C/N requirements apply for each direction; the C/N achieved in the circuit at any particular time is less than or equal to the poorer of the two C/N's.

- Bent-Pipe versus Processing Satellite Repeater.
  Although both repeater types add up and downlink, outages, what constitutes an outage may differ. The C/N received at the ground is computed differently in the two cases.

7.3.5.1 <u>Suballocation of Outages and Signal to Noise Ratio.</u>

One important element in this phase is the sub-allocation of outages. We have a specification on the permitted outage time for a service or circuit, which comprises 2, 4, or perhaps more links. It is clear that in general

$$\text{Outage total} = \sum \text{link outages} + \begin{pmatrix}\text{jointly} \\ \text{determined} \\ \text{outages}\end{pmatrix}$$

The definitions of link outages are usually obvious once the system architecture has been defined. If the permitted total outage time is small (<1%), the jointly determined outages are extremely small and can be ignored. For example, if $(S/N)_{composite} < 10$ dB is an outage, then for a bent pipe repeater either $(S/N)_{up} < 10$ dB or $(S/N)_{down} < 10$ dB would constitute link outage events. Now, a variety of combinations (e.g., $(S/N)_{up} = 13$ dB and $(S/N)_{down} < 13$ dB) can also result in an outage condition. However, assuming uncorrelated statistics and a small percentage of time criterion, these joint contributions can be ignored with only slight error, since they are very small. Therefore it is reasonable for the initial design, even with bent pipe repeaters, to suballocate the total outage time to up- and downlinks according to the rule

$$1 - \begin{pmatrix}\text{total}\\ \text{availability}\end{pmatrix} = 2 - \left[\begin{pmatrix}\text{uplink}\\ \text{availability}\end{pmatrix} + \begin{pmatrix}\text{downlink}\\ \text{availability}\end{pmatrix}\right]$$

In general, the sub-allocation of signal to noise ratios among the several links, given a composite* desired C/N, is more difficult. For example, suppose we want a composite C/N of 20 dB to exist under "nominal" conditions (e.g. median value). What should the C/N values be on each link? Again, this is a synthesis problem, difficult to solve in general. Whereas for outage time we dealt with a small percentage times and so could ignore joint effects, here we may be dealing with the frequently present nominal values, so joint statistics may be important. The degree of importance depends upon the system architecture. Both the multiple access techniques and the processing used (e.g., demodulation and remodulation on the spacecraft) affect the relationships between the individual link statistics and the statistical distribution of the received C/N.

Fortunately, most initial system designs are carried out according to an outage time philosophy. This is particularly appropriate in digital systems where only a few dB separate nominal and barely acceptable performance. The nominal performance <u>analyses</u> (not syntheses) are performed in iterations subsequent to the initial design. These performance analyses

---

* The composite C/N is the C/N received at the ground terminal.

must not be neglected, however, since a system design that meets a particular outage or availability criterion does not necessarily meet its other performance criteria (e.g., nominal performance). This is particularly important in analog systems where there can be a wide gap between what is considered an outage and what is required most of the time. Since it appears that most satellite systems being designed for above 10 GHz are digital, this difficulty is perhaps academic. In practice, the use of availability alone, or in conjunction with outage duration characteristics, is prevalent in the design of such systems.

In Table 7.3-1, we give the simplifying rules of thumb which may usually be employed for suballocation of outage time, T_{OUT}. In the duplex case, the exact value of T_{OUT} relative to its upper and lower bounds depends on the type of repeater and on the joint statistics of outage (i.e., the correlations between outages). The lower bound will apply if a perfect correlation of outages exists on the up- and downlink to a single terminal.

7.3.5.2 Further Development of Design Examples. For the digital system example, the following assumptions are made:

1) Initial design will be based on the outage value of C/N (9 dB), since there is only a 1.7 dB difference between the nominal and outage values.

2) The system will be assumed to operate in a simplex (one-way) mode for purpose of availability calculation (the necessary acknowledgments of data are assumed to occur at much lower data rates, therefore much higher availability).

3) TDMA is assumed. Therefore power sharing in the repeater is not a problem.

4) For initial system design, we will split the total outage time evenly between up and downlinks. This is the worst-case situation.

Table 7.3-1
Outage Time Allocation

Allocation Relations:

<u>Simplex Circuit Outage</u>

$$T_{OUT} = T_{AS} + T_{SB}$$

<u>Duplex Circuit Outage Bounds</u>

$$T_{AS} + T_{SB} + T_{BS} + T_{SA} \geq T_{OUT} \geq \text{Larger of} \begin{Bmatrix} (T_{AS} + T_{SB}) \\ \text{or} \\ (T_{BS} + T_{SA}) \end{Bmatrix}$$

Definition of Terms:

Total Outage Time	: T_{OUT}
Uplink outage, Terminal A to Satellite	: T_{AS}
Downlink outage, Satellite to Terminal B	: T_{SB}
Uplink outage, Terminal B to Satellite	: T_{BS}
Downlink outage, Satellite to Terminal A	: T_{SA}

5) Nominal (long term) propagation characteristics will be assumed to apply, on the average, on both up and downlinks at the same times. Outage level fades in up and down directions will be assumed uncorrelated.

6) No terminal diversity will be employed.

Since assumptions 1 and 4, especially, greatly simplify the design procedure in this example, there is little work needed at this phase. It is perhaps useful, however, to do an uplink power budget analysis under the following additional system assumptions:

- G_S = satellite uplink antenna gain = 33 dBi
- T_S = satellite receive noise temperature = 1000 K
- L_{fs} = free space loss = 206.4 dB
- G_t = terminal transmit antenna gain = 50 dBi

Suppose the ground station transmitter has 1 watt (0 dBW). Then

$$C/N = 0 + 50 + 33 - 206.4 + 228.6 - 77.3 - 30 = -2.1 \text{ dB}$$

Because of assumption 4) above, and since the up and downlink frequencies are similar, we desire the nominal uplink C/N to be 3 dB larger than the composite 11 dB previously given. Since P = 0 dBW gives C/N = -2.1 dB, to obtain C/N = 14 dB, a P of about 16 dBW, or 40 watts, is required in the absence of margin for rain and other propagation effects (to be added in the next phase).

For the analog example, the following assumptions are made:

1) Initial system sizing will assume that the uplink and the downlink at a given terminal reach threshold (outage) simultaneously, so that both directions of a duplex path are simultaneously lost. There is no need to be capable of transmitting when one cannot receive.

2) Design and link calculations will be performed on a worst-link basis. That is, we will design for the link interconnecting two terminals in the same rainy area. (In an actual system design, the various links would have to be individually treated to come up with total system design parameters. With complex systems, computer assistance would be necessary).

3) FDMA power sharing will be calculated on the basis that at the time when the given uplink is experiencing a fade, all other uplinks are operating at their nominal (unfaded) levels.

4) Dual site diversity will be applied for downlinks except for locations where litle rain occurs. We assume diversity will not be used to enhance uplink reliability.

To further develop this example, the following considerations or tradeoffs must be addressed either at this stage or later in the process:

1) Earth terminal antenna gain and receiver noise temperature. Here, assume T = 200 K, so that G_r = 63 dBi at 20 GHz. Then G_t = 66.5 dBi at 30 GHz.

2) Satellite receive (uplink) G/T. We will initially assume a modest value of 3 dB for this parameter.

3) Number of trunks (120 channels each) which share each repeater passband. This parameter could be selected now, a priori, or it can be a result of later tradeoff calculations. Here, we defer the selection.

The uplink power budget can be calculated here on a first-cut basis. For a normalized 1 watt (0 dBW) transmitter,

$$C/kT = 0 + 66.5 + 3 - 213.5 + 228.6 = 84.6 \text{ dB}$$

This is almost exactly the 84.1 dB C/kT needed on a composite basis to achieve 10,000 pW0p (the nominal performance criterion). To this, margins must be added, of course.

It should be evident by now that, even prior to explicitly incorporating the various propagation elements, the system design process involves an iterative and interactive series of choices of parameter values. Each choice must be tempered by pragmatic considerations. There are in the above examples numerous unstated assumptions. For example, for the 12/14 GHz digital system, the earth terminal antenna diameter of about 3 meters is appropriate for a direct user to user application. Subsequent tradeoffs might influence a change to, say, 5 meters at most. It is not feasible, nor appropriate, to set down all of these system engineering considerations in this Handbook.

7.3.6 Propagation Analysis and Iterations Phase

7.3.6.1 Compute Rain Margin (less diversity gain) and Adjust System Parameters Accordingly. The rain margin is the increase in system transmission parameters (such as power or gain) needed to offset the attenuation caused by rain and other precipitation. Note that since precipitation also increases the effective noise temperature on downlink paths, the margin should include this effect as well. If the system employs diversity (particularly, but not exclusively, space diversity), there is an effective "diversity gain" which can be obtained. This diversity gain can be subtracted from the rain margin. All of these calculations are described in detail in Chapter 6 of this Handbook. The (possibly adjusted) rain margins must be applied on the up and downlinks in accordance with the performance suballocation decisions made in the previous phase. Once again, this is best illustrated through the examples.

We address the digital system example first. Assume the earth stations are in rain climate region D_3 and the elevation angle is 20^o. From Chapter 6, the rain rate exceeded 0.5% of the time is 7 mm/hr. For this case, we calculate a rain path length of 11 km, and the procedure in Figure 6.3.1 gives an attenuation value of 2.9 dB for 0.5% of the time. A similar value may be obtained by using the graphical procedure in Engelbrecht (1979). Thus, if the up and downlink each are provided with about 3 dB of margin, the system outage probability should be below 1%*. If we wish to leave the terminal antenna size alone, the additional margin for the downlink would need to be provided by increasing the satellite EIRP. Instead, we choose the other alternative, noting that an increase in antenna size to 5 meters would provide 4.4 dB more gain. Therefore, the initial design will employ a 5 meter antenna. (Note that system users located in drier locations may get by with 3 meters.) On the uplink, where a 40 watt transmitter was previously specified, an increase is needed. Using rationale similar to that for the downlink, the transmitter size is increased to 100 watts, for 4 dB of margin.

For the analog example, assume rain climate region D_3 and a 20^0 elevation angle. Then the rain rate exceeded 0.15% of the time is 18 mm/hr, and the attenuation predicted is 18.4 dB at this percentage. From Figure 6.5-3, up to 12 dB of diversity gain could be obtained at large separations. Here, we will assume about 10 dB is obtained, so that the net equivalent attenuation exceeded only 0.15% of the time is 8.4 dB. When the rain attenuation is 18.4 dB, the sky noise is about 240 K, so the effective noise temperature of the earth terminal is increased by this amount. Consequently, the received C/N is degraded by a total of 12 dB, 0.15% of the time. Recall, however, that C/N for the overall link 0.3% of the time (i.e., the degraded mode) is allowed to be 10 dB poorer than the nominal value. Therefore, only 2 dB margin is needed above the previously calculated system values. We will choose to acquire this through an increase in satellite transmitter power. The satellite transmitter power was previously computed to be -10.5 dBW. To

---

* Note that we are working here with long term (percent of the year) statistics. In some cases, this may be misleading because the worst-month availability can be much lower than the annual average availability.

assure that the minimum acceptable C/N exist on duplex circuits for 99.7% of the time, this power value (for each downlink) should be increased to -8.5 dBW. Now we can determine how to share the satellite channels. Given that FDMA requires "backed off" operation for linearity, and that solid state transmitter technology is limited to a few watts, we may decide that about 8 trunk-paths (4 duplex connections) should be established per satellite transponder channel. Following established practice at lower frequencies, these transponder channels will be 35 to 40 MHz wide.

For the uplinks at 30 GHz, scaling of attenuation using the method in paragraph 6.3.4.3. may be employed. Specifically,

$$\frac{A(30)}{A(20)} \approx \frac{a(30)}{a(20)} + \frac{0.162}{0.626} = 2.6$$

Since diversity is initially assumed not to be employed on the uplink, the path attenuation at 20 GHz, A(20) is 18.4 dB. Then A(30) = 47 dB. Previously, a 0 dBW transmitter was shown to yield an uplink C/kT of 84.6 dB - Hz with no margin. To obtain the "degraded" value of 74 dB - Hz, then, a 37 dBW (5000 W) transmitter would be needed. This is not practical, so we are faced here with a system trade-off. To avoid the 5000W transmitter, either the satellite G/T value must change, or the assumption about no diversity on the uplink must be abandoned. Consideration of technological factors is required. A dramatic increase in the G/T is not practical without use of pencil-beams on the spacecraft, and 30 GHz earth terminal transmitter tubes larger than about 1 kW are impractical. Therefore, it is concluded that diversity will be needed on the uplink.* Because the attenuation value is so large (47 dB), the concept of diversity gain is not useful or accurate. Instead, diversity advantage or improvement factors would be useful. This data is less generally available. But because uplinks are usually conservatively designed, rough estimation of uplink diversity performance is acceptable.

---

* This presents a minor technology problem of its own: the switchover of uplink transmissions is more difficult and potentially more disruptive to circuit integrity than diversity switching of downlink signals.

Suppose we stipulate that 100 watts is available per uplink and that C/kT = 80 dB - Hz or better is acceptable. Then up to 24.6 dB of attenuation can be accommodated, which corresponds (at 30 GHz) to a single terminal outage of less than 0.5%. Thus a diversity advantage of about 4 would be needed. Most available data (Engelbrecht-1979 and Hogg and Chu-1975) indicates that such values should easily be obtainable.

7.3.6.2 <u>Apply Depolarization Analysis.</u> The transmission of two orthogonally polarized signals from one satellite is employed to double the spectrum utilization by frequency reuse. Not every system, of course, will need to employ this technique, in view of the additional complexity and the added potential contribution to propagation caused outages.

The term "depolarization" is commonly employed to designate the reduction in cross-polarization discrimination seen at the receiving location under some propagation conditions. When this occurs, each of the two received channels (polarizations) contains an interference signal from the other polarization. Therefore, this signal is similar to interference which may occur from other satellites, terrestrial systems, or other beams of the same satellite.

Depolarization is caused by rain, as well as by ice layers, in the troposphere. The rain can cause strong depolarization events, in which the cross-polarization discrimination drops to 20 or 15 dB. Ice depolarization is quantitatively milder, but appears to occur more often. It is therefore convenient to treat two cases of depolarization effects, strong and weak.

Strong depolarization events should be correlated with deep attenuation events, since both stem from the same physical cause, namely rain. Both the deep attenuation fades and the strong depolarization intervals can cause outages. In order to perform a composite outage analysis, it is convenient to have joint statistical data, for example in the form introduced by Arnold, et. al. (1979). In Figure 7.3-2, we show a hypothetical version of such a joint outage plot. The parameter on the curves represents the threshold value of depolarization above* which the given system is inoperable,

---

* Here depolarization in dB is given a minus sign so that the term "exceeded" can correctly apply.

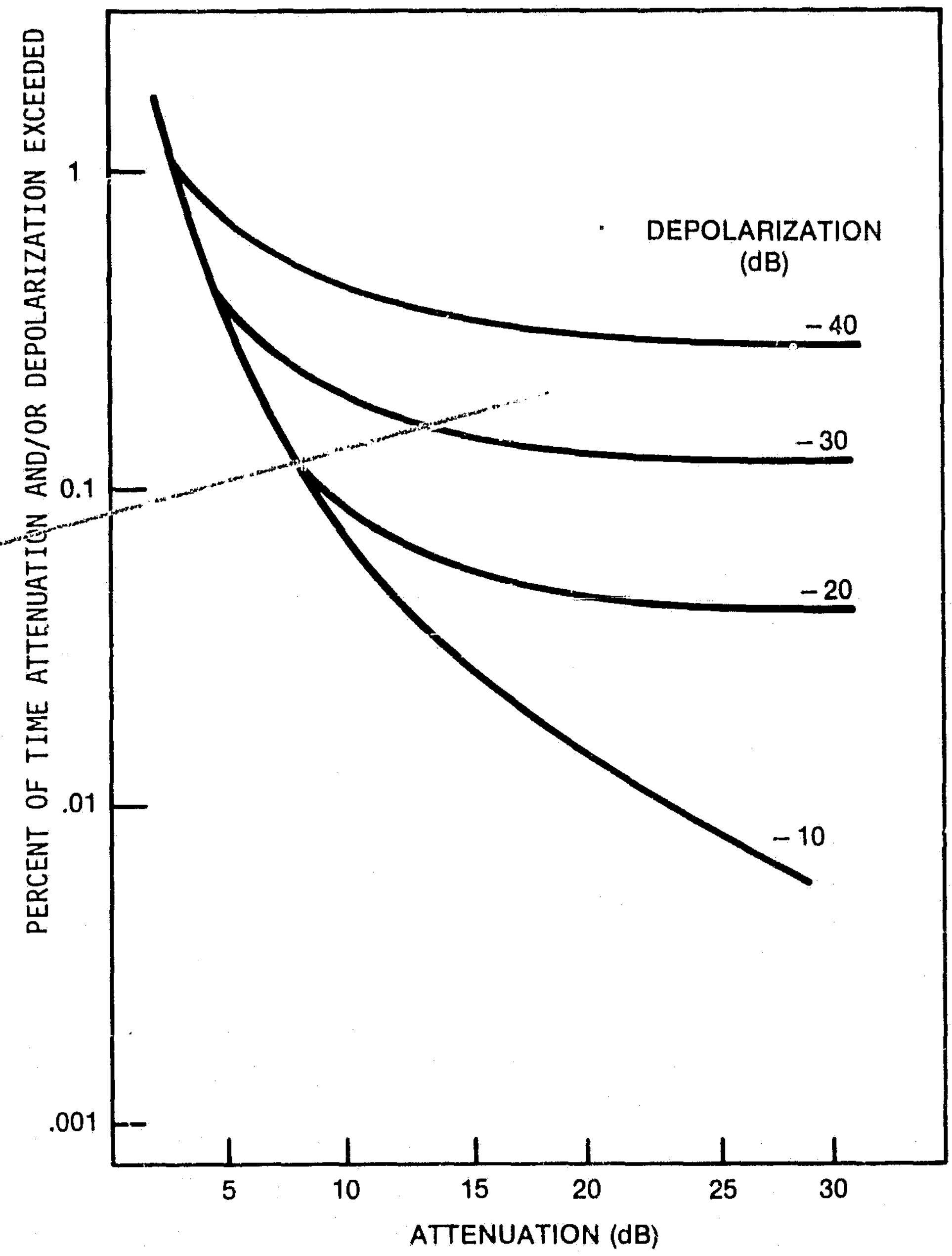

Figure 7.3-2. Composite Outage Versus Attenuation with Depolarization as a Parameter (Hypothetical Case)

i.e., an outage exists. It can be seen that there may be many combinations of attenuation and depolarization that will result in any given probability of outage. Typically, the threshold depolarization is not an independent variable, but is fixed by the modulation parameters. Then, it can be immediately determined whether the previously computed rain margin is sufficient for the desired system availability.

In most cases, such joint statistics are not available. Section 6.7 presents methods for prediction of depolarization statistics, including functional relationships between attenuation and depolarization statistics. Using these prediction methods, it is possible to approximate curves like those in Figure 3, though the exact shape of each curve will not be mathematically precise. For example, the curve for "percent of time attenuation or depolarization exceeded" for the depolarization parameter equal to -10 dB is essentially the same as the attenuation versus percent exceeded curve alone (since depolarization is effectively "never" so large). For intermediate values of the depolarization parameter such as -25 dB, the appropriate curve is horizontally asymptotic to the percentage of time that depolarization alone exceeds the percentage. Each such horizontal asymptote then smoothly curves into the attentuation only curve. Only this curved portion involves estimation by eye, and will introduce negligible error for initial design purposes.

The effect of diversity in reducing depolarization outage has not been studied to date. The procedure outlined above applies to single-terminal attenuation and depolarization. When outages from attenuation and depolarization are each of the same order of magnitude, it is not clear that the concept of diversity gain is appropriate, since diversity should reduce depolarization outages as well.

In contrast to the "outage" values of depolarization, the smaller but more frequent values of depolarization can be accommodated in the system power margins. In almost all satellite communications systems, the thermal noise is the dominant portion of the total noise and interference. Small cross-polarized components may therefore be treated like any other interference. Castel and Bostian (1979) make a case for incorporating the depolarization in digital systems as an equivalent C/N degradation, using the classic "Rosenbaum bound" (Rosenbaum-1970 and Rosenbaum, Glave-1974).

Similar procedures apply in analog systems. In practice, the equivalent noise powers from all thermal noise and interference sources, including intermodulation and depolarization, are added together, in pW0p for example, to produce a total link noise power which must meet the appropriate performance criterion (e.g., 10,000 pW0p). This adjustment to the system noise budget results in a further modification to the previously calculated system parameters. For example, the INTELSAT V system has been designed to meet a 10,000 pW0p criterion (Gray and Brown-1979). The composite received downlink must meet 7500 pW0p, with the remaining 2500 allocated to terrestrial and intersystem interference. This 7500 pW0p corresponds to a C/N of about 14 dB, yet the composite downlink thermal noise C/N is about 5 to 8 dB larger than this value, to allow for intermodulation products and for frequency reuse interference.

We do not consider here the employment of adaptive techniques to cancel cross-polarized components and to enable systems to operate at high levels of depolarization (e.g., 10 dB). By using such techniques, one pushes the outage threshold level of depolarization back to a value which effectively "never" occurs, so that the outages stem from attenuation alone.

7.3.6.3 Apply Lesser Propagation Effects. Attenuation effects from other than precipitation generally are of "second order" for system design purposes. Indeed, they may not need to be considered in the first iteration. They will be needed, however, for later, more accurate, estimates of performance.

"Clear air" attenuation, in excess of free space path loss, will typically be less than one decibel except at the shortest millimeter wavelengths (or near absorption bands). These values may be calculated as shown in Figure 6.2-3. Adjustments are then made to the nominal performance power budgets (previously computed on a free-space-loss basis).

Cloud, fog, and dust attenuation factors may be very difficult to incorporate unless adequate statistics for their occurrence are available. These phenomena have significant effect only in unusual system designs, because both their magnitude (in dB of loss) and their frequency of occurrence are relatively low. In general, a system with a fair amount of rain margin will also have sufficient margin to operate through clouds. In addition, clouds and fog are not likely to occur so often as to influence the nominal performance value (50 or 80% of the time). Where appropriate, however, the system designer may incorporate an additional margin to allow for these attenuation effects. Similarly, signal fluctuations and antenna gain degradations, as treated in Paragraph 6.6, are relatively small and need be considered only in later iterations of performance analysis, at which time the effect can be accounted for through small margin adjustments to the nominal path loss.

7.3.6.4 Adjust System Parameters and Analyze System Performance. In the foregoing, adjustment of system parameters has been carried out simultaneously with the development of the examples. The system designer may choose to use this approach, or to defer these adjustments until this point in the process. To do this in an organized manner, one should accumulate all propagation impairments which are (or can be equated to) attenuations or losses into a composite margin. Increases in sky noise, and the interference components, can be equated to losses in signal power, as previously discussed. This composite margin will be offset by power or gain adjustments. These margins and consequent system parameter adjustments are applied to the nominal system performance budget. In the analog example, this was the 10,000 pWOp criterion. Separately, the more severe effects which cannot be offset by (reasonable) margin are treated according to an outage criterion, i.e., by addition of outages contributed by each. Adjustments to system parameters resulting from a deficiency in meeting this criterion often involve fundamental changes in qualitative system design rather than simply margin changes. As an example, if the outage time is excessive because the system concept is very sensitive to mild depolarization, it may be necessary to use a different type of polarization, adaptive polarization techniques, or a different modulation technique.

In order to illustrate this step of the design process using the examples, a recapitulation of the constraints and parameters determined up to this point is in order. This is done in Table 7.3-2 for the digital system, and in Table 7.3-3 for the analog system.

When the digital system analysis is now carried out in detail using these parameters, it is found that the downlink C/kT is inadequate to provide the nominal composite C/kT of 88 dB-Hz. The previous work assumed that in order to provide adequate margin against rain outages, 5-meter antennas could be employed instead of 3-meter. But now we see that this leaves the 3-meter terminals with inadequate performance. The satellite EIRP is adjusted upwards to 43 dBW to correct this. The power budgets, incorporating this one change, are shown in Table 7.3-4. It would also be possible to reduce somewhat the terminal transmitter power. Instead, if it is left at 100 watts, the predicted path availability will be improved, or extra margin will be available for other unpredicted phenomena.

With respect to the analog system, notice that we have increased the transponder power to 3 watts*. The final analysis of this system involves a number of detailed parameters and data which can only be roughly estimated at this time. For example, interference from other satellite and terrestrial systems has not been included here. The power budgets and pertinent assumptions are in Table 7.3-5 . Note that power control of uplinks is necessary. The budgets assume each uplink is set at a nominal C/kT of 90 dB-Hz. Under clear air conditions, this is some 12 dB below the maximum power capability of the earth terminal. However, it would not be advisable to reduce this power requirement, because the margin is needed to achieve the required availability. This system was assumed to not employ frequency reuse through dual polarization, but adjacent antenna beams may be alternately

---

* After backoff for intermodulation reduction, this represents a nominal 10 to 15 watts saturated power capability.

Table 7.3-2 Digital System Summary

Specified Performance	P_e	$\leq 10^{-4}$	$\geq$ 80% of the time
		$\leq 10^{-6}$	$\geq$ 99% of the time (outage time 1%)

System Characteristics

- 40 Mbps, QPSK with coding
- Necessary Received C/kT for $P_e = 10^{-6}$: 88 dB-Hz
  10^{-4} : 86.3 dB-Hz
- 12 GHz down/14 GHz up
- Satellite

  EIRP = 40 dBW
  G/T = 3 dB/K
- Earth Terminal
  T_r = 300K
  G = 50 dB (dry areas)
  54 dB (rainy areas)
  Transmitter Power= 100W
- TDMA (no power sharing or intermodulation in repeater)

Table 7.3-3 Analog System Summary

Specified Performance Criteria	≤10,000 pWOp ≥80% of the time ≤100,000 pWOp ≥99.7% of the time "Outage" exists when 500,000 pWOp is reached
Modulation and Performance	120 channel FDM-FM trunks pWOp — C/kT 10,000 — 84.1 100,000 — 74.1 500,000 — 67.1
System Parameters	20 GHz downlinks, 30 GHz uplinks Dual (site) diversity up and down
Satellite	Antenna gain (transmit): 36 dBi Receive G/T: 3 dB/K Total transmit power per Transponder (with Backoff): 5 dBW Number of trunks (multiplex carriers per transponder): 8 Transponder channel bandwidth: 40 MHz
Earth Terminal	Receive Noise Temperature — 200K Receive Antenna Gain — 63 dBi Transmit Antenna Gain — 66.5 dBi Transmitter Power — 100 watts per trunk

Table 7.3-4. Digital Example Power Budgets

	UPLINK	DOWNLINK	COMMENTS
Transmit Power, dBW	20		
Antenna Gain, dBi	50		
EIRP, dBW	70	43	
Free Space Path Loss, dB	-206.4	-205	(G/T is 29 with optional 5-meter antenna)
G/T, dB/K	3	24.8	
Boltzmann's constant	-(-228.6)	-(-228.6)	
C/kT, dB-Hz	95.2	91.4	
Nominal Propagation Loss Allowance	-1	-1	Rough estimate
Nominal Link C/kT, dB-Hz	94.2	90.4	Composite C/kT = 88.9 dB-Hz
Outage threshold Value for that Link	88.5	87.2	Assumes other link is at nominal. Composite C/kT for outage 86.3 dB-Hz
Margin for Propagation Effects, dB	5.7	3.2	

Table 7.3-5. Analog Example Power Budgets

	UPLINK	DOWNLINK	COMMENTS
Transmit Power, dBW	20	-4	5 dBW - 9 dB for sharing of 8 carriers
Antenna gain, dBi	66.5	36	
Free space path loss, dB	-213.5	-210	
G/T, dB/K	3	40	
Boltzmann's constant	-(-228.6)	-(-228.6)	
Clear air and other nominal propagation losses, dB	-2	-1.5	
Imperfect Power Control losses, dB	N/A	-2	
Nominal Link C/kT, dB-Hz	102.6	87.1	
Composite Received C/kT	N/A	85.3	Up and down combined
Intermodulation $(C/I)_o$	N/A	91	-25 dB intermods over 4 MHz
Composite Received C/N_o	(Normal operating point 90 dB-Hz)	84.3	Thermal and intermods
Degraded Value, C/N_o	80	74.1	$\leq$.15% of time
Allowable Margin for Propagation Degradations	22.6	10.2	UPLINK: Single terminal availability $\geq$99.5% and diversity improvement factor of 4 assumed available DOWNLINK: Plus $\geq$8 dB diversity gain to obtain 18 dB margin for $\leq$.15%

C-4

polarized, and operate on the same frequencies. Any interference from these adjacent beams would have to be added to the composite downlink C/N calculation. If this system were so configured, it would be able to tolerate considerble depolarization. For example, by staggering the carrier frequencies of trunks on alternate polarizations within the same 40 MHz channel, 15 dB cross-polarization isolation would be adequate, and outages from depolarization would not be significant. Then if -35 dB depolarization from ice were to be included, the normalized per hertz equivalent (assuming B = 2 MHz = 63 dB-Hz) C/I_0 would be 35 + 63 = 98 dB-Hz, thus degrading the composite C/kT about 0.2 dB.

7.3.6.5 Iterate System Design and Analysis. This phase needs little explanation. If the initial design does not, per analysis, deliver the level of performance required, the design must be changed in some way. Various trade-off techniques may be used to assist the design engineer in deciding what to change, but there is no substitute for good system engineering judgment. In some cases, a critical look at the system requirements themselves must be taken. The examples that have been presented here were simplified in several respects, so that the several modifications to initial design assumptions could be made as the design proceeded. In an actual, real-world design, more refined analyses and iterations would be needed. Both of the examples used a particular terminal rain rate and elevation angle assumption. For a real system with a distribution of terminals in various locations, considerable refinement of the approaches would be possible, and could have significant impact in reduction of power requirements and/or outage times. Also, the examples did not illustrate the consideration of criteria other than long term (outage percentage) statistics.

7.4 REFERENCES

Arnold, H.W., D.C. Cox, H.H. Hoffman, and R.P. Leck (1979), "Characteristics of Rain and Ice Depolarization for a 19 and 28 GHz Propagation Path from a COMSTAR Beacon," Record, Int'l Conf. on Comm. (IEEE CH 1435-7/79/0000-0220), June.

Brayer, K., (1978), "Time, not Throughput, for Net Designs. Part 1: Techniques," Data Communications, October.

Castel, R.E. and C.W. Bostian (1979), "Combining the Effects of Rain-Induced Attenuation and Depolarization in Digital Satellite Systems," IEEE Transactions Aerosp. Elect. Syst., Vol. 15 No. 2, p. 299-301, March.

CCIR (1978) "Allowable Noise Power in the Hypothetical Reference Circuit for Frequency-Division Multiplex Telephony in the Fixed Satellite Service," Recommendation 353-3, XIVth Plenary Assembly, Kyoto.

Computer Sciences Corp. (CSC) (1971), "Automated Satellite Terminal Control," RADC-TR-70-229, Volume I, for U.S. Air Force, Rome Air Development Center, March.

Engelbrecht, R.S. (1979), "The Effect of Rain on Satellite Communications Above 10 GHz," RCA Review, June.

General Telephone & Electronics (GTE) Lenkurt Inc. (1972), Engineering Considerations for Microwave Communications Systems.

Gray, L.F. and M.P. Brown (1979), "Transmission Planning for the First U.S. Standard C (14/11 GHz) INTELSAT Earth Station," COMSAT Technical Review, Volume 9, Number 1, Spring.

Hogg, D.C. and T.S. Chu (1975), "The Role of Rain in Satellite Communications," Proc. IEEE, September.

Kirk, K.W. and J.L. Osterholz (1976), "DCS Digital Transmission System Performance," Defense Communications Engineering Center (DCEC) Technical Report No. 12-76, November.

Northrop, G.M. (1966), "Aids for the Gross Design of Satellite Communication Systems," IEEE Transactions Comm., Vol. COM-14, February.

Parker, D.E. (1977), "Design Objectives for DCS LOS Digital Radio Links," Defense Communications Engineering Center (DCEC) Engineering Publication No. 27-77, December (DDC AD Number A065354).

Rosenbaum, A.S. (1970), "Binary PSK Error Probabilities with Multiple Cochannel Interferences," IEEE Transactions on Communications, June.

Rosenbaum, A.S. and F.E. Glave (1974), "An Error-Probability Upper Bound for Coherent Phase-Shift Keying with Peak-Limited Interference," IEEE Transactions on Communications, January.

Schwartz, M., W.R. Bennett, and S. Stein (1966), Communication Systems and Techniques, McGraw-Hill.

Spilker, J.J., Jr. (1977), Digital Communications by Satellite, Prentice-Hall.